The extracellular matrix as a biomaterial to optimize skeletal muscle regeneration

Aurélie Trignol

Aurélie Trignol. The extracellular matrix as a biomaterial to optimize skeletal muscle regeneration. Tissues and Organs [q-bio.TO]. Université de Lyon, 2019. English. NNT : 2019LYSE1029 . tel-03103200

HAL Id: tel-03103200
https://theses.hal.science/tel-03103200v1

Submitted on 8 Jan 2021

N°d'ordre NNT : 2019LYSE1029

THESE de DOCTORAT DE L'UNIVERSITE DE LYON
opérée au sein de
l'Université Claude Bernard Lyon 1

Ecole Doctorale N°205
Ecole Doctorale Interdisciplinaire Science et Santé

Spécialité de doctorat :
Discipline : PHYSIOLOGIE ET BIOLOGIE DES ORGANISMES

Soutenue publiquement le 05/03/2019 par :

Aurélie Trignol

The extracellular matrix as a biomaterial to optimize skeletal muscle regeneration

---

Devant le jury composé de :

KRETZ-REMY Carole	Professeure des Universités, Université Claude Bernard Lyon 1	Présidente
ALBANESE Patricia	Professeure des Universités, Université Paris Est-Créteil	Rapporteure
KOULMANN Nathalie	Professeure du Val de Grâce	Rapporteure
LUTOMSKI Didier	Professeur des Universités, Université Paris 13	Rapporteur
CHAZAUD Bénédicte	Directrice de Recherches, INSERM	Directrice de thèse
BANZET Sébastien	Professeur du Val de Grâce	Co-directeur de thèse

“Twenty years from now you will be more disappointed by the things that you didn't do than by the ones you did do. So throw off the bowlines. Sail away from the safe harbor. Catch the trade winds in your sails. Explore. Dream. Discover.”

H. Jackson Brown Jr.

UNIVERSITE CLAUDE BERNARD - LYON 1

Président de l'Université	**M. le Professeur Frédéric FLEURY**
Président du Conseil Académique	M. le Professeur Hamda BEN HADID
Vice-président du Conseil d'Administration	M. le Professeur Didier REVEL
Vice-président du Conseil Formation et Vie Universitaire	M. le Professeur Philippe CHEVALIER
Vice-président de la Commission Recherche	M. Fabrice VALLÉE
Directeur Général des Services	M. Alain HELLEU

COMPOSANTES SANTE

Faculté de Médecine Lyon Est – Claude Bernard	Directeur : M. le Professeur J. ETIENNE
Faculté de Médecine et de Maïeutique Lyon Sud – Charles Mérieux	Directeur : Mme la Professeure C. BURILLON
Faculté d'Odontologie	Directeur : M. le Professeur D. BOURGEOIS
Institut des Sciences Pharmaceutiques et Biologiques	Directeur : Mme la Professeure C. VINCIGUERRA
Institut des Sciences et Techniques de la Réadaptation	Directeur : M. le Professeur Y. MATILLON
Département de formation et Centre de Recherche en Biologie Humaine	Directeur : Mme la Professeure A-M. SCHOTT

COMPOSANTES ET DEPARTEMENTS DE SCIENCES ET TECHNOLOGIE

Faculté des Sciences et Technologies	Directeur : M. F. DE MARCHI
Département Biologie	Directeur : M. le Professeur F. THEVENARD
Département Chimie Biochimie	Directeur : Mme C. FELIX
Département GEP	Directeur : M. Hassan HAMMOURI
Département Informatique	Directeur : M. le Professeur S. AKKOUCHE
Département Mathématiques	Directeur : M. le Professeur G. TOMANOV
Département Mécanique	Directeur : M. le Professeur H. BEN HADID
Département Physique	Directeur : M. le Professeur J-C PLENET
UFR Sciences et Techniques des Activités Physiques et Sportives	Directeur : M. Y.VANPOULLE
Observatoire des Sciences de l'Univers de Lyon	Directeur : M. B. GUIDERDONI
Polytech Lyon	Directeur : M. le Professeur E.PERRIN
Ecole Supérieure de Chimie Physique Electronique	Directeur : M. G. PIGNAULT
Institut Universitaire de Technologie de Lyon 1	Directeur : M. le Professeur C. VITON
Ecole Supérieure du Professorat et de l'Education	Directeur : M. le Professeur A. MOUGNIOTTE
Institut de Science Financière et d'Assurances	Directeur : M. N. LEBOISNE

ÉCOLE DU VAL DE GRACE

A Monsieur le médecin général Humbert BOISSEAUX

Directeur de l'École du Val-de-Grâce

Professeur agrégé du Val-de-Grâce

Chevalier de la Légion d'honneur

Officier dans l'Ordre National du Mérite

Chevalier de l'Ordre des Palmes académiques

A Madame le médecin-chef des services hors classe Catherine CRÉACH nom d'usage THIOLET

Directrice-adjointe de l'École du Val-de-Grâce

Professeur agrégé du Val-de-Grâce

Chevalier de la Légion d'honneur

Officier dans l'Ordre National du Mérite

Remerciements

Je tiens tout d'abord à remercier l'ensemble des membres du jury d'avoir accepté d'évaluer ce travail de thèse et, de par vos conseils, permis l'amélioration de ce manuscrit.

A Madame la Professeure Carole Kretz-Remy, je vous remercie pour la justesse du regard que vous avez posé sur ce travail, ainsi que pour l'honneur que vous m'avez fait d'accepter de présider cette soutenance.

A Madame la Professeure Nathalie Koulmann, merci tout d'abord d'avoir accepté d'évaluer ce travail en tant que rapporteure ainsi que pour vos remarques avisées en tant que spécialiste de la physiologie musculaire. Je vous remercie sincèrement pour votre confiance et surtout, de m'avoir enseignée que la recherche ne peut se concevoir qu'avec rigueur et bienveillance.

A Madame la Professeure Patricia Albanese, je vous remercie d'avoir accepté d'être rapporteure pour ce travail, et pour l'exigence avec laquelle vous avez fait cheminer mes réflexions.

A Monsieur le Professeur Didier Lutomski, merci d'avoir jugé ce travail en tant que rapporteur. Au-delà de vos précieux conseils, je vous remercie pour le positivisme avec lequel vous encouragez chacun à s'améliorer.

Je tiens également à remercier mes encadrants de thèse,

A Madame la Docteur Bénédicte Chazaud, merci pour l'encadrement scientifique tout au long de ce travail et pour m'avoir accueillie au sein de votre laboratoire.

A Monsieur le Professeur Sébastien Banzet, merci de m'avoir proposé ce sujet de thèse et pour les conseils techniques et scientifiques apportés durant ce travail.

A Madame la Docteur Geneviève Milon, je vous remercie chaleureusement pour vos nombreux conseils ayant permis d'améliorer ce travail, et surtout, pour la vision d'une recherche faite de rigueur, de bienveillance et de curiosité que vous continuez à transmettre à de nombreux étudiants.

A Madame la Professeure Sylvie Ricard Blum et à Madame la Docteur Christelle Bonod, je vous remercie grandement pour vos conseils scientifiques sur la matrice extracellulaire durant les suivis de thèse et pour tous vos encouragements pleins de bienveillance.

Au Docteur Cédric Thépenier, je te remercie pour les nombreuses discussions scientifiques et conseils qui ont permis d'améliorer le manuscrit ainsi que les analyses statistiques de ce travail.

Au Docteur Pierre Goossens, je te remercie tout particulièrement pour les nombreuses remarques et questions scientifiques sur ce travail ainsi que pour la préparation de la soutenance.

Je tiens à remercier toute l'équipe Environnement des cellules souches musculaires et homéostasie du muscle strié squelettique de l'Institut NeuroMyoGene, et tout particulièrement les thésards (Thibaut, Linda, Jessica, Jimmy, Sophie) pour l'entraide au quotidien. Je remercie de nouveau Jessica Bouvière, pour son remarquable travail sur la partie RGTA® ainsi que pour tous ses conseils. Merci également au Docteur Marine Théret pour son dynamisme, pour l'aide et les conseils apportés dès mon arrivée dans le laboratoire. Je remercie également le Docteur Emmeran Le Moal pour son aide, ses conseils et encouragements. Merci également à Sabrina Ben Larbi pour tout ce que tu m'as appris sur différentes techniques ainsi que pour ton aide efficace sur une partie du projet. Merci à Peggy Del Carmine pour sa grande dextérité chirurgicale et pour les injections intramusculaires. Merci au Docteur Rémi Mounier pour avoir également réalisé ces injections durant une partie du projet et pour avoir répondu à mes nombreuses questions. Merci au

Docteur François Morlé pour tous vos encouragements et les échanges sur la bibliographie. Merci au Docteur Michèle Weiss-Gayet et au Docteur Gaëtan Juban pour tous vos conseils durant mon séjour au sein du laboratoire.
Merci au Docteur Julien Courchet et au Docteur Virginie Courchet pour leur aide ainsi que pour leurs conseils sur l'anesthésie-analgésie.

Je remercie également toute l'équipe du département Soutien Médico-Chirurgical des Forces, de l'UMTI et de l'équipe H&B du CTSA pour tous vos conseils et votre gentillesse. Je remercie Emilie Rousseau pour son remarquable travail préliminaire sur la décellularisation musculaire. Merci tout particulièrement à Marie Emmanuelle Goriot, pour ta rigueur et ton enthousiasme pour travailler ensemble sur ce projet. Au Docteur Dorothée Girard, je te remercie chaleureusement pour tes nombreux conseils et encouragements durant cette dernière année de thèse. Merci également à Camille Flageollet pour ses remarques sur la partie RGTA®. Merci également au Docteur Anne Christine Mendes pour la mise au point de la lyophilisation de nos échantillons.

Au Professeure Dulce Papy-Garcia, je vous remercie chaleureusement d'avoir accepté de nous faire bénéficier de votre expertise sur les glycosaminoglycanes et d'utiliser si régulièrement votre lyophilisateur.

Merci au Professeur Denis Barritault et toute son équipe de la société OTR3. Je tiens à vous remercier pour avoir répondu à mes questions sur les molécules RGTA® que vous nous avez fournies durant ce travail.

Au Docteur Florence Poirier, je te remercie pour la réalisation des analyses protéomiques et pour les nombreux échanges pour améliorer le protocole spécifique pour la matrice extracellulaire. Merci à toute l'équipe pour l'accueil toujours chaleureux quand je venais au laboratoire et également pour ton cours privé sur les techniques de protéomique.

Je tiens à remercier le Docteur Julien Burger et l'ensemble de l'équipe du Professeur Jean Nicolas Tournier pour les acquisitions en microscopie biphotonique et pour leurs nombreux encouragements. Merci également à l'équipe Imagopole de l'Institut Pasteur pour leur gentillesse et la reconstruction des images.

Aux cliniciens du service de Médecine Physique et Réadaptation de l'Hôpital Percy pour leur aide pour mieux comprendre la prise en charge et les potentielles séquelles des patients avec perte de substance musculaire. Merci tout particulièrement au Professeur Eric Lapeyre, au Docteur Stéphanie Truffaut, au Docteur Léo Borrini et au Docteur Marie Thomas pour avoir pris de leur temps pour discuter ensemble de ce projet de thèse.

Je remercie également mon futur département Environnements Opérationnels pour l'accueil chaleureux et pour leur aide dans la préparation de la soutenance. Merci tout particulièrement au Docteur Mounir Chennaoui, au Professeur Fabien Sauvet, au Docteur Danièle Gomez-Merino, à Catherine Drogou, à Théo Vanneau et à l'ensemble de l'unité Fatigue et Vigilance. Je remercie également la Docteur Alexandra Malgoyre ainsi que l'ensemble de son unité Physiologie de l'Exercice et des Activités en Conditions Extrêmes, et tout particulièrement le Docteur Julien Siracusa pour toute son aide durant ces années de thèse. Merci également au Docteur Adrienne Anginot et au Docteur Diane Riccobono pour leur intérêt et leurs conseils sur ce travail. Je remercie également le Professeur Fréderic Canini pour sa bienveillance et ses conseils sur ce travail.

Merci également à toutes les nombreuses personnes, en particulier à Pasteur, pour leur aide à la bonne réalisation de ce travail. Je remercie mes amis, ma famille pour leur soutien et tout spécialement mon conjoint Cyril pour ses encouragements quotidiens.

Résumé

Le muscle strié squelettique possède de grandes capacités de régénération grâce à ses cellules souches, les cellules satellites. Après une lésion, le processus de régénération musculaire qui se met en place est finement régulé dans le temps et l'espace par le microenvironnement, constitué de cellules avoisinantes mais également par des éléments de la matrice extracellulaire (MEC). Cette dernière se compose de molécules structurales comme les collagènes et de composants possédant un rôle trophique comme les glycosaminoglycanes (GAGs). La MEC musculaire est peu étudiée à cause d'une organisation tridimensionnelle complexe rendant son exploration difficile. Lors d'une lésion avec perte de substance musculaire, la régénération est altérée, associée à une fibrose et une inflammation chronique. Ce type de lésion est fréquemment rencontré en traumatologie mais survient également chez le blessé de guerre. Malgré un traitement optimal, une invalidité fonctionnelle persiste chez ces patients. L'utilisation d'un biomatériau décellularisé, constitué de MEC pourrait fournir ce support physique et trophique faisant défaut dans ce type de lésion.

Dans ce travail, nous avons entrepris l'établissement d'une MEC d'origine musculaire et nous avons établi un protocole de décellularisation permettant d'obtenir un biomatériau conservant l'architecture spécifique de la MEC musculaire avec une élimination de la majorité des antigènes cellulaires afin d'éviter une réponse immunitaire délétère après implantation. Néanmoins, le protocole retenu ne permet de conserver certaines molécules trophiques d'intérêt comme les GAGs.

Les « ReGeneRaTing Agent$^{®}$» (RGTA$^{®}$) sont des mimétiques fonctionnels de ces GAGs, utilisés en clinique pour améliorer la cicatrisation cutanée et cornéenne. Ces mimétiques conservent une capacité de liaison aux facteurs de croissance avec une résistance aux dégradations enzymatiques. Nous avons évalué l'utilisation de ces molécules au cours de la réparation musculaire, dans un modèle *in vivo* chez le rongeur. Nous avons réalisé une analyse histologique précoce (8^{e} jour de régénération) mettant en évidence une augmentation du nombre de noyaux par myofibre en faveur d'une augmentation de la fusion, validée également *in vitro* sur des progéniteurs musculaires. Nous avons également observé une augmentation du nombre de vaisseaux, suggérant une amélioration de l'angiogenèse. Le nombre de gouttelettes lipidiques, marqueur d'une mauvaise régénération, était en diminution. L'exploration histologique plus tardive (28^{e} jour de régénération) n'a retrouvé que l'augmentation du nombre de vaisseaux en faveur d'un effet durable sur l'angiogenèse.

Ces RGTA$^{®}$ peuvent être couplés aux biomatériaux et sont particulièrement résistants dans un environnement inflammatoire pouvant être rencontré dans les lésions avec perte de substance musculaire. Des chimiokines et des facteurs de croissance pourront également être ajoutés au biomatériau matriciel afin de favoriser la migration des différents progéniteurs nécessaires à une néoformation musculaire. L'efficacité thérapeutique de ces biomatériaux optimisés nécessitera d'être évaluée dans un modèle *in vivo* de perte de substance.

Mots-clés: régénération musculaire, matrice extracellulaire, glycosaminoglycanes, biomatériau décellularisé

Institut NeuroMyoGène – UMR 5310 – INSERM U1217 Université Claude Bernard Lyon 1
Faculté de Médecine et de Pharmacie, 8 Avenue Rockefeller
69008 Lyon

Institut de Recherche Biomédicale des Armées
INSERM UMRS-MD 1197
Antenne CTSA, 1 rue du lieutenant Raoul Batany
92140 Clamart

Abstract

Skeletal muscle exhibits high capacity for regeneration after an injury that relies on resident stem cells. Muscle regeneration is tightly regulated by both the immune response and other resident cells, as well as by cues from the local extracellular matrix (ECM), contributing to a coordinated repair process. Muscle ECM is a network of structural macromolecules with a large majority of collagens and trophic molecules such as glycosaminoglycans (GAGs). In the skeletal muscle tissue, ECM was overlooked due to its complex organization making investigations difficult. Muscle regenerative ability can be overtaken in large muscle wasting, such as in volumetric muscle loss (VML), leading to fibrosis formation and chronic inflammation. This type of injury predominantly occurs in traumatology and in war-wounded patients, with functional disability despite an optimal treatment. The use of biomaterials could provide the biochemical and physical cues that are missing in this pathologic repair.

In this work we have focused on obtaining a biomaterial composed of skeletal muscle ECM. We have tested several decellularization protocols both to preserve the three-dimensional architecture of the muscle ECM and to completely remove cell components in order to avoid a deleterious immune response after implantation. However, the protocol did not allow the preservation of trophic molecules such as GAGs, in the scaffold.

"ReGenerating Agents" (RGTA®) are functionally analogous of GAGs with a crucial property to resist enzymatic degradation. They function to restore a proper microenvironment for tissue healing with already a clinical application in skin and corneal repair. We have explored the effects of RGTA® in muscle regeneration using an *in vivo* model in mouse. At early time of regeneration (day 8), we performed histologic analysis. We showed that regenerating myofibers contained more nuclei in the treated animals, in favor of an increase of progenitor fusion, which has been validated *in vitro* in myogenic cultures. The number of capillaries was higher in favor of a better angiogenesis. Lipid droplets, a marker of impaired regeneration, were reduced by RGTA® administration. At later time of regeneration (day 28), capillary number was still improved in favor of a durable effect of RGTA® on angiogenesis.

RGTA® could be incorporated into biomaterials and are particularly resistant in an inflammatory environment, such as that occurring after a VML injury. Chemokines and growth factors could also be added in ECM-based scaffolds to promote the migration of progenitors that are essential for myofiber neoformation. Therapeutic efficacy of these optimized biomaterials will require to be evaluated in an *in vivo* model of VML.

Keywords: skeletal muscle regeneration, extracellular matrix, glycosaminoglycans, decellularized biomaterial

Institut NeuroMyoGène – UMR 5310 – INSERM U1217 Université Claude Bernard Lyon 1
Faculté de Médecine et de Pharmacie, 8 Avenue Rockefeller
69008 Lyon

Institut de Recherche Biomédicale des Armées
INSERM UMRS-MD 1197
Antenne CTSA, 1 rue du lieutenant Raoul Batany
92140 Clamart

Summary

Abbreviations 11

Introduction 14

I-A) Skeletal muscle extracellular matrix (ECM) 14
- I-A-1) Skeletal muscle tissue 14
- I-A-2) ECM is a dynamic component of the microenvironment 14
- I-A-3) The complex tri-dimensional organization of muscle ECM 16
- I-A-4) Muscle ECM biomechanical properties are crucial for force transmission 18
- I-A-5) Skeletal muscle ECM composition 19
    - Collagens family 19
    - Proteoglycans family 20
    - Glycoproteins family 24
    - Global composition of muscle ECM 25

I-B) Skeletal muscle regeneration 28
- I-B-1) Muscle stem cells 28
    - Intrinsic factors regulating MuSC fate 28
    - Extrinsic factors controlling satellite cell behavior 29
- I-B-2) Non-muscle cells are involved in muscle regeneration, partly through soluble factors 30
    - Immune cells 31
    - Endothelial cells 32
    - Fibrogenic cells 32
    - Neural cells 32
- I-B-3) ECM modifications during muscle regeneration 34
    - Dynamic modifications of ECM composition 34
    - ECM as a physical support 39
- I-B-4) Dysregulation leading to fibrosis 40

I-C) Challenging treatment for volumetric muscle loss (VML) injuries 43
- I-C-1) Severe limb injuries 43
    - Limb injuries are extremely frequent in general traumatology 43
    - Limb injuries are also observed in military trauma wounds 44
- I-C-2) VML injuries 45
    - Epidemiology of VML 46
    - Physiopathology of VML 46
- I-C-3) Current therapies for patients with VML injury 48

I-D) Regenerative medicine: a new hope for patients with VML 49
- I-D-1) Biomaterial strategies for VML injuries 50
- I-D-2) Synthetic biomaterials 51
- I-D-3) Natural biomaterials 52
    - Biomaterials composed of natural components 52
    - Decellularized biomaterials 53

I-E) ECM-based therapy for skeletal muscle injuries 56
- I-F-1) Decellurized scaffolds in VML 57
    - Non-muscle ECM based scaffold 57
    - Muscle-based ECM 58
- I-E-2) ReGeneraTive Agent® (RGTA®) components 59
    - Synthetic GAG mimetics 59
    - Molecular mechanisms of action of RGTA® 60
    - RGTA® in tissue repair 61
    - RGTA® in skeletal muscle repair 61

Aim of the study 62

Results 63

Part I- Decellularized muscle ECM for a future therapeutic use in VML model 63

MATERIALS AND METHODS 63

- Skeletal muscle samples 63
- Decellularization processes 63
- Histological analysis 66
- Quantitation of remaining DNA in ECM scaffold and non-decellularized muscle 67
- Electrophoresis of Myosin Heavy Chains 68
- Quantification of GAGs 68
- Proteomic analysis 68
- Statistical analyses 69

RESULTS 69

- R-I-1) Comparison of three different decellularization methods 69
- R-I-2) Improvement of the Trypsin-Triton protocol by modulating enzymatic timing and detergent choice to enhance GAG content 81
- R-I-3) Detergent choice to preserve the endomysium structure 88
- R-I-5) Proteomic analysis of decellularized muscle scaffolds 93

DISCUSSION 96

- New technics to optimize decellularization 96
- Persistence of undesirable cellular components 97
- Maintenance of skeletal muscle ECM specificities 98
- Necessary *in vivo* explorations 99

Part II- Exploration of RGTA® administration in skeletal muscle regeneration 102

MATERIALS AND METHODS 102

- Skeletal muscle injury 102
- GAG mimetic treatment 102
- Histological analysis 102
- Myoblast culture 104
- MuSC labeling 104
- Statistical analyses 104

RESULTS 105

- R-II-1The selection of optimal RGTA® dose 105
- R-II-2) Accelerated muscle regeneration after RGTA® administration 107
- R-II-3) RGTA® administration has a long-term effect on angiogenesis 114
- R-II-4) *In vitro* explorations on the cellular effects of RGTA® 117

DISCUSSION 120

- Adequate RGTA® dose 120
- RGTA® in toxic model of muscle regeneration 120
- RGTA® in other models of muscle regeneration 121
- *In vitro* analysis of RGTA® effects on myogenic cells 121
- Mechanisms of action 122

Perspectives 123

References 125

Scientific Publications and Communications 153

Annex 1 155

Abbreviations

AchR: Acetylcholine Receptor
ADAMTS: A Disintegrin And Metalloproteinase with Thrombospondin motifs
Ang1: Angiopoietin 1
Bp: Base pair
BMP: Bone Morphogenetic Protein
BSA: Bovine Serum Albumin
C/F: Capillaries per Fiber ratio
CCL-2: C-C motif chemokine Ligand-2
CNA-35: Collagen-binding Adhesion protein 35
CS: Chondroitin sulfate
CSA: Cross-Sectional Area
CTGF: Connective-Tissue Growth Factor
CTX: Cardiotoxin
CXCL-12: C-X-C motif chemokine Ligand 12
CXCR-4: C-X-C chemokine Receptor type 4
Cy3: Cyanine 3
C57/Bl6 mice: C57 Black 6 mice
DAMPs: Damage Associated Molecular Patterns
DGC: Dystrophin-associated Glycoprotein Complex
DMD: Duchenne Muscular Dystrophy
DMEM: Dulbecco's Modified Eagle's medium
DNA: Deoxyribonucleic Acid
DPI: Day Post Injury
Ds: Double-Stranded
EC: Endothelial Cell
ECM: Extracellular Matrix
EDTA: Ethylene Diamine Tetraacetic Acid
ERK: Extracellular signal-Regulated Kinases
EXT: Exostosin
FAP: Fibro/Adipogenic Precursor
FASP: Filter-Aided Sample Preparation
FBS: Fetal Bovine Serum
FGF: Fibroblast Growth Factor
FGFR: Fibroblast Growth Factor Receptor
FITC: Fluorescein-5-isothiocyanate
Fzd: Frizzled
GAG: Glycosaminoglycan
GDF: Growth Differentiation Factor

GMP: Good Manufacturing Practices
Has 1: Hyaluronan synthase 1
HBGF: Heparin-Binding Growth Factors
HE: Hemalun Eosin
HES: Hemalun-Erythrosin-Saffron
HGF: Hepatocyte Growth Factor
HS: Heparan Sulfate
HSPG: Heparan Sulfate ProteoGlycan
IEF: IsoElectric Focusing
IFN: Interferon
IGF: Insulin Growth Factor
IgG: Immunoglobulin G
IL: Interleukin
KCl: Potassium Chloride
KI: Potassium Iodide
LOX: Lysyl Oxidases
LTBP: Latent TGFβ binding protein
MAPK: Mitogen-Activated Protein Kinase
MCP-1: Monocyte Chemoattractant Protein-1
MHC: Myosin Heavy Chain
MMP: Metalloproteinase
MRF: Myogenic Regulatory Factor
MSC: Mesenchymal Stromal Cell
MTJ: Myotendinous Junction
MuSC: Muscle Stem Cell
NA: N-acetylated
NanoLC-MS/MS: Nanoscale Liquid Chromatography coupled to tandem Mass Spectrometry
NDST: N-deacetylase/N-sulfotransferase
NH3: Ammoniac
NMJ: NeuroMuscular Junction
NO: Nitric Oxide
NS: N-sulfated
Pax: Paired box protein
PDGF: Platelet-Derived Growth Factor
PDGFR: Platelet-Derived Growth Factor Receptor
PG: ProteoGlycan
qPCR: Quantitative Polymerase Chain Reaction
RGTA®: ReGeneraTive Agent®
ROS: Reactive Oxygen Species
SDF-1: Stromal cell Derived Factor-1

SDS: Sodium Dodecyl Sulfate
SDS-PAGE: Sodium Dodecyl Sulfate PolyAcrylamide Gel Electrophoresis
SEM: Standard Error of Mean
SERCA: Sarcoplasmic/Endoplasmic Reticulum Calcium ATPase
SLRPG: Small Leucine-Rich ProteoGlycan
SMAD: Small Mothers Against Decapentaplegic
SIS: Small Intestinal Submucosa
TA: Tibialis Anterior
TBE: Tris-Borate-EDTA
TGF: Transforming Growth Factor
Th: T helper
TIMP: Tissue Inhibitors of Metalloproteinases
TNF: Tumor Necrosis Factor
UBM: Urinary Bladder Matrix
v/v: volume per volume
VEGF: Vascular Endothelial Growth Factor
VML: Volumetric Muscle Loss
WHO: World Health Organization
Wnt: Wingless/Int

Introduction

I-A) Skeletal muscle extracellular matrix (ECM)

I-A-1) Skeletal muscle tissue

Skeletal muscle is predominantly composed of muscle fibers (myofibers) which are large cells organized with nearly a parallel alignment, mainly along the longitudinal axis[1]. Each fiber is a multinucleated cell, forming a syncytium with nuclei distributed at the periphery (close to blood vessels[2]). Skeletal muscle has a longitudinal striated appearance when observed in polarized light and in electron microscope with alternating dark and light bands. They represent myofibrils composed of myosin (thick filament-dark band) and actin (thin filament-light band) in repeated units termed sarcomeres, which are the functional contractile element of the myofiber. Skeletal muscle tissue (Figure 1) holds a specific three-dimensional architecture necessary to maintain posture and to produce movement.

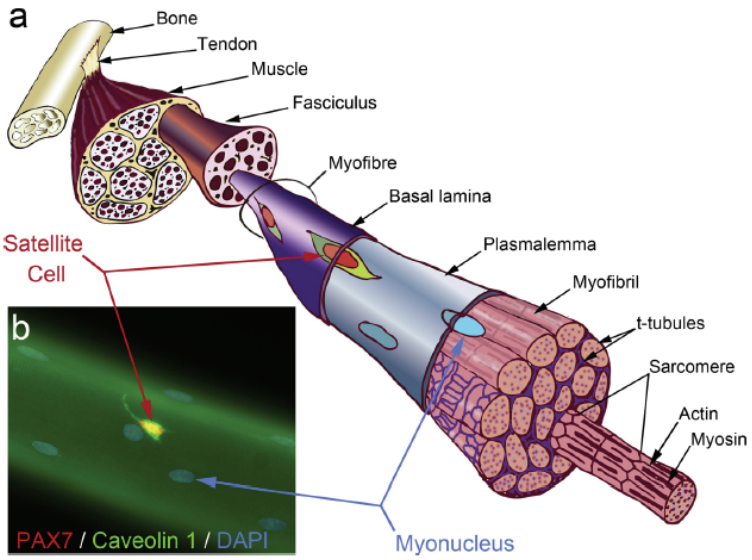

Figure 1. A) Skeletal muscle structure and B) satellite cell localization[3].

I-A-2) ECM is a dynamic component of the microenvironment

ECM forms a meshwork of macromolecules and smaller components[4], filling the extracellular space in tissues, but also acting as a major element of the stem cell microenvironment. It can be divided in two parts, the basement membrane, a thin layer of specific molecules, which forms an interface between cells and a more diffuse interstitial matrix. ECM is highly conserved between species, composed of a majority of fibrils, typically cross-linked and insoluble, making its study difficult. Over previous decades, ECM was seen as an inert structural support and received little attention. But advances in proteomics have provided a higher diversity of ECM components, referred to as the "matrisome", which constitutes around 1% of the proteome in mammals[4–6]. Initially focused on cancer microenvironment, these studies have underscored the crucial role of ECM composition in cell behavior through both physical and biochemical means (Figure 2).

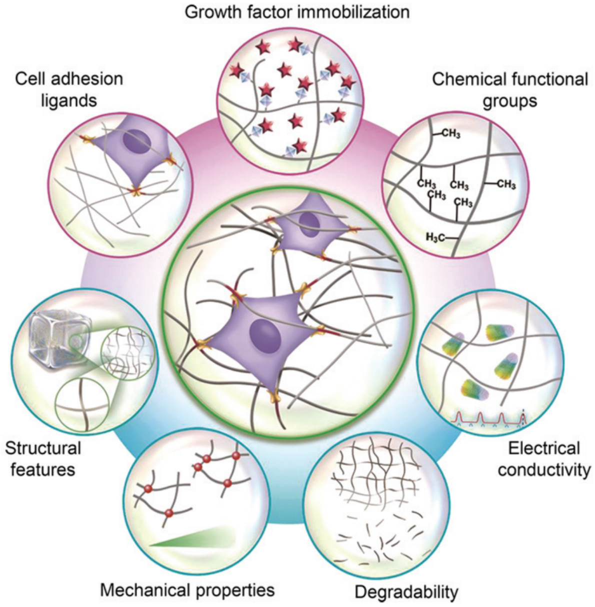

Figure 2. ECM biochemical (in pink) and biophysical (in blue) properties[7].

ECM mechanical characteristics (rigidity, deformability and porosity) provide crucial information that can affect gene expression and modulate the fate of adjacent cells[8–10]. Matrix proteins contain multiple folded domains with diverse functions. Some bind to cell receptors to mediate cell adhesion, to trigger cell polarity and to transduce signals directly into cells. Other domains link soluble growth factors and regulate their spatial distribution, creating a gradient of signaling molecules, as well as modifying their activation and binding to cells[11–13]. Fragments of ECM proteins can also be released by proteolysis and provide alarm signals, intrinsic growth factors (also called matrikines), or other regulators of angiogenesis[14,15]. Furthermore, the interactions between cells and matrices are reciprocal. ECM molecules are flexible and mechanical tensions induced by the cells can uncover cryptic sites, which could have a biological impact. It should be noted that ECM is not a static entity. It undergoes modifications during development and across lifespan, providing a high adaptation to diverse constrains[16,17], but is affected during disease[18]. Remodeling involves cleaving of ECM proteins by proteolytic enzymes such as matrix metalloproteinases (MMPs), release of several molecules, as well as diverse mechanisms of cross-linking[13].

Thus, ECM is now considered as a dynamic actor, involved in many developmental, physiological and pathological processes, including cell proliferation, differentiation and apoptosis, in addition to adhesion and cell migration[5,6,19].

ECM is extremely specific of each tissue, adopting various shapes and rigidities[19]. For example, bone ECM is extremely rigid by its mineralization[20] whereas ECM in cornea is transparent with refractive properties[21]. In skeletal muscle, ECM displays a complex tri-dimensional architecture, particularly adapted to the specificities of this tissue[22].

I-A-3) The complex tri-dimensional organization of muscle ECM

The early morphological analysis of skeletal muscle[23] has divided the interstitial matrix into three levels of organization: the endomysium surrounding each myofiber and its basement membrane, the perimysium gathering groups of muscle fibers into bundles and the epimysium wrapping the whole muscle (Figure 3).

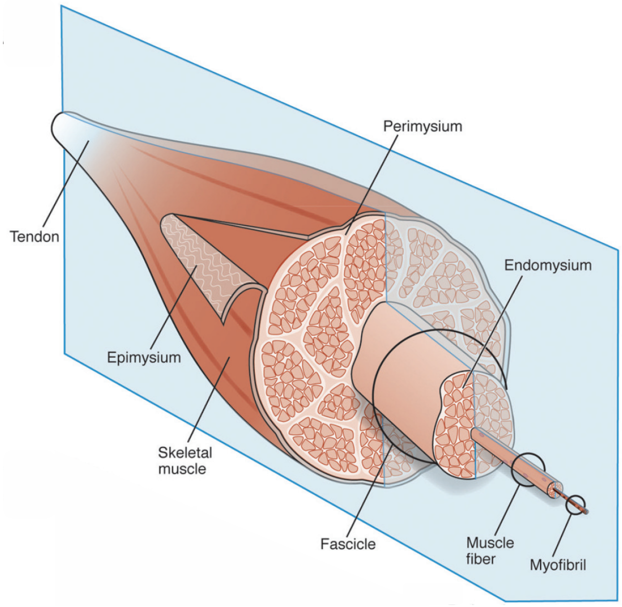

Figure 3. Schematic organization of the muscle tissue[24].

In the 1980s[25–28], detailed descriptions of muscle ECM by electronic microscopy confirmed these demarcations. Briefly, endomysium was described as pentagonal multi-sheets, composed by a loose and random framework of collagen fibers closely related to basal membrane and connecting adjacent myofibers by perpendicular fibrils. Perimysium also contains multiple layers, with larger ordered wavy collagen networks as well as loose collagen fibrils without specific direction. At each extremity, muscle connection ends by the myotendinous junction, a specialized structure allowing the attachment and force transmission from myofiber to tendon, with distinctive tendon finger-like processes inside the muscle tissue[29].

The difficulty is defining which structures are assigned to either the perimysium or the endomysium since two dimensional images do not allow a precise delimitation[27] (Figure 4). Interestingly, these ECM descriptions were made in various muscles from different anatomic locations and species, with mainly quantitative difference between muscles of different parts of the body, possibly reflecting specific functions[30].

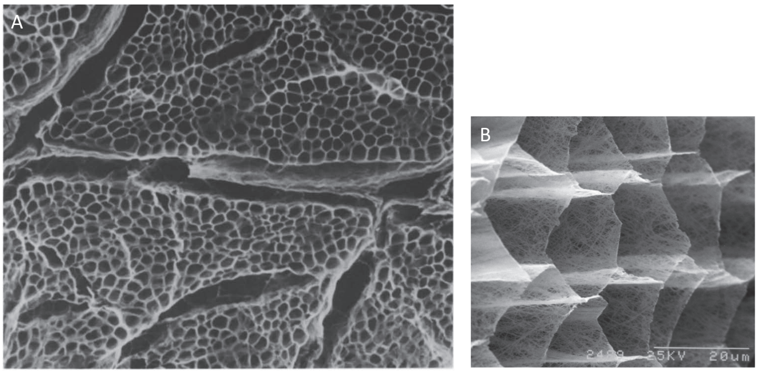

Figure 4. Muscle after sodium hydroxide digestion observed by scanning electron micrographs with A) transversal endomysium separated by perimysium structure at low magnification and B) oblique endomysium at higher magnification[31].

A deeper understanding of ECM morphology was recently obtained using three-dimensional reconstruction[24,32,33] of serial immunolabelled sections, observed by electron microscopy or confocal microscopy. This allowed a more precise observation of each multiple-layered ECM, that is strongly interconnected with each other, such as the epimysium, which is composed of very large and wavy collagen fibers as observed in tendons[24].

Three-dimensional visualization also highlighted interactions with specific cells or substructures. Indeed, perimysium includes different levels of organization with large wavy fibers with well-defined orientation and collagen fibers between adjacent myofibers, adhering to the myofiber plasma membrane (sarcolemma). These focal domains or "perimysial junctional plates" co-localize with capillary branches. They interact with specific myofiber regions characterized by an accumulation of subsarcolemmal myonuclei and mitochondria[32] (Figure 5). The function of such a colocalization needs to be elucidated.

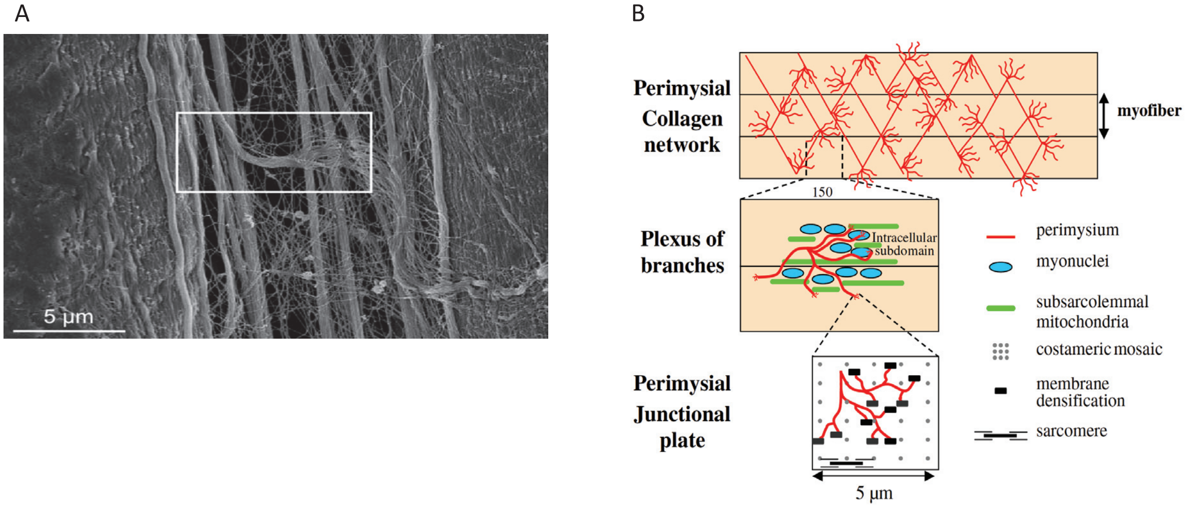

Figure 5. Perimysium A) in scanning electron micrograph[24] and B) model of its organization with plexi branches adhering to myofiber surface displaying at its intracellular subdomain an accumulation of nuclei and mitochondria[32].

Additionally, coupling immunolabelling with stretching applied on muscle samples revealed that the large fibers become less wavy and realign towards the direction of strain[24], probably playing a biomechanical role. The complexity of the myotendinous junction (MTJ) was better visualized with deeper tendon protusions[34], increasing contact surface, crucial for transmitting longitudinal forces from muscle to tendon.

New tools will continue to improve our knowledge on ECM architecture as second generation harmonic microscopy that provides more specific in-situ quantification of fibrillar protein structures[35,36]. The use of strong fluorescent probes for pan–collagen such as CNA35 (Collagen-binding Adhesion protein 35), allow a more precise visualization of ECM fibers[37,38] and their reorganization during muscle contractions, essential for force transmission.

I-A-4) Muscle ECM biomechanical properties are crucial for force transmission

Skeletal muscle is a contractile tissue with the ability of sustaining recurring mechanical loads. Muscle contraction is based on the formation of bridges between the myosin and actin myofilaments, followed by the sliding of myosin filaments along actin bundles. Sarcomeres get shorten (sliding filament theory[39]) and contractile force is regulated by optimal length of sarcomere[40].

Because ECM was initially viewed as an inert structural support, first descriptions of its characteristics focused on its passive elasticity properties[41] and resistance to constraints[42]. Force production was described as a direct transmission to conjunctive tissue in series, through tendon via the MTJ. Morphological analyses have shown multidirectional orientations of collagen fibers inside the muscle tissue[22] and myofiber terminations within the muscle, before reaching the MTJ[29]. Tensile forces can be transferred laterally to the basement membrane, and then be integrated within the muscle ECM before longitudinal transmission to the tendons. Thus, muscle contraction is currently modeled by contractile elements in series with elastic components in parallel[43,44] (Figure 6).

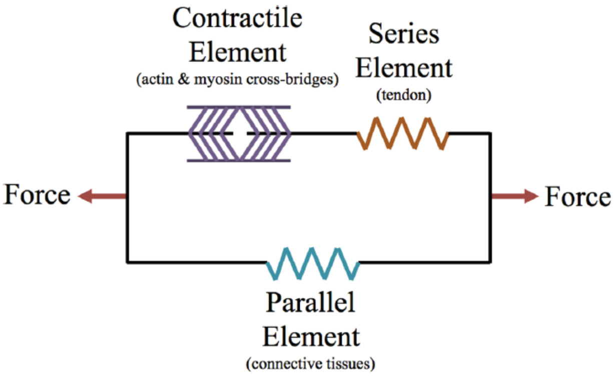

Figure 6. Hill's three-element model of muscle contraction[45].

The anchorage of myofibers to ECM is another essential feature for force transmission and also protects muscle fibers from over-extension. Myofilaments are linked to the plasma membrane by specialized transmembrane complexes named “costameres”[46], where force transmission is concentrated[47]. Myofibers are anchored to ECM through transmembrane receptors including the integrins and the dystrophin-associated glycoprotein complex (DGC), a large association of membrane-associated proteins[48]. They both bridge the basement membrane to the cytoskeleton contributing to force transmission.

Modifications in ECM composition or in ECM interactions with myofibers have severe functional impacts by restricting active muscle contraction[49].

I-A-5) Skeletal muscle ECM composition

Skeletal muscle ECM represents around 1-10% of the tissue weight and its composition varies between muscles, especially in the perimysium[50]. This difference is already present in early development[51] and is not affected by the type of fiber (slow or fast-twitch)[52]. Despite this variability, ECM is composed of common macromolecules, some of them acting as signaling and adhesive molecules, whereas others are more structural (Figure 7).

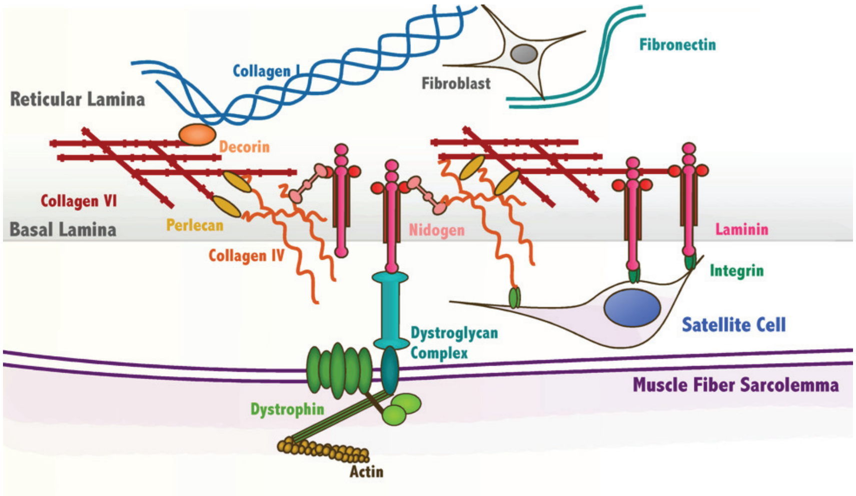

Figure 7. Schematic skeletal muscle ECM[53].

- Collagens family

Collagens are a heterogeneous family characterized by polypeptide chains organized in a triple helix with the presence of recurring triplets[54,55]. They are the major structural proteins in skeletal muscle ECM[52,56,57], displaying various supramolecular organization (Figure 8). In the basement membrane, as in other tissues, collagen IV forms a branching network. Microfilaments of collagen VI anchor this basement membrane to the endomysium[58]. Fibrillar collagens are abundant, since epimysium and endomysium are made by an almost equal amount of collagens I and III whereas collagen I is predominant in perimysium[24,30,56].

Multiplexins, such as Collagens XV and XVIII, harbor both structural features of collagens and proteoglycans (PGs)[59].

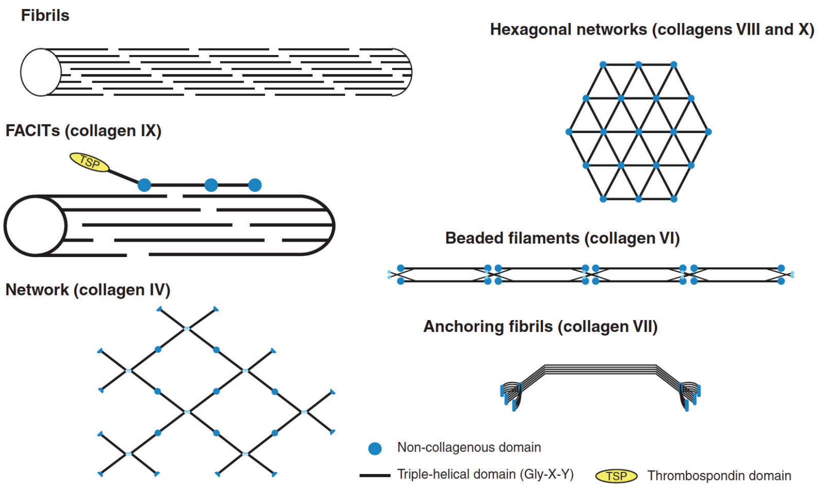

Figure 8. Schematic representation of the supramolecular organization of collagens[55].

- Proteoglycans family

○ The complexity of proteoglycans

The muscle ECM contains various PGs, which consist of a core protein with one or more chains of glycosaminoglycans (GAGs) covalently attached to it. PGs are extremely heterogeneous, and are currently classified according to their localization[59,60]. PGs can be located extracellularly, pericellularly (corresponding to the basement membrane zone), at the cell surface, or intracellularly (Figure 9). Another way that PGs can be classified is by the main types of GAGs that they harbor. PGs can be described as homogenous or heterogeneous (with multiple subtypes of GAGs) containing various combinations for each that are dependent on the tissue or the cell type that PG originates from. PGs are currently known to have two main functions[60]: a structural role in which interact with others components of ECM, and biological purpose where the GAGs moieties play a main role independently of the core protein.

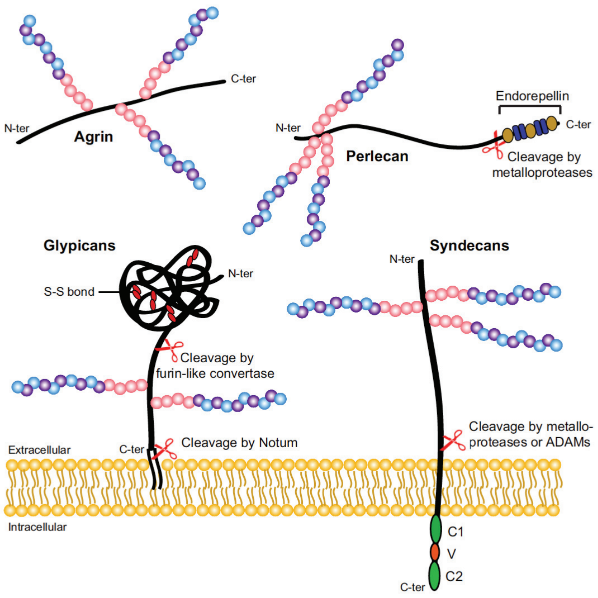

Figure 9: Main cell surface and extracellular heparan sulfate proteoglycans[61].

Structure and function of glycosaminoglycans

GAGs are composed of linear polysaccharides chains containing specific repetitions of an amino sugar[60] (e.g. N-acetylglucosamine or N-acetylgalactosamine) associated with an uronic acid residue (D-glucuronic or iduronic acid), with Keratan sulfate being the exception. Additionally, all except Hyaluronan have a sulfate ester located on the disaccharide in various positions. Their constituents give rise to the different families of GAGs (Figure 10). Due to their negative charges, these molecules retain water conferring space-filling and lubrication functions. GAGs also participate in many biological processes through interactions with various biomolecules.

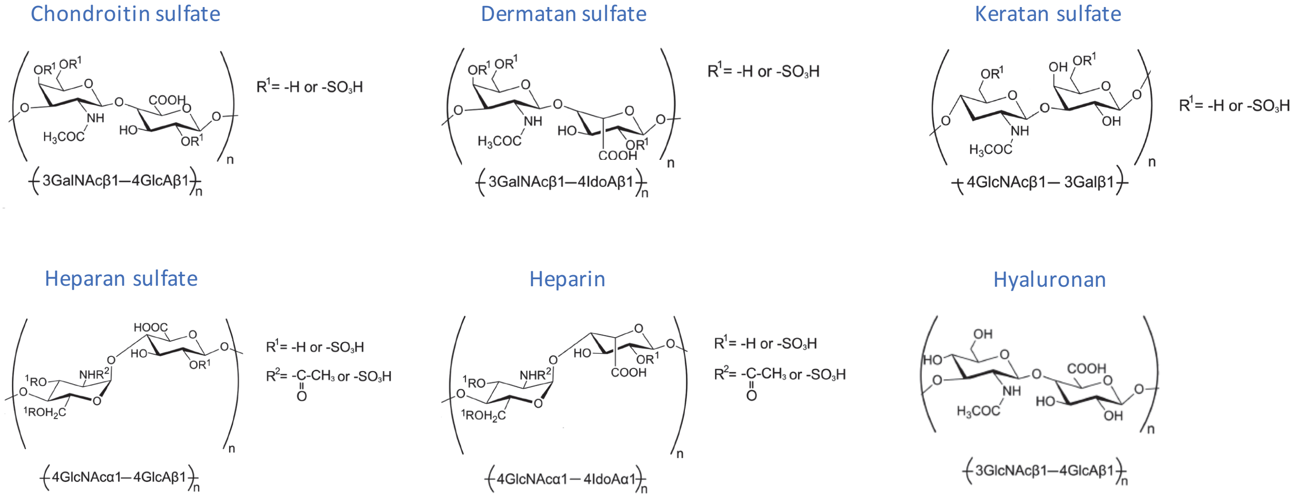

Figure 10. Structures of repeating disaccharides of glycosaminoglycans. Adapted from[60].

Abbreviations: Gal, galactose; GlcA, glucuronic acid; IdoA, iduronic acid; GalNAc, N-acetylgalactosamine; and GlcNAc, N-acetylglucosamine.

The characteristics of GAGs varies and are described below.

Hyaluronan is a high-molecular weight polymer and the only GAG without sulfation or a covalently linked core protein. Its degradation is highly regulated, while its function relies on the size of its chain. For example low weight fragments of hyaluronan are known to lead to an inflammatory response[62].

Others GAGs have structural modifications, such as sulfation, that give rise to various subtypes of chondroitin sulfates (CS), illustrated in Figure 11.

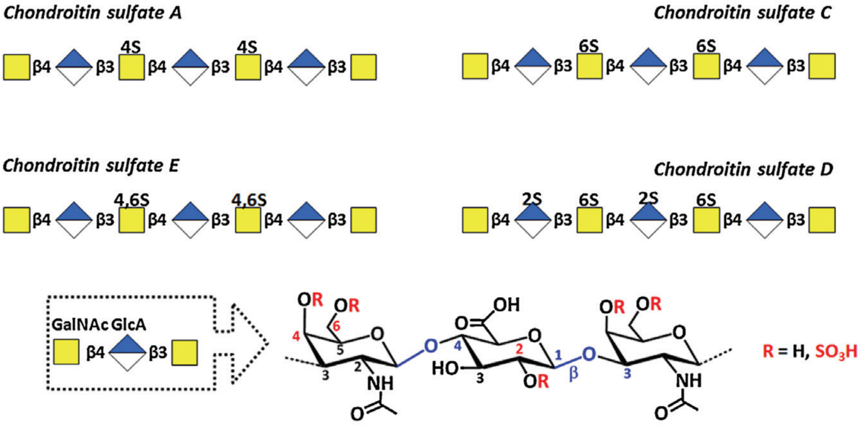

Figure 11: Chondroitin sulfates classification according to the position(s) of sulfation[63].

However, Heparan sulfate (HS) and heparin are the most complex due to the variable in their disaccharide constituents, sulfation, and hydrophobic region. HS are ubiquitous, and exhibit more acetylated glucosamine and fewer sulfates than heparin[64] which is only secreted by mastocytes.

The HS family was particularly studied in skeletal muscle[65]. HS chains comprise around 50–200 disaccharides with variable modifications based on the originating tissue and cell type. The HS chain contains three distinct domains categorized by their degree of sulfation: the NA domains have contiguous N-acetylated disaccharide units, the NS domains are highly N-sulfated, and the mix domains are a combination of NA/NS domains (Figure 12).

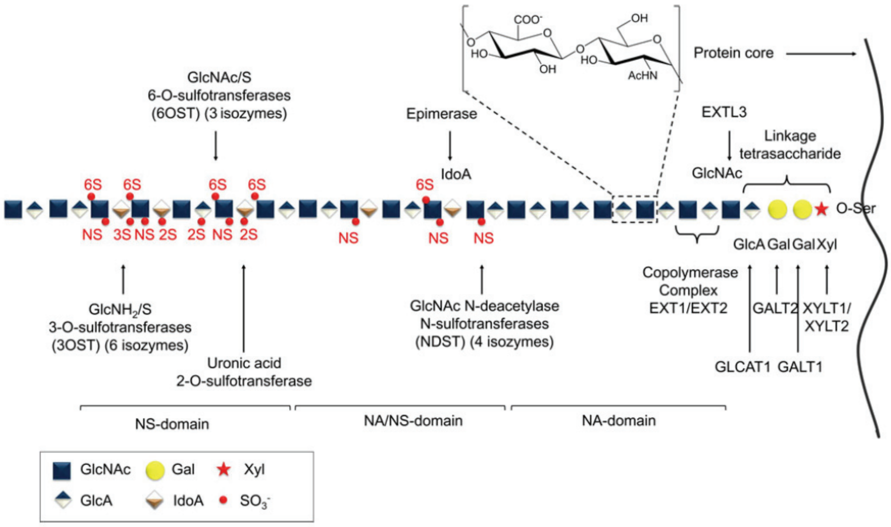

Figure 12: HS structure with enzymes involved in biosynthesis and modifications[66].

PGs containing HS chains are termed heparan sulfate proteoglycans (HSPG). Their structural diversity is due to a complex biosynthesis, which is initiated through a tetrasaccharide on the protein core. HS chain polymerization is enzymatically catalyzed by the exostosin (EXT) polymerase family. The modifications to HSPGs are initiated by N-deacetylase/N-sulfotransferases (NDST) which replace the acetyl group of glucosamine with an N-sulfate group. Others modifications including epimerization, and gradual O-sulfation by sulfotransferases are performed simultaneously (Figure 12). HSPGs are finely regulated while the HSPG's structure dictates interactions with signaling molecules[67].

Indeed, GAGs have many biological functions as illustrated with HS (Figure 13). They can sequester growth factors that can be released with the cleavage of GAG chains by enzymes (heparanase) for cell signaling. They can also act as a co-receptor or as an endocytic receptor that participates in its own clearance. They can create a haptotactic (immobilized) gradient of signaling molecules, such as chemokine C-X-C motif chemokine Ligand-12 (CXCL-12), involved in leukocyte or progenitor cell recruitment[68]. HSPGs can facilitate cell-ECM or cell–cell attachment, and cell motility[69].

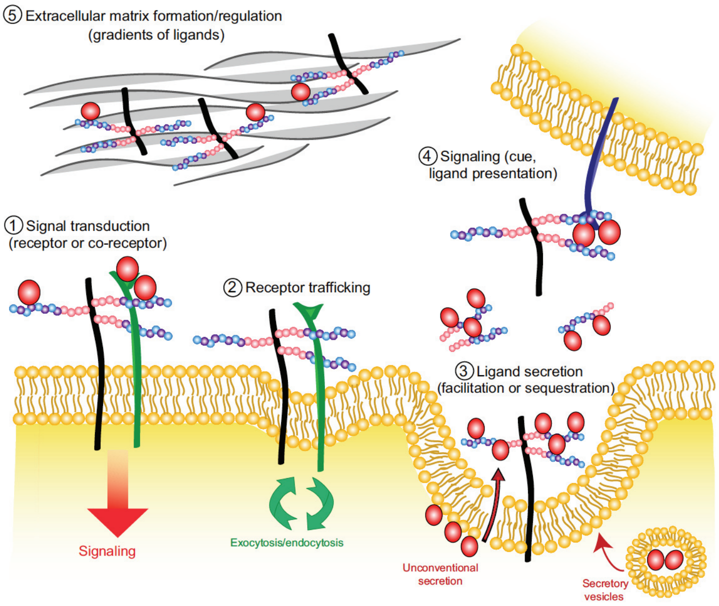

Figure 13: The regulation of cell signaling pathways by HSPGs[61].

In skeletal muscle HSPGs are mainly found in the endomysium and the basal membrane. In contrast, the perimysium is rich in dermatan/CS PGs[70].

- Glycoproteins family

Many glycoproteins are present in the ECM. They allow ECM assembly and act as linker molecules, between the basement membrane and sarcolemma. Some of their domains promote outside-in or inside-out signaling and other domains bind growth factors. Laminins are a family of multidomain glycoproteins forming an essential network of the basement membrane (Figure 14). They interact with the collagen IV network, either directly or via other glycoproteins (nidogens) and perlecans[71,72]. In adult muscle, the predominant laminin α2 chain is combined with both laminin β1 and β2 chains forming laminin 211 (α2β1γ1) and laminin 221 (α2bβ2γ1). Laminins are localized all around the sarcolemma[71], but some of them may be concentrated at the costameres[47]. The laminin globular domains are linked to α-dystroglycan (a DGC molecule) or integrin, creating crucial interactions for basement membrane formation, force transmission and cell signaling[48,72].

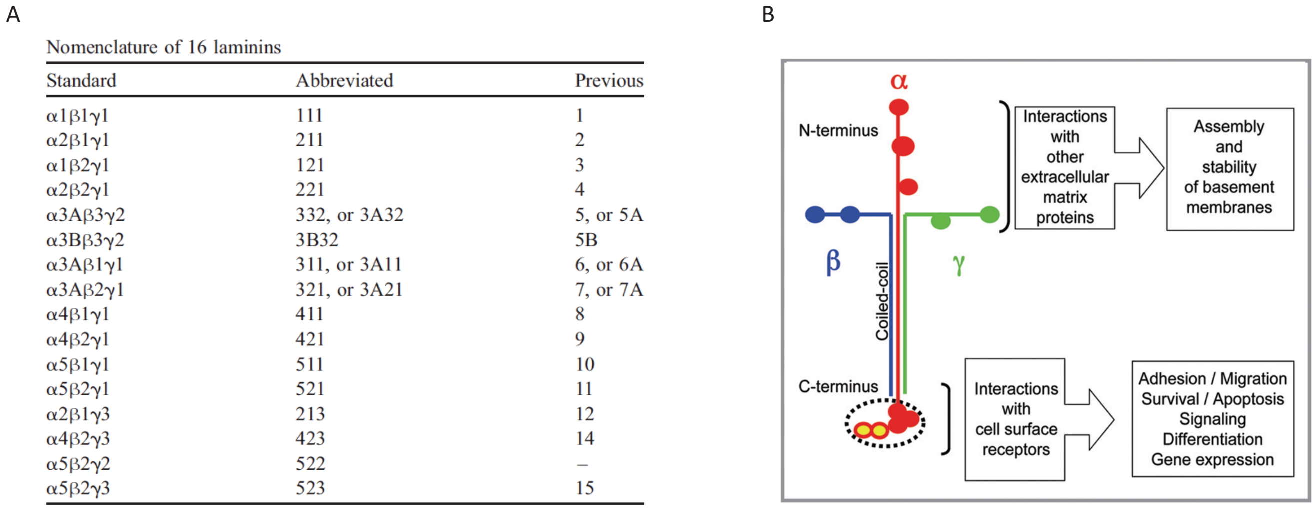

Nomenclature of 16 laminins

Standard	Abbreviated	Previous
α1β1γ1	111	1
α2β1γ1	211	2
α1β2γ1	121	3
α2β2γ1	221	4
α3Aβ3γ2	332, or 3A32	5, or 5A
α3Bβ3γ2	3B32	5B
α3Aβ1γ1	311, or 3A11	6, or 6A
α3Aβ2γ1	321, or 3A21	7, or 7A
α4β1γ1	411	8
α4β2γ1	421	9
α5β1γ1	511	10
α5β2γ1	521	11
α2β1γ3	213	12
α4β2γ3	423	14
α5β2γ2	522	–
α5β2γ3	523	15

Figure 14. Laminin A) nomenclature[74] and B) functional substructures[75].

Another key glycoprotein in skeletal muscle is fibronectin, a dimeric molecule with multiple globular domains, forming an interstitial network with collagen VI[76] and binding integrins. Changes in the conformation of fibronectin can activate or deactivate many cryptic binding sites[77] (Figure 15).

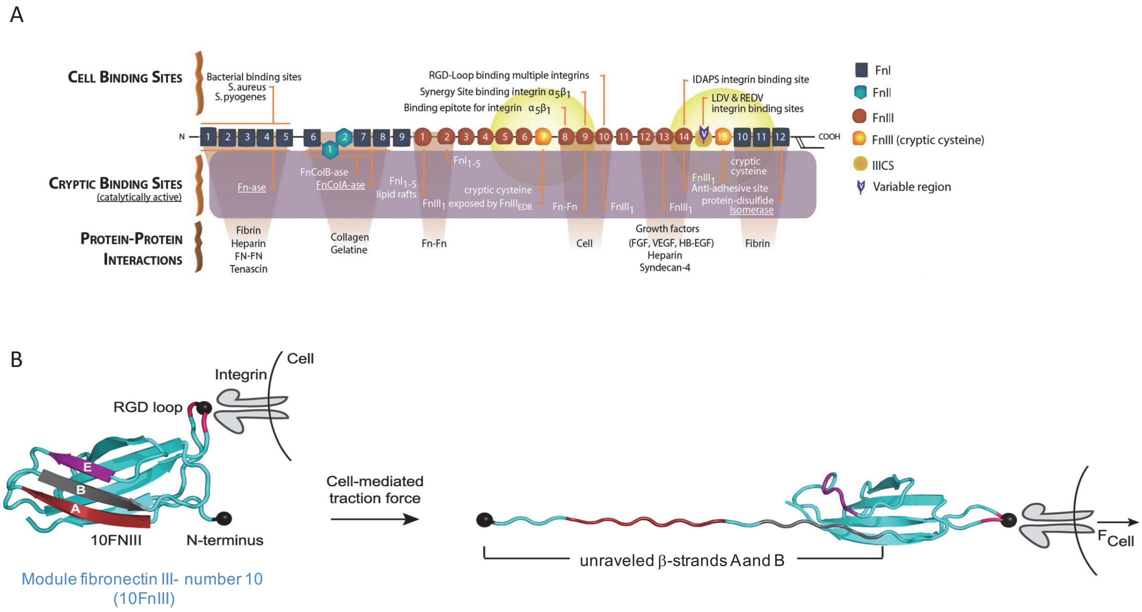

Figure 15. A) Multidomains of monomeric fibronectin and its binding sites[78]. B) Conformation modification of type III module (number 10) by cell traction force after RGD binding. Adapted from[79]. Fn, fibronectin; FCell, cell traction force; RGD, tripeptide Arginine-Glycine-Aspartate; FnCol, fibronectin type IV collagenase.

- Global composition of muscle ECM

Proteomic and bioinformatic analyses have more precisely defined the “matrisome“ which has turned out to be extremely complex[5,80]. It contains collagens, proteoglycans and glycoproteins grouped under the term “core matrisome”. A second category was identified, the “matrisome associated” proteins, composed of ECM-affiliated molecules, ECM-regulators such as MMPs and ECM-secreted factor such as growth factors. In skeletal muscle, proteomic explorations of ECM are still challenging because this tissue contains a high cell density, requiring ECM-enrichment[81,82] or decellularization methods[83]. Interestingly, a first proteomic study[81] has identified several ECM-associated molecules in skeletal muscle. Table 1 summarizes ECM components found in skeletal muscle tissue, including ECM-associated molecules, which are essential for signaling and maintaining ECM organization. ECM-secreted molecules also include a variety of growth factors and homologs as Bone Morphogenetic Proteins (BMPs) or TGFβs, chemokines and interleukins.

However, it should be underscored that the three-dimensional localization of each component is still poorly explored because of current technical limitations. Although expensive, clearing techniques[84,85] allow the combination of three-dimensional architecture exploration and the identification of molecule composition, and may provide key information in healthy as well in regenerative or pathological muscle. ECM is a very dynamic network with modifications throughout the lifespan. In response to perturbation, ECM shows a high degree of adaptation including post-translational modifications such stabilization of collagen fibrils by covalent cross-linking by lysyl oxidases (LOX)[86]. ECM is also highly modified all during muscle regeneration.

	ECM components	Localization	References
CORE MATRISOME	**Collagen family**		
	Collagen I	Epimysium, perimysium, endomysium	[52,56,87]
	Collagen III	Epimysium, endomysium	[56,57,87]
	Collagen IV	Basement membrane	[52,56]
	Collagen V	Epimysium, perimysium, endomysium	[52,56]
	Collagen VI	Between basement membrane and endomysium	[52,56,58]
	Collagen VII	Sparse	[88]
	Collagen VIII	Sparse	[88,89]
	Collagen IX	Sparse in interstitial ECM	[90]
	Collagen XI	Sparse in interstitial ECM	[91–93]
	Collagen XII (FACIT)	Perimysium, (endomysium?)	[87,94]
	Collagen XIII (MACIT)	Basement membrane and sarcolemma, NMJ	[95]
	Collagen XIV (FACIT)	Perimysium, (endomysium?)	[87]
	Collagen XIX	Sparse, in basement membrane?	[96]
	Collagen XXIII	Sparse in interstitial matrix	[97,98]
	Proteoglycans		
	Heparan sulfate proteoglycans		
	Collagen XVIII (Multiplexin)	Basement membrane?	[70]
	Perlecan	Basement membrane, NMJ and sarcolemma	[70,99]
	Testican 1 (or SPOCK)	NMJ	[98,100]
	Chondroitin sulphate proteoglycans		
	Biglycan (also a SLRPG)	Basement membrane and NMJ	[70,101]
	Collagen XV (Multiplexin)	Basement membrane	[70]
	Dermatan sulphate proteoglycans		
	Decorin (also a SLRPG)	Basement membrane, endomysium and perimysium	[70,101]
	Keratan sulfate proteoglycans		
	Fibromodulin (also a SLRPG)	Between basement membrane and endomysium	[70]
	Lumican (also a SLRPG)	Between basement membrane and endomysium	[70]
	Small leucine-rich proteoglycan (SLRPG)		
	Asporin	Basement membrane, endomysium and perimysium?	[102]
	Osteoglycin (or Mimecan)	Unknown	[103–105]
	Hyaluronan (GAG without protein core)	Epimysium, perimysium, endomysium	[106]
	Glycoproteins		
	Laminins	Basement membrane and NMJ	[72,107,108]
	Fibronectin	Between basement membrane and endomysium, NMJ	[109,110]
	Elastin	Epimysium, perimysium, endomysium	[56,57]
	Nidogen (entactin)	Basement membrane and NMJ	[111]
	Matrilin-2	Perimysium	[112,113]
	Tenascin-C	Myotendinous junction	[114]
	Tenascin-X	Endomysium and perimysium	[115]
	Thrombospondins	Endomysium and perimysium	[116,117]
	Periostin	Sparse in interstitial matrix	[118]
	Fibulin-1 and -2	Basement membrane	[103,119]
	Vitronectin	Myotendinous junction?	[120]
	Fibrillin-1	Unknown	[121]
	LTBP-2	Interstitial matrix	[122]
	Dermatopontin (or TRAMP)	Sparse in perimysium	[123,124]
	SMOC-2	Unknown	[125]
MATRISOME ASSOCIATED	**ECM affiliated proteins**		
	Osteopontin	Sparse in interstitial matrix	[126,127]
	Annexins	Sarcolemma	[128]
	Heparan sulfate proteoglycans		
	Agrin	NMJ stabilisation	[129]
	Glypican 1	In lipid raft domain anchored in sarcolemma	[70]
	Syndecans	In non- raft domain in sarcolemma	[70]
	ECM secreted factors		
	Angiopoietin 1 and 2	Endomysium?	[130,131]
	Follistatin	unknown	[132,133]

Table 1. ECM components of skeletal muscle.

Abbreviations: FACIT, fibril-associated collagens with interrupted triple helices; MACIT, membrane-associated collagens with interrupted triple helices; NMJ, neuromuscular junction.

I-B) Skeletal muscle regeneration

I-B-1) Muscle stem cells

Skeletal muscle is known for its high capacity of regeneration, relying on resident stem cells termed satellite cells (or MuSCs, Muscle Stem Cells). These cells owe their name to their location, between the cell membrane of myofibers and the basal lamina (Figure 16).

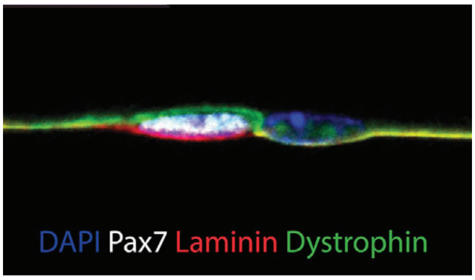

Quiescent satellite cell (Pax 7+) between myofibers (immunostained by dystrophin) and the basal lamina (immunostained by laminin)[134].

They constitute a heterogeneous population[135], indispensable for muscle regeneration. Indeed, their absence impairs muscle regeneration[136,137] although other interstitial stem cells with potential myogenic fate can participate anecdotally to regeneration[138].

In resting adult skeletal muscle, quiescent satellite cells are located close to capillaries[139] and express the paired-box transcription factor 7 (Pax7), a specific marker for MuSCs in the muscle tissue[140,141]. After an injury, satellite cells are activated and massively proliferate to generate myogenic progenitors (also called myoblasts). Then, they differentiate in myocytes and fuse to form new myofibers, whereas a subset of activated MuSCs returns to quiescence to replenish the muscle stem cell pool, to face further injuries during lifetime.

MuSC fate is finely regulated, involving both intrinsic factors and extrinsic signals produced by the neighboring cells (tissue resident and inflammatory cells).

- Intrinsic factors regulating MuSC fate

Myogenic regulatory factors (MRFs) are the main transcription factors regulating MuSC fate, composed of four members (Myf5, MyoD1, Myogenin, and MRF4) with overlapping functions.

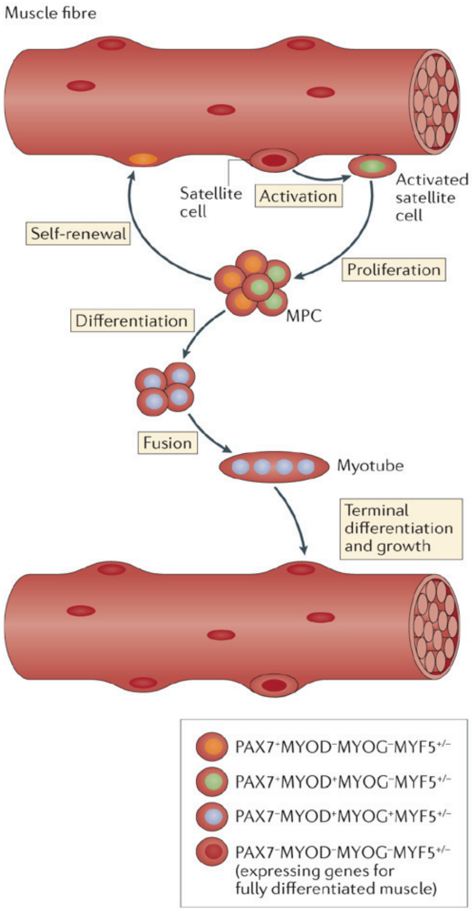

Figure 17. Myogenic regulatory factor expression during muscle regeneration[142].

In resting condition, quiescent satellite cells display a variable expression of Myf5 protein[3,143]. After activation, Myf5 level rises, still associated with Pax7 expression[144]. During proliferation, MyoD1 expression is induced[145] and is essential for cell amplification, allowing commitment into myogenic differentiation. Then, some progenitors turn off Pax7 expression and engage in differentiation program, by cell cycle exit and expression of late MRFs, Myogenin and MRF4. These myocytes fuse together or with preexisting myofibers to form new fibers. Other myoblasts switch off MyoD1 expression while they maintain Pax7 to induce self-renewal and return to quiescence to maintain the stem cell pool (Figure 17). The specific expression patterns of Pax7 and Myod1 are used to distinguish between quiescent (Pax7+/MyoD1-), activated (Pax7+/MyoD1+) and differentiated (Pax7-/MyoD1+) MuSCs[146].

- Extrinsic factors controlling satellite cell behavior

Extracellular signaling from myofibers and their microenvironment plays a major role in the regulation of satellite cell behavior. The main growth factors[147] regulating MuSC activation and proliferation are hepatocyte growth factor (HGF) which acts synergistically with fibroblast growth factors (FGFs)[148] via Mitogen-Activated Protein

Kinases/Extracellular signal-Regulated Kinases (MAPK/ERK) signaling pathway[149]. Insulin-like Growth Factors (IGFs), Platelet-Derived Growth Factor (PDGF) and Vascular Endothelial Growth Factor (VEGF)[147,150] are also implicated. These factors, as well as several FGFs, are secreted by satellite cells[151,152]. Other pathways are involved, such as nitric oxide (NO) and Notch, that decline after satellite cell activation and increases later during proliferation[153,154].

Migration of myogenic progenitors is essential during regeneration. The chemokine CXCL-12 (or SDF-1, Stromal cell Derived Factor 1) and its receptor C-X-C chemokine Receptor type 4 (CXCR-4)[68,155], or growth factors such as HGF[148,156], are key players in myoblast mobilization.

Differentiation of progenitor cells is enhanced by growth factors stimulating also the proliferation stage, such as IGFs[150,157], but by acting through variable local concentration[158] or interacting with various receptors such as Fibroblast Growth Factor Receptor-4 (FGFR-4) transiently expressed during differentiation[159]. On the contrary, TGFβ signaling inhibits the differentiation step[147,160]. Wnts (Wingless/Int) are secreted lipid-modified glycoproteins and the Wnt canonical pathway is involved in the conversion from proliferation to differentiation[161], with a switch from high Notch expression to a high Wnt/β-catenin signaling.

Terminal differentiation consists in the fusion of myocytes together or with remaining myofibers. It can be described in four main steps[162]. First, cell adhesion to each other, followed by lipid bilayer rearrangements (also described as hemifusion), generation of a fusion pore, leading to the formation of a syncytium by lateral expansion. Actin plays an essential role in this process by controlling membrane protrusions[163]. Among several molecules involved in myogenic cell fusion, two specific proteins were discovered on the surface of merging cells[162,163], independently controlling the distinct steps of the process[164] (Figure 18), such as Myomaker associated with cell membrane and Myomerger-Minion in contact with the cytoskeleton[165,166] . Phosphatidylserine is also involved, with a transient presence in the extracellular sheet of the sarcolema[167], enhancing the fusion process. The hemi fusion step depends on extracellular components as well as annexins A1 and A5[168].

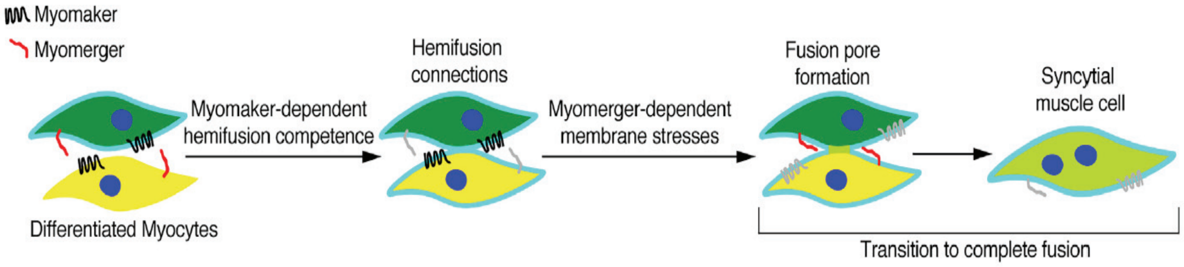

Figure 18. Myomaker and Myomerger act on two distinct steps of myogenic cell fusion[164].

I-B-2) Non-muscle cells are involved in muscle regeneration, partly through soluble factors

The response to injury and MuSC fate are highly regulated by both the immune response and other resident cells, contributing to a coordinated process of muscle regeneration (Figure 19).

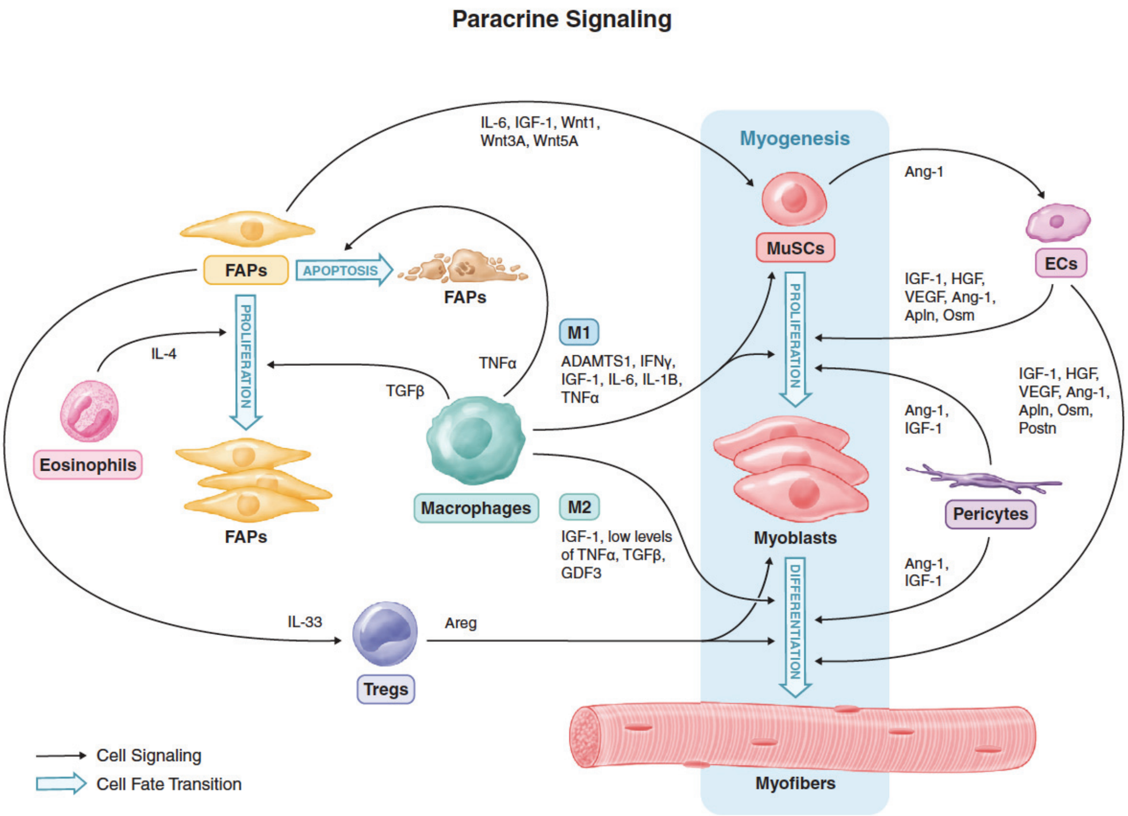

Paracrine Signaling

Figure 19. Paracrine signaling between MuSCs and other cells involved in muscle regeneration[169]. Abbreviations: M1 and M2, macrophages; FAPs, fibroadipogenic progenitors; MuSCs, muscle stem cells; Tregs, regulatory T cells; ECs, endothelial cells; Apln, apelin; Postn, periostin; Osm, oncostatin M.

- Immune cells

Neutrophils are the first cells invading the injured area, generating a sterile inflammatory environment by production of reactive oxygen species (ROS) and proteolytic enzymes. These cells also produce cytokines[170,171] such as Interferon γ (IFNγ), Interleukin-1β (IL-1β) and Tumor Necrosis Factor α (TNFα). In association with molecules released by necrotic cells, termed damage-associated molecular patterns (DAMPs), they provide signaling molecules to recruit additional immune cells.

Circulating monocytes infiltrate the injured muscle, attracted by chemokines such as macrophage chemoattractant protein 1 (MCP-1, also called CCL-2)[170,172] and they differentiate into macrophages, key actors of muscle regeneration. Indeed, their absence impairs the regeneration process[173]. Initially, macrophages hold a pro-inflammatory profile and produce cytokines as IGF-I, IL-6, IL-1β and TNFα which stimulate MuSC activation and proliferation[174,175]. Then, by metabolic modifications at a specific timing[176,177], they skew to regenerative macrophages, which stimulate differentiation via IGF-I and low level of TNFα[174]. They also release GDF-3, a growth factor from the TGFβ family recently identified as acting specifically on the fusion step[178]. Other cells such as eosinophils[179] and regulatory T cells[180] also infiltrate the damaged muscle but in limited number as compared with the massive monocyte infiltrate.

- Endothelial cells

Myogenic progenitors and adjacent vessels display reciprocal interactions during muscle regeneration[181]. After an injury, the number of endothelial cells peaks around 7 days post-injury (DPI) and they promote proliferation then differentiation of myogenic cells via growth factors (IGF-I and HGF)[139]. More recently, a couple of secreted molecules were also identified[182]. Apelin increases MuSC proliferation and differentiation while periostin acts on MuSC differentiation. Regenerative macrophages orchestrate the coupling between myogenesis and angiogenesis via the secretion of oncostatin M[182]. Then, during the regenerative phase, periendothelial cells (pericytes or smooth vascular cells) induce the return into MuSC quiescence via Angiopoietin 1 (Ang1)[183]. In addition, growth factors enhance muscle angiogenesis such as FGFs[184], PDGF-BB and VEGF[185,186].

- Fibrogenic cells

Skeletal muscle tissue contains a heterogeneous population of fibro/adipogenic precursors (FAPs), which shares some similarities with mesenchymal stromal cells (MSCs). After an injury, FAPs rapidly expand with a maximum around 3 DPI and then this population decreases to normal values around 7 DPI[187–189]. They provide an optimal ECM production, and secrete signaling molecules for myogenic cells such as IGF-I, IL-6 and Wnts[187]. A reciprocal communication between FAPs and immune cells also occurrs. Indeed, FAP number is regulated via apoptosis by TNFα derived from inflammatory macrophages. During the regenerative phase, macrophages stimulate FAP ECM secretion via TGFβ[188]. In addition, IL-4 produced by eosinophils prevents FAP conversion into adipocytes[179]. Fibroblasts produce ECM components such as collagens and directly act on myogenic cell behavior[190]. Via TGFβ signaling, they differentiate into myofibroblasts[191] but their roles during physiological muscle regeneration need further exploration. Fibroblast production of ECM could be modulated by satellite cells via exosomes, as illustrated in a model of muscle overload[192].

- Neural cells

Nerves are damaged during muscle injury despite a majority of mature motoneurons survives at distal axotomy, in close contact with Schwann cells[193]. Neurotrophic factors can stimulate reinnervation such as IGF-II produced by myotubes, which enhances neurite growth and synapse formation[194]. FGF-5 is up-regulated after denervation and acts as an autocrine regulator of Schwann cells[195]. Interestingly, macrophage secretion may be essential since these cells are involved in the regulation of Schwann cell maturation in a model of nerve injury[196].

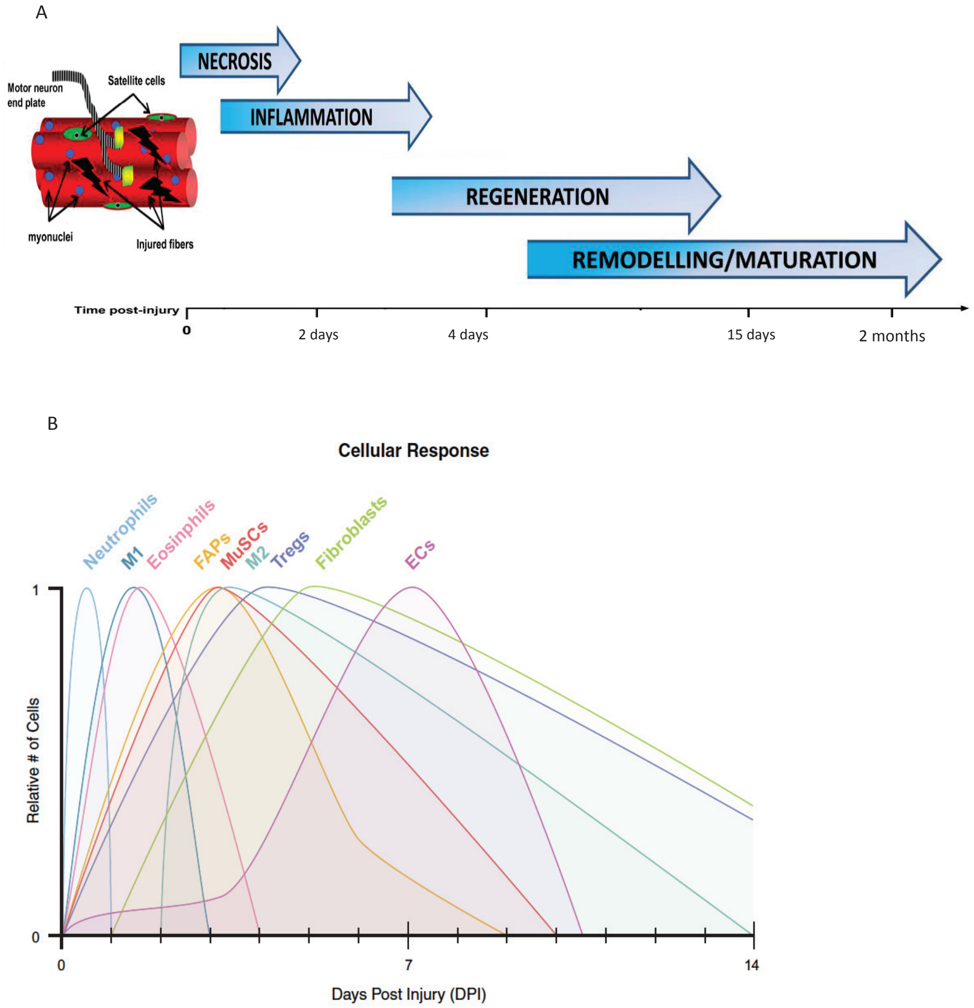

Figure 20. A) Muscle repair phases adapted from[197]. B) Cellular modifications during the first two weeks of skeletal muscle regeneration[169]. Abbreviations: M1 and M2, macrophages; FAPs, fibroadipogenic progenitors; MuSCs, muscle stem cells; Tregs, regulatory T cells; ECs, endothelial cells.

Overall, skeletal muscle regeneration can be divided in four interrelated phases: myofiber degeneration, acute inflammation, regenerative phase, and ECM remodeling associated to muscle maturation (Figure 20A). The timing of cellular modifications is well-described in myotoxin-induced lesions (Figure 20B) which allow *ad integrum* regeneration by the conservation of ECM and vascularization[198]. Indeed, muscle regeneration needs specific structural and trophic cues to fully regenerate, with events close to those occurring in muscle development. However, depending on the type of injury[199], muscle regeneration could be more or less effective due to alterations in:

- the ECM structure,
- the inflammatory response,

- the revascularization and reinnervation.

Therefore, modifications in this complex temporal and spatial process leads to fat and fibrotic tissue deposition associated with muscle function impairment, that are observed during aging and pathologic processes.

I-B-3) ECM modifications during muscle regeneration

Extrinsic signals play a key role in regulation of satellite cell behavior during muscle regeneration. Many studies focused on soluble molecules secreted by cells involved in the process. Physical and chemical signals provided by muscle ECM are also essential to drive an optimal muscle repair (Figure 20). ECM composition and stiffness sustain dynamic modifications with various transitional ECMs providing specific spatial and temporal signaling during the myogenesis process[200]. In addition, ECM directly acts on cell behavior or by modifying activities of several biomolecules and growth factors.

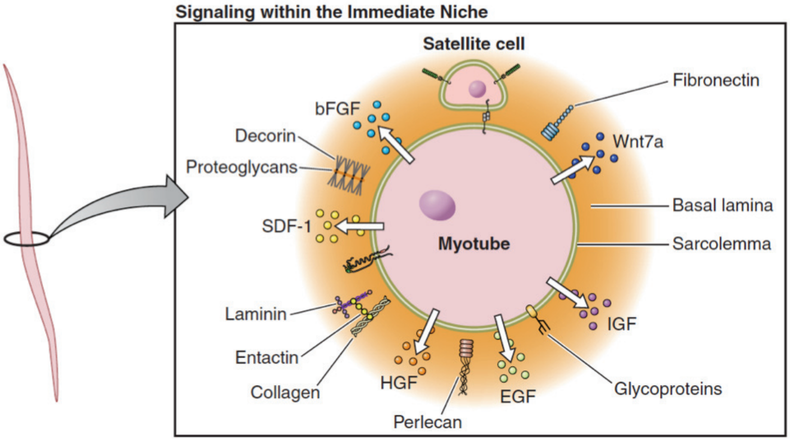

Figure 20. The satellite cell niche[201].

- Dynamic modifications of ECM composition

Identification of the complexity of ECM composition is not yet completely reachable notably their spatial distribution in skeletal muscle tissue. Therefore, current explorations to understand the role of ECM composition during regeneration is mainly based on *in vivo* identification of key ECM molecules at specific regeneration time points by immunostaining[190,202–204] or specific isolation from muscle samples[205]. These investigations are completed by quantitative Polymerase Chain Reaction (qPCR) analysis on whole tissue[200] or isolated MuSCs at different stages of the myogenic process[109] to speculate about what could be secreted. Another common approach is to study a specific ECM component in *in vitro* analysis focused on MuSC behavior[202,203,206] including migration, proliferation and differentiation/fusion, that can not always predict *in vivo* function. Therefore, it is completed with silencing or overexpression in various *in vivo* rodent models of muscle regeneration[109].

Several ECM molecules interact with each other and act in combination to modify cell behavior during muscle regeneration. However, their exact biological functions are not fully understood. We detail here the main advances for each component family.

Identified specific ECM molecules

The main fibrillar collagen in healthy muscle is collagen I, but after an injury there is an increase of collagen III content around 5 DPI, that leads to an inversion of collagen I/III ratio, with a reduced value as compared with resting muscle[205]. In addition, neo-synthesized collagen is initially stabilized by cross-link with embryonic characteristic[205]. Lastly, fibrillar collagens ratio and cross-link pattern gradually returns to uninjured state within two months. Other collagens have specific actions in muscle regeneration (Table 2) such as collagen VI involved in satellite cell self-renewal[202].

	Collagen family	**Expression and function during muscle regeneration**
CORE MATRISOME	Collagen I	Enhances myoblast proliferation and migration in vitro[207].
	Collagen III	Rapid increased expression at 5 DPI with transitory decrease of the I/III collagen ratio[205].
	Collagen IV	Increases myoblast adhesion and differentiation in vitro[204].
	Collagen V	Notch-Collagen V-Calcitonin receptor to maintain quiescence of satellite cells[203].
	Collagen VI	Self-renewal of satellite cells via modulation of the niche stiffness[202].
	Collagen VIII	Increases myoblast proliferation in vitro[208].

Table 2. Collagens in skeletal muscle regeneration.

The most studied glycoproteins are fibronectin and laminins (Table 3). Fibronectin has multiple actions in muscle regeneration depending on its spatio-temporal distribution. Indeed, satellite cells can remodel their niche by transient and local expression of fibronectin, promoting their symmetric expansion via non-canonical Wnt signaling[109]. This specific high expression is absent in aging, with alteration in satellite cell function[98]. During muscle maturation, myofibroblasts interact with myotubes to deposit fibronectin on their sarcolemma, sufficient to trigger nuclei towards the cell periphery by specific integrin interaction[110]. It is important to underline that conformation of fibronectin molecule affects its function[209] and could explain its various actions observed *in vitro* on myoblast fate.

	Glycoprotein family	Expression and function during muscle regeneration
CORE MATRISOME	Laminins	- Myoblast adhesion and migration on laminins 211 and 221 via α7β1 integrin[210]. - Laminin α5 expression increases during muscle regeneration[211]. - Laminin 521 improves *in vitro* myoblast proliferation and myotube formation[212]. - Ct terminal fragments of laminins 211, 332, 411 and 511 support self-renewal of satellite cells[213].
	Fibronectin	- Self-renewal of satellite cells via Wnt7a/Fzd7 (as co-receptor of syndecan 4)[109]. - Increased expression at day 5 and decrease after 2 weeks (CTX injury)[109]. - Implied in local peripheral nuclear positioning[110]. - Improves myoblast fusion via collective migration favoring cell-cell alignment[214].
	Entactins (Nidogens)	- Promotes adherence of contractile myotubes *in vitro*[215]. - High levels of entactin-1 enhance myoblast proliferation. Expression of the entactin-2 is induced during myogenic differentiation whereas entactin-1 expression decreases[216]. - Combination of laminin/entactin on collagen I scaffold enhance myotube formation[217].
	Matrilin-2	- Transiently up-regulated with induction of terminal myogenic differentiation[218]. - Promotes neurite outgrowth, Schwann cell migration and NMJ formation[112].
	Tenascins	- Tenascins are expressed around regenerating myofibers in rodent[219,220]. - In newt, tenascin-C is present in transitional ECM *in vivo* and increases myoblast proliferation and migration *in vitro*[221].
	Thrombospondins	- Initial increased expression during crush regeneration model[222]. - Adhesion and migration of myoblasts[223].
	R-spondin-1	Regulation of Wnt signaling pathways and limits myogenic cell fusion[224].
	Periostin	- Increased expression at day 7 and decrease after 2 weeks (laceration injury) and promotes fibroblast migration into injured muscle[225]. - Transiently up-regulated in regenerative phase after CTX injury, localized around regenerating myofibers. Increased expression during myoblast differentiation[118]. - Secreted by endothelial and myogenic progenitors to promote myogenic differentiation/fusion and angiogenesis. It higher expression level is in FAPs[182].
	Vitronectin	- Regulated during muscle regeneration. - Adsorbed vitronectin promotes myotubes formation of C2C12 muscle cell line[226].
	Osteonectin (SPARC)	- Increases differentiation/fusion of C2C12. Modulates expression of their mitochondrial proteins and some ECM components (collagen I and fibronectin)[227]. - SPARC overexpression decrease myogenic differentiation[228].

Table 3. Glycoproteins in skeletal muscle regeneration.

Abbreviations: Wnt, Wingless/Int; Fzd,Frizzled; CTX, Cardiotoxin ; NMJ, neuromuscular junction

PGs are essential for muscle regeneration, since inhibition of their synthesis impairs myotube formation[229]. However, they contain a ratio of various type of GAGs, with specific localizations in muscle ECM and cell membrane. This complexity[60] causes additional difficulties to identify their specific action during muscle regeneration, summarized in table 4.

	Proteoglycan family	**Expression and function during muscle regeneration**
CORE MATRISOME	**Proteoglycans** Heparan sulfate (HS) proteoglycans Perlecan	- Transiently increased in muscle after barium chloride injury[230]. - Decreased expression during myogenic differentiation *in vitro*[231].
	Chondroitin sulphate (CS) proteoglycans Biglycan (also a SLRPG)	- Transiently up-regulated expression[200,232] decreasing during skeletal muscle differentiation and maturation[232]. - Participates to the clustering of acetylcholine receptors (AchR)[233].
	Versican	Its cleavage by ADAMTS (A Disintegrin And Metalloproteinase with Thrombospondin motifs) proteinase facilitates myogenic cell fusion[234].
	Dermatan sulphate proteoglycans Decorin (also a SLRPG)	- Modulation of TGFβ1 signaling[235]. - Increases myoblast migration on collagen I via inhibition of TGFβ2[236] - Enhance myoblast proliferation *in vitro* by inhibition of myostatin expression[237] and activity[238].
	Keratan sulfate proteoglycans Fibromodulin (also a SLRPG)	- Involved in expression of collagen I and Myogenin via Ca^{2+} influx[239]. - Inhibition of myostatin during myoblast differentiation[240].
	Hyaluronan (GAG without protein core)	- Accumulates around necrotic fibers via Has1 (hyaluronan synthase 1) and during myogenic differentiation via Has 2[106].
MATRISOME ASSOCIATED	ECM affiliated proteins Heparan sulfate (HS) proteoglycans Agrin	Participates to the clustering of AchR via HGF[241].
	Glypican 1	- Increased expression during differentiation *in vitro*[242] - Can sequester FGF-2 in lipid raft domains[243] - Required for HGF signaling to increase myoblast migration[244].
	Syndecans	- Overexpression of syndecan 1 inhibits differentiation via FGF-2[245,246]. - Syndecan-3 interacts with Notch[247] and is down regulated during muscle differentiation[248]. - Syndecan-4 increases satellite cell proliferation via FGF-2[249] and migration[250]. Its expression is down regulated during muscle differentiation[251].

Table 4. Proteoglycans and GAGs in skeletal muscle regeneration.

All families of GAGs, including their core protein[252,253], can modulate growth factors[70,148,254], signaling pathways[109,247] and chemokines such as CXCL-12 to trigger a more efficient myoblast adhesion and migration[155].

Another strategy is to investigate the ratio of different GAGs. It is known that the HS/CS ratio changes during myogenesis since a higher amount of CS is maintained for two months in an ischemic muscle regeneration[255] model. Sulfation and chain size also increased in HS and CS. This is associated with a modification in the binding of growth factors, such as FGF-2, leading to an increase in biological activity[255]. Specific modifications by extracellular HS 6-O-endosulfatases could enhance myogenic differentiation by repressing FGF-2 signaling[256]. Muscle differentiation[65,257] is also accompanied by a modification of HS localization, with a higher amount of cell-associated HS[257]. In activated MuSCs these components, localized in the sarcolemma, are mainly syndecans[258,259], and after muscle differentiation[260] are mostly glypican 1 allowing for the sequestering of FGF-2 (Figure 22).

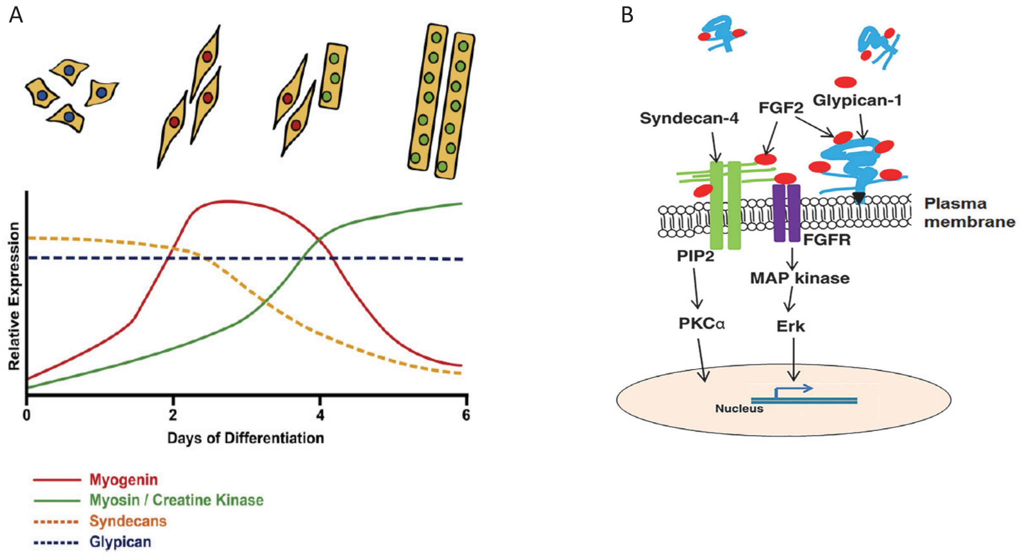

Figure 22. A) The expression of syndecans but not glypican-1 is down-regulated during skeletal muscle differentiation[70]. B) Interactions of FGF-2 and syndecan-4 and glypican-1[261].
Abbreviations: FGF-2, fibroblast growth factor 2; FGFR, fibroblast growth factor receptor; MAP kinase, mitogen-activated protein kinase; PI3 kinase, phosphatidylinositol 3-kinase; PKCa, protein kinase C a.

Other ECM affiliated proteins have a specific action on muscle regeneration as osteopontin, a small glycoprotein, acting during early phase[262]. Interestingly, this molecule is secreted by multiple cells including myoblasts, with a dual effect *in vitro* depending on its soluble or immobilized presentation[126]. Indeed, solubilized osteopontin increases myoblast proliferation whereas coated-osteopontin stimulates myoblast migration and myogenic fusion.

o Transiently remodeled ECMs

During muscle regeneration, ECM is extensively remodelled, since degradation of macromolecules is crucial for cell migration. Therefore, transient ECMs regulate muscle regeneration although their specific role and full composition still need further explorations. Key molecules, such as fibronectin, tenascin C and hyaluronan are interesting candidates of transient ECMs, since they are the main components of the blastema formation after amputation in amphibian[221] and zebrafish[263] followed by *ad integrum* skeletal muscle regeneration.

ECM remodeling requires proteinases (MMPs) that are secreted in latent form and are converted to active form at specific timing by proteolytic activation cascade. Tissue inhibitors of metalloproteinases (TIMPs) inactivate MMPs. During muscle regeneration, MMP-9 is active during the inflammatory phase while active MMP-2 operates during regenerative phase.

Finally, even if ECM composition is modified during muscle regeneration, a given component can modify cell fate depending on its specific timing and localization. For instance, fibronectin[109,110] acts on both satellite cell niche and nuclei localization in myotubes. In addition, various associations of ECM molecules have different cell actions through specific integrins[12,264–267].

- ECM as a physical support

Muscle ECM provides a physical support for migration and alignment of myogenic cells during the formation of neomyofibers[268]. Injury models in which the basal lamina is maintained display *ad integrum* muscle regeneration[269]. Indeed, laminin and collagen IV are maintained in toxic injury, these remaining ECM structure are called "ghost fibers"[268,270,271]. By *in vivo* imaging, fluorescent myoblasts are observed migrating along these ghost fibers before fusing to replace the injured muscle. On the contrary, neomyofibers are disorganized in the absence of basal lamina[268] (Figure 23).

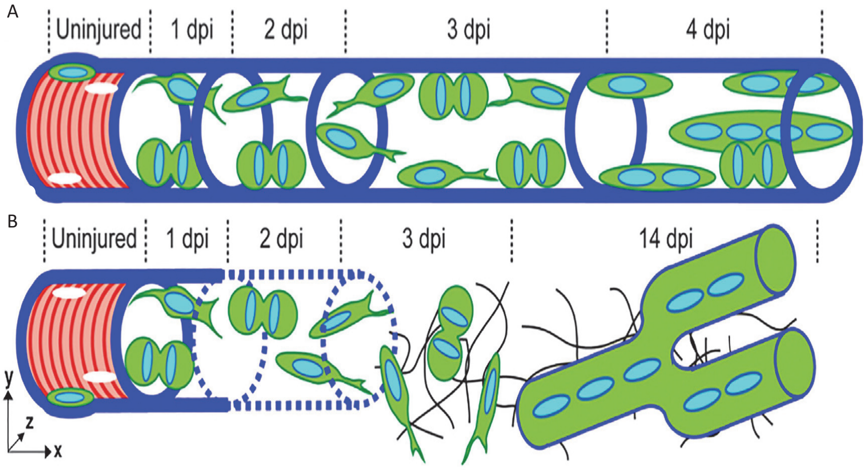

Figure 23. Muscle regeneration sustained by A) ghost fibers maintained as a guide for myogenic cell migration and formation of nascent myotubes. B) If the ghost fibers are damaged, myogenic cells migrate to interstitial ECM along random migratory path causing disorganized regenerated muscle[268].

In addition, ECM stiffness has a proper function. Transitional ECM in amphibian exhibits lower tissue stiffness, promoting migration and inhibition of terminal differentiation of myoblasts[221]. Higher content in collagen III and looser fibrillar collagen[272] also promote migration. *In vitro* analysis have emphasized that substrate stiffness close to that of the skeletal muscle tissue improves myogenic behavior[273].

Therefore, an increase in ECM production during muscle regeneration provides scaffolding for nascent myofibers. But in some cases, disorganized depositions are deleterious since pathological accumulation of ECM impedes muscle repair and mechanical function (Figure 24).

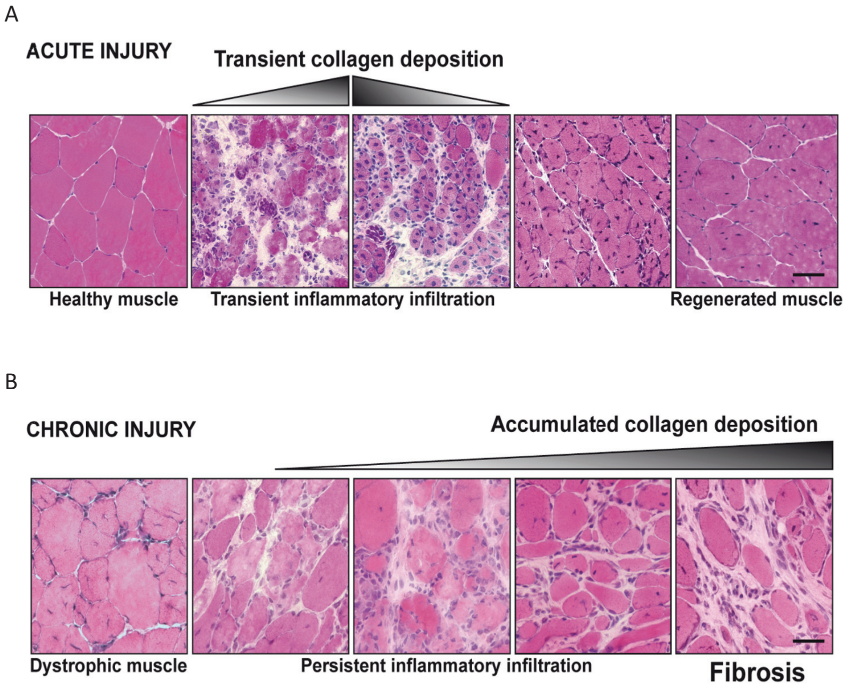

Figure 24. ECM modification in A) acute and B) chronic muscle regeneration[18].

I-B-4) Dysregulation leading to fibrosis

Fibrosis represents the advanced stage of several muscular diseases, mainly dystrophies and myopathies[274]. The most investigated is Duchenne Muscular Dystrophy (DMD), caused by mutation/deletion in the gene encoding for dystrophin and leading to a severe form of childhood muscular dystrophy. Myofiber necrosis results from continuous injuries and fibers are progressively replaced by a fibro-adipose tissue[275]. The consequence is a gradual loss of muscle and severe impairment of muscle function.

Fibrosis is observed in other organs and share common mechanisms corresponding to an excess of ECM components associated to high levels of growth factors, cytokines and proteolytic enzymes[35]. TGFβ is the main pro-fibrotic molecule[276], exhibiting complex signaling networks in multiple tissues[277] and acting in crosstalk with Wnt pathway[278] and renin angiotensin system[279]. Myostatin, a member of TGFβ super family, is another key actor in skeletal muscle fibrosis[280].

In healthy tissues, TGFβ is stored inactive inside the ECM, binding to LTBP-4 (Latent TGFβ binding protein 4) and its activation requires the release of TGFβ from this complex[122]. TGFβ acts via its receptor on target cells to activate SMAD (Small Mothers Against Decapentaplegic) and non-canonical MAPK pathway (Figure 25) to induce a fibrotic program with synthesis of several ECM components and positive auto-feedback loop.

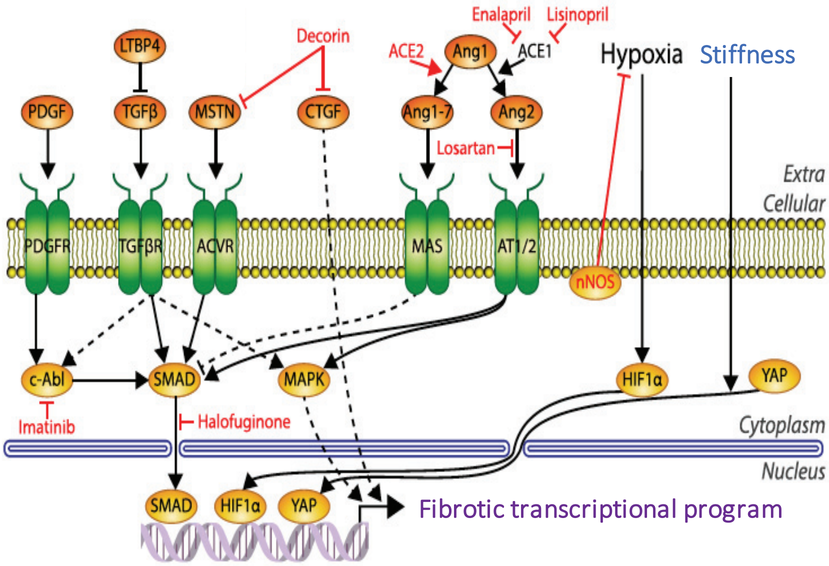

Figure 25. Fibrotic signaling pathways in skeletal muscle. Adapted from[281].
Dashed lines indicate indirect effects. Abbreviations: MSTN: myostatin; ACVR: activin type 2 receptor; AT1/2: Angiotensin II receptor type I and II; ACE: angiotensin converting enzyme.

During fibrosis, ECM composition is modified with a major increase of collagen I or collagen IV content[35]. Glycoprotein content is also enhanced such as fibronectin[282]. The CS/HS ratio is modified with a rise of decorin and biglycan in dystrophic muscles[283], although decorin can act as an anti-TGFβ and Connective-Tissue Growth Factor (CTGF)[284]. The presence of osteopontin is also observed in inflammatory areas[285]. In addition, qualitative modifications occur with initial collagen crosslinking by LOX enzymes (upregulated by TGFβ) whereas pyridinoline content is associated with severe fibrosis[35]. Viscoelasticity is impaired[286] leading to higher muscle stiffness and muscle functional disabilities. Fibrosis also results from a reduced ECM degradation[287] while modifications and disorganization of ECM can impair its enzymatic degradation by MMPs. TIMPs are regulated by TGFβ and their expression is increased in muscle and plasma of DMD patients[288]. However, some MMPs are upregulated, especially those transiently activated during the inflammatory phase of physiological muscle regeneration such as MMP-9[289], suspected to increase fibrosis. Interestingly, some MMPs and ECM fragments are released from synthesis or degradation and could be used as biomarkers[290] (Table 5).

Type of marker	Related to process	Application in muscle
C1M, C3M	Collagen 1,3 degradation	Inflammation in muscle tissue
PINP, C1M	Collagen I synthesis, ECM remodeling	Fibrosis
CAF	Agrin fragmentation	Functional disintegration in neuromuscular junction, sarcopenia

Table 5. Peptides produced by specific cleavage of ECM with clinical relevance as potential biomarkers for neuromuscular diseases. Adapted from[290].

At a cellular level, TGFβ and stiff ECM induce the differentiation of various progenitors into myofibroblasts, the main actors of fibrosis[291], leading to ECM disorganization that in turn induces myofibroblast transformation (Figure 26). Chronic elevation of TGFβ is deleterious to myoblasts with induction of apoptosis[292] and their differentiation into myofibroblasts[293]. In addition, the increase in ECM stiffness can impair myogenic properties such as self-renewal[273] and proliferation[294], with fibrotic differentiation[295].

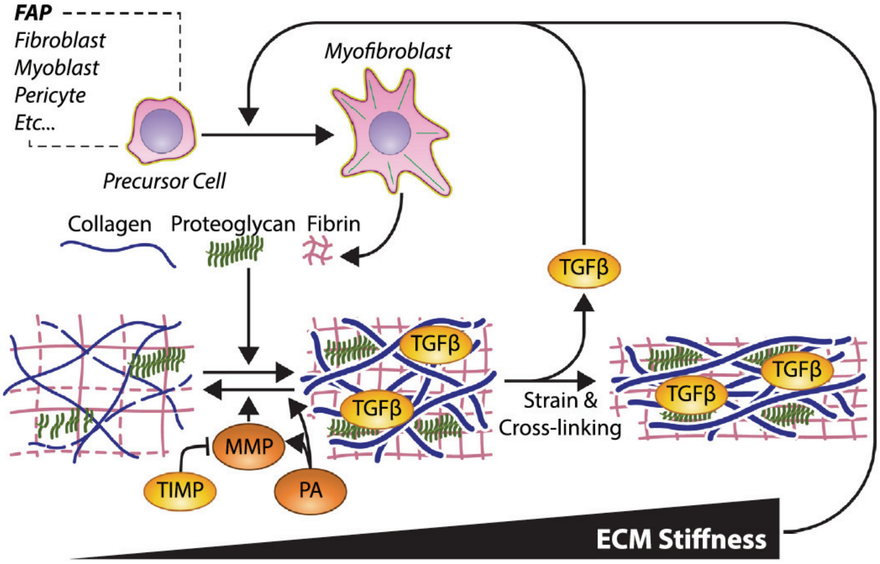

Figure 26. Profibrotic feedback loop with myofibroblasts secreting ECM components and the increase of ECM stiffness leading to more numerous myofibroblasts[281]. Abbreviations: PA, Plasminogen activator; MMP, Metalloproteinase; TIMP, Tissue Inhibitors of Metalloproteinases; TGF, transforming growth factor.

Fibrosis is characterized by a chronic inflammation with persistence of macrophages, leading to FAP long-term survival since apoptosis signal from TNFα is disrupted by TGFβ present at the same time[296] (Figure 27).

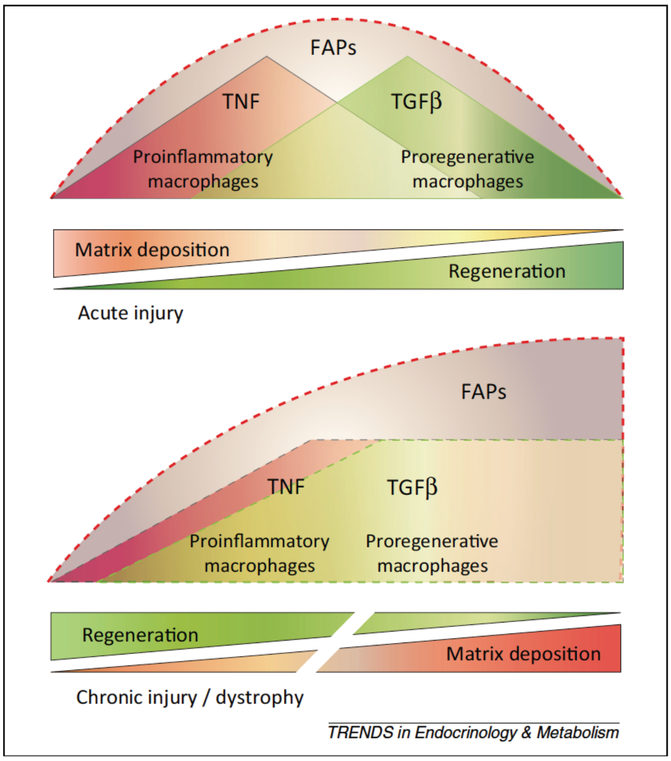

Figure 27. Interactions between macrophages and FAPs in skeletal muscle during A) acute injury with sequential pro- and anti-inflammatory macrophages and transient expansion of FAPs. B) In chronic injuries, inflammatory profile of macrophages is disturbed, with simultaneous production of TNF and TGFβ leading to FAP persistence and fibrosis[296]. Abbreviations: FAP, fibro/adipogenic progenitor; TGF, transforming growth factor; TNF, tumor necrosis factor.

I-C) Challenging treatment for volumetric muscle loss (VML) injuries

I-C-1) Severe limb injuries

"Every day, 16,000 people die from injuries, and several thousand more are injured, many of them with permanent sequelae. Injuries account for 16% of the global burden of disease" (WHO Guidelines for essential trauma care)[297].

- Limb injuries are extremely frequent in general traumatology

The majority of trauma-induced death and disability is overwhelmingly caused by road traffic crashes[298,299]. Indeed, road injuries are still increasing[300] and WHO estimates they will become the third leading cause of "Disability Adjusted Life Years loss" in 2020[301]. Moreover, extremity injuries are frequently observed in this type of road trauma[302] but they also occur during practice of extreme sports[303]. Natural disasters are another prominent cause of casualties presenting with a high proportion of open fractures[304] associated with large soft tissue wounds and specific infections[305].

In most cases, patients are polytraumatized and need intensive care in order to receive massive blood transfusion, correction of ionic and clotting troubles, or mechanical ventilation[306]. Definitive tissue repair strategies require a patient stable enough and are realized after multiple debridement, until wounds are macroscopically clean[307] (Figure 28). Soft-tissue injuries are extremely frequent in these patients but without specific treatment, often limited to a delayed soft-tissue coverage by specific surgery (flaps technic) to prevent infection and enhance bone healing[308].

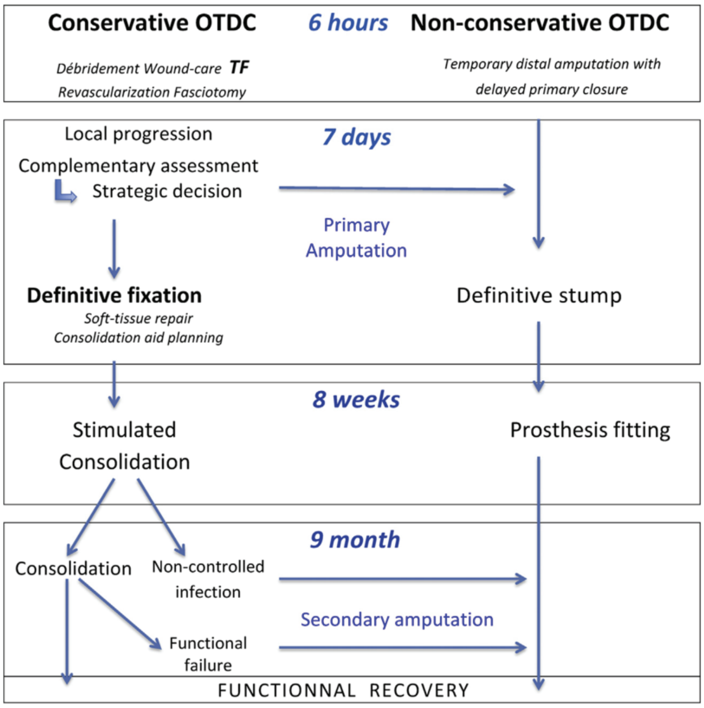

Figure 28. Management of severe limb injuries[309].
Abbreviations: OTDC, orthopedic trauma damage control; TF, temporary fixation.

- Limb injuries are also observed in military trauma wounds

War injuries lead to high rate of physical disabilities (more than 10% after civil wars in African countries[310]).

In current conflicts, improvised explosive devices have become extremely frequent[311,312]. The resulting blast-related injuries are due to direct or indirect mechanisms[312,313] (Figure 29) and these lesions are complex with important tissue destruction and contamination. Conversely, gunshot-injury incidence decreases[311,314] but they lead to an increasing proportion of open fractures.

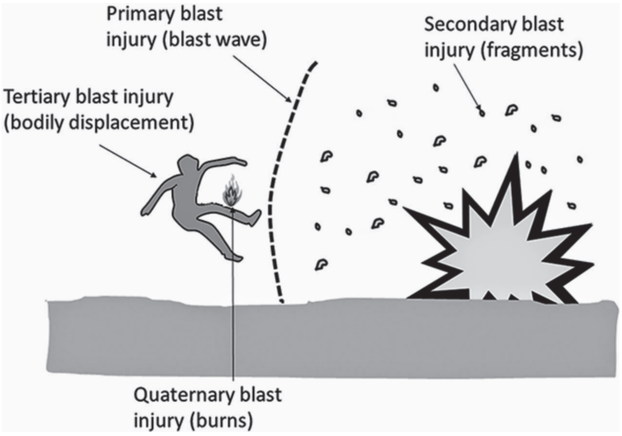

Figure 29. Blast-related injuries[315].

The protection of both the trunk and the head has been improved, but the limbs are unprotected, leading to one or multiple extremity lesions[311,316]. Furthermore, efficient medical care and rapid evacuation toward a field hospital have increased the overall survival of injured soldiers, who often suffer from multiple and complex lesions that were formerly lethal[317]. Medical interventions are gradually sequenced. During initial care, the emergency is to control haemorrhage by efficient and easy technics. When evacuated, the injured soldier is treated by surgeons according to the principles of damage-control[318,319], with an aggressive debridement of soft-tissues, vascular shunting and fracture stabilization[320]. Therefore, disabling limb lesions represent 50-70% of military wounds[311,314,316,317,321–323].

In many countries, the civilian population is increasingly subjected to blast[312] or gunshot[324]-related injury due to the terrorist threat or mass shootings. Most victims sustain musculoskeletal injuries as well, the majority in extremities and 40% of survivors will not be able to return to their pre-injury occupations[325].

These limb injuries have in common to concern young people, leading to a high rate of disability, without specific and efficient treatment for soft tissue lesions. Current orthopedic strategies attempt to preserve the limb integrity but amputation is necessary in 10-20% of cases[314,326,327], at initial time or later after failure of limb salvage attempts. Consequently, these extremity injuries have a high medical cost with long inpatient stays and frequent re-hospitalization[316,322,328].

I-C-2) VML injuries

VML injury is defined by a sudden removal of skeletal muscle mass overwhelming its capacity of regeneration. The term describes not only the initial mechanical muscle loss but also the evolution of the remaining muscle tissue (Figure 30).

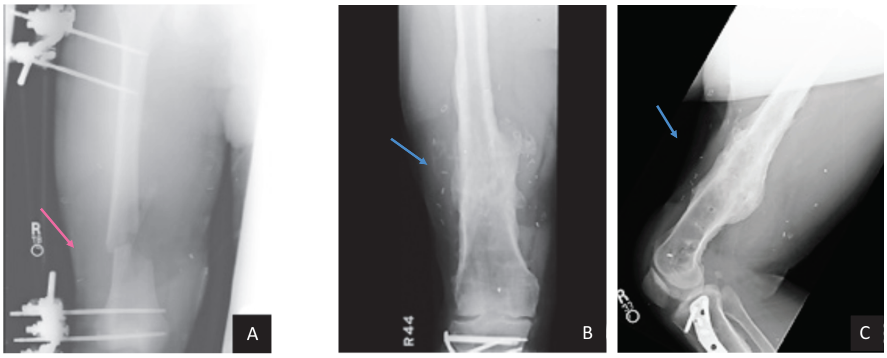

Figure 30. Patient with open fracture at right lower extremity. A) Anteroposterior radiography at initial care with external fixator then, B) after bone healing with C) lateral radiography. Adapted from[329]. Arrows illustrate VML evolution in the quadricep muscle.

- Epidemiology of VML

Traumatic VML can be a direct consequence of the injury or occurs after surgical care with multiple debridement and fasciotomy[330,331]. No precise threshold of muscle loss defines this pathologic process, which depends on muscle size and localization (more severe in transverse-oriented injuries). However, it is usually observed for losses above 20% of the initial muscle volume, despite being observable from 10%. The clinical consequence is muscle weakness and chronic disability[332].

In traumatology, VML has long been underestimated and was not always noticed because no specific therapy and follow up were available. VML could be frequent since only 50 to 70 % of patients return to duty after major trauma[333–335]. In addition, the difficulty in quantifying VML may increase its underestimation. Indeed, smaller disabilities induced by VML, that do not categorize patients as invalid, may hinder muscle function. Complex fractures repair with the use of various technics as fixator and/or biomaterial, but disabilities may persist because skeletal muscle condition is altered[336,337].

Muscle impairment is also among the most common disabilities found in injured soldiers. In a cohort of war-injured[338], a disability rate of 65% due to VML was observed after orthopaedic treatment and of around 10% in general war injuries. Indeed, more than 80% of open fractures present soft tissue defects, where muscle wound can result from initial lacerations or debridement of necrotic tissue. Consequently, VML is extremely frequent after open fractures.

Beside the trauma context, VML has also been described after surgical removal of muscle tumor-like extremity soft tissue sarcoma. It is observed in young patients with rhabdomyosarcoma[339] as well as in older patients[340,341] with an impaired muscle function, where age-related sarcopenia and chronic diseases already combine to foster muscle deconditioning.

- Physiopathology of VML

Several VML models have been investigated in preclinical studies, mainly in limb muscles of rodent or swine, confirming that the process of muscle regeneration is overwhelmed. Three weeks following VML, only moderate myofiber formation is observed, without reaching a healthy muscle-like recovery[342] even after six months[343].

Another notable observation is the onset of a persistent and major muscle deficit, larger than could be predicted from the initial lesion volume (Figure 31).

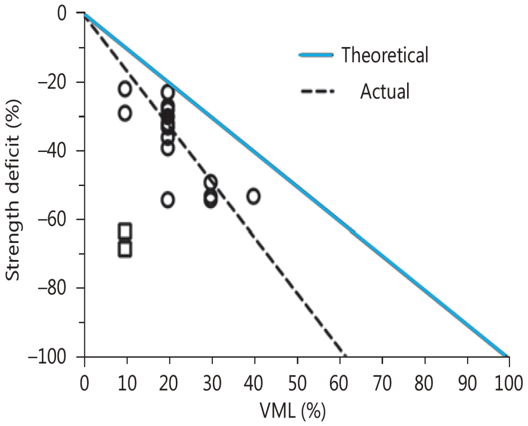

Figure 31. Regression analysis of force deficit after a VML (after 1–4 months) relative to the initial muscle loss. Adapted from[331].

For example, a volumetric loss (mainly transversal) as little as 10% of total muscle mass, can lead to a 60% decrease in muscle force. A complete loss of muscle strength could be observed despite one third of muscle mass remaining. This functional deficit is observed even after strength normalization to muscle weight[332]. In addition to regeneration impairment, VML relies on functional alterations in the remaining muscle.

Several hypotheses have been put forward to explain these observations:

- repartition of the mechanical strain from a large muscle section to a more restricted one,
- loss of essential signals such as innervation or vascularization,
- deleterious inflammatory mediators originating from the lesion site.

A rodent model highlighted an axotomy of 80% of the motoneurons three weeks post injury[342]. Then, denervation could alter the remaining muscle by several mechanisms such as atrophy[344] or capillaries loss[345]. A persistent and extremely detrimental inflammatory response has been described, leading to chronic fibrosis and fat deposition[343,346]. After VML, a set of genes[332,346–348] are durably upregulated (more than 2 months), particularly in pathways related to inflammation and ECM remodelling, such as Transforming Growth Factor β (TGFβ) and Wnt. Persistent infiltration of immune cells (mainly macrophages with mixed pro/anti-inflammatory phenotype[349]) and chronic fibrosis are observed in most animal models, even after therapeutic interventions such as debridement[348]. The functional consequence is a higher muscle stiffness due to higher collagen content with an increase in the collagen I/III ratio. Overall, because of functional alterations associated to fibrosis, the volume of residual musculature does not reflect its functionality.

Clinical case reports are limited but have provided some valuable data on the specific pathologic processes involved in VML[331], but their precise participation in VML pathological process need further explorations. Patients with VML also display a 20-30% of peripheral nerve injury[350]. Histologic explorations found a prolonged inflammatory cell infiltration and a chronic fibrosis, as well as myofibers with durable centrally located nuclei[351,352] in the remaining muscle, suggesting chronic alterations and/or denervation. In a case report, muscle rigidity appears to restrict torque production[332]. In addition, the length–tension relationship is also impaired, possibly by a reduced optimal sarcomere length, highlighted by a functional deficit variable depending on angle joint[332].

Finally, the pathologic elements involved can be schematically described as:

- Local loss of essential actors of regeneration, cell elements as satellite cells, or topographical cues such as "ghost fibers" shaped by basal membrane/endomysium[268], or gradients of signaling and chemo-attractive molecules.
- Functional overload in remnant muscle with persistence of non-resolving inflammation, leading to chronic fibrosis which compromises muscle force transmission (Figure 32).

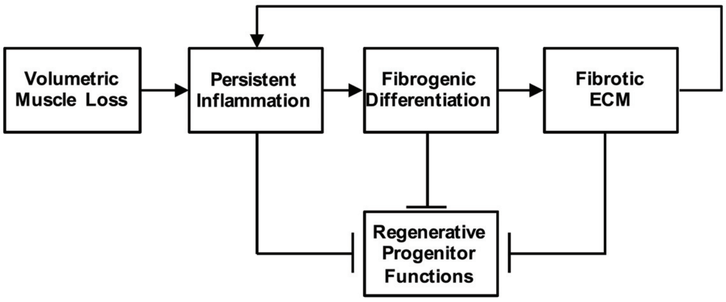

Figure 32. VML model as a feedback loop of inflammation and fibrosis[353].

Further explorations are necessary to dissect the complexity of VML physiopathology and especially to investigate the dysregulation in resident stem cells and other actors involved in muscle regeneration, such as macrophages and fibrogenic cells, that have been pointed out in aging or dystrophies. Composition of the fibrous tissue also needs to be further analyzed because other ECM modifications could occur during fibrosis, even at the basal membrane level[35].

I-C-3) Current therapies for patients with VML injury

Soft tissue wounds are frequently contaminated, causing a delayed closure and multiple scar revision, sometimes very distant from the initial lesion (until 10 years[351]). The initial muscle loss is surgically filled with fasciocutaneous or muscle flaps, with their own vasculature, requiring specific surgery[354,355] (Table 6). However, their utilization can be limited by multiple and large sites to cover, leading to donor site morbidity[354]. Even after a muscle tissue engraftment, these strategies will not achieve muscle strength restoration[355] but could participate in ameliorating bone repair[356].

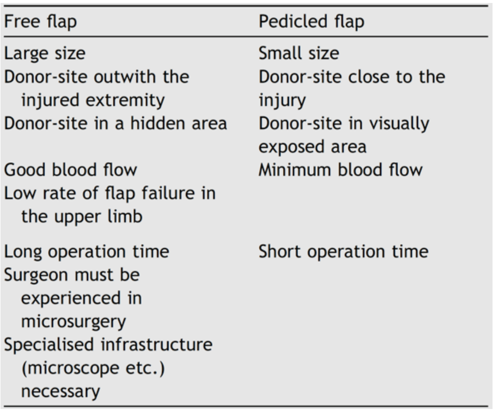

Free flap	Pedicled flap
Large size	Small size
Donor-site outwith the injured extremity	Donor-site close to the injury
Donor-site in a hidden area	Donor-site in visually exposed area
Good blood flow	Minimum blood flow
Low rate of flap failure in the upper limb	
Long operation time	Short operation time
Surgeon must be experienced in microsurgery	
Specialised infrastructure (microscope etc.) necessary	

Table 6. Free flaps versus pedicled flaps[308].

Physical rehabilitation is also frequently delayed for VML patients and particularly complex for those displaying multiple severe injuries with other tissue damage as neural lesion. There is a physiologic limit in muscle strength gain; physical therapies will optimize the utilization of the remaining musculature to improve the quality of life by restoring some functional autonomy (Figure 33). However, functional deficits persist[329,332,351,352,357,358] and will keep on declining with time[359], especially when the remaining muscle displays secondary injuries due to mechanical overload.

Despite an improvement in limb salvage, full functional recovery cannot be reached in patients displaying severe disabilities and pain, sometimes leading to secondary amputation allowing utilization of efficient orthosis[360].

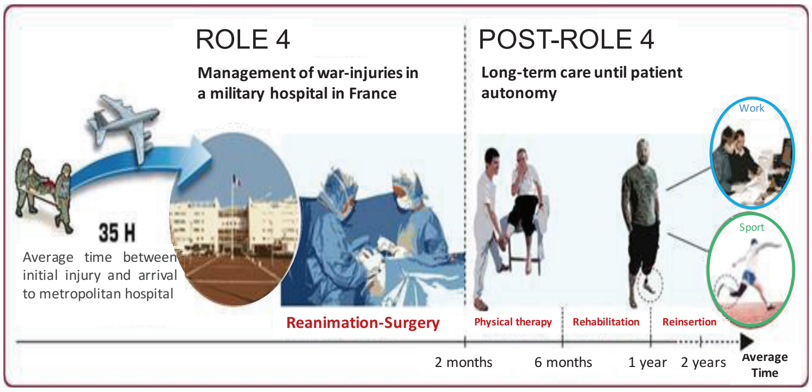

Figure 33. Treatment of war-wounded in French military hospital.
Adapted from French military staff source of images.

Overall, VML are heterogeneous and complex injuries leading to an impaired muscle regeneration although skeletal muscle owns high capacities of regeneration.

I-D) Regenerative medicine: a new hope for patients with VML

Regenerative medicine aims at replacing defective tissues or organs in order to restore physiological functions. Since VML shows no recovery, the aim of developing a regenerative therapy approach is to restore elements of the lacking muscle. The hypothesis is that biomaterial engraftment, associated or not with stem cells, will provide the missing physical support and trophic cues, to promote *de novo* myofiber regeneration. However, advances in VML knowledge are more in favor of multiple therapeutic targets to improve in parallel the remaining muscle displaying chronic fibrosis and inflammation[347,353]. In the present thesis, we will focus on the first therapeutic axis, i.e. the use of an optimal biomaterial for VML.

I-D-1) Biomaterial strategies for VML injuries

A biomaterial can be used to modify the form of a tissue or to replace it. To achieve this, scaffolds provide mechanical and trophic cues to attract or/and modify the behavior of endogenous cells and can also be used to transport exogenous cells or bioactive molecules[361]. A biomaterial can be composed of either natural components or synthetic molecules, sometimes both. It must be biocompatible, and in most cases, bioresorbable. Implanted biomaterials induce an initial immune response and in some deleterious cases, can lead to chronic inflammation also called host “foreign body reaction”[362]. Briefly (Figure 34), neutrophils invade the implant area, followed by macrophages which fuse to form foreign body giant cells. These cells release cytokines and growth factors, leading to fibroblast proliferation and a fibrous encapsulation around the implant[363].

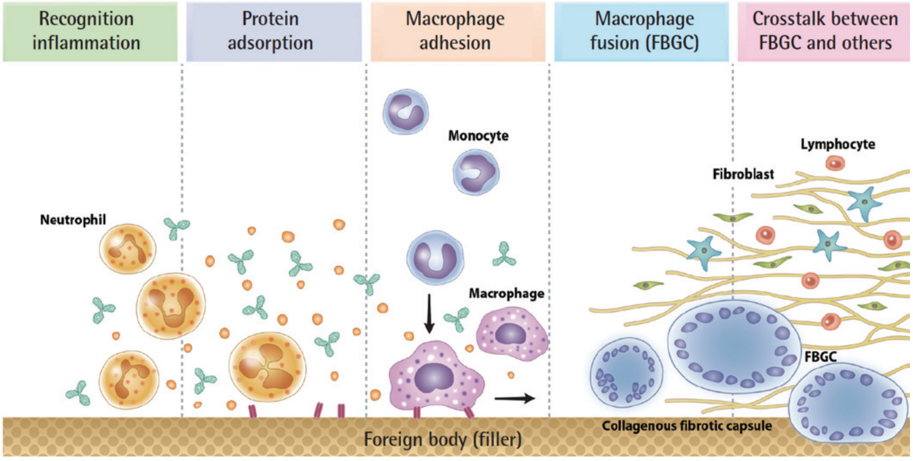

Figure 34. Different phases of the formation of foreign body reaction[364].

This inflammatory response mainly depends on the biomaterial composition. Biomaterial physical and chemical properties can be more or less controlled depending on:
- its chemical composition,
- its structure as pore size and uniformity,
- its mechanical properties as viscoelasticity and stiffness,
- its biological interaction, between cells and the biomaterial.

Considering VML, biomaterial could serve as a surrogate for one or more of the missing components essential for muscle regeneration and for recreating *de novo* muscle tissue that could be integrated to the remaining host musculature (Figure 35).

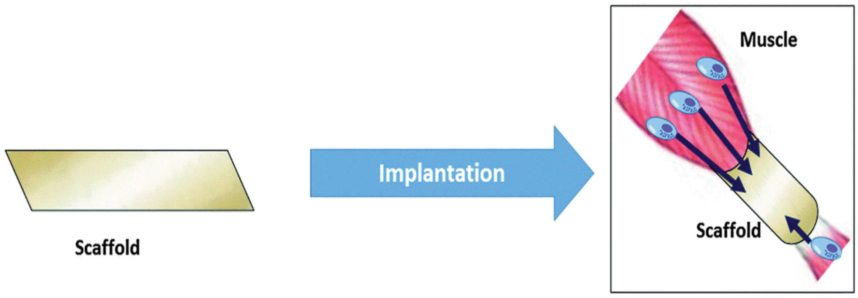

Figure 35. Biomaterial strategy for VML injury: recruitment of endogenous myogenic cells and favorable host immunologic responses post-implantation[365].

More importantly, scaffold should be able to attract satellite cells from the surrounding healthy muscle to induce adequate spatiotemporal events leading to muscle regeneration. It should also provide an efficient vascularization to avoid the formation of a necrotic core. For skeletal muscle applications, biomaterials of interest[366] are summarized in Table 7 and we will detail some of them, specially decellularized scaffolds which are the main goal of the present thesis.

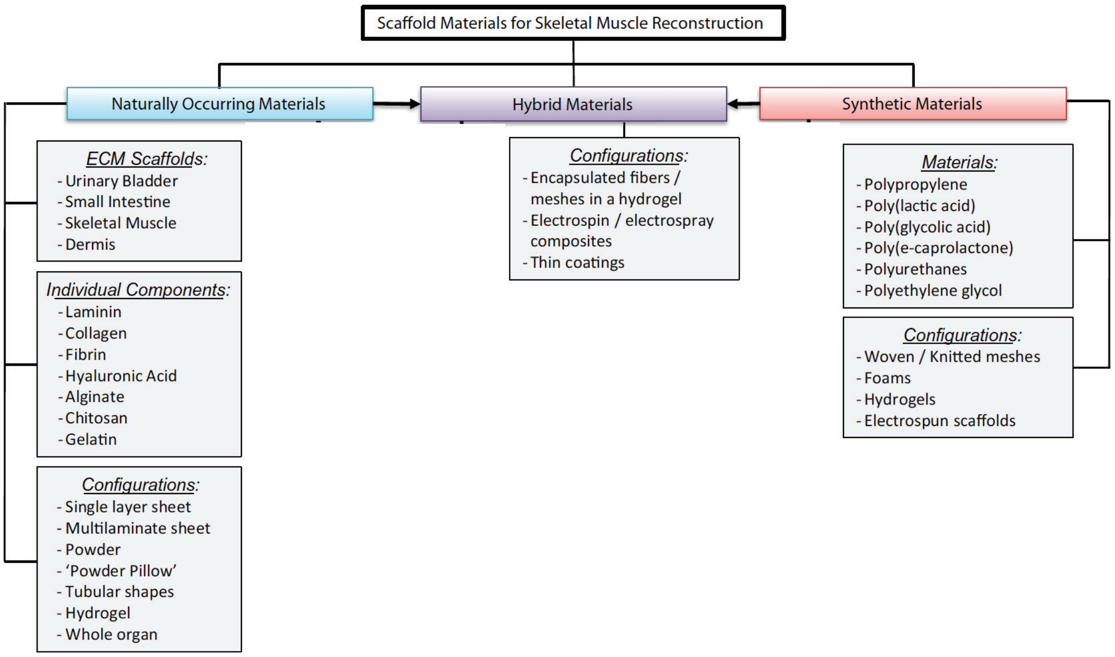
Scaffold Materials for Skeletal Muscle Reconstruction

Naturally Occurring Materials

ECM Scaffolds:
- Urinary Bladder
- Small Intestine
- Skeletal Muscle
- Dermis

Individual Components:
- Laminin
- Collagen
- Fibrin
- Hyaluronic Acid
- Alginate
- Chitosan
- Gelatin

Configurations:
- Single layer sheet
- Multilaminate sheet
- Powder
- ‘Powder Pillow’
- Tubular shapes
- Hydrogel
- Whole organ

Hybrid Materials

Configurations:
- Encapsulated fibers / meshes in a hydrogel
- Electrospin / electrospray composites
- Thin coatings

Synthetic Materials

Materials:
- Polypropylene
- Poly(lactic acid)
- Poly(glycolic acid)
- Poly(e-caprolactone)
- Polyurethanes
- Polyethylene glycol

Configurations:
- Woven / Knitted meshes
- Foams
- Hydrogels
- Electrospun scaffolds

Table 7. Biomaterials investigated for skeletal muscle applications. Adapted from[366].

I-D-2) Synthetic biomaterials

The advantage of synthetic components is to obtain a reproducible biomaterial with a precise characterization of its physical and chemical properties. Meshes of polypropylene are commonly used for hernia repair[367] and were described as an "inert" biomaterial despite they induce a localized foreign body response[368]. A variety of biodegradable biomaterials were evaluated to improve skeletal muscle formation *in vitro*[369]. A few of them were implanted in *in vivo* VML models[370]. For example, polyesters such as poly(lactic acid)[371] already have clinical authorization with a porous configuration allowing cell adhesion and vascularization. Polyurethane polymers[372] have also interesting properties with controlled stiffness and the capacity to be conjugated with bioactive compounds and growth factors.

These biomaterials display various configurations. Hydrogels hold viscoelastic properties close to native tissues and can be organized in precise shape and size while delivering cells and bioactive molecules. Interestingly, electrospinning can provide nanofibrous scaffolds[373] promoting myogenic cell alignment in vitro.

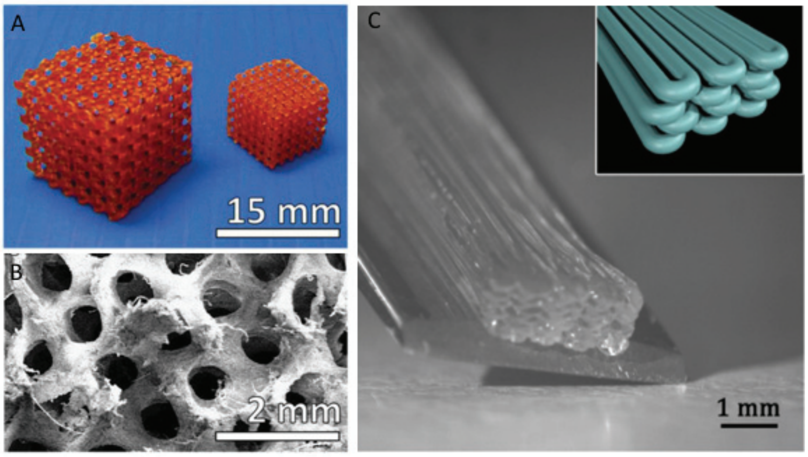

Figure 36. Biomaterials obtained by 3D bioprinting composed of A) chitin nanofibril scaffold[374] with B) structural characterization by scanning electron microscopy and C) unidirectional aligned PEG-Fibrinogen hydrogel with representation of fiber arrangement[375].

Overall, synthetic biomaterials are most often robust, may be useful for some applications in skeletal muscle tissue, which is exposed to high mechanical constraints. Currently, complex forms of synthetic biomaterials are starting to be produced, especially with the use of bioprinting[374–376] (Figure 36). But, as compared with native ECM scaffolds, these synthetic biomaterials hold less complexity in their composition and three-dimensional architecture. They also trigger foreign body reaction after implantation[363]. We therefore focused our work on natural biomaterials.

I-D-3) Natural biomaterials

Utilization of natural components for biomaterials is now developed to recreate the proper microenvironment of tissues.

- Biomaterials composed of natural components

Some biomaterials are obtained with purified proteins or polysaccharides. The main

ECM protein used is collagen I due to its easy isolation and modification. Xenogeneic collagen implantations have been used for years with a few severe complications despite some allergies could occur[377]. Also, fibrin mesh is interesting because its stiffness is close to that of skeletal muscle[378]. Polysaccharides, such as alginate[379] or hyaluronic acid[380] are also explored, often mixed with other materials to enhance their mechanical properties.

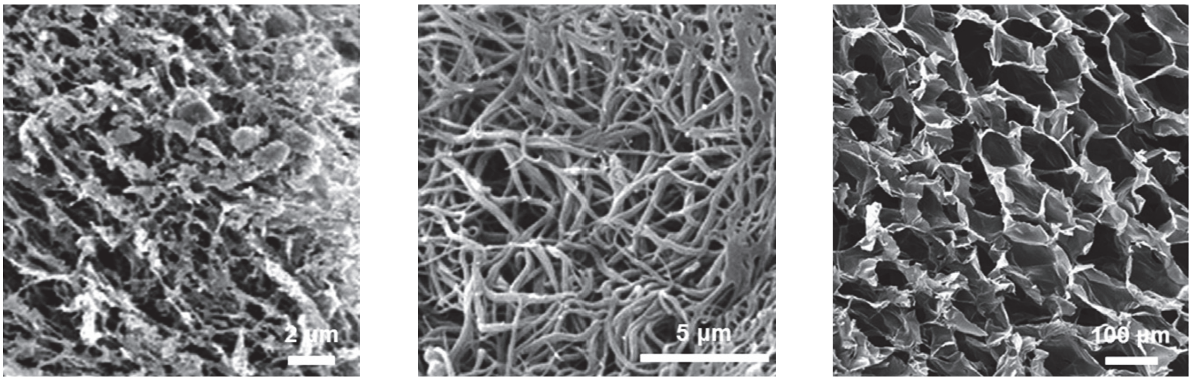

Hydrogel of Collagen I

Fibrin

Alginate

Figure 37. Biomaterials structure by scanning electron microscopy such as A) collagen[381], B) fibrin[382] and C) alginate[383] hydrogels.

The utilization of natural polymers improves cell interactions and adhesion but they lack three-dimensional architecture (Figure 37) and adequate mechanical strength. To obtain a scaffold closer to tissue complexity, decellularized scaffolds have emerged and seem the most promising.

- Decellularized biomaterials

Decellularized ECM-based biomaterials are derived from whole tissue from which cellular components are removed, maintaining only structural and functional ECM molecules. As compared with synthetic or single natural components, decellularized biomaterials hold the complexity of specific biological cues (such as cell adhesion sites), mechanical properties closer to the native tissues, intact vascular network[384] and a better host integration after implantation[385].

Therefore, they have several advantages for VML therapy because of the conserved native ECM composition and architecture, and even more if they are obtained from skeletal muscle maintaining its tissue-specific ECM (Figure 38).

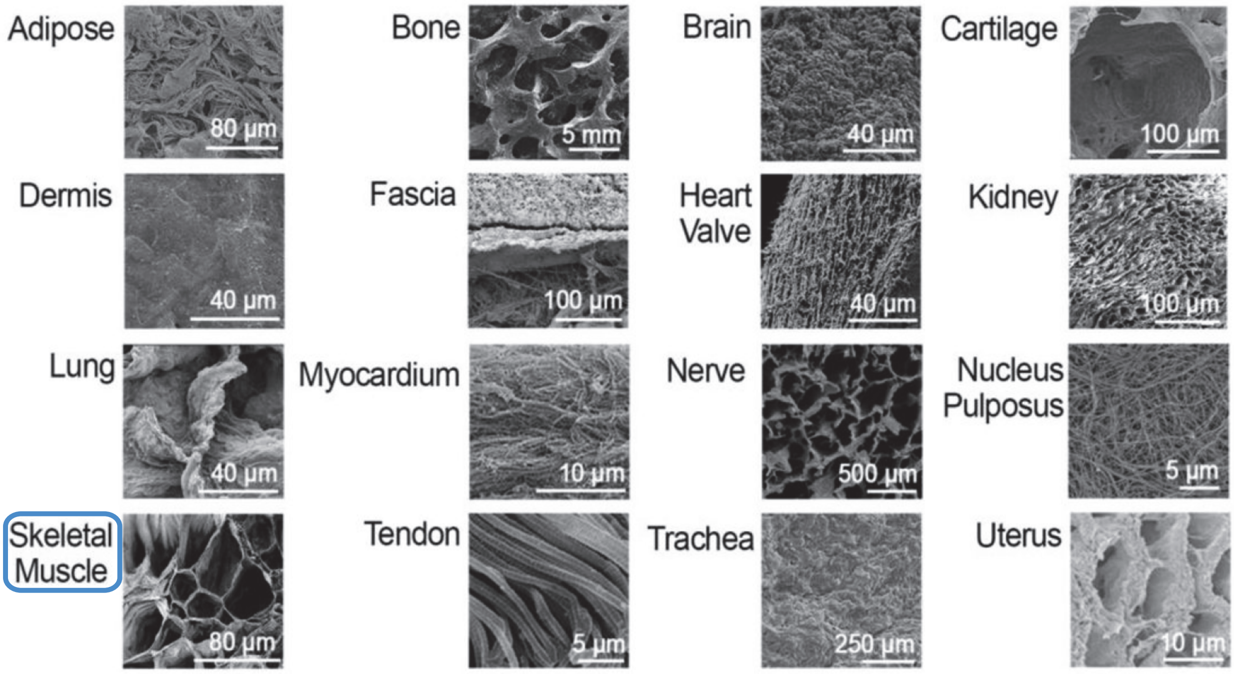

Figure 38. Microarchitecture of different decellularized tissues by scanning electron microscopy[386].

There are several decellularization procedures, leading to different types of biomaterials.

○ Multiple decellularization process

Decellularization consists in lysing cells and removing their debris. Multiple steps and agents can be used in various combinations depending on the future use and the tissue source. Therefore, the optimal protocol for a specific use should be established. The most popular methods are illustrated by categories in Table 8.

Briefly, physical treatments such as freezing-thawing are used to break down cells and minimize the use of chemical agents such as detergent or digestion enzymes. Most ECM-scaffolds are non-cross-linked in order to be biodegraded and avoid chronic inflammation[387]. Chemical remnants can be toxic and necessitate multiple washes for their elimination. Then, the last step for a complete process is sterilization which involves gamma irradiation or chemical agents such as peracetic acid.

Each step could damage ECM, especially chemical agents, thus short time administration is preferable. Decellularization processes depend on the density and the volume of the tissue or organ. Harsh processes are effective but they denature ECM molecules. Therefore, the ideal protocol is a balance between cell removal and key ECM component conservation, but any protocol inevitably removes or alters the desired molecules and the native architecture.

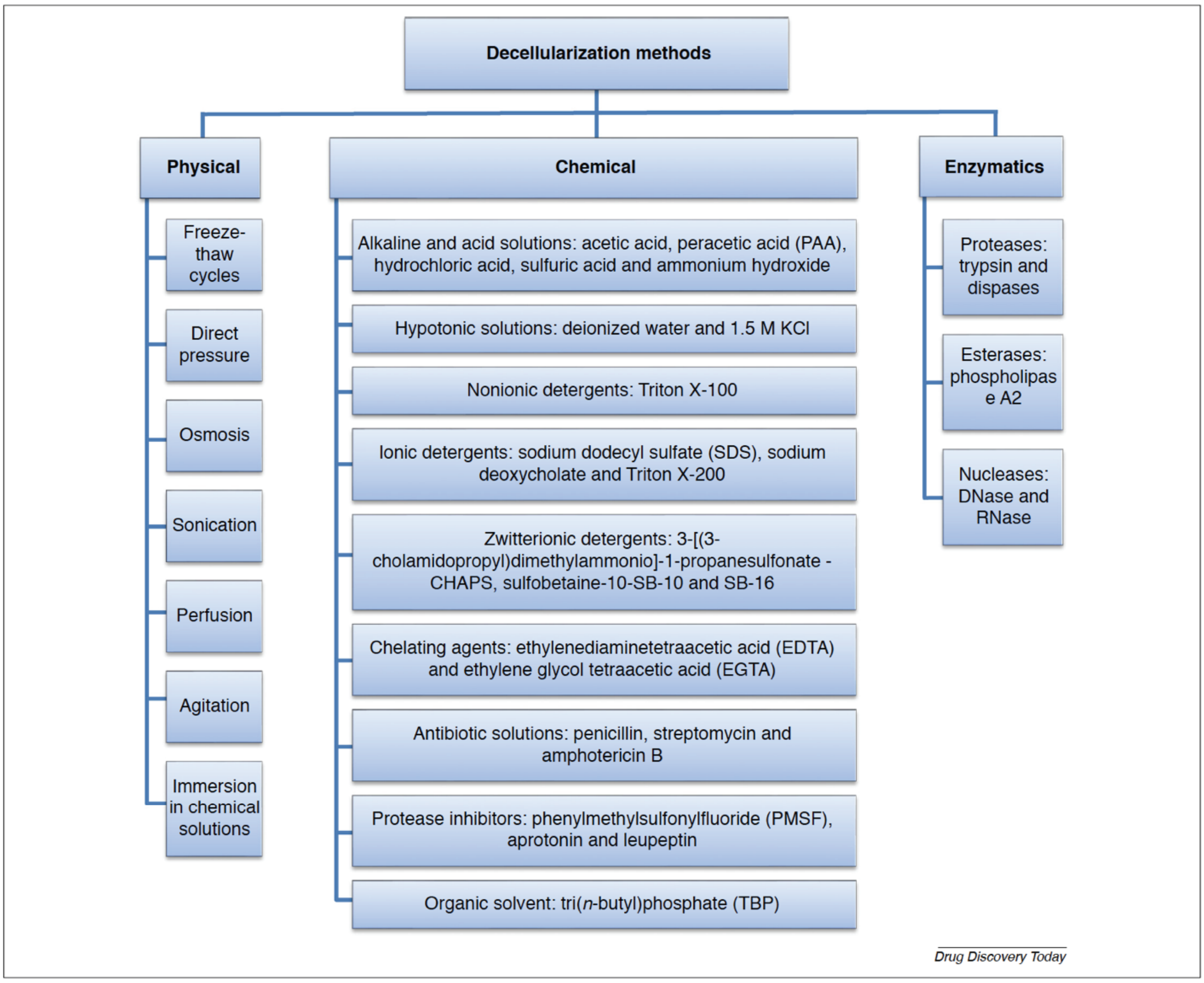

Table 8. Decellularization methods[388].

○ Characterization of decellularized biomaterial

Because both tissues and decellularization processes are heterogeneous, scaffold characterization is essential because variable compositions and structures could have an impact after *in vivo* implantation. There is no consensus about which biologic components must be monitored and it depends mainly on the application and tissue of origin. They can be subdivided in two categories:

- Unwanted components, which may be due to uncomplete cell removal and may trigger undesirable immune response. The validation is based on residual DNA amount and size with thresholds below 50 ng per mg of dry ECM and less than 200 base pairs (bp)[389]. Some components, which stimulate acute inflammatory response, need to be investigated such as cell-based antigen and endotoxins (e.g. Lipopolysaccharide, LPS) that could be found within biomaterial without living bacteria. Toxic remnants due to the decellularization process could also be deleterious and are also quantified[390].
- The conservation of key ECM components maintaining their specific spatial distribution and structure. ECM is composed of hundreds of molecules but the most

frequently explored in decellularized scaffolds are collagens, elastin, GAGs and growth factors. Less common investigations include mechanical strength (mainly elastic modulus) and *in vitro* interaction with intrinsic abilities to promote cell adhesion and growth.

Commercially available decellularized biomaterial

Xenogeneic tissues are already used for clinical applications. Most of them are derived from swine tissues such as urinary bladder matrix (UBM) and small intestinal submucosa (SIS) and are prepared with physical methods with few chemical intervention[389]. Their main utilizations are surgical reinforcement of soft tissues[391] and managements of various wounds[392].

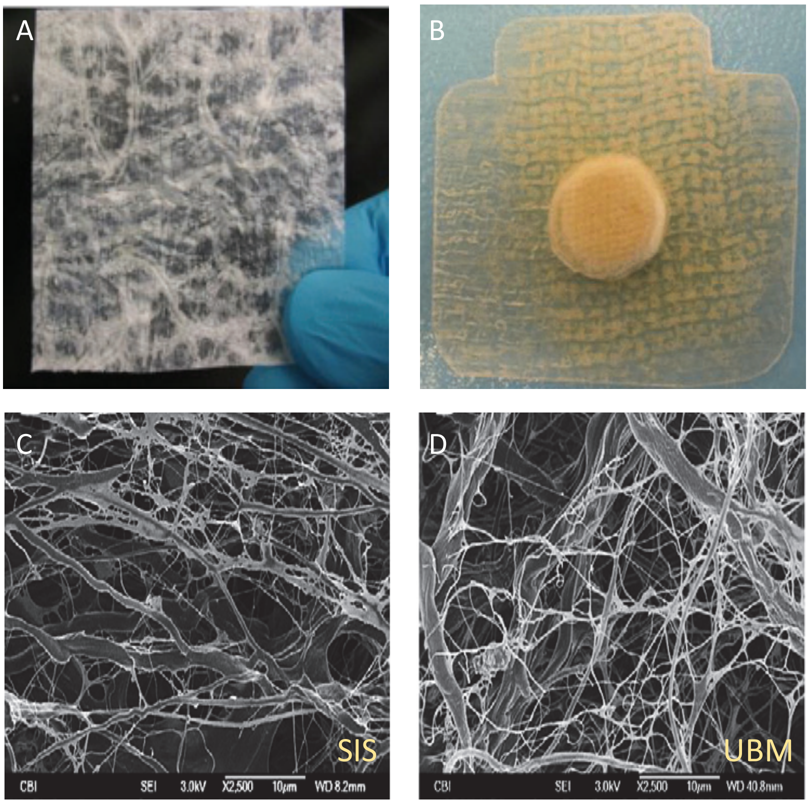

Figure 39. Variable configurations of most used decellularized scaffolds such as A) sheet and B) powder pillow devices[366]. Abluminal surface by SEM of C) SIS scaffold and D) UBM scaffold[393]. Scale bar represents 10 µm.

However, their three-dimensional architectures, and probably their compositions, are extremely different from that of skeletal muscle ECM (Figure 39).

I-E) ECM-based therapy for skeletal muscle injuries

Biomaterial-based intervention is a field of matrix-based regenerative therapy aiming at recreating extracellular structures participating in cell behavior through mechanical and biochemical properties[394], and at modifying the local kinetics of released growth factors or enzymes. Such a rationale has led to the development of components such as GAG mimetics[395,396].

I-F-1) Decellurized scaffolds in VML

ECM-biomaterials derived from several sources and species have already been investigated in different models of VML and in a small cohort of patients. We will focus here on extremity lesions.

- Non-muscle ECM based scaffold

Preclinical studies were performed in models of VML, investigating several species (rodents[343,397–403], canine[404,405] and swine[406,407]) and injuries (isolated, rarely multiple sites with bone defect[379]). The ECM used are mainly commercial acellular biomaterials (UBM and SIS). Only one study has obtained a complete regeneration after SIS-scaffold implantation in canine musculo-tendinous injury. However the study has no control group and the muscle neoformation was strikingly tardive at 6 months after 3 months of fibrosis scar[404]. Other studies display slight improvements in muscle function whereas histologic explorations show only few isolated muscle cells inside a fibrotic tissue[343,397,401,405]. Similar observations are made in a larger animal model (swine), where no functional improvement are reported after SIS and UBM scaffold implantation[406].

In patients, one longitudinal clinical cohort[351,352] and several case reports are published[329,408]. A first clinical observation was conducted on VML in quadriceps receiving a multi-layer of SIS-scaffold followed by a rehabilitation performed one month after the surgery. Four months later, the patient had functional improvements associated with de novo soft tissue in imaging but no histological exploration was performed to confirm muscle neoformation[329]. The same team followed a cohort with functional and histological explorations for the first five patients[351]. All of them displayed at least 25% loss of muscle mass or function. During surgery, they benefited from fibrosis debridement and an UBM scaffold implantation, with rehabilitation starting at 48h. Six months post-surgery, medical imaging showed dense tissues. However, histological analyses found only isolated myofibers with central nuclei associated with perivascular cells. Functional improvement was obtained for three patients. A second publication of the same cohort enriched to thirteen patients[352] treated with various commercial scaffolds (UBM, SIS, scaffold with a dermal origin). Half of the patients had improved strength but again, with a poor histological improvement and final scar aspect (Figure 40).

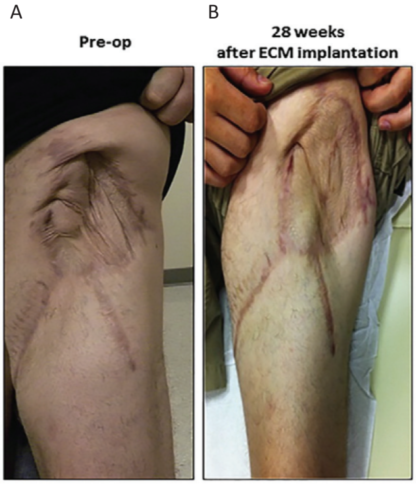

Figure 40. Injury site of patient with VML in quadriceps A) after 18 months of the initial lesion without ECM scaffold and B) at 7 months post-ECM implantation[352].

Overall, the use non-muscle ECM biomaterials displays encouraging results with functional improvements and the recruitment of perivascular stromal cells despite few muscle neoformation. Complexity of spatiotemporal events occurring in muscle regeneration is not obtained after implantation of these biomaterials. ECM scaffolds derived from skeletal muscle may be more suitable for reconstructive tissue remodeling than non-specific tissue sources.

- Muscle-based ECM

A variety of muscle-derived ECM preparations were evaluated[265,343,384,399,401–403,409–411] because the process is more challenging due the cell density, without the possibility to use physical procedure. However, the three-dimensional architecture of skeletal muscle is rarely maintained until recently[384,400,403].

Muscle ECM-based scaffold implantation were performed in various VML models. In limb injuries performed in rodents[343,397,399–402] or swine[409], the mean muscle loss was 20-30% of various muscles such as Tibialis anterior (TA)[343,397,399,402], quadriceps[409] and gastrocnemius[400,401]. At early (1 week[401]) and later time (until 6 months[343]) of histological evaluation, few myofibers were observed, close to the remaining musculature, with various levels of organization and maturity, mainly misaligned and surrounded by fibrosis (Table 9). Functional improvements observed could be due to fibrosis since isolated myofibers are not sufficient to provide strength. Interestingly, muscle ECM scaffold prevented the degradation of the remaining muscle tissue. Collectively, decellularized biomaterials partially restore muscle function, with variability due to different sources of scaffold and decellularization processes (Table 9).

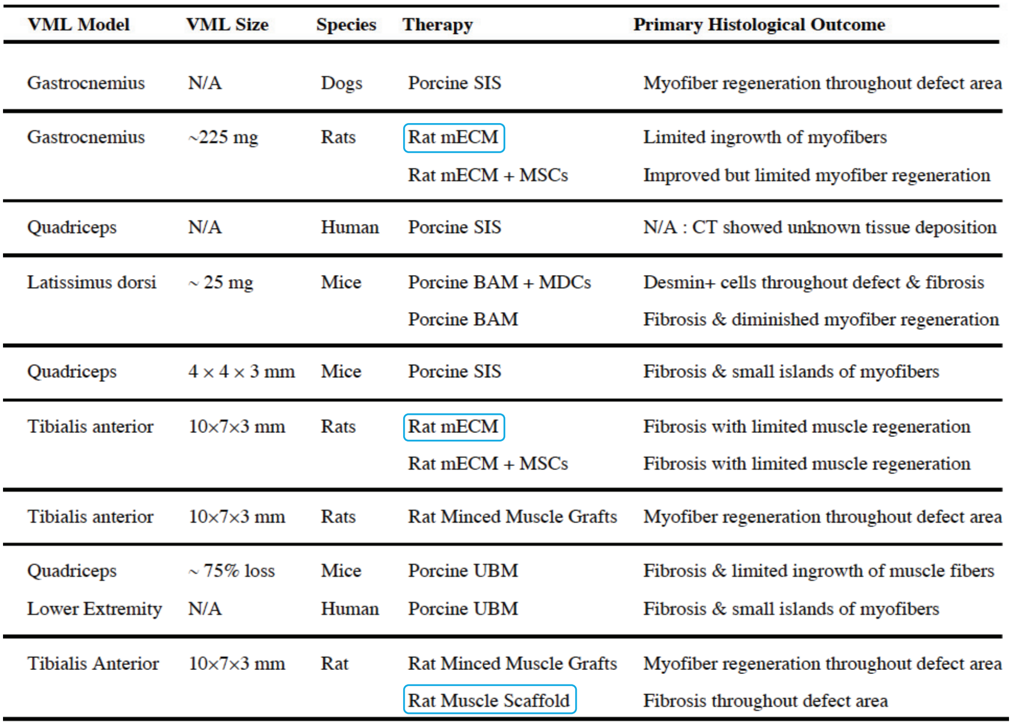

VML Model	VML Size	Species	Therapy	Primary Histological Outcome
Gastrocnemius	N/A	Dogs	Porcine SIS	Myofiber regeneration throughout defect area
Gastrocnemius	~225 mg	Rats	Rat mECM	Limited ingrowth of myofibers
			Rat mECM + MSCs	Improved but limited myofiber regeneration
Quadriceps	N/A	Human	Porcine SIS	N/A : CT showed unknown tissue deposition
Latissimus dorsi	~ 25 mg	Mice	Porcine BAM + MDCs	Desmin+ cells throughout defect & fibrosis
			Porcine BAM	Fibrosis & diminished myofiber regeneration
Quadriceps	4 × 4 × 3 mm	Mice	Porcine SIS	Fibrosis & small islands of myofibers
Tibialis anterior	10×7×3 mm	Rats	Rat mECM	Fibrosis with limited muscle regeneration
			Rat mECM + MSCs	Fibrosis with limited muscle regeneration
Tibialis anterior	10×7×3 mm	Rats	Rat Minced Muscle Grafts	Myofiber regeneration throughout defect area
Quadriceps	~ 75% loss	Mice	Porcine UBM	Fibrosis & limited ingrowth of muscle fibers
Lower Extremity	N/A	Human	Porcine UBM	Fibrosis & small islands of myofibers
Tibialis Anterior	10×7×3 mm	Rat	Rat Minced Muscle Grafts	Myofiber regeneration throughout defect area
			Rat Muscle Scaffold	Fibrosis throughout defect area

Table 9. Main studies of VML repair with ECM scaffolds in 2014. Adapted from[412].

Abbreviations: mECM, muscle ECM; UBM, urinary bladder matrix; SIS, small intestine submucosa; MSC, mesenchymal stem cell; CT, computed tomography; BAM, bladder acellular matrix; MDCs, muscle-derived cells.

VML necessitates a biomaterial from which skeletal muscle regeneration may be initiated. Advances in muscle ECM knowledge will allow identifying key components, which are essential to preserve or to obtain an optimal biomaterial, in addition to the structure supporting correct alignment of the neomyofibers.

I-E-2) ReGeneraTive Agent® (RGTA®) components

- Synthetic GAG mimetics

GAGs, composed of linear polysaccharide chains containing repeats of disaccharides, participate in many biological processes through interactions with various biomolecules (described in Part I-A-5). GAG mimetics include various polymeric molecules that mimic their capacities to interact with signaling molecules[413]. Some natural mimetics exist such as Chitosan[414] and Fucoidan[415]. However, the use of synthetic molecules is preferred over natural ones as they provide a more homogenous constitution which reduces variability.

The main synthetic components are poly/oligosaccharides (RGTA®), polypeptides, and polymers[416] with functional residues, such as sulfate groups, attached.

The current components of RGTA® are composed of a dextran polymer, harboring uniform sulfated and carboxymethylated groups[417]. Some forms of RGTA® are clinical-grade molecules generated under Good Manufacturing Practices (GMP) with the two main molecules OTR-4120 (Figure 40) and OTR-4131 containing an additional acetyl group[417]. This confers higher affinity to signaling molecules such as FGF-2 and CXCL-12[418] (ref). They also have distinct effects on different cell types while OTR-4131 has more efficient action on proliferation of endothelial[419], and stromal[420], and hematopoietic progenitor cells[421].

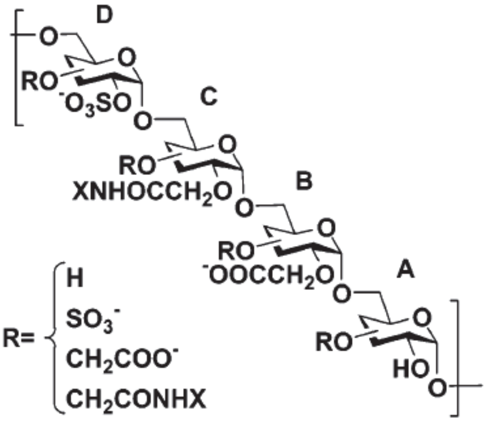

OTR4120 composition : A<1%, B=32%, C=0%, and D=67%

Figure 40. General structure of OTR-4120[417].

- Molecular mechanisms of action of RGTA®

RGTA® act as HS mimetics[422,423], close to heparin but without anticoagulant activity[424] except at high doses. Growth factors known to interact with HS are termed Heparin-Binding Growth Factors (HBGFs) and include molecules such as FGFs, VEGF, CXCL-12 (SDF-1) or TGFβ (Table10). Therefore, RGTA® stabilize and protect some of these factors from enzymatic degradation[423].

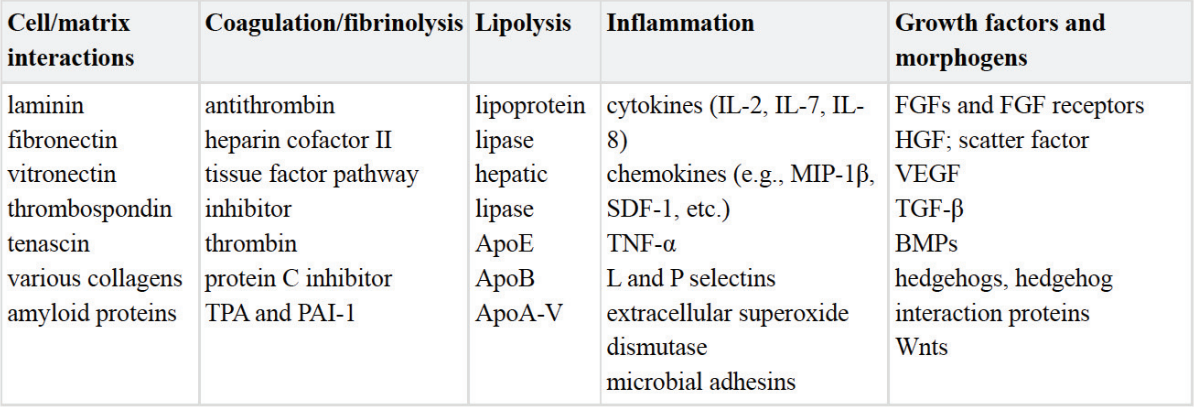

Cell/matrix interactions	Coagulation/fibrinolysis	Lipolysis	Inflammation	Growth factors and morphogens
laminin fibronectin vitronectin thrombospondin tenascin various collagens amyloid proteins	antithrombin heparin cofactor II tissue factor pathway inhibitor thrombin protein C inhibitor TPA and PAI-1	lipoprotein lipase hepatic lipase ApoE ApoB ApoA-V	cytokines (IL-2, IL-7, IL-8) chemokines (e.g., MIP-1β, SDF-1, etc.) TNF-α L and P selectins extracellular superoxide dismutase microbial adhesins	FGFs and FGF receptors HGF; scatter factor VEGF TGF-β BMPs hedgehogs, hedgehog interaction proteins Wnts

Table 10. Main proteins binding to sulfated GAGs[425].

RGTA® possess mechanical properties and are resistant to glycanase, while they inhibit other enzymes degrading matrix components such as neutrophil elastase[426], plasmin[427] or heparanase[428]. RGTA® are well tolerated, they can be administrated by both local and systemic injections.

- RGTA® in tissue repair

RGTA® has shown promising repair properties with few side effects[424] in various models of tissue repair such as: skin[395,429,430], bone[431–433], tendon[434], and periodontitis[435,436]. In addition, RGTA® is currently being evaluated for clinical applications for wound healing[437] and corneal repair[438–440] via local administration. RGTA® action is dose-dependent in a bell-shaped curve manner. It is hypothesized that an excess of RGTA® outcompetes growth factor receptor for growth factors binding. The complex is then eliminated into the bloodstream[435,441,422] explaining the decrease in potency of higher dosages. RGTA® likely interacts with VEGF, as the improvement of angiogenesis is a recurrent effect seen in diverse models of tissue repair[430,432].

- RGTA® in skeletal muscle repair

In skeletal muscle repair, RGTA® have thus far only been explored in the acute phase of several preclinical models, making the distinction between inflammatory factors adsorption and regeneration-enhancing properties somewhat difficult.

In studies utilizing crush[442–446] and ischemic lesions[255,447] of rat hind limbs, RGTA® were always injected immediately after injury. In these studies, the action of the RGTA® proved to be independent from the way it was administrated (intramuscular versus systemic injection)[446]. After a single RGTA® administration, these different studies observed an acceleration in muscle regeneration. The size and number of new myofibers increased, their maturation was faster[255,444], and there was an improvement in innervation[443]. In addition, RGTA® induced a decrease in fibrosis and protected myofibers against degeneration[447]. Only one study used clinical grade RGTA® in a preclinical model of muscle injury[255] and showed a higher number of nuclei in myofibers. In all models, an improvement in muscle angiogenesis[255,442,447] was also seen, along with a local increase of proangiogenic factors (VEGF) in their tissue samples[255].

RGTA® also acts as an enzymatic inhibitor, with an observed decrease in calpain activity during muscle regeneration that was confirmed in myogenic progenitors cell cultures[445,448]. In vitro studies that used myogenic cell lines or rat primary cells showed that the effects of RGTA® were also dose-dependent with efficient concentrations promoting both cell growth and fusion[257,448,449]. Its effect on myogenic proliferation was mainly driven through potentiating FGF-2[449], while its biological action on fusion was associated to calcium mobilization and calpain activity[448].

While encouraging, these results need furthers investigations to elucidate the treatment window and mechanism of action of RGTA® on the various cell types that are involved in muscle regeneration.

Aim of the study

Skeletal muscle has a high capacity for regeneration. However large muscle wasting, as in VML, can overtake this ability, leading to fibrosis and chronic inflammation. This pathologic process has recently received particular attention due to recent military conflicts where a high rate of extremities lesions occurred, leading to invalidity in this young population.

Complementary to physical rehabilitation, a regenerative medicine approach focuses on reaching a better recovery. The most promising strategy is the use of biomaterial to attract local progenitors while providing physical and trophic cues to reactivate a process of muscle repair in a fibrotic environment. Intensive researches are focused on synthetic biomaterials as well as on natural ECM-based decellularized scaffolds obtained from various tissue sources. The use of skeletal muscle-derived ECM is an interesting approach since it contains specific trophic molecules of the target tissue and exhibits its three-dimensional architecture, if can be maintained.

To provide an optimal muscle ECM-based biomaterial, the present thesis work has investigated two complementary directions. Indeed, decellularization might remove some trophic molecules necessary for a proper muscle regeneration, in addition to mechanical properties and preservation of a guiding shape. Therefore, we have investigated the role of key ECM components such as glycosaminoglycans (often lost during the decellularization process) in muscle regeneration.

The current work has 2 experimental parts:

- PART I investigates the obtention of a biomaterial composed of skeletal muscle ECM. We compared several decellularization techniques, by analyzing the efficiency of removal of cellular components and the maintenance of their three-dimensional architecture.

- PART II investigates the effects of RGTA® on muscle regeneration in a myotoxin-injured rodent model, completed with *in vitro* analysis on primary myogenic cells.

Results

Part I- Decellularized muscle ECM for a future therapeutic use in VML model

The direct in vivo grafting of xenogeneic or allogeneic muscle tissue is mainly hampered by the local reaction triggered by both antigenic signals and the presence of DAMPs such as DNA. The decellularization protocols described in the literature consist in chemical, physical and enzymatic associations, aiming at lysing cells and removing or denaturating the components that trigger the immune response.

We conducted a series of experiments comparing and improving established protocols of decellularization. Our outcomes included both the preservation of muscle specific tridimensional architecture and trophic ECM components as well as a decrease in putative deleterious cell-derived signals.

MATERIALS AND METHODS

- Skeletal muscle samples

Female Wistar rats were housed 2 per cage, in a room with regulated temperature and light-dark cycle (22°C and 12h light: 12 h dark). They were maintained on a standard diet with water and food ad libitum, with environmental enrichment in compliance with French and European recommendations. Investigators were certified for experimental surgery and the local ethical committee have validated the protocol. They were euthanized with sodium pentobarbital overdose (150 $mg.kg^{-1}$) by intraperitoneal injection and Plantaris and TA muscles were gathered. Muscles were either directly snap-frozen in liquid nitrogen for control condition or were decellularized in accordance with the selected protocol.

- Decellularization processes

Skeletal muscle contains a high cellular density with a specific ECM three-dimensional organization. Define an adequate protocol to obtain a biomaterial useful in VML will require simultaneously the elimination of cell residues and the preservation of ECM (structure and key components). Therefore, we have explored four different decellularization strategies, based on preexisting protocols used in skeletal muscle tissue[343,401,402,411]. However one method without enzymatic and detergent step[411] was rapidly inappropriate to thick tissues (data not shown). Then, we focused on three main methods (corresponding to the first decellularization analysis) followed by the improvement of the most promising one (corresponding to the second and third decellularization analyses).

- First decellularization with three different methods

For this first evaluation, Plantaris and TA muscles were used owing to their difference in size, weight and pennation[450,451].

- SDS protocol[402]

This protocol evaluated a powerful ionic detergent, SDS (#L3771, Sigma-Aldrich), to solubilize cell and nuclear membranes in addition to denature proteins. However, SDS was described as being responsible for disrupting the ultrastructure or removing GAGs and growth factors. Briefly, this single-step protocol was rapid and extremely easy, involving only SDS detergent[402]. After being harvested, muscles were immersed in a 1% SDS solution under constant agitation during 24-48 h until cellular elements were removed and muscles became transparent. ECM scaffolds were then rinsed 3 times in PBS for a total time of 30 min.

- Trypsin-Triton protocol[343]

For this protocol, we chose a non-ionic detergent, Triton X-100 (#T9284, Sigma-Aldrich), to remove cells by disrupting lipid–lipid and lipid–protein interactions, while leaving protein-protein links intact. However, Triton could lead to a mild disruption of ultrastructure and removal of GAGs (to a lower extent than SDS). Consequently, we combined it with trypsin to reduce overall duration and limit GAG removal. This protocol included multiple steps[343,452] with freezing and osmotic shock for cell lysis, enzymatic digestion and detergent for cell removal. Muscles were directly frozen at -20°C for one day then immersed in ultrapure water during 72h at 4°C. Next, an enzymatic digestion was performed by trypsin 0.15% (m/v) in DMEM at 37°C during 1h, the enzyme was then neutralized with 10% (v/v) fetal bovine serum (FBS) in DMEM overnight at 4°C. Thereafter, muscles were soaked in 3% (v/v) Triton X-100 solution (diluted in PBS) at 4°C under constant agitation until muscles became clear (2 changes per week). Finally, ECM scaffolds were rinsed in ultrapure water during 3 days with daily changing.

- Chloroform-SDS protocol[401]

This 3-step protocol[401] used osmotic shock for cell lysis, chloroform to remove lipids and SDS detergent for cell removal. After being harvested, muscles were dipped in ultrapure water during 24h at 4°C. Thereafter, muscles were soaked in a chloroform solution under constant agitation during 4 or 5 days followed by rinse with ultrapure water. Muscles were then immersed in SDS 2% (v/v) (diluted in PBS) solution under constant agitation until muscles became translucent with the solution being changed twice a week. Finally, the ECM scaffolds obtained were rinsed in ultrapure water during 5 days with daily changing.

- Second decellularization with variable digestion time and detergent

We have used only TA muscles in order to focus on a future utilization in VML injury model.

- Trypsin-SDS protocol and Trypsin-Triton/NH3 protocol

Fascia and tendons were discarded to facilitate the decellularization process. Muscles were frozen at -80°C for at least 1 day. A maximum of three muscles were pooled together in tubes and soaked in ultra-pure water (25 mL for 1 g muscle) for 3 days, under constant agitation at 4°C. Water was changed daily. Samples were next immersed in 10 mL of 0.15% trypsin EDTA (diluted in PBS, #11560626, Gibco) at 37°C in a shaking bath (EDTA, by chelating divalent cations, is hypothesized to improve the disruption of cell-ECM adhesion).

Depending on the protocol, trypsin digestion was performed during 30 min, 45 min or 60 min. Trypsin was then neutralized with 10% (v/v) FBS-DMEM overnight, shaking at 4°C.

Thereafter, muscles were soaked in detergent (25 mL for 1 g muscle):

- For the trypsin-SDS protocol in SDS 1% (diluted in cold ultra-pure water)
- For the trypsin-Triton/NH3 protocol in Triton X-100 0.3% with ammoniac (NH3) 2% (diluted in cold ultra-pure water). Ammoniac was combined with Triton X-100 to decrease its concentration. Indeed, base agents catalyze hydrolytic degradation and cleave collagen fibrils with crosslink disruption but may eliminate growth factors[453].

The samples were placed at 4°C with constant agitation for 4 to 5 days and the solution was changed daily. Muscles were subsequently rinsed with ultra-pure water (25 mL for 1 g muscle) for 2 days (changed once a day), under constant agitation at 4°C. Thereafter, samples were immersed in PBS for 1 day and stored at -20°C.

Third decellularization to determine detergent

Fascia and tendons of TA muscles were discarded and muscles were frozen at -80°C for at least 1 day. A maximum of three muscles were pooled together in tubes and soaked in cold ultra-pure water (25 mL for 1 g muscle, changed once a day) for 3 days, under constant agitation at 4°C. Next, samples were immersed in 10 mL of 0.15% trypsin EDTA (diluted in PBS) at 37°C in a shaking bath during 45 min. Trypsin was then neutralized with 10% FBS-DMEM overnight, shaking at 4°C.

Muscles were subsequently soaked in each protocol-specific detergent:

- for Trypsin-SDS-DNAse protocol, in an adequate volume (25 mL for 1 g muscle) of SDS 1% (diluted in cold ultra-pure water). Tubes were shaken at 4°C for 4 or 5 days and solution changed once a day. Then, samples were incubated with DNase I (1 kU.mL^{-1}; #04716728001, Roche) at 37°C for 2 h.

- for Trypsin-Chloroform-Triton/NH3 protocol, in chloroform solution during 5 days followed by an immersion in an adequate volume (25 mL for 1 g muscle) of 0.3% Triton X-100-2% NH3 (diluted in cold ultra-pure water), under agitation at 4°C for 4 or 5 days (solution changed daily).

Thereafter, for both protocols, the ECM scaffolds obtained were rinsed under agitation at 4°C, with ultra-pure water for 2 days followed by PBS for 1 day and then, stored at -20°C.

- Histological analysis

  - Histological staining

ECM scaffolds were embedded in cryomatrix, frozen in liquid nitrogen and kept at -20°C until analysis (Figure 41).

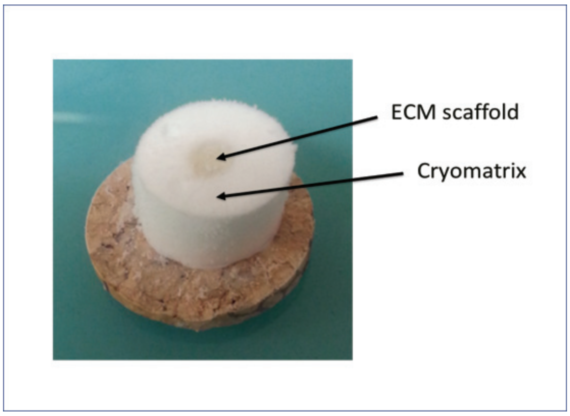

Figure 41. ECM scaffold preparation for histological analyses.

Cryosections (8μm) of muscle ECM scaffolds and muscles were performed transversally, at -19°C. The following histochemical stainings were performed:

- **Hemalun-Phloxine-Saffron (HPS):** briefly, the different steps were fixation by alcohol with ether, Mayer's Hematoxylin staining, washed in distilled water, Phloxine staining, dehydration with alcohol (70%, 95% and 100%), Saffron staining, washed in alcohol, clearing with Histosol and slides were mounted with Eukitt®. HPS allowed the vizualisation of saffron-stained ECM structures as well as any remaining muscle cells, nuclei and cytoplasm adsorbing Hemalun and Erythrosin, respectively.

- **Masson's trichrome staining:** slides were stained with Mayer's Hematoxylin, washed in distilled water, then dyed with Ponceau Fuchsin solution. To improve collagen staining, samples were differentiated in Phosphomolybdic acid solution, counterstained with Light Green and rinsed twice with acetic acid solution. Next, slides were dehydrated very quickly in Alcohol (70%, 95% and 100%), then cleared in Histosol and slides mounted in Eukitt. This staining was performed to more precisely visualize collagenous fibers in tissue sections.

- **Alcian Blue staining:** briefly, slides were soaked in Mayer's Hematoxylin, rinsed with distilled water, then immersed in Lithium carbonate and washed with distilled water. Then, they were stained with a solution of Alcian Blue (1%) and Acetic acid (1%). Next, samples were differentiated in Phosphomolybdic acid solution and counterstained with Nuclear fast red (0.02%). Slides were dehydrated in Alcohol (70%, 95% and 100%) followed by a clearing in Histosol and mounted in Eukitt. This staining aims at visualizing GAGs within samples. For some slides, Alcian Blue staining was performed after a treatment by nitrous acid to remove heparan sulfates.

All slides were entirely scanned by an AxioScan Z1 (Zeiss, Oberkochen, Germany). Endomysium size was determined using ImageJ software with a minimum of 200 measurements per scaffold.

○ Immunofluorescence analysis

Cryosections were permeabilized in 0.5% (v/v) Triton X-100 and non-specific staining blocked with 2% bovine serum albumin (w/v) (A-3059, Sigma-Aldrich) in PBS for 1 hour. Slides were then labeled with antibodies directed against Laminins (#11575, Abcam), Dystrophin (#ab3149, Abcam), Collagen I (#AB755P, Millipore) or Collagen III (#7778, Abcam) and revealed with FITC-conjugated secondary antibody (#711-095-152, Jackson). Nuclei were labeled with Hoechst 33342 ((#FP41387A, Interchim) before mounting slides in Fluoromount (#FP483331, Interchim). For each sample, randomly chosen fields among the whole cryosection were recorded with a Leica GmbH DMI6000 microscope (Leica Microsystems, Germany) at 10X of magnification.

- Quantitation of remaining DNA in ECM scaffold and non-decellularized muscle

○ DNA extraction

Total DNA was extracted with DNA DNeasy Blood and Tissue Kit (#69504, Qiagen) according to manufacturer's protocol. Briefly, 25 mg of samples are cut into small pieces and digested with proteinase K at 56°C under agitation during 1-3 h. All lysates were dropped onto the DNeasy Mini spin column and rinsed according to the protocol. Then, DNA was eluted in 50 µL water. In last dosage, muscle scaffolds were lyophilized before DNA extraction, to quantify remaining DNA under the same conditions as those establishing standards threshold in decellularized biomaterial[389].

○ DNA quantification

- By spectrophotometer (Nanodrop): DNA concentration was initially measured with a micro-volume spectrophotometer (absorbance at 260nm) but the accuracy of the DNA quantification was not appropriate for small amount of DNA obtained in ECM scaffold.

- By fluorometry (Qubit 2.0 Fluorometer, Invitrogen): DNA concentration was quantified using the Qubit double-stranded (ds) DNA Broad-Range assay (Invitrogen). The dosage technic is highly selective for dsDNA and the measure is accurate for low concentrations (from 100 pg/µL to 1 mg/µL). Samples and DNA standards were diluted in buffer and 1-10 µL were deposited onto the Qubit®, which automatically provided the final DNA concentration.

Electrophoresis to visualize large DNA fragments

Agarose gel electrophoresis is the most effective way of separating DNA fragments of various sizes. Gels were prepared with TBE 1X buffer for a final concentration of 1% agarose. DNA samples were stained with Syber Safe and blue loading dye, with a 1:10 (1 Syber: 10 loading) dilution. DNA ladder of 1000 base pair were included for dsDNA quantification. Agarose gels were then run at 100 volts during 2h and visualized using an UV camera.

Electrophoresis of Myosin Heavy Chains

Myosin heavy chains (MHC) represent the majority (80%) of skeletal muscle proteins. MHC content was investigated by a specific SDS-PAGE electrophoresis[454]. Briefly, frozen muscles were minced with scissors in a buffer solution (0.3 M NaCl, 0.1 M NaH2PO4, 0.05 M Na2HPO4, 0.01 M Na4P2O7, 1 mM MgCl2-6H2O, 10 mM EDTA, and 1.4 mM 2β-mercaptoethanol, pH = 6.5). After incubation for 24h at 4 °C, samples were entirely digested and the supernatant mixture was then diluted ½ in glycerol. Extracts were stored at −20 °C until use or were diluted to $1/10^{e}$ (extracts from whole muscles were diluted to $1/1000^{e}$). Electrophoresis was performed using a Mini Protean II system (BioRad, Marne-la-Coquette, France) with 8% and 4% acrylamide-bis (50:1) separating and stacking gels, respectively, containing 0.4% sodium dodecyl sulfate (SDS). Samples were denatured with the SDS incubation medium according to the method of Laemmli. Gels were run at constant voltage (72 V) at +4°C for 31 h and then silver stained. The MHC protein isoform bands were scanned and quantified using a densitometer GS 800 driven by Quantify One 4.6.1 (BioRad).

Quantification of GAGs

GAGs were measured with the Blyscan™ assay (Biocolor), a quantitative dye-binding method for sulfated GAGs, according to the manufacturer’s instructions. Briefly, 25 mg of sample were digested by proteinase K at 50°C during 24h under agitation. Sulfated GAGs were precipitated by adding 1,9-dimethylene blue, then sediments were resolved by using a provided dissociation buffer and their absorbance was measured at 620 nm using a plate reader.

Proteomic analysis

Whole muscle ECM scaffold

The protein extraction protocol relies on a publication by Li about proteomic analysis of decellularized tissues[83]. Briefly, muscle ECM scaffolds were immersed in SDT solution (4 % SDS, 0.1 M Tris-HCl at pH 7.6 and 0.1 M dithiothreitol) and manually ground with a Potter on ice. Samples were then heated at 95 °C for 7 min and sonicated on ice for 3x10 min, followed by an ultracentrifugation (150,000 g).

Proteins from the supernatant were precipitated overnight (−20 °C) in cold acetone/methanol (8:1). After centrifugation (10,000 g for 30 min), proteins were solubilized with Laemmli solution (BioRad) and separated by a short SDS-PAGE to remove contaminants (acrylamide/bis-acrylamide 8%, 120V, 5 min, preformed wells in agarose 2%, no stacking gel). After Coomassie colloidal staining, the unique band of the total protein sample was in-gel digested by trypsin before identification in nanoscale liquid chromatography coupled to tandem mass spectrometry (nanoLC-MS/MS).

○ Ground ECM scaffold

Muscle ECM scaffolds were difficult to solubilize, therefore we included additional steps where ECM was ground and denatured[452], to improve its identification. Briefly, after freezing, muscles were finely sliced before undergoing the formerly described Trypsin-Triton/NH3 protocol. Next, ECM scaffolds were lyophilized before cryogrinding followed by a urea-denaturation step. Finally, urea was removed by dialysis and samples were lyophilized a second time before storage at -20°C. For this second proteomic analysis, we used the protocol recommended by the Matrisome project [80,455] where extraction was performed in Laemmli buffer 3X (with 100mM of dithiothreitol) and before trypsin digestion, samples were precipitated with Acetone/methanol solution.

- Statistical analyses

Results are expressed as means ± SEM. Statistical analyses were undertaken with Prism software (version 6.0h for Mac). Data were explored with a parametric two-way ANOVA and post-hoc test (Tukey's multiple comparison test) were performed except in cases of two protocol groups where the Mann-Whitney test was used. R (3.4.1) and Rstudio (1.0.153) software’s were used for a three-way permutation ANOVA followed by one-way permutation ANOVA. An α-error of 0.05 per sub-figure was used to set a threshold of significance.

RESULTS

- R-I-1) Comparison of three different decellularization methods

We first compared 3 methods differing widely in duration and mechanisms (Figure 42).

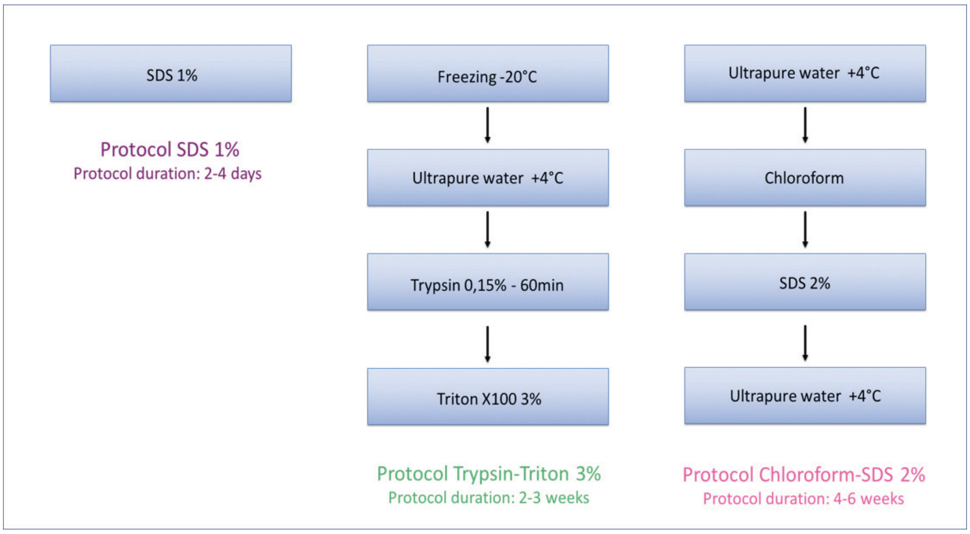

Figure 42. Evaluation of three different decellularization methods.

One protocol involved only the strongly ionic detergent SDS. A second protocol involved cell lysis through freezing and osmotic lysis, protein degradation by trypsin and solubilization of remnants in the non-ionic surfactant Triton X-100. A last one, involved osmotic lysis, lipid solubilization in chloroform followed with ionic detergent by SDS. TA and Plantaris muscles were used.

○ Macroscopic aspect of ECM scaffolds (Figure 43)

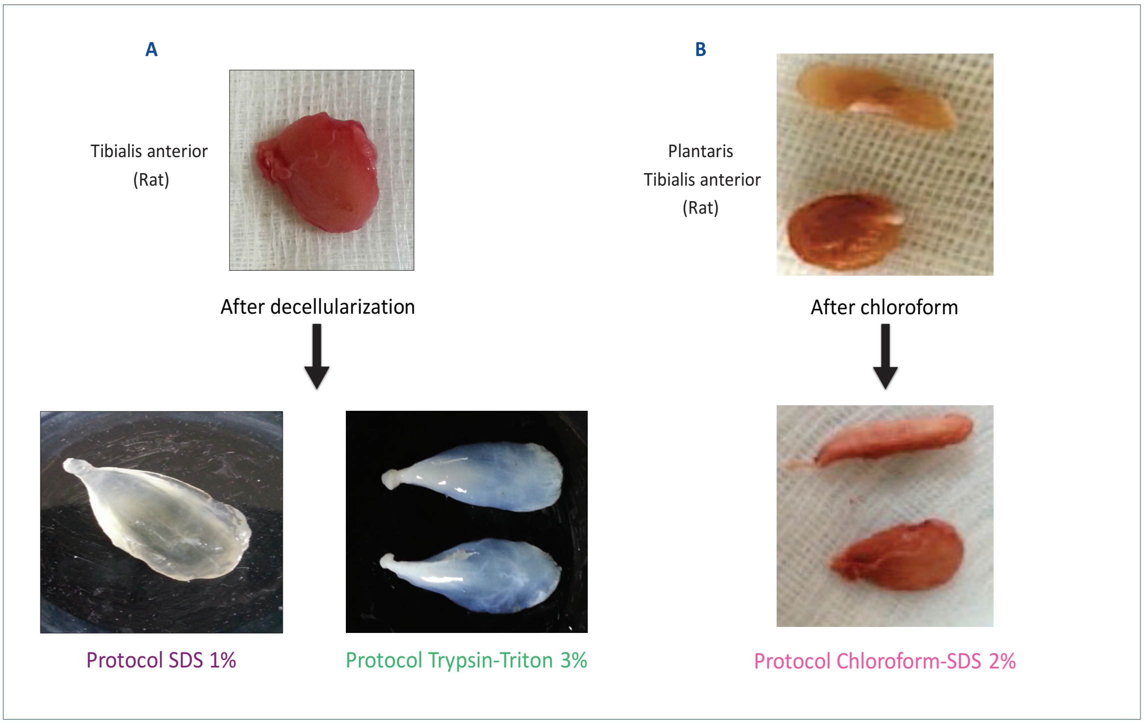

Figure 43. Macroscopic aspect of ECM scaffolds. Illustrations of A) transparent ECM scaffolds after complete decellularization (protocols SDS and Trypsin-Triton) and B) modification of muscle rigidity after chloroform bath (protocol Chlorofrom-SDS).

In the SDS protocol, the ECM scaffolds became transparent but appeared dilated as compared with non-decellularized muscles. In the Trypsin-Triton protocol, the ECM scaffolds were softer without size modification. In the chloroform-SDS protocol, after chloroform soaking, the ECM scaffolds were less soft and became rigid.

- Altered three-dimensional architecture in all protocols

Hematoxylin-Phloxine-saffron (HPS) staining allows the description of two major cell structures, the cytoplasm and nucleus, by their adsorption of eosin, and hemalun respectively. For each protocol, we observed a cell loss in ECM scaffolds as compared with whole muscles (Figure 44A). ECM proteins were colored in light pink and saffron. In SDS protocol, the perimysium appeared intact while the endomysium was lost (Figure 39B). Nevertheless, it was conserved in Trypsin-Triton protocol despite being structurally deteriorated (Figure 44C), probably due to endomysium fragility during cryosections. Conversely, Chloroform-SDS protocol maintained endomysium but at the cost of a thickening (Figure 44D).

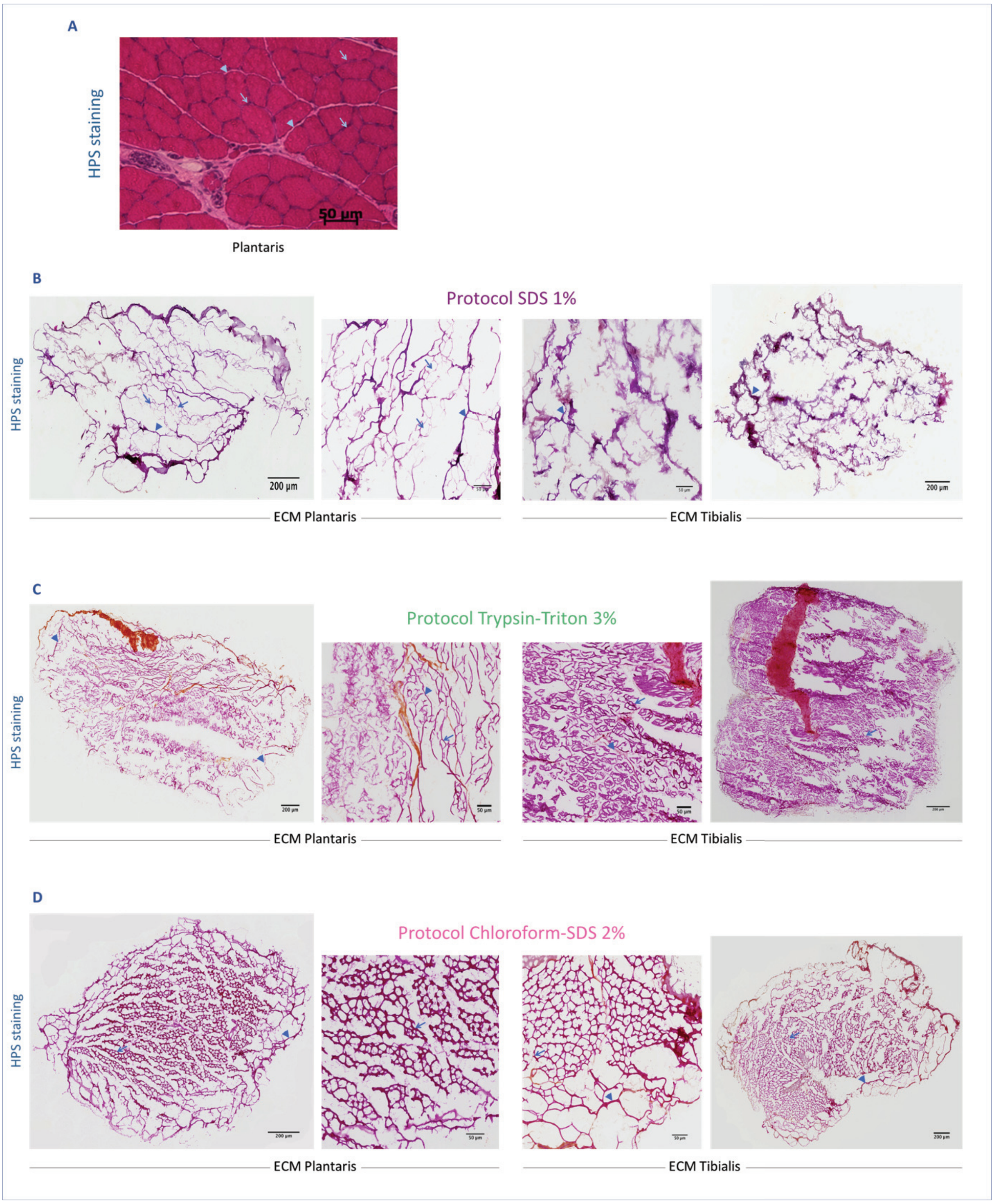

Figure 44. Hematoxylin-Phloxine-saffron (HPS) staining. A) Plantaris muscles were compared with ECM scaffolds obtained from TA and Plantaris muscles by B) SDS protocol, C) Trypsin-Triton protocol and D) Chloroform-SDS protocol. Arrowheads show perimysium and arrows indicate endomysium. Scale bars represent 200 µm in whole scaffold and 50 µm in zoom area.

Masson's trichrome staining allows to visualize collagens in light green and muscle cells in red as it can be seen in the Plantaris used as a control (Figure 45A).

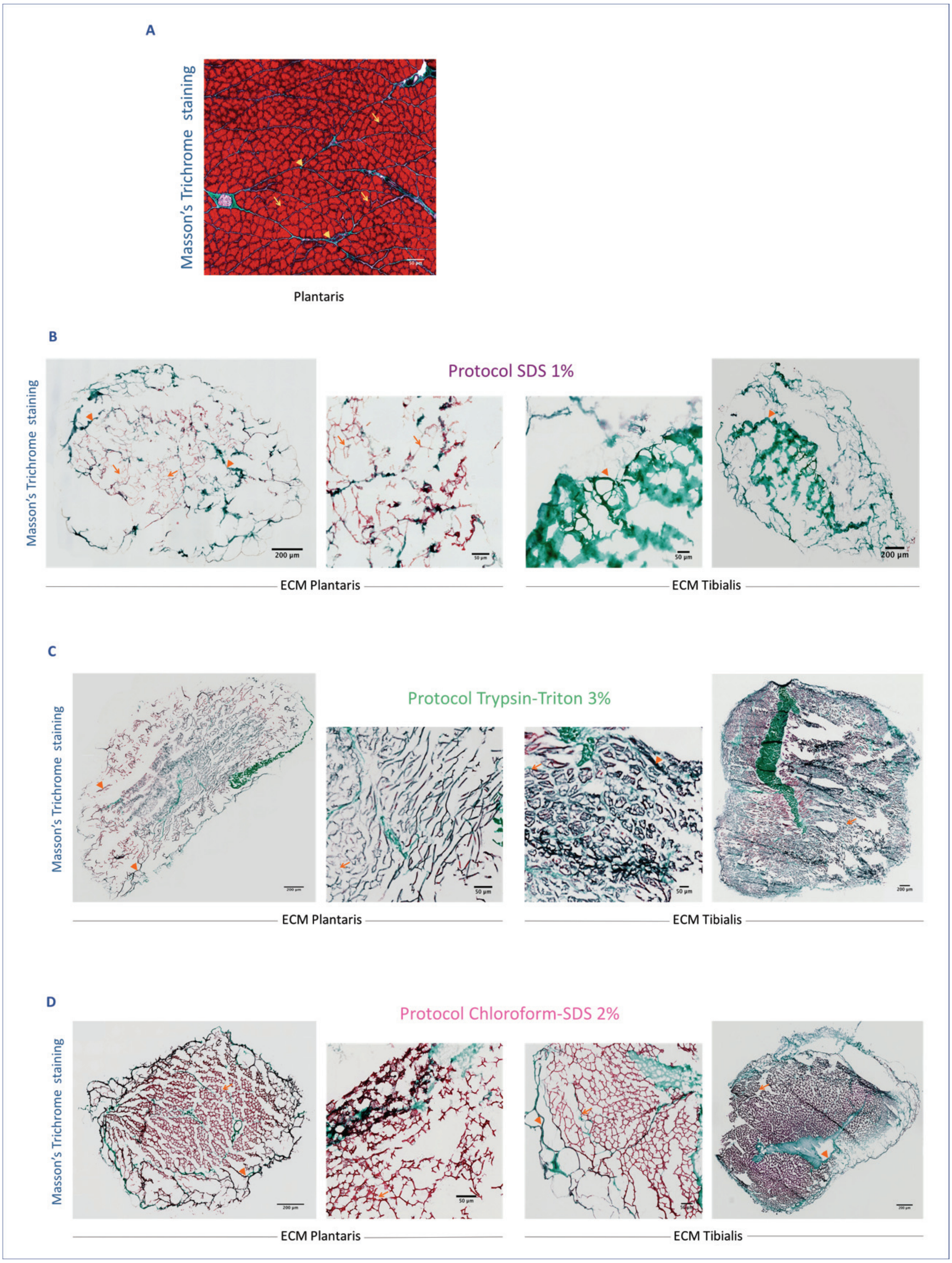

Figure 45. ECM structure in Masson Trichrome staining. A) Plantaris muscles were compared with ECM scaffolds obtained from TA and Plantaris muscles by B) SDS protocol, C) Trypsin-Triton protocol and D) Chloroform-SDS protocol. Arrowheads show perimysium and arrows indicate endomysium. Scale bar represent 200 µm in whole scaffold and 50 µm in zoom area.

ECM scaffolds were stained in light green as expected, despite a proportion staining in red-brown. We confirmed the results obtained with HPS staining, with a complete cell removal. Endomysium was lost in SDS protocol (Figure 45B) whereas it was maintained in the two other protocols but smashed by cryosections in Trypsin-Triton protocol (Figure 45C) and thickened in Chloroform-SDS protocol (Figure 45D). Indeed, Cross-Sectional Area (CSA) of virtual endomysium displayed a major decrease, particularly in Plantaris ECM (99,67μm^2) as compared to whole muscle (892 μm^2).

Laminins are the main molecules of basal membrane (Figure 46A). We used a pan-laminin polyclonal antibody to investigate its preservation after decellularization as well as the specific three-dimensional architecture of basal membrane. Laminins were present in ECM scaffolds of each protocol and basal membrane architecture were identical to native endomysium, showing a disorganization in the SDS protocol (Figure 46B), apparently fragile and altered in Trypsin-Triton protocol (Figure 46C) and thickened in Chloroform-SDS protocol (Figure 46D).

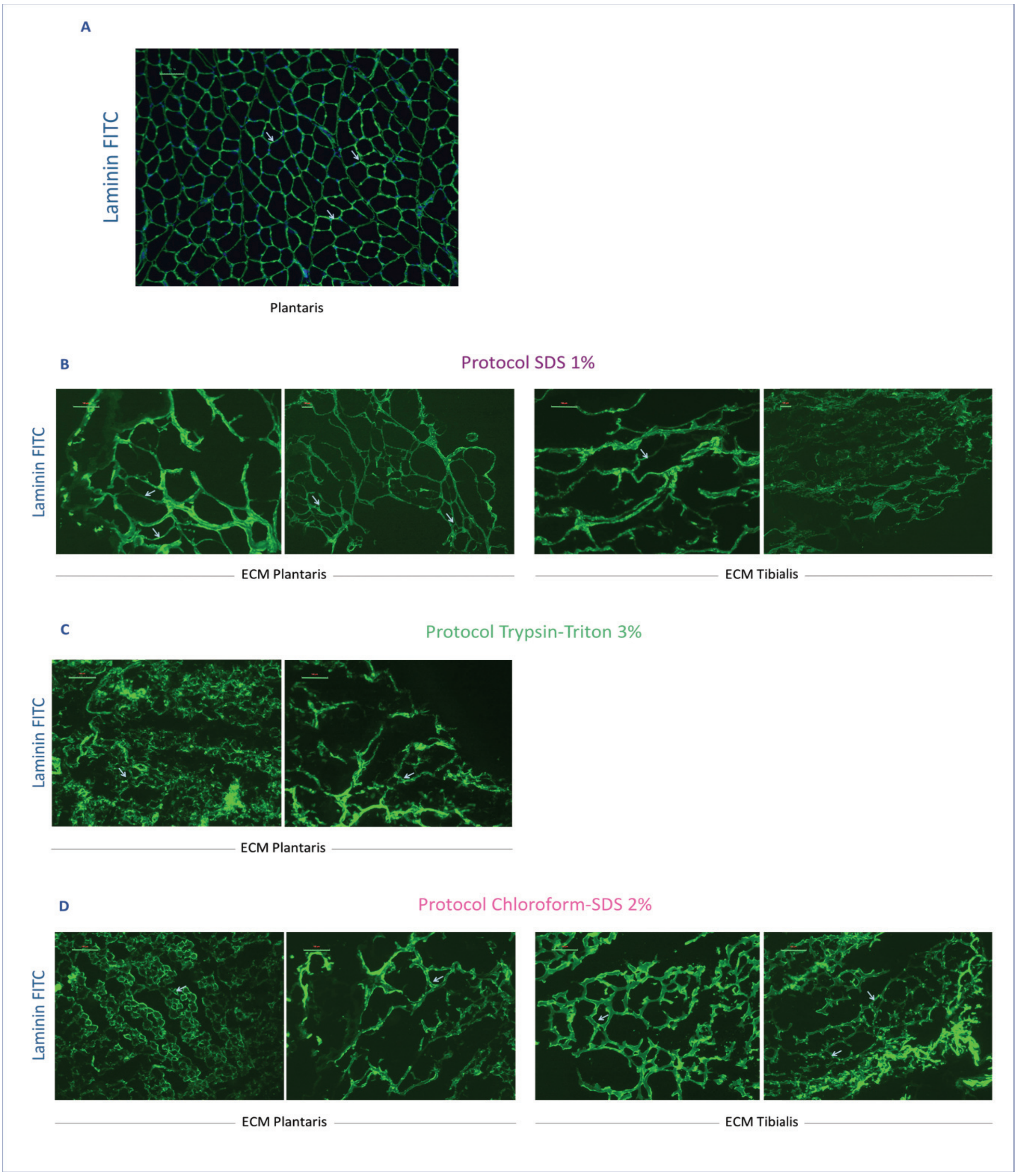

Figure 46. Laminin immunostaining to visualize basement membrane. Laminin signal and basement membrane structure of A) Plantaris muscles were compared with ECM scaffolds (from TA and Plantaris) obtained by B) SDS protocol, C) Trypsin-Triton protocol and D) Chloroform-SDS protocol. Arrows indicate basement membrane with a maintained 3D structure. Scale bars represent 100 μm.

- Efficient decellularization except for SDS

DNA content

Residual DNA content was investigated with two complementary techniques. First, we used Hoechst labeling to visualize DNA with a fluorescence microscope. As expected, nuclei were localized at the periphery of myofibers (Figure 47A). In SDS and Trypsin-Triton protocols no signal could be observed (data not shown) whereas in Chloroform-SDS protocol spots of fluorescence appeared compatible with the presence of DNA nuclei remnants (Figure 47B).

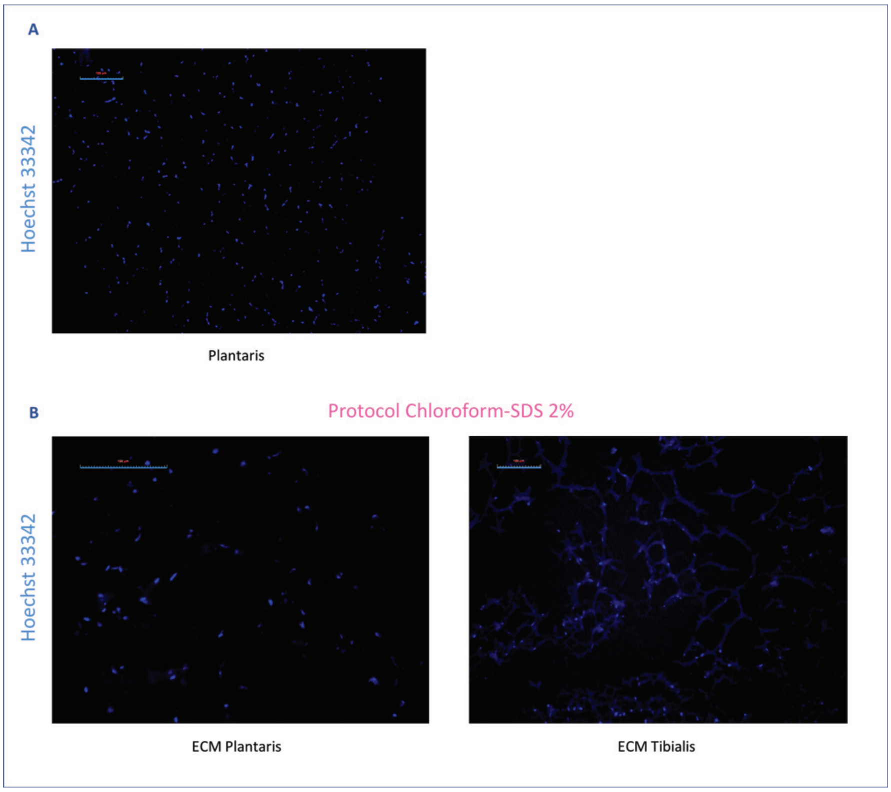

Figure 47. Hoechst labelling to visualize residual nuclei. A) Plantaris muscles were compared with B) ECM scaffolds obtained with Chloroform-SDS protocol (from TA and Plantaris). Scale bars represent 100 μm.

We then performed DNA extraction and quantified the amount of residual DNA by spectrometry at 260 nm (Figure 48).

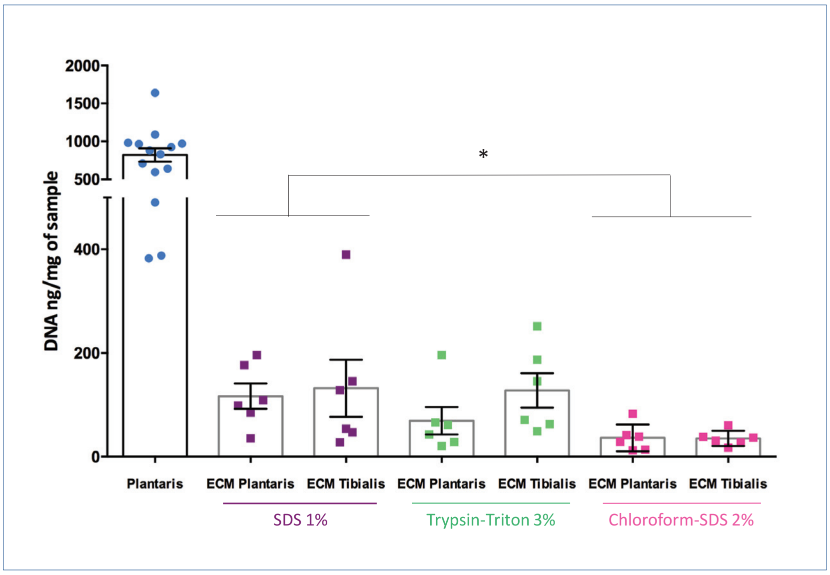

Figure 48. Residual DNA quantified by spectrometry. DNA extraction was performed from ECM scaffolds (n=6) and Plantaris muscle (n=14). Parametric two-way ANOVA with post-hoc test (Tukey's multiple comparisons test) were performed and * represent p<0.05.

In whole muscles (Plantaris), we obtained an average DNA content of 820 ng per mg of muscle. For ECM scaffolds of Plantaris and TA, in SDS protocol the average DNA content was 124 ng per mg of sample. In Trypsin-Triton protocol, the average value was 99 ng of DNA per mg of sample. The smaller amount was found for Chloroform-SDS protocol with an average DNA amount of 36 ng per mg of sample. There was a significant difference between SDS and Chloroform- SDS protocols (p=0.018) but no difference between ECM scaffolds from TA and those from Plantaris (p=0.337). The presence of large DNA fragments in ECM scaffolds was further investigated by electrophoresis in a 1% agarose gel and Plantaris muscles were used as a control (Figure 49).

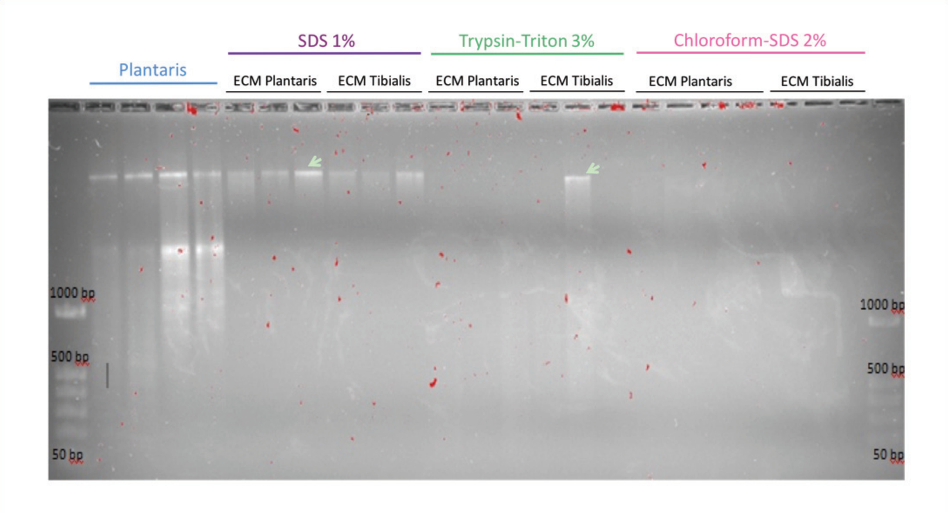

Figure 49. Migration of DNA fragments in electrophoresis. DNA was extracted from Plantaris muscle (n=4) and ECM scaffolds (n=3 per condition) and migration was performed in 1% agarose gel to explore large DNA fragments. Arrows indicate large DNA fragments.

DNA electrophoresis results were in accordance with DNA quantification. In SDS protocol as in whole muscles, we observed large DNA fragments whereas we obtained only faint smears in Chloroform-SDS protocol. In Trypsin-Triton protocol, most samples yielded only trace smears, while one sample showed large DNA fragments.

Cytoplasmic and membrane proteins

To evaluate residual cellular protein content, we performed MHC electrophoresis because MHC represent the majority of cytosolic proteins in skeletal muscle (figure 50).

Figure 50. Analysis of myosin heavy chain (MHC) by specific electrophoresis. For each protocol, extracts of ECM scaffolds (n=2 or 4) and whole muscles (n=1 or 2) have migrated 31 h in electrophoresis (SDS gel) before silver staining. Arrows indicate lighter proteins also present.

For each protocol, we observed no MHC as compared with Plantaris and TA muscles. However, lighter proteins were also present specially in SDS protocol. In addition, we explored by immunofluorescence the presence of dystrophin, a major membrane protein of skeletal muscle for ECM anchoring. For each protocol, no fluorescent signal was obtained (data not shown).

○ GAGs were lost during the Trypsin-Triton protocol

We quantified GAG content in ECM with **Blyscan™ assay**, a quantitative dye-binding method for sulfated GAGs with absorbance measured at 620 nm by a plate reader (Figure 51).

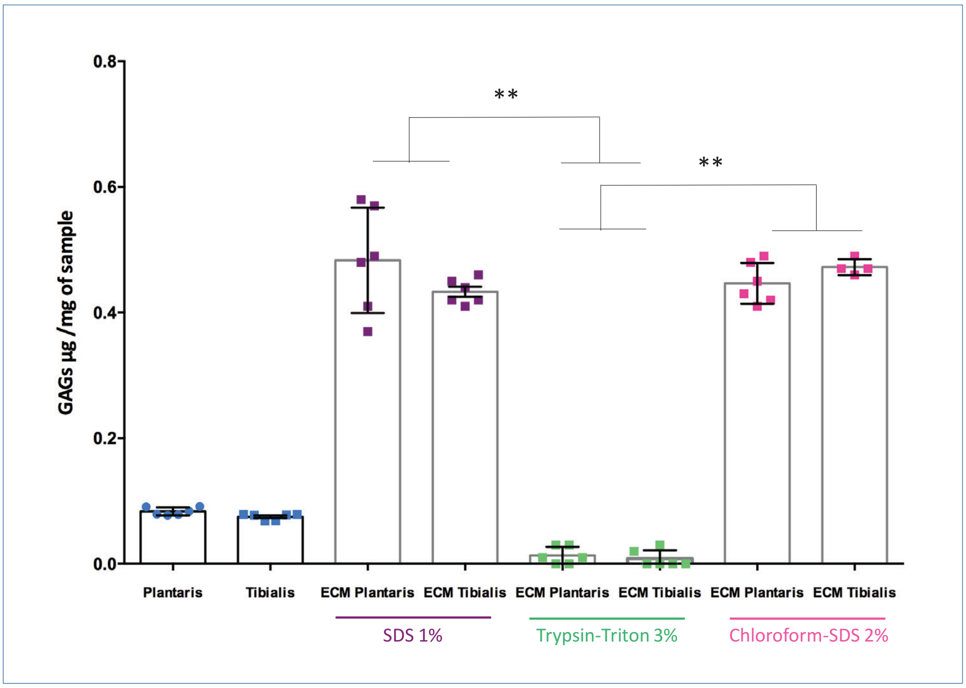

Figure 51. GAG quantification by Blyscan™ assay. For each protocol, extracts of ECM scaffolds (n=6) and whole muscles (n=6) were used to quantify total GAGs content by a dye-binding method with signal measured at 620 nm. Parametric two-way ANOVA with post-hoc test (Tukey's multiple comparisons test) were performed and ** represent p<0,01.

We obtained an average value of 0.08 µg per mg of sample for whole muscles. For SDS and Chloroform-SDS protocols we quantified an average amount of 0.46 µg per mg of sample, higher than in the whole muscle because the concentration of GAGs is relative to the sample weight, much lighter in ECM scaffolds as compared to muscles. However for Trypsin-Triton protocol we found a drastic GAG loss ($p<0.0001$), with an average amount of 0.01µg per mg of sample. There was no significant difference between ECM scaffolds from TA than those from Plantaris.

In addition, we performed a specific **staining with Alcian Blue** to visualize the presence of GAGs on ECM scaffolds. In whole muscle cryosections it was not interpretable because of an alteration of muscle cells by the staining. For ECM scaffolds, the results were in accordance with the Blyscan™ assay, with blue staining in favor of GAGs for SDS (Figure 52A) and Chloroform-SDS protocols (Figure 52C) whereas a major decrease in signal were observed on slides from the Trypsin-Triton protocol (Figure 52B).

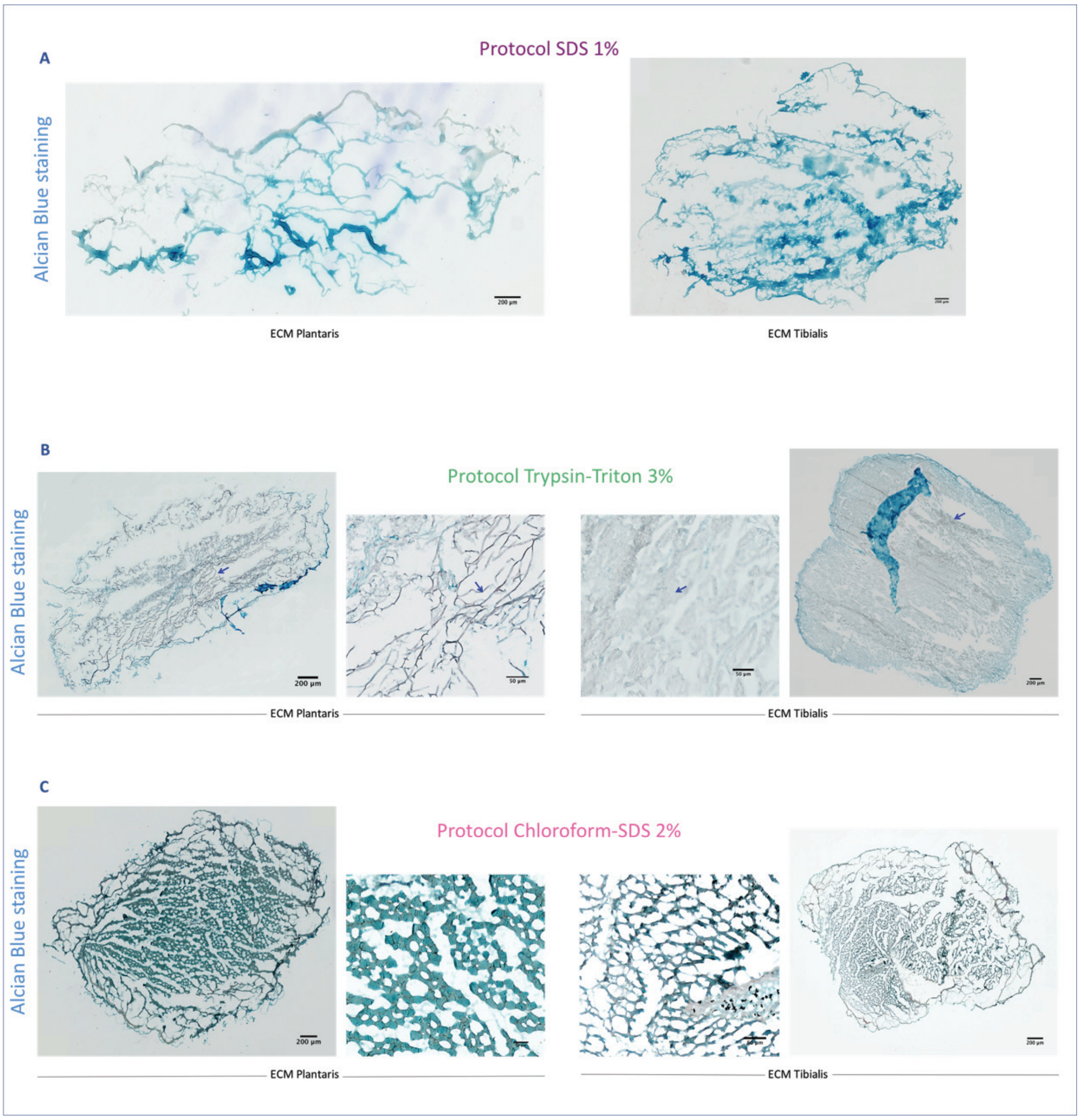

Figure 52. Alcian Blue staining to visualize the presence of GAGs. This staining was performed only on ECM scaffolds (from TA and Plantaris) obtained by A) SDS protocol, B) Trypsin-Triton protocol and C) Chloroform-SDS protocol. Whole muscle cryosections were altered by the pH of the process (data not shown). Arrows indicate area with absence of GAGs staining. Scale bars represent 200 µm in whole scaffold and 50 µm in zoom area.

To sum up, using SDS protocol we obtained an efficient decellularization, a preservation of GAG content but at the cost of an altered three-dimensional architecture, as evidenced by the loss of endomysium.

For Chloroform-SDS protocol, the decellularization was also effective while maintaining GAG content and endomysium. However, the latter was extremely thickened, which could be a difficulty for future neomyofiber formation.

Trypsin-Triton protocol allowed to efficiently decellularize samples while conserving an intact, although fragile, endomysium with a drastic GAG loss.

We chose to focus on maintaining three-dimensional architecture, and therefore decided to improve the Trypsin-Triton protocol.

- R-I-2) Improvement of the Trypsin-Triton protocol by modulating enzymatic timing and detergent choice to enhance GAG content

To minimize the denaturation due to the protocol, we decreased the time of trypsin digestion. Because ECM scaffolds from SDS protocols retained GAGs, we also compared the use of SDS and we combined a basic chemical agent ammoniac (NH3) with Triton X-100 to decrease its concentration ten-time (Figure 53). Bases solubilize cytoplasmic components of cells, disrupt nucleic acids, and tend to denature proteins. On the other hand, there is a need to strike a delicate balance because basic agents can catalyze hydrolytic degradation, leading to the complete elimination of growth factors from the ECM and cleavage of collagen fibrils with disruption of collagen crosslinks.

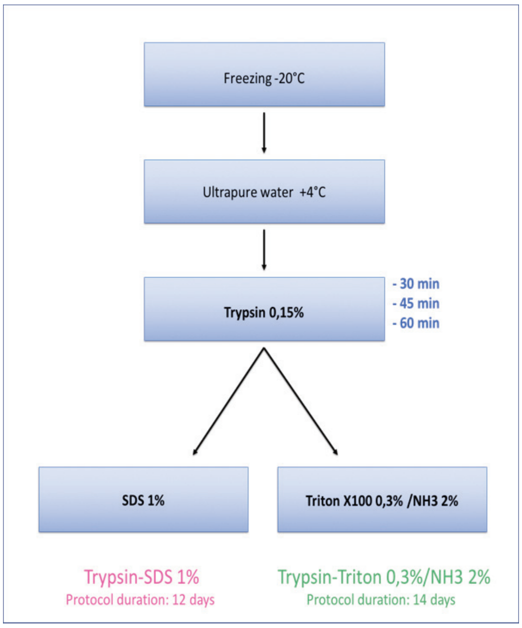

Figure 53. Modifications of the protocol maintaining ECM structure to enhance GAG content. Various digestion times and two detergents were investigated.

○ Preservation of the three-dimensional architecture

For each protocol, **HPS staining** allowed to visualize cell loss (Figures 54-55).

In Trypsin-SDS protocol, we found a thin endomysium (Figure 54A) a better conservation was found in Trypsin-Triton/NH3 protocol without deterioration during cryosections (Figure 55A). The same observations were made with **Masson trichrome staining** on ECM scaffolds from Trypsin-SDS protocol, where light green are observed (Figure 54B). On the contrary, in Trypsin-Triton/NH3 protocol ECM exhibited a mix of brown-green staining (Figure 55B).

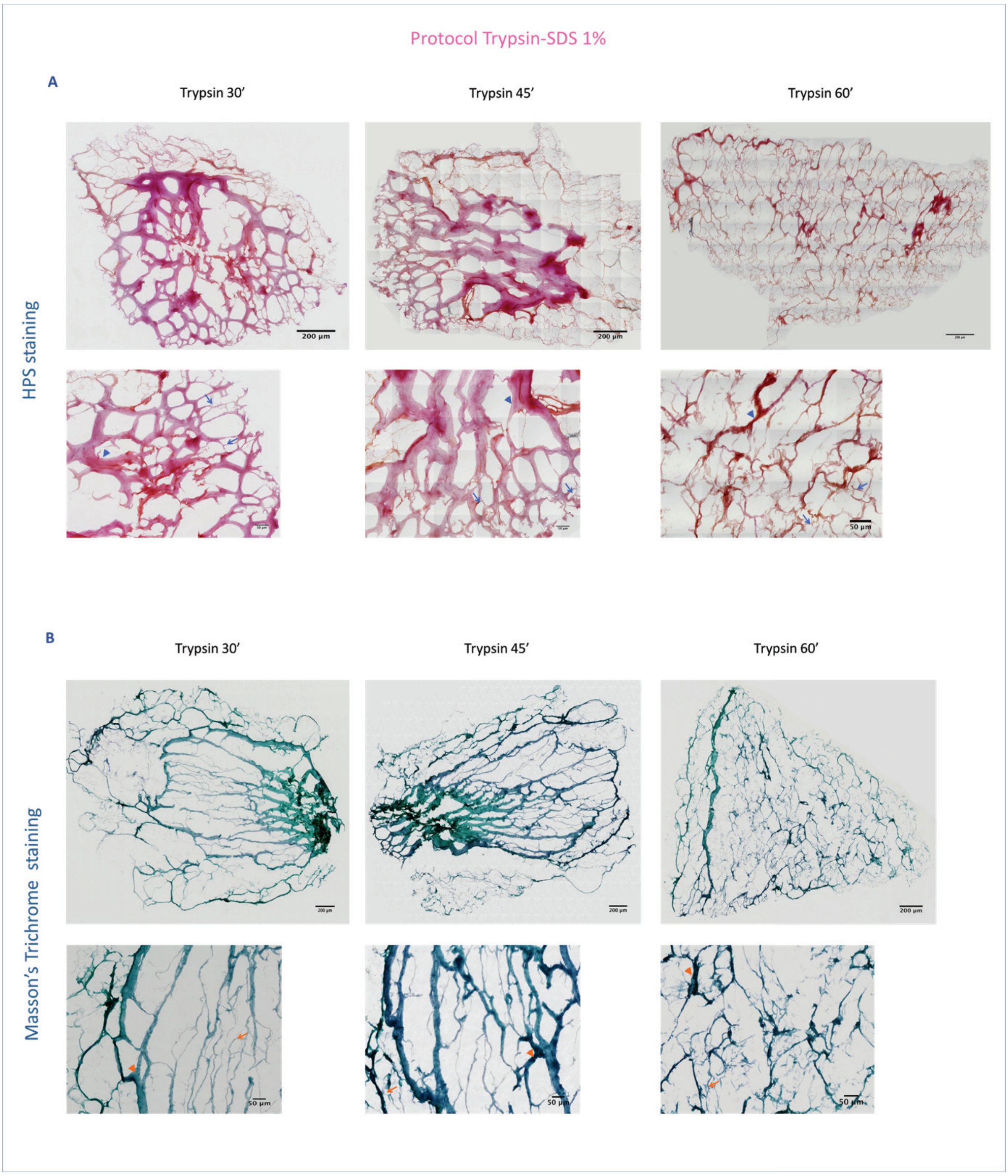

Figure 54. A) Hematoxylin-Phloxine-saffron (HPS) and B) Masson's trichrome staining. ECM scaffolds from TA muscle obtained in Trypsin-SDS protocols with three different times of enzymatic digestion were analyzed. Arrowheads show perimysium and arrows indicate endomysium. Scale bars represent 200 µm in whole scaffold and 50 µm in zoom area.

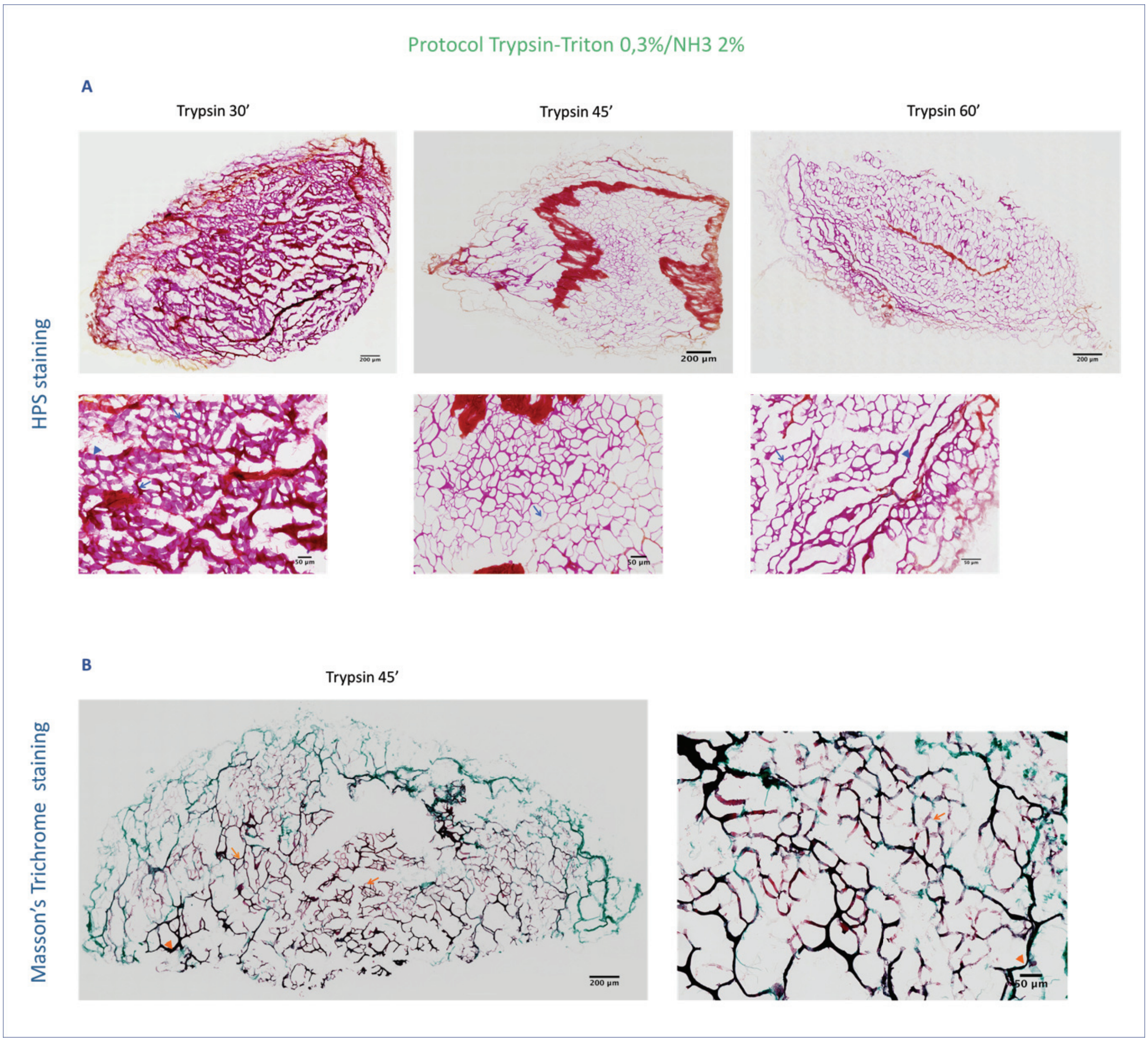

Figure 55. A) Hematoxylin-Phloxine-saffron (HPS) and B) Masson's trichrome staining. HPS were undertaken for all ECM scaffolds from TA muscle by Trypsin-Triton/NH3 protocol. Masson trichrome staining was only performed for ECM scaffolds obtained with 45 min of enzymatic digestion to confirm the endomysium structure. Arrowheads show perimysium and arrows indicate endomysium. Scale bar represent 200 μm in whole scaffold and 50 μm in zoom area.

Basal membranes were visualized by **laminin immuno-staining** (Figures 56-57). Laminin architecture appeared more deteriorated in Trypsin-SDS protocol (Figure 56A) than after the Trypsin-Triton procedure (Figure 56A). **Collagen I and III** architecture was also more structured in ECM scaffold from Trypsin-Triton/NH3 protocol, especially with 45 min of digestion (Figures 57B-C) when compared with Trypsin-SDS protocol (Figures 56B-C).

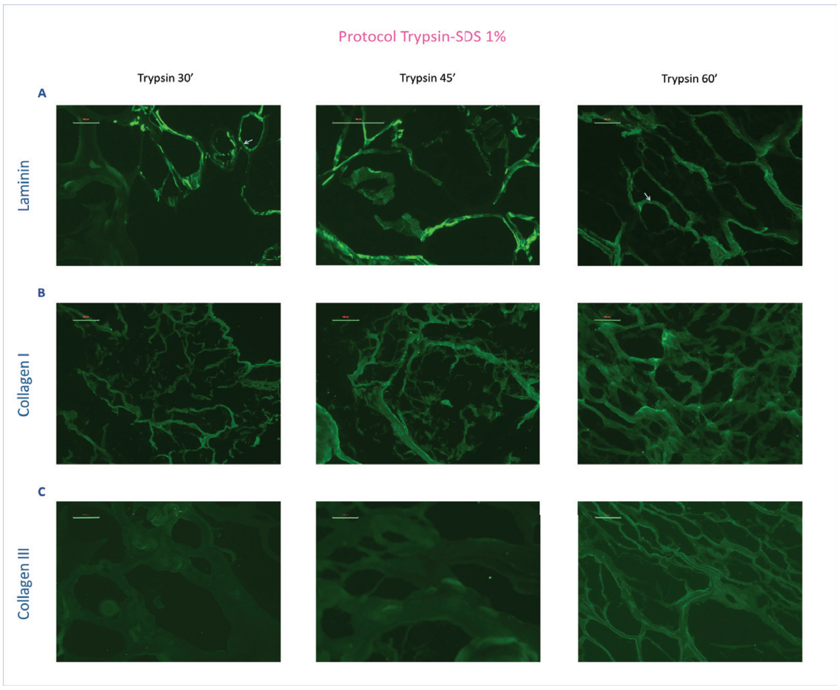

Figure 56. Investigation of ECM structure and composition (Trypsin-SDS protocols). A) Laminin immunostaining was performed. Arrows visualize basement membrane. B) Collagen I and C) collagen III immunostaining investigated endomysium and perimysium. Scale bars represent 100 μm.

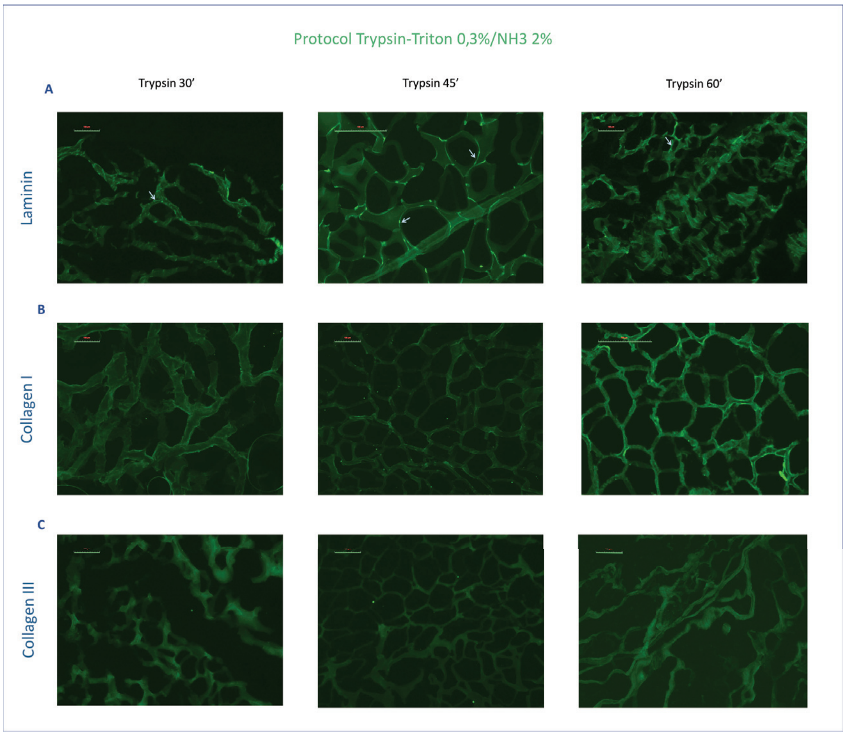

Figure 57. Investigation of ECM structure and composition (Trypsin-Triton/NH3 protocols). A) Laminin immunostaining was performed. Arrows visualize basement membrane. B) Collagen I and C) collagen III immunostaining to visualize basement membrane. Collagen I and III immunostaining investigated endomysium and perimysium. Scale bars represent 100 μm.

- Decellularization with persistent large DNA fragment with SDS as a detergent

We quantified residual **DNA content** after extraction from ECM scaffolds by spectrometric and fluorometer quantification (Figure 58).

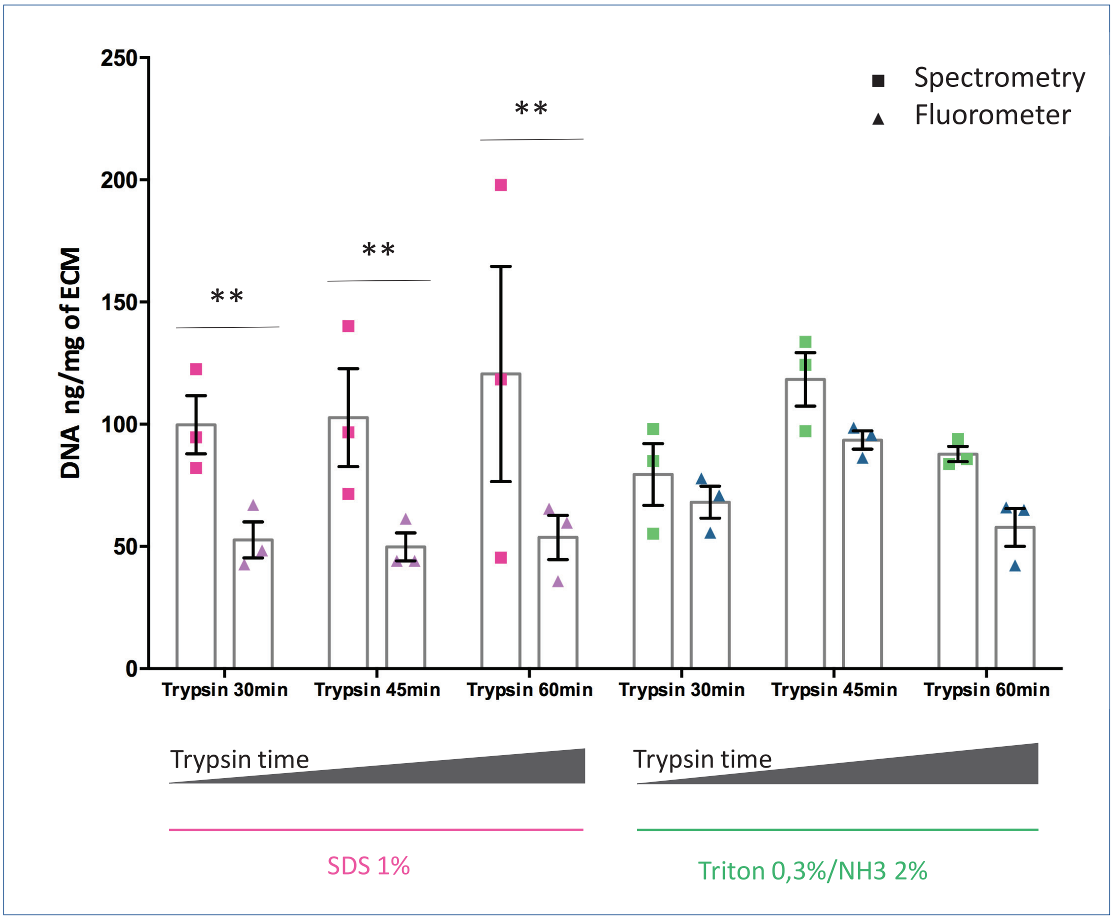

Figure 58. Fluorometer and spectrometry quantification of residual DNA content. DNA was extracted from all ECM scaffolds (n=3) with comparison of different digestion times and two detergents. Three-way permutation ANOVA followed by one-way permutation ANOVA per detergent level was performed.

All protocols with SDS had a lower average value (p=0.002) by fluorometry, with residual DNA at 48.4 ng per mg of sample. In Triton/NH3 protocol, the mean DNA content was 70.9 ng per mg of sample. Current recommendations for decellularized scaffold applications in clinic are a residual DNA below 50 ng per mg of dry sample. Only ECM scaffolds from all protocols with SDS were below the standard threshold, however samples were not lyophilized, leading to an underestimation of residual DNA. Indeed, after a final lyophilizing step, these scaffolds displayed an average value of 140.3 ng DNA per mg of dry sample.

The **DNA electrophoresis** (Figure 59) showed large fragments of DNA.

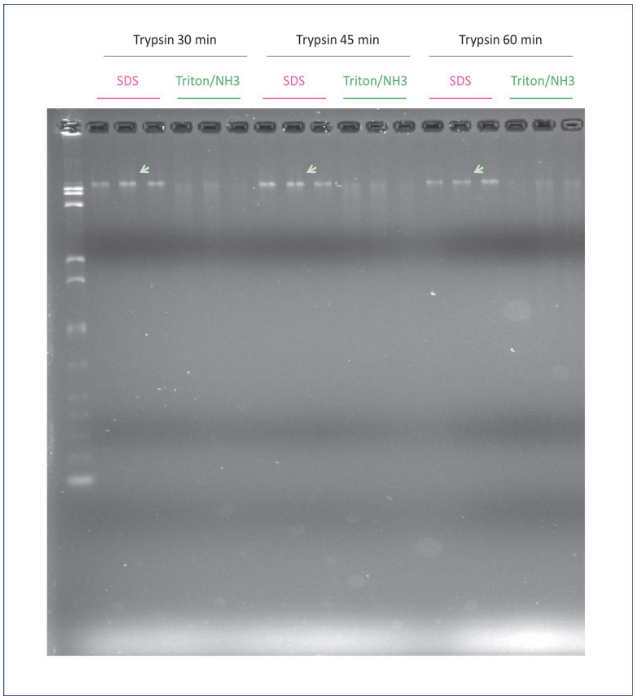

Figure 59. Migration of DNA fragments in electrophoresis. DNA was extracted from all ECM scaffolds (n=3 per condition) and migration was conducted in 1% agarose gel to explore large DNA fragments. Arrows indicate large DNA fragments.

○ Evaluation of GAGs

We measured GAGs in ECM scaffolds by **Blyscan™ assay** (Figure 60). For all ECM scaffolds from Trypsin-SDS protocols, we quantified an average 4.1µg of GAGs (per mg of sample) whereas in Trypsin-Triton/NH3 protocols, we observed a complete loss of GAGs ($p<0.0001$).

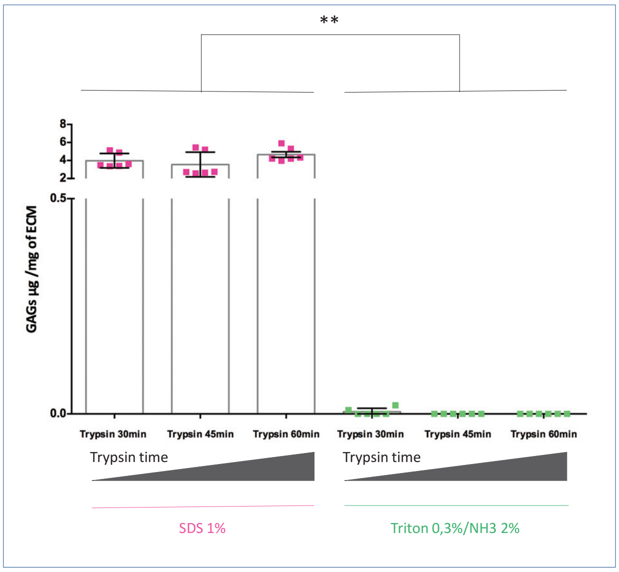

Figure 60. GAG quantification by Blyscan™ assay. For each protocol, extracts of ECM scaffolds (n=6) were used to quantify total GAGs content by a dye-binding method with signal measured at 620 nm. Parametric two-way ANOVA was performed.

In addition, an **Alcian Blue staining** was performed to confirm the absence of GAGs in part of ECM scaffolds. For ECM scaffolds from SDS protocols, we observed a homogeneous blue color staining (Figure 61A) whereas for in Triton/NH3 protocol, we observed no blue (Figure 61B), thereby confirming Blyscan™ results, and indicating GAG loss regardless of enzymatic digestion time.

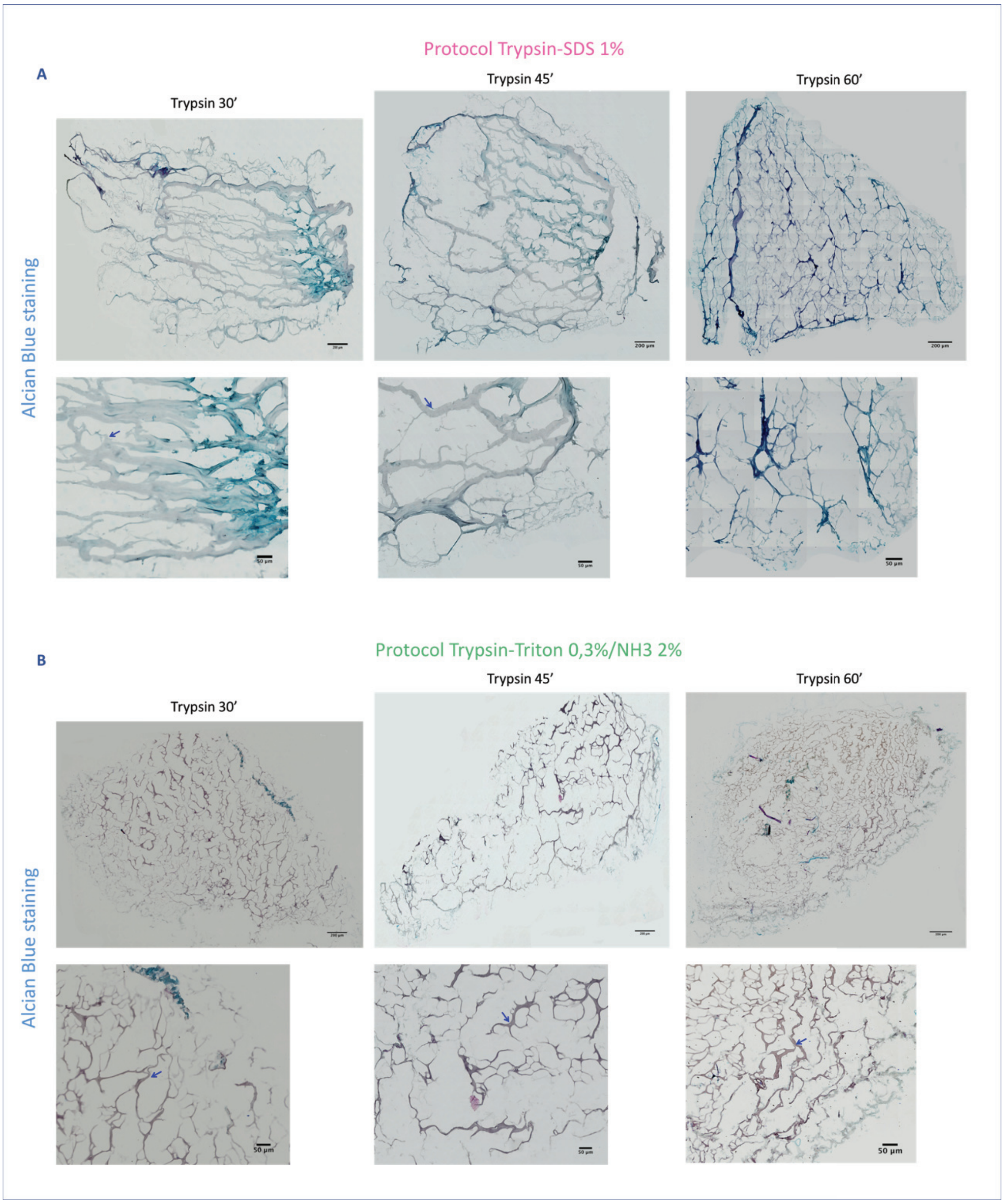

Figure 61. Alcian Blue staining to visualize presence of GAGs. The staining was performed on all ECM scaffolds for A) Trypsin-SDS protocols and B) Trypsin-Triton/NH3. Arrows indicate area with absence of GAGs staining. Scale bars represent 200 µm in whole scaffold and 50 µm in zoom area.

Nevertheless, DNA is known to be one of a false positive cause for these both techniques of GAG evaluation. Consequently, we cannot exclude that results obtained in ECM scaffolds from SDS protocols were overestimated by the presence of remaining large fragments of DNA.

To conclude, we obtained a more preserved endomysium architecture using Triton/NH3 as a detergent. Decellularizations were efficient, even with the shortest digestion time, with no myofiber presence in histological staining or large DNA fragment despite dosages of residual DNA remaining above recommendations. GAGs were still absent despite a decrease of enzymatic digestion duration. Each protocol using SDS displayed large DNA fragments which are known to be highly immunogenic.

- R-I-3) Detergent choice to preserve the endomysium structure

To maintain GAGs in ECM scaffolds, we tried to further improve the decellularization process (Figure 62).

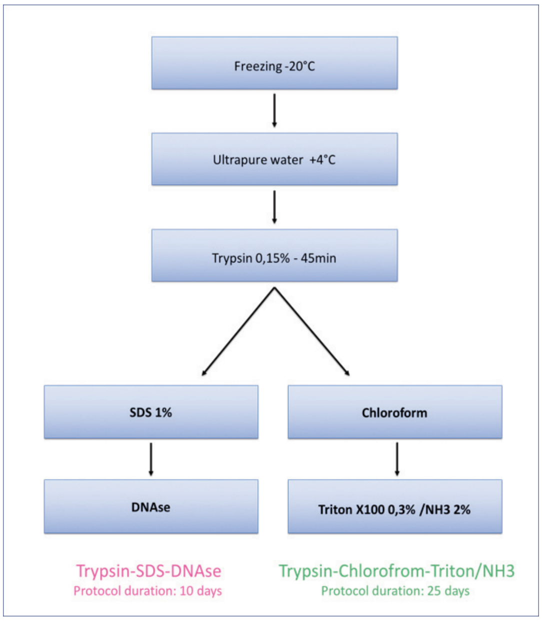

Figure 62. Protocol modification to determinate detergent choice. In order to preserve GAGs, chloroform was added before Triton/NH3 detergent. To avoid large DNA fragment, DNAse was added after SDS detergent.

For each protocol, we decreased trypsin digestion time to 45 min. We also included a chloroform soaking step in the Triton/NH3 protocol. Utilization of SDS seems to sustain GAGs, therefore we added a last step with DNAse to remove large fragments of DNA, that could be immunogenic and responsible for an overestimation of GAG content.

A preserved three-dimensional architecture with efficient decellularization

In the SDS-DNAse protocol (Figure 63A), endomysium could be visualized with **Masson trichrome staining**, but a finer and more homogeneous conservation of its architecture was reached with Chloroform-Triton/NH3 protocol (Figure 63B). Cell removal was achieved with both protocols.

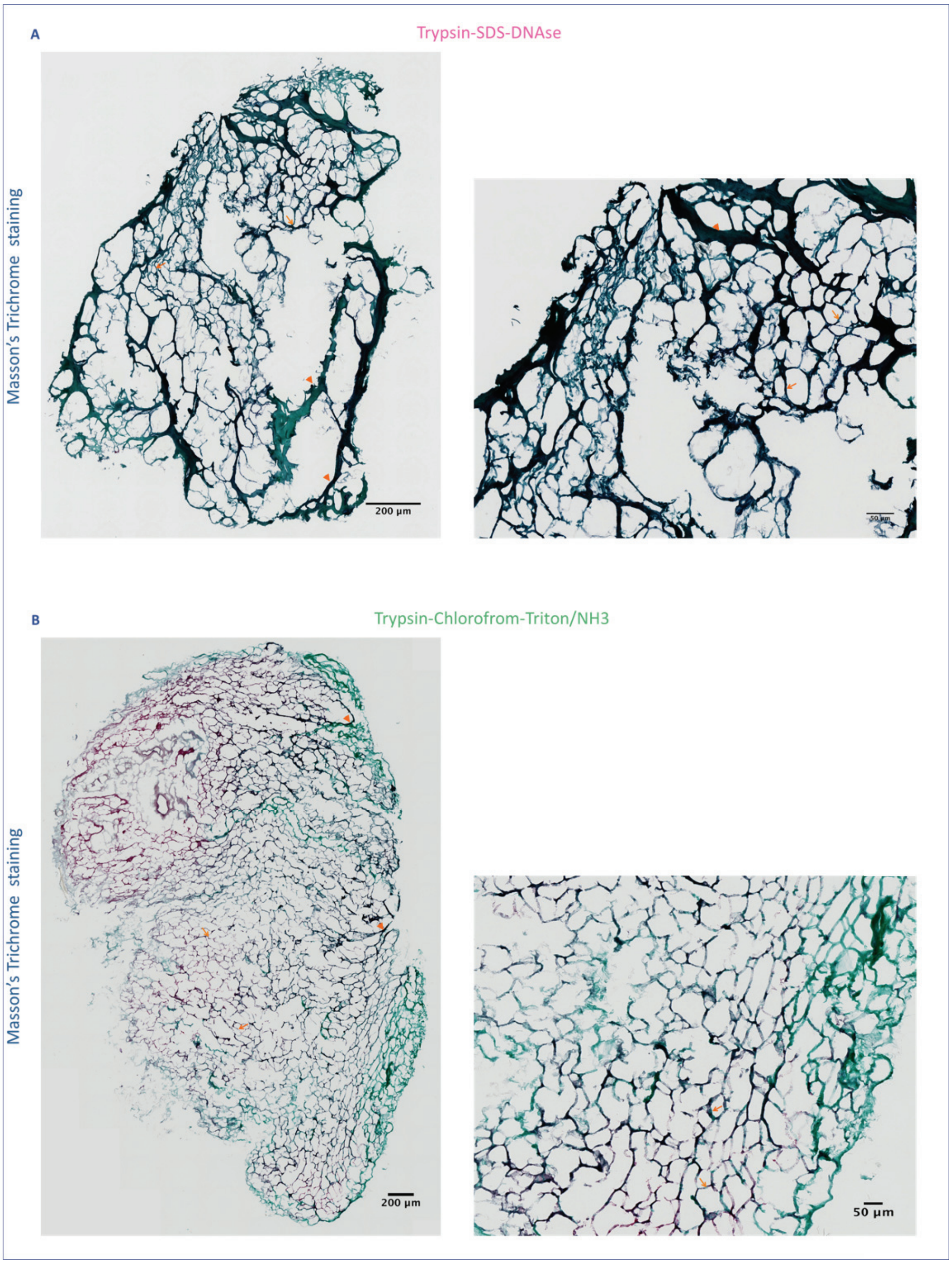

Figure 63. ECM structure in Masson Trichrome staining. ECM scaffolds obtained from A) Trypsin-SDS-DNAse and B) Trypsin-Chloroform-Triton/NH3 protocols were analyzed. Arrowheads show perimysium and arrows indicate endomysium. Scale bars represent 200 µm in whole scaffold and 50 µm in zoom area.

Residual DNA was quantified by **fluorometry** and was negative in the SDS-DNAse protocol (Figure 64A).

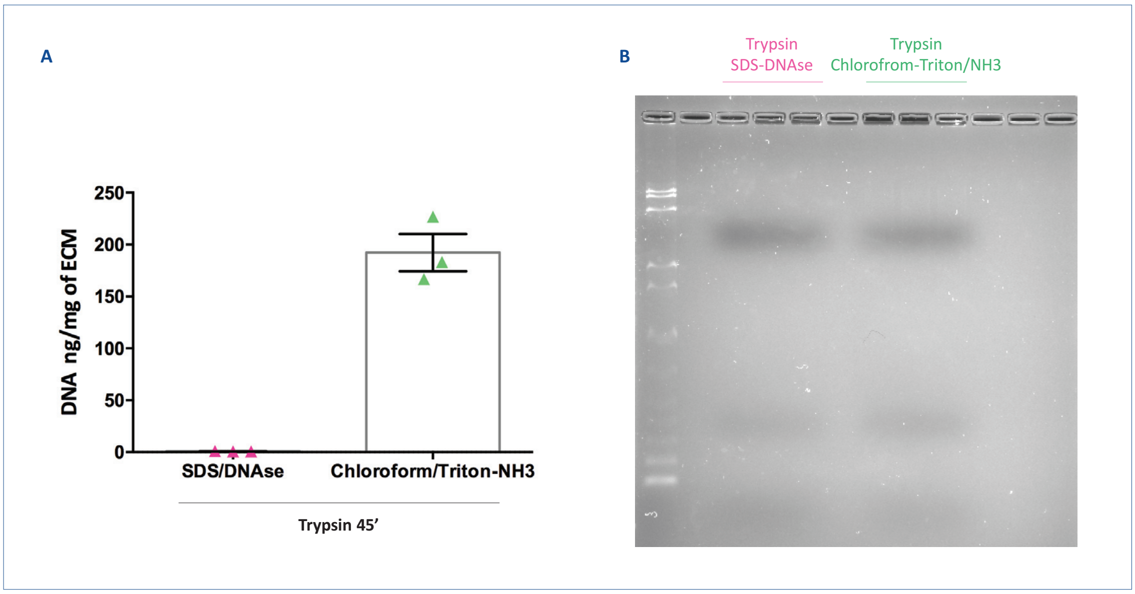

Figure 64. Investigation of residual DNA. DNA was extracted from ECM scaffolds (n=3 per condition). A) Fluorometer quantification of residual DNA and B) Migration of DNA fragments in electrophoresis (1% agarose gel) was realized.

In Chloroform-Triton/NH3 protocol, residual DNA was quantified at an average of 192.2 ng per mg of sample, almost 3-fold more than previous Triton/NH3 protocol without chloroform. Trace of fluorescent nuclei were also noticeable in **Hoechst labelling** for this protocol (Figure 65).

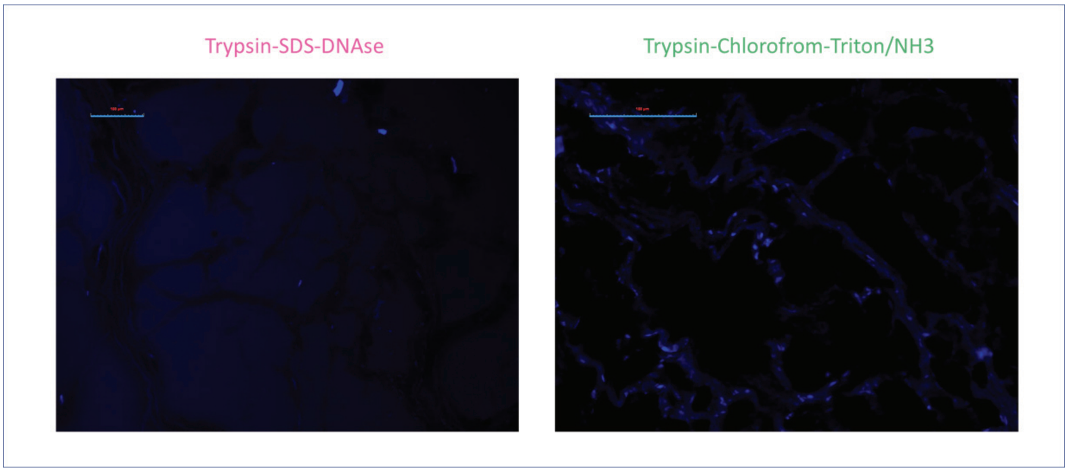

Figure 65. Hoechst immunolabelling to visualize residual nuclei. Hoechst labelling was performed in cryosections of ECM scaffolds for both protocols. Scale bars represent 100 μm.

However, it should be noted that we were unable to detect any large DNA fragment in **electrophoresis** for both protocols (Figure 64B).

- Trophic molecules including GAGs

Dosage of GAGs by **Blyscan™ technique** found an average of 0.66µg of GAGs per mg of sample with the Chloroform-Triton protocol and a trend towards a lower value with the SDS-DNAse protocol, at 0.43µg of GAGs per mg of ECM scaffold (Figure 66).

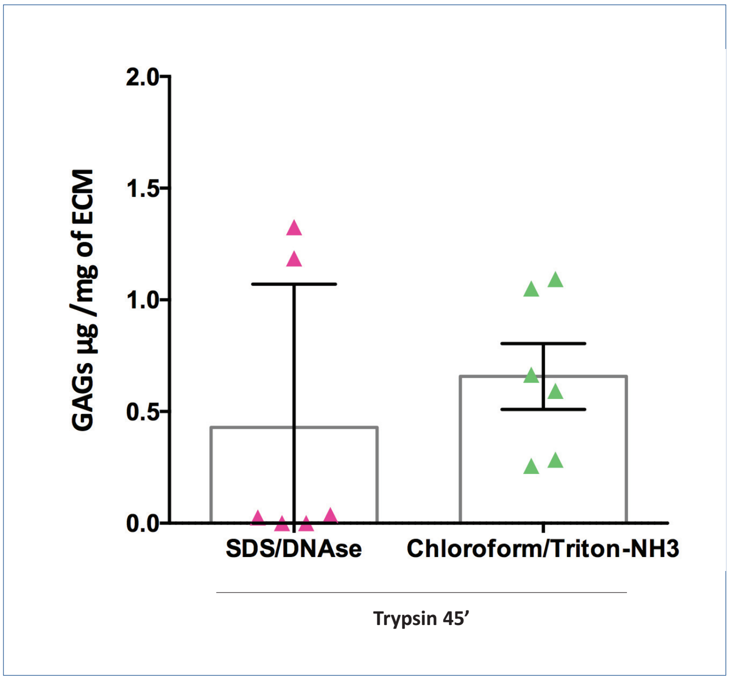

Figure 66. GAG quantification by Blyscan™ assay. For each protocol, extracts of ECM scaffolds (n=6) were used to quantify total GAG content by a dye-binding method with signal measured at 620 nm. Mann-Whitney test was performed.

Alcian blue staining was subsequently performed and in Chloroform-Triton/NH3 protocol, we observed few regions with blue staining (Figure 67C), confirming Blyscan™ results. For ECM scaffold from SDS DNAse, usual Alcian blue staining was also realized to confirm the presence of HS (Figure 67A) by comparing with the nitrous acid treated slides (Figure 67B), in favor of HS presence in some histological regions.

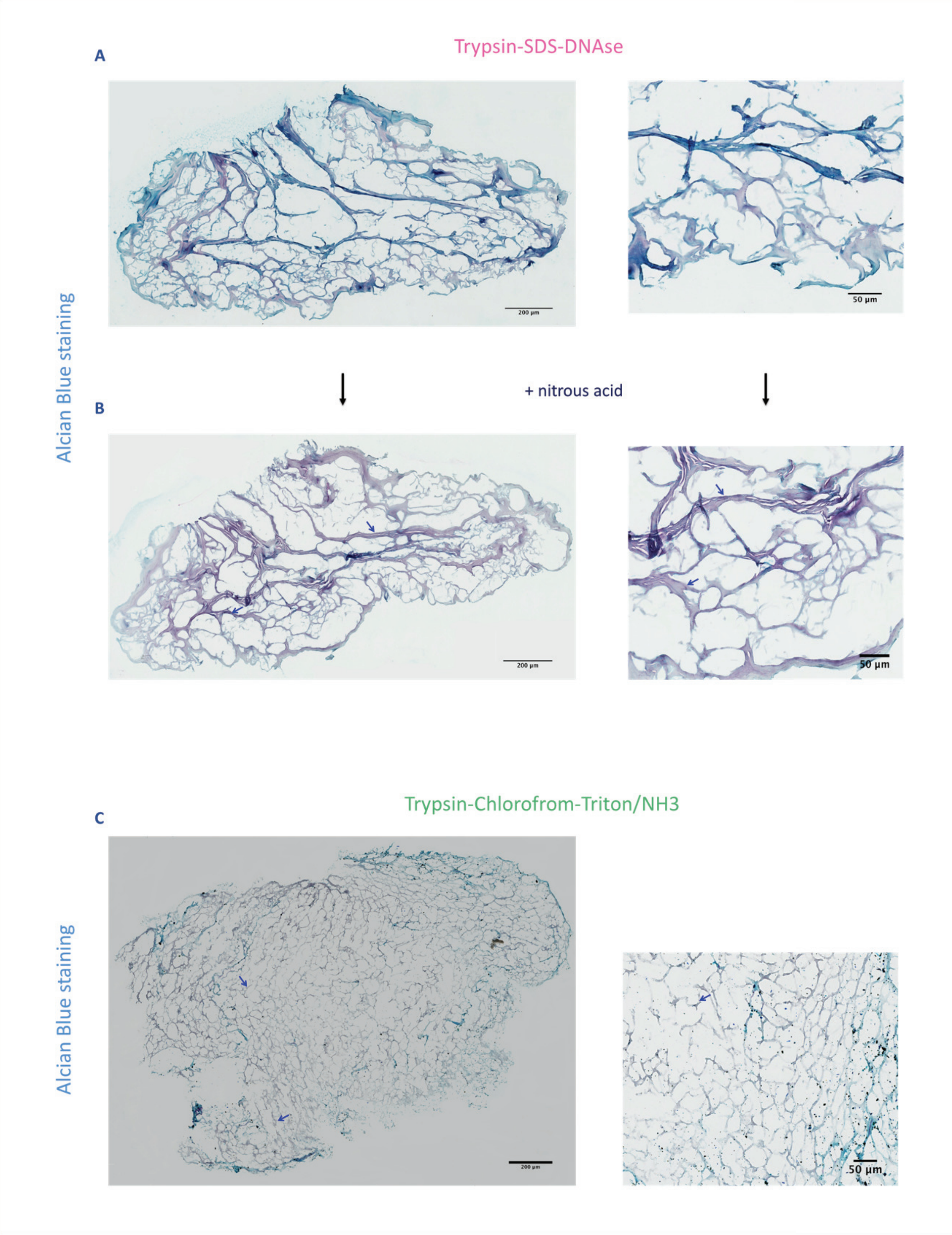

Figure 67. Alcian Blue staining to visualize presence of GAGs. A) For SDS DNAse protocol, some slides were pretreated by B) nitrous acid to degrade heparan sulfate (HS) in order to confirm their presence by comparing GAG coloration with usual staining. C) Only Alcian Blue staining was performed on ECM scaffolds from Trypsin-Chloroform-Triton/NH3. Arrows indicate area with absence of GAGs staining. Scale bars represent 200 μm in whole scaffold and 50 μm in zoom area.

To definitively conclude on the choice of decellularization process, we retained Trypsin-Triton/NH3 protocol. The rationale behind this was the hypothesis that spatial organization of ECM could be essential for a future biomaterial in VML injury, but also that GAGs are hardly sustained in decellularization protocols. Therefore, we focused on obtaining the most conserved three-dimensional architecture.

- R-I-5) Proteomic analysis of decellularized muscle scaffolds

To get a better insight in ECM composition after Trypsin-Triton/NH3 decellularization protocol, we chose a hypothesis-free technique sequentially involving liquid chromatographic separation of solubilized molecules, followed by electrospray ionization and mass spectrometry based on the time of flight of released peptides (nanoLC-MS/MS). This technic relies on our ability to solubilize the targeted molecules, and we accordingly sought to optimize the post-decellularization protocol using the range of detected known ECM molecules with nanoLC-MS/MS as main criteria.

○ Three-dimensional ECM scaffold

Raw ECM scaffolds were extremely elastic and were difficult to slice. Elasticity was not lost on ice, making manual grinding inefficient. Chemical solubilization by isoelectric focusing (IEF) solution was not sufficient to denature and solubilize ECM so we finally used a solution containing SDS (Solution SDT) using recommendations of the Matrisome project. After a brief migration in SDS-PAGE, one band was detected. Its isolation was followed by trypsin digestion before identification in nanoLC-MS/MS. This first proteomic analysis only yielded the detection of Collagens I and VI among known ECM molecules (Figure 68).

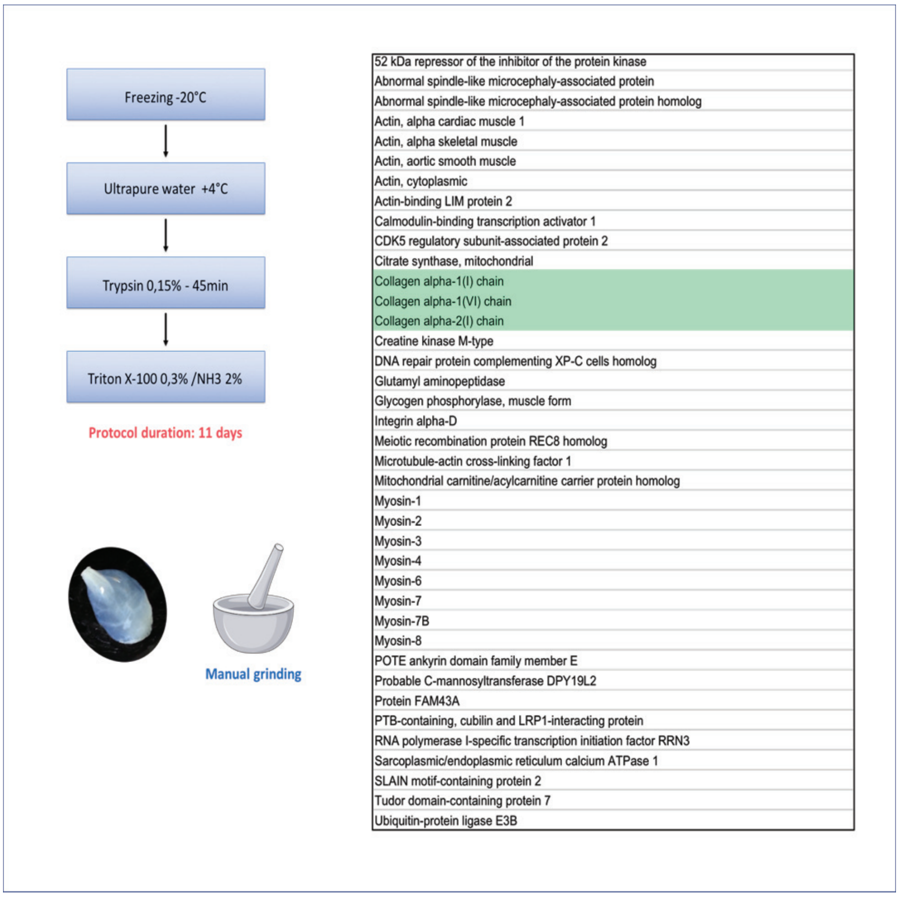

52 kDa repressor of the inhibitor of the protein kinase
Abnormal spindle-like microcephaly-associated protein
Abnormal spindle-like microcephaly-associated protein homolog
Actin, alpha cardiac muscle 1
Actin, alpha skeletal muscle
Actin, aortic smooth muscle
Actin, cytoplasmic
Actin-binding LIM protein 2
Calmodulin-binding transcription activator 1
CDK5 regulatory subunit-associated protein 2
Citrate synthase, mitochondrial
Collagen alpha-1(I) chain
Collagen alpha-1(VI) chain
Collagen alpha-2(I) chain
Creatine kinase M-type
DNA repair protein complementing XP-C cells homolog
Glutamyl aminopeptidase
Glycogen phosphorylase, muscle form
Integrin alpha-D
Meiotic recombination protein REC8 homolog
Microtubule-actin cross-linking factor 1
Mitochondrial carnitine/acylcarnitine carrier protein homolog
Myosin-1
Myosin-2
Myosin-3
Myosin-4
Myosin-6
Myosin-7
Myosin-7B
Myosin-8
POTE ankyrin domain family member E
Probable C-mannosyltransferase DPY19L2
Protein FAM43A
PTB-containing, cubilin and LRP1-interacting protein
RNA polymerase I-specific transcription initiation factor RRN3
Sarcoplasmic/endoplasmic reticulum calcium ATPase 1
SLAIN motif-containing protein 2
Tudor domain-containing protein 7
Ubiquitin-protein ligase E3B

Figure 68. Proteomic analysis of ECM scaffold. ECM scaffold was manually ground, precipitated in acetone/methanol, solubilized with Laemmli solution and separated by a short SDS-PAGE. Then, the unique band was digested by trypsin before identification in nanoLC-MS/MS.

Conversely, despite an apparently efficient microscopic cell removal, it should be highlighted that we still found traces of intracellular molecules such as myofilaments (actin and myosin) or mitochondrial components as citrate synthase, but also membrane bound molecules such as integrins.

○ Ground ECM scaffold

To further optimize molecule identification, we used a complementary process with a slicing step prior to perform the decellularization protocol. This was followed by cryogrinding and denaturation with urea to solubilize ECM molecules included in decellularized scaffolds. In parallel, we also improved proteomic process using recommendations of the Matrisome project[80,455]. We realized preliminary cryogrinding tests and this step appeared to be pivotal in increasing the range of detected ECM molecules. NanoLC-MS/MS uncovered more molecules, mostly belonging to the core matrisome, such as collagens (I, IV, VI, XXV) and two glycoproteins, Fibrillin 1 and Cartilage intermediate layer 2 (Figure 69). However, by adding more handling steps, samples appeared to be contaminated with human keratins, possibly leading to the underestimation of poorly represented molecules.

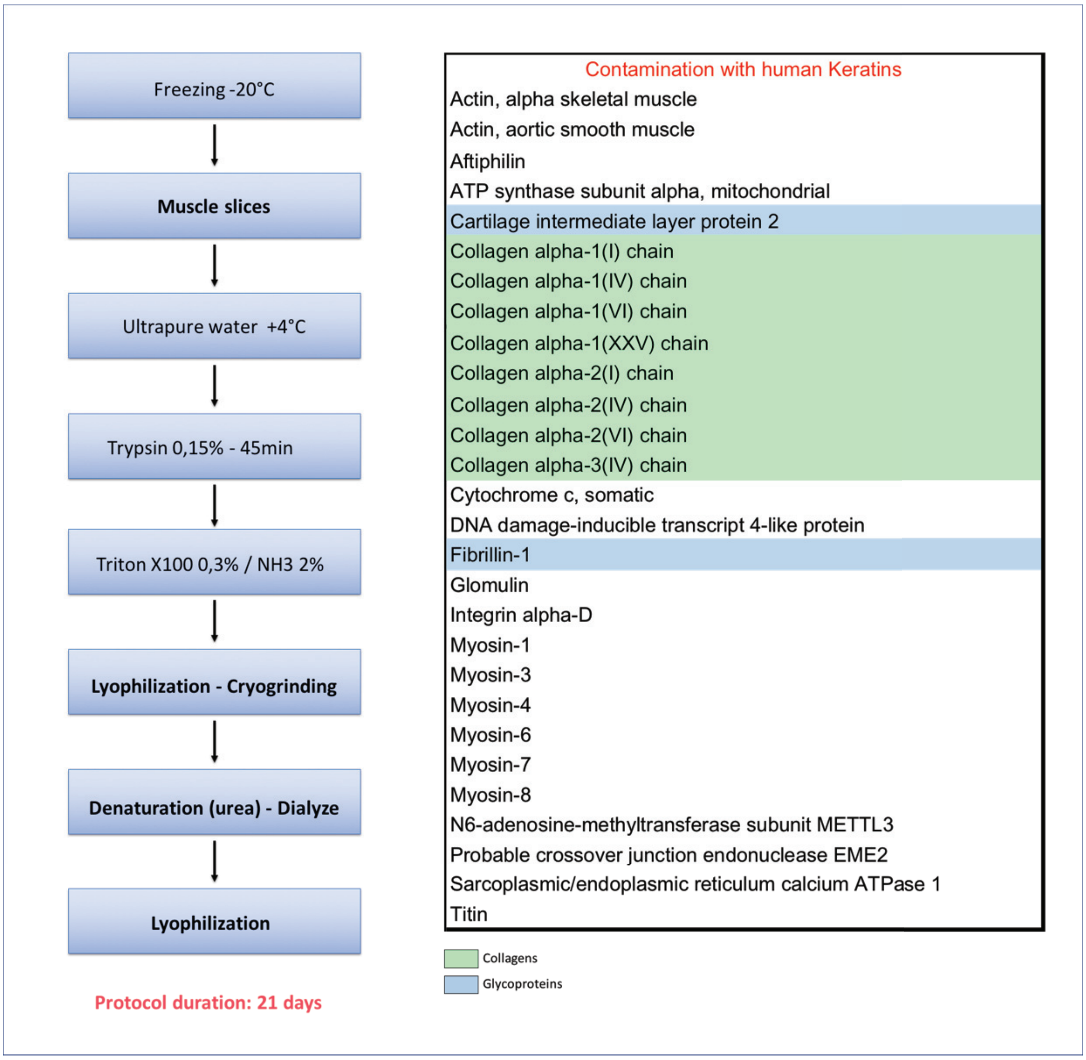

	Contamination with human Keratins
	Actin, alpha skeletal muscle
	Actin, aortic smooth muscle
	Aftiphilin
	ATP synthase subunit alpha, mitochondrial
🟦	Cartilage intermediate layer protein 2
🟩	Collagen alpha-1(I) chain
🟩	Collagen alpha-1(IV) chain
🟩	Collagen alpha-1(VI) chain
🟩	Collagen alpha-1(XXV) chain
🟩	Collagen alpha-2(I) chain
🟩	Collagen alpha-2(IV) chain
🟩	Collagen alpha-2(VI) chain
🟩	Collagen alpha-3(IV) chain
	Cytochrome c, somatic
	DNA damage-inducible transcript 4-like protein
🟦	Fibrillin-1
	Glomulin
	Integrin alpha-D
	Myosin-1
	Myosin-3
	Myosin-4
	Myosin-6
	Myosin-7
	Myosin-8
	N6-adenosine-methyltransferase subunit METTL3
	Probable crossover junction endonuclease EME2
	Sarcoplasmic/endoplasmic reticulum calcium ATPase 1
	Titin

🟩 Collagens
🟦 Glycoproteins

Figure 69. Proteomic analysis of ground muscle ECM. Pre-treatment were realized to enhance solubilisation of ECM components (n=4). Before decellularization, muscles were sliced. Then, decellularized muscle fragments were cryoground and denaturated. Ground muscle ECM were precipitated in acetone/methanol, solubilized with Laemmli solution, separated by SDS-PAGE and then digested by trypsin. Identification of ECM molecules was performed by nanoLC-MS/MS (data shown are obtained with optimal grinding condition).

With an improvement of ECM solubilization by grinding/denaturation, we have obtained an enhancement of detected ECM molecules. In our proteomic analysis, we have highlighted some elements belonging to the core matrisome, such as collagens (I, IV, VI, XXV) and two glycoproteins, Fibrillin 1 and Cartilage intermediate layer 2.

DISCUSSION

Skeletal muscle is a high cellular content tissue with a specific three-dimensional organization. Maintaining its ECM microarchitecture in a biomaterial can be crucial for a future application in VML injury, to drive progenitor migration and spatial alignment of neoformed myofibers. For a future implantation, ECM-based biomaterial need to be biocompatible, requiring an adequate cell removal to avoid endogenous molecules (DAMPs and antigens) leading to deleterious immune response. Therefore, we focused our work on ECM structure preservation since some trophic molecules such as GAGs could be added in a second phase after transplantation. In addition, the majority of muscle ECM-based scaffolds published so far exhibited showed no preserved, or non-investigated three-dimension integrity[456].

To explore different strategies, we have investigated four distinct decellularization protocols. Then, we chose to retain a protocol which combines physical-enzymatic-detergent step allowing maintaining ECM microstructure but to the detriment of GAG content, that hardly preserved during decellularization. However, homogeneous delivery of decellularizing agents instead of immersion procedure could be beneficial, as discussed in more detail below. Though not exhaustive, characterization of scaffolds will allow us to identify which element of structure and/or component could be essential for improving muscle regeneration without inadequate immune response.

- New technics to optimize decellularization

Obtaining an optimal balance between the elimination of cell residues and the preservation of ECM relies on fine duration and concentration of enzymatic/chemical agent treatment. Another strategy to avoid deleterious effect on ECM of enzymatic/chemical agents is to develop decellularization protocols avoiding these steps such as the combination of actin depolarization agent and ionic bath-DNAse. Unfortunately this process is mainly efficient on thin tissues[411] or muscle slices[457]. Thus, when we used this protocol on rat TA (data not shown), we did not obtained a correct cell removal (as observed in another study[403]), or a satisfying ECM structure and composition, with GAG loss. Interestingly, another team has also elaborated a process without enzymatic step, which preserves microarchitecture and GAG content of nerve ECM, by favoring cell detachment with an apoptotic agent[458]. The generated apoptotic bodies avoid the release of intracellular components and are eliminated without using chemical clearance.

For a long time, decellularization processes were mainly custom-made, increasing procedure variability. However, some of these procedures can be automatized now[459]. Indeed, automatization is mainly achievable by vascular perfusion technics, which provide a more delicate and homogenous agent delivery, minimizing ECM damage as well as considerably accelerating the process[399]. However, the vasculature is not easily accessible in small skeletal muscle samples, therefore we used an immersion method. Nevertheless, studies have developed interesting approaches such as the use of needle directly perforating the muscle[459] or harvesting all the limb to perfuse distant muscle by iliac artery[403]. Moreover, vascular access is particularly relevant to larger samples for clinical translation since it was realized in an arm originating from animals (rodent and primate)[460] and even human[384]. They have obtained ECM-based scaffolds using mainly SDS or a mix with short administration of Triton X-100, leading to conservation of the vascular network[384], muscle ECM structure and composition, including GAG content[384,460].

- Persistence of undesirable cellular components

Various decellularized ECM-based biomaterials are commonly used for various clinical applications. However there is not yet a definitive consensus[361,461] on unwanted cellular residues that should be measured or explorated to predict an absence of deleterious immune response after implantation. DNA content is one of the most investigated parameter with a standard threshold proposed at less than 50 ng per mg of dry sample[389] and size below 200 bp[389] because large DNA fragments are suspected to be more immunogenic[462]. We have obtained ECM-scaffolds holding higher DNA content, around 450 ng per mg of dry ECM, but nonetheless without large fragment. Studies using muscle ECM-based scaffolds have also obtained DNA quantification above this limit (150 to 350 ng per mg of dry ECM)[384,460,463]. These measurements are not always reported to a dry weight, leading to an underestimation. Moreover, DNA thresholds do not foresee a future immune response since *in vitro* activation of immune cells could be described with smaller DNA fragments[464], whereas clinically used biomaterials such as SIS or UBM scaffolds contain higher DNA[465] levels. The choice of the detergent determines residual DNA as well, but we have recurrently obtained higher DNA amount with SDS utilization despites studies have made the opposite observation[466]. Solvents could also have an impact while nuclei fragments seem to be trapped in ECM with chloroform. The addition of a DNAse step allowed us to efficiently eliminate DNA without alteration of ECM. This step could be applied if limited residual DNA in ECM-scaffolds would turn out to be detrimental after implantation.

Other DAMPs or cell antigens can potentially persist after decellularization. The most investigated are the major histocompatibility complex-I and for xenogeneic transplantation, the galactose alpha1,3 galactose (α-gal) epitope expressed in rodent and pig tissues[467] but absent in humans, who own natural antibodies[468]. We have chosen to explore the most abundant proteins present in myofibers (myosin heavy chains) and dystrophin localized in the sarcolemma. They were absent in the majority of our biomaterials. An apparent discrepancy exists between the identification of several myosins in proteomic analysis and their absence in specific electrophoresis. However, the proteomic approach used for this study is strictly qualitative and may identify proteins that are present at low level. Therefore, it is not possible to extrapolate their immunogenicity. This is the case for other intracellular proteins identified, such as SERCA. In addition, we cannot avoid traces of residual cells except with harsh processes, deleterious for ECM structure and composition. It should be noted that clinical-grade SIS scaffolds contain many DAMPs and antigens such as DNA[469] and α-gal epitope[470], without immune rejection in patients[468,471].

- Maintenance of skeletal muscle ECM specificities

Sufficient retention of ECM molecules

GAG content decreases on a time-dependent manner during the decellularization processes, notably o-sulfated GAGs[472]. They are particularly sensitive to detergent and SDS has maintained them more efficiently as compared with Triton X-100 that completely eliminated them. But protocols using SDS triggered higher DNA that could act as a false positive, majoring the results in Blyscan ™ measurement or Alcian Blue staining. We have also evaluated main fibrillar collagens of skeletal muscle. Collagen I is maintained in ECM-scaffolds but collagen III displays weaker signals in immunofluorescence staining and is absent in proteomic analysis. It could be due to a higher susceptibility to decellularization process or a lower solubilization in proteomic preparation, preventing its identification.

ECM scaffolds such as SIS maintain endogenous growth factors as highlighted by ELISA measurement[473,474] but we did not investigate them because most growth factors are bound to the GAGs. Despite the fact that a study on skeletal ECM with steps quite similar to the ones we used found VEGF and IGF-I[456], our proteomic study identified no growth factor. In addition, other groups have decellularized porcine muscle using physical step and detergents, leading to a decrease in GAG content but maintaining several growth factors, as shown by multiplex cytokine kits and growth factors ELISA kits[475].

Because muscle ECM composition is not fully identified, using a proteomic approach allowed us to have a large overview of matrisome and associated molecules contained within the ECM scaffolds. Investigating ECM composition by proteomic remains very challenging[80,82], frequently leading to incomplete identifications because ECM components are highly hydrophobic and protease resistant. So results are biased towards a better detection of the components that are easier to digest. Thus, ECM proteomics necessitates more stringent protocols as illustrated by an improvement of ECM identification with grinding/denaturation to enhance solubilization. We also used the protocol recommended by the matrisome project[455] which is the most used and efficient for ECM proteomic. Indeed, contrary to the first proteomic characterization of UBM[476], this method has identified more than 500 proteins quantitatively represented by 78 % of matrisome and associated molecules[477], mainly collagens and glycoproteins, proteoglycans and secreted factors. Some cellular residues such as actin, desmin or hemoglobin were also present.

Muscle ECM architecture

Detergent/solvent had a strong impact on muscle ECM architecture conservation. SDS led to a poorly conserved structure as compared with Triton X-100. Chloroform maintained ECM microarchitecture but at the cost of a thickened and size reduced endomysium, that could impair myofiber formation. In the definitive protocol, we maintained muscle ECM microarchitecture, specially endomysium and basal lamina, where progenitors could potentially migrate. Scaffolds with a conserved ECM structure have allowed the formation of properly aligned myotubes[460] by *in vitro* recellularization. However, there are few explorations focusing on the impact of ECM structure on muscle tissue formation in VML models.

In synthetic materials, the three-dimensional structure strongly influences cell behavior such as macrophage polarization and fibrosis[478]. A few studies have studied this parameter on decellularized scaffolds, although their pore size had an impact on cell infiltration[479] and repopulation[480]. ECM stiffness is another parameter acting on cell fate and decellularized scaffolds have mechanical characteristics close to those of original tissues, although long decellularization processes could increase stiffness[466,472,481]. The use of trypsin in decellularization process could alter mechanical behavior of ECM-based biomaterials with less waviness or modified alignment of collagen fibers. This can however be mitigated by short duration or low trypsin concentration (less than 0.5%) as we performed[482].

- Necessary *in vivo* explorations

Concerning ECM based-biomaterials, there is an important variety in the source of tissue, specie, age that may influence the final ECM composition that will have an impact on host response, especially the immune response. Therefore, implantation investigations often focus on the immune response and the repair process. Before initiating any *in vivo* investigations, some *in vitro* analysis can be beneficial to preselect more promising repair conditions and anticipate some deleterious host response.

o Preliminary *in vitro* analysis

Macrophages play a key role in host response after scaffold implantation and most investigations performed *in vitro* focused on their adhesion and inflammatory status. Solubilized fragments of ECM (custom-made or from commercial scaffolds) induce a regenerative polarization of macrophages[483] despite skeletal muscle ECM leads to a more mixed profile[483]. Whether this is due to ECM composition or decellularization process remains unclear and more studies are needed[477]. Interestingly, our selected protocol maintained collagen VI which efficiently supports macrophage migration, as compared with collagen I[484]. We also highlighted a preferential adhesion of macrophages on collagen VI by realizing a screening of multiple combinations of ECM components (Micromatrix™, data not shown).

In vitro analysis can trace cell colonization of biomaterial[403] as well as ECM effects on myogenic progenitors and others cell involved in muscle regeneration. Conditioned-media from macrophages in contact with SIS-ECM fragments, enhance migration and differentiation of a myogenic cell line[485]. Ground ECM obtained using process close to ours were tested on myoblast culture and showed an increase of their proliferation[343,452]. Specific biomaterial degradation can be investigated by enzymatic digestion and biological activity of ECM fragments can be explored such as small peptides from SIS that are chemoattractants for endothelial cells[486].

However, some caution needs to be taken about cell effects of ECM fragments while they act in a dose-dependent manner and depend on the tissue.

Therefore, to explore the complexity of host responses but also evaluate its capacities on muscle repair and particularly in pathologic conditions such as VML injury, *in vivo* explorations will be necessary.

- *In vivo* explorations

The knowledge of the host response to decellularized biomaterials comes from *in vivo* explorations mainly performed with non-muscle ECM scaffolds. However, we will focus here on muscle ECM-based scaffolds. All synthetic scaffolds lead to foreign body response whereas decellularized biomaterials provide a more “constructive remodeling response”. This is illustrated by observations from clinical applications in abdominal wall repair, even if ECM biomaterials have not shown their clinical superiority[487]. Macrophages are major players. They harbor a high ratio of regenerative/inflammatory markers early after biomaterial implantation[477]. The immune response also involves the adaptive immune response, as illustrated by biomaterial implantation in subcutaneous or in VML injury, showing that regenerative macrophages are dependent on Th2 cells, through an IL4-dependent pathway[488]. Some deleterious characteristics, such as crosslinking (avoiding ECM degradation) or incomplete decellularization, lead to an inflammatory host response[489] therefore, we used no crosslinking procedure and focus on a complete cell removal.

The chronic activation of macrophages could lead to an excessive ECM production and deposition by fibroblasts leading to fibrosis, frequently observed after their implantation in VML injury. Finally, a better understanding of both the innate and adaptive immune responses towards the biomaterials we developed will be helpful to promote efficient repair. Indeed, we can make the hypothesis that recapitulating the proper inflammatory timing found in muscle regeneration, such as a fine-regulated inflammatory phase, could be beneficial, with a growing interest on neutrophils, suspected to have immunomodulatory properties[490].

Before using biomaterial directly into VML injury, some subcutaneous explorations can provide information on the host response, its vascularization and the rarely obtained ectopic muscle formation[491]. Incomplete decellularization impairs tissue neoformation[403]. Studies have investigated muscle ECM biomaterials obtained with protocols similar to ours[343] leading to muscle fibrosis and few formation of myofibers in the periphery of the biomaterials.

Therefore, it is obvious that the ECM-based strategy needs improvements. Maintaining the three-dimensional structure as close as the native tissue is a major point in our work. However, in light of recently published studies, we think that further amelioration is necessary. The migration of progenitors in the ECM seems to be a major limiting factor and needs to be improved. Promoting the recruitment of myogenic and other cells involved in muscle regeneration, such as endothelial cells and immune cells, is necessary to induce efficient muscle regeneration. Adding trophic molecules such as GAGs and chemokines and/or growth factors could be useful. We found that GAGs are difficult to maintain together with 3D structure and sufficient decellularization. They are key components of the ECM and major actors in numerous regenerating or repair processes. Commercially available GAGs are proposed to improve tissue repair. In order to understand their importance in skeletal muscle repair, we studied RGTA®, which are clinical grade mimetics. We investigated the effects of GAG administration in a model of muscle regeneration.

Part II- Exploration of RGTA® administration in skeletal muscle regeneration

GAGs are major components in ECM and their roles in various tissue repair models have been reported. They are mainly proposed to both stabilize and protect growth factors within the regenerating tissue. In this part of our work, the aim was to study the benefits of the administration of clinical grade GAG mimetic (RGTA®) on skeletal muscle regeneration. To do so, we used both in-vitro and in-vivo models. Cardiotoxin injury model was used because it is extremely reproducible and well characterized.

MATERIALS AND METHODS

- Skeletal muscle injury

Male C57/Bl6 mice were bred in compliance with French and European recommendations. Investigators are certified for animal experimentation and the protocol was validated by the ethics committee. A preliminary study included mice aged of 18 weeks in average. A second study was performed with animals of 8 weeks of age. Mice were anesthetized with isoflurane and muscle injury was induced by injection of 50µL cardiotoxin (CTX, 12 µM, Latoxan) in each TA muscle.

- GAG mimetic treatment

The GAG mimetic ([OTR-4131], OTR3 Company, Paris, France) is a synthetic dextran polymer comparable to heparin, differing by its lower acetyl group ratio[417]. To evaluate its effect, [OTR-4131] solution was injected into regenerating muscle at day 3 after cardiotoxin injection. A preliminary study was performed to choose the most appropriate dose, based on previous rat studies[255,442,447], and muscles were analyzed at 8 days post-injury (DPI). Tested doses ranged from 0.01 to 1µg of RGTA® by muscle, in a constant volume of 10 µL. According to the results obtained, in the second study, we have injected [OTR-4131] at a concentration of 100 µg.mL^{-1} (corresponding to 1µg per muscle). The control group received a 10 µL saline injection.

- Histological analysis

At 8 and 28 DPI, regenerating muscles were harvested, weighed, snap-frozen in nitrogen chilled isopentane and kept at -80°C until analysis. Muscle cryosections were performed (10 µm thickness). Then, they were used for hemalun eosin (HE) staining to confirm an entire regeneration process in muscle, allowing to eliminate muscles not correctly injected with CTX. Briefly, the different steps were Mayer Hematoxylin staining, washed in water, then slides were transferred to bluing solution (lithium carbonate) followed by eosin staining, dehydration with alcohol (70 and 100%), clearing with xylene and finally slides were mounted with Eukitt®.

Sudan black staining was performed to highlight lipid droplets. Slides were fixed with Ethanol 70% and then immersed in a buffered Sudan Black B solution. After water rinse, slides were counterstained with Mayer Hematoxylin, washed in water and mounted with Fluoromount-G Mounting Medium (# FP-483331, Interchim). The entire muscle section was scanned with Axio Scan. Z1 (Zeiss) at 20X of magnification connected to a 3 CCD HV-F 2025 color camera (Hitachi). Stained area was quantified by image J and represented by a percentage of the entire muscle section area.

For the CSA analysis, cryosections were labeled with antibodies directed against Laminin (#L9393, Sigma-Aldrich) and revealed with FITC–conjugated secondary antibody. Pictures covering the whole muscle cryosection were recorded with a Timelapse (Zeiss) at 10X magnification. CSA was determined using ImageJ software[492] (see Annex 1). The whole muscle section was analyzed.

For angiogenesis exploration, antibodies directed against CD31 (Abcam), and Laminin (#L9393, Sigma-Aldrich) revealed with Cy3- and FITC-conjugated antibodies respectively (Jackson Immunoresearch Inc) were used. Nuclei were labeled with Hoechst (Sigma-Aldrich). This immunolabelling was also used to quantify the number of nuclei per fiber.

For ECM compartment exploration, antibodies used were directed against Collagen I revealed with Cy3-conjugated antibodies. This labelling was combined to a necrosis fiber evaluation by using FITC-conjugated antibodies anti-mice immunoglobulin G (IgG) to detect agglomerates of immunoglobulins caught in necrotic fibers.

For macrophage exploration, antibodies against F4-80 (#ab6640, Abcam) were revealed with Cy3-conjugated antibodies and nuclei were labeled with Hoechst 33342 (#B2261, Sigma-Aldrich).

Fibroblastic cells were analyzed with antibodies against PDGFRα (#AF1062, R&D Systems) revealed with Cy3-conjugated antibodies.

For satellite cell analysis, fresh cryosections were fixed and permeabilized with 100% methanol at -20°C. After three washes in PBS, slides were sequentially incubated at 90°C for 5 min in two baths of citric acid (10 mM, pH 6) for antigen unmasking. After an additional wash step, muscle cryosections were saturated with 4% Bovine Serum Albumin (BSA) in PBS at room temperature. Slides were then incubated with antibodies directed against Pax7 (Hybridoma bank), Ki67 (#ab15580, Abcam) and MyoD (#sc-31942, Santa Cruz) overnight at +4°C in 2% BSA. Secondary Cy3-conjugated antibodies were used to reveal Ki67 labelling and biotin (#BA-2000, Vector) followed by DTAF-conjugated streptavidin (#PN IM0307, Beckman Coulter) to amplify Pax7 labelling. Nuclei were visualized with Hoechst 33342 (#B2261, Sigma-Aldrich).

Pictures were recorded with an Axio Imager.Z1 (Zeiss) at 20X of magnification connected to a CoolSNAP Myo CCD Camera (Photometrics). For each analysis, 10 randomly chosen fields were counted. For cell analysis, excepted PDGFRa IF, the number of cells was manually counted and expressed as number per mm^2. PDGFRα staining and Collagen I staining were analyzed as a percentage of staining area.

- Myoblast culture

Muscle stem cells (MuSCs) were extracted from mouse muscle hind limbs from 1 to 5 weeks of age (male or female) animals. Muscles were carefully dissected and gently minced with scissors. Then, they were digested several times with protease (#P8811, Sigma-Aldrich) at 37°C. Next, supernatants were passed through a 100-µm cell strainer and MuSCs were collected by centrifugation at 2000 rpm for 5 min. They were initially seeded at low density (200 to 500 cells per well) in 12 well plates coated with gelatin (#G1393, Sigma-Aldrich) for amplification in proliferation medium [DMEM/F12 (#11524436, Gibco), 20% Fetal Bovine Serum (#10270106, Gibco) and 2% Ultroser™ G serum substitute (#15950-017, Pall Inc)].

To study proliferation, MuSCs were seeded at 3000 cells.cm^{-2} in proliferating medium with or without [OTR4131].

To study differentiation, MuSCs were seeded at 30000 cells.cm^{-2} in proliferating medium for 6 h then switched to differentiation medium [DMEM/F12, 2% horse serum (#11520516, Gibco)] containing or not [OTR-4131].

For in vitro assay, [OTR-4131] was initially used over a dose range of 1 to 50 µL.mL^{-1} and compared with saline solution.

- MuSC labeling

Cells were fixed with 4% paraformaldehyde, permeabilized with 0.5% Triton X-100 (in PBS) at room temperature.

For proliferating exploration, Ki67 staining (#ab15580, Abcam) was performed associated with nuclei labeling by Hoechst. In vitro fluorescent immunolabelling were recorded with a Zeiss Observer Z1 microscope connected to a Coolsnap HQ. (Photometrics) camera at 20X magnification. Ki67 positive cells were quantified manually using ImageJ software and expressed as a % of total cells.

For differentiation experiments, Phalloidin staining (Sigma-Aldrich) was used to labeling actin in cells associated with nuclei labeling by Hoechst. Immunolabelling images were obtained with a Zeiss Observer Z1 microscope at 10X magnification and for each condition, 6 randomly chosen fields were counted. The number of labeled nuclei per cells was determined manually using ImageJ software and expressed as a percentage of total nuclei. Fusion index was calculated as the number of nuclei within myotubes divided by the total number of nuclei.

- Statistical analyses

Results are expressed as means ± SEM. Statistical analyses were undertaken with Prism software (version 6.0h for Mac). For the prestudy, Kruskal–Wallis and post-hoc test (Dunn's multiple comparisons test) were performed. For the main study, 8 DPI data were explored with a parametric two-way ANOVA whereas 28 DPI data were analyzed with Mann-Whitney test. For *in vitro* data, Wilcoxon matched-pairs signed ranks test was used. An α-error of 0.05 per sub-figure was used to set a threshold of significance.

RESULTS

- R-II-1The selection of optimal RGTA® dose

In order to determine the dose effect of RGTA® on several parameters relevant to regeneration, we tested five RGTA® doses ranging from 0.01 to 1µg per muscle, injected locally at 3 DPI (Figure 70).

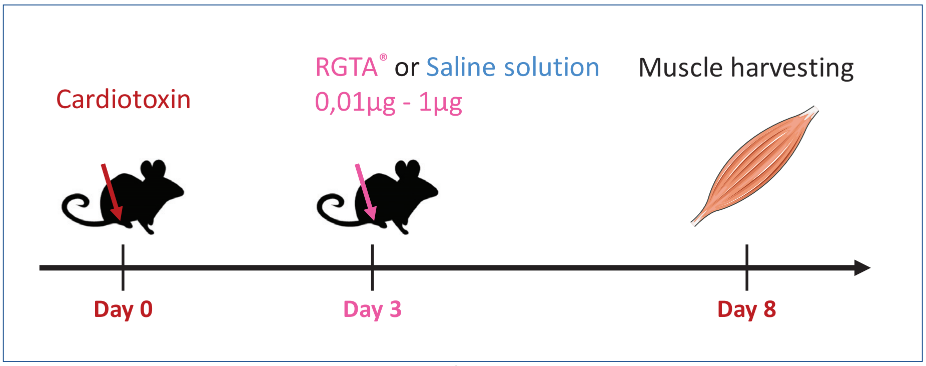

Figure 70. Protocol used to determinate RGTA® optimal dose. At day 0, CTX was injected in both TA muscles. Then, RGTA® (5 increasing doses) or saline solution (control condition) was injected in TA 3 DPI. Muscles were analyzed at 8 DPI.

At 8 DPI, TA muscles were weighted, tissue architecture evaluated by HE staining, CSA and nuclei per myofiber quantified after laminin and Hoechst immunofluorescence respectively. The highest dose of RGTA® (i.e. 1 µg per muscle) yielded a mean of **relative muscle weight** to body mass ratio at 0.148 % versus 0.132 % for control muscles (Figure 71A). A Kruskal-Wallis test searching for a dose-effect was not significant (p=0.24), whereas the relationship between muscle weight and RGTA® dose was linear (linear regression with p=0.025 and 95%CI slope: 0.0018-0.024), with a significant increase in mass when enhancing the dose, probably due to the osmotic effect of the molecule. **The number of nuclei per fiber** was significantly different depending on RGTA® dose (p=0.02). With the 1µg dose, the number of nuclei per fiber tended to be higher (p=0.075, Figure 71B) with a mean at 1.97 versus 1.62 in the control group. The **mean CSA** (Figure 71C) was significantly different for the lowest RGTA® dose (i.e. 0.01 µg per muscle) with a mean value at 743.4 μm^2 as compared with 517.5 μm^2 in control muscles (p=0.016) whereas for the highest dose, the mean CSA was at 764.4 μm^2 (p=0.16).

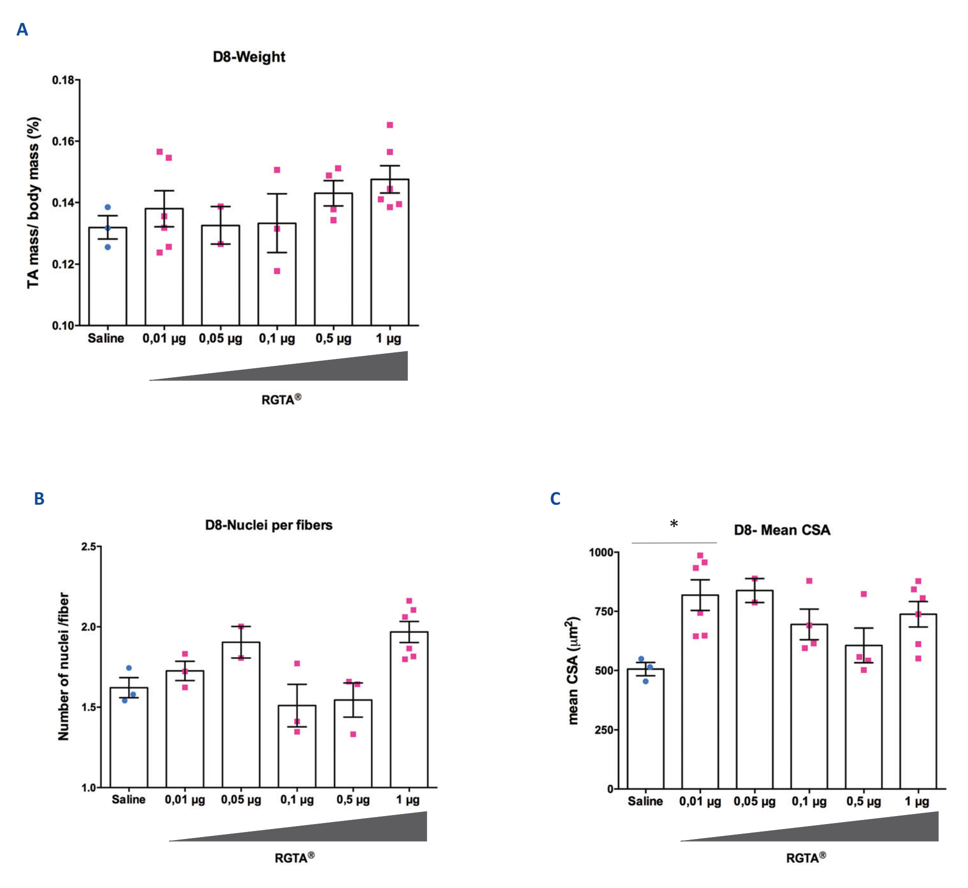

Figure 71. Effects of increasing dose of RGTA® on skeletal muscle regeneration. Muscles were injected with saline solution (n=3 mice, 1 muscle correctly injected per animal) or RGTA® (5 increasing doses, n=2 or 3 mice per condition, 1 or 2 muscles per animal) and were analyzed at 8 DPI. A) ratio of TA mass per body mass; B) Number of nuclei per fiber and C) mean of myofiber cross-sectional area were analyzed. Kruskal–Wallis and post-hoc test (Dunn's multiple comparisons test*)* were performed. * represents $p<0.05$.

In **HE staining**, the 1µg dose RGTA® yielded visually less necrosis and inflammatory infiltrate than saline condition (Figure 72A). Necrosis was quantitated in muscle cryosections stained with HE for the two extreme dosages (control and 1µg). The highest RGTA® dose led to a decrease in the number of necrotic fibers with a mean of 35.5 necrotic fibers per total muscle after RGTA® administration versus 87.3 fibers in control muscles (Figure 72B, p=0.024). The mean number of fibers was not different between muscle treated with 1 µg of RGTA® (2 320 fibers per muscle section) and muscles receiving saline condition versus (2 592 fibers, p>0.99).

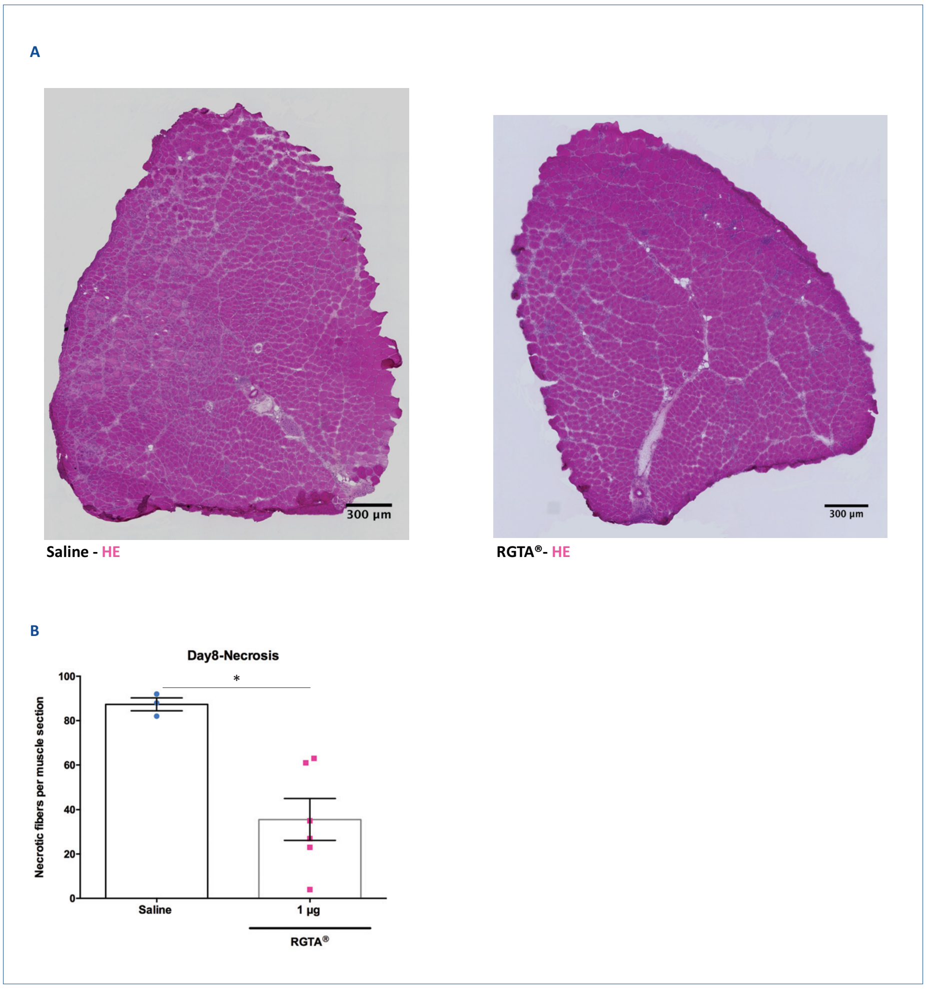

Figure 72. Effects of RGTA® on during skeletal muscle regeneration. Necrotic myofibers were analyzed at 8 DPI in TA injected with saline solution (n=3 mice,1 muscle correctly injected per animal) or with the higher dose of RGTA® (n=3 mice, 1 or 2 muscles per animal). A) Hematoxylin–eosin staining of TA muscles and B) Number of necrotic fibers per muscle section were analyzed. Mann-Whitney test was performed.

We therefore chose to conduct subsequent experiments using 1 µg per muscle as the most promising dose based mainly on 2 parameters: a decrease in the number of necrotic fibers and the number of nuclei per fiber tended to be higher but with no significant modification of the mean CSA.

- R-II-2) Accelerated muscle regeneration after RGTA® administration

We undertook a more exhaustive histological analysis on muscles treated from the preliminary study with the 1µg dose or saline solution. We explored different parameters of muscle regeneration including the myogenic, angiogenic and connective compartments. These first results were termed as the first experiment. The same protocol (Figure 73) comparing only 1µg to saline was performed on a second group of animals and labelled the second experiment. All the histological analyses were examined at 8 DPI.

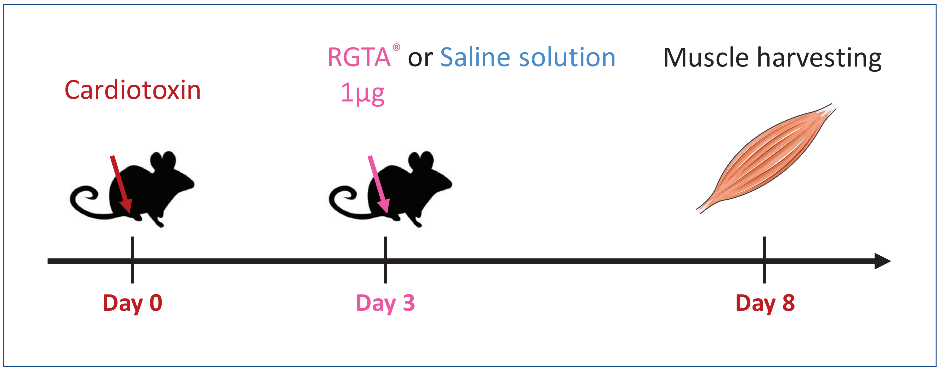

Figure 73. Protocol used to evaluate RGTA® in early phase of muscle regeneration (experiment 2). At day 0, CTX was injected in both TA muscles. Then, RGTA® (n=3 mice) or saline solution (n=3 mice) was injected in TA 3 days after injury. Muscles were analyzed at 8 DPI.

- Slight enhancement of TA relative weight associated with an increase in the number of nuclei per myofiber with RGTA® treatment

Relative muscle weight increased slightly after RGTA® administration (p=0.099, Figure 74A). The **number of myofibers** per muscle section remained unchanged (p=0.6149, Figure 74B) in the second experiment.

The fiber **CSA**, quantified on the whole muscle section (Figures 74C-D), was not significantly influenced by RGTA® (p=0.548). Compared with the first experiment, younger animals (i.e. second experiment) had a higher CSA value (p=0.031), however there was no difference between saline and RGTA® groups (969.4 and 953.4 μm^2 respectively).

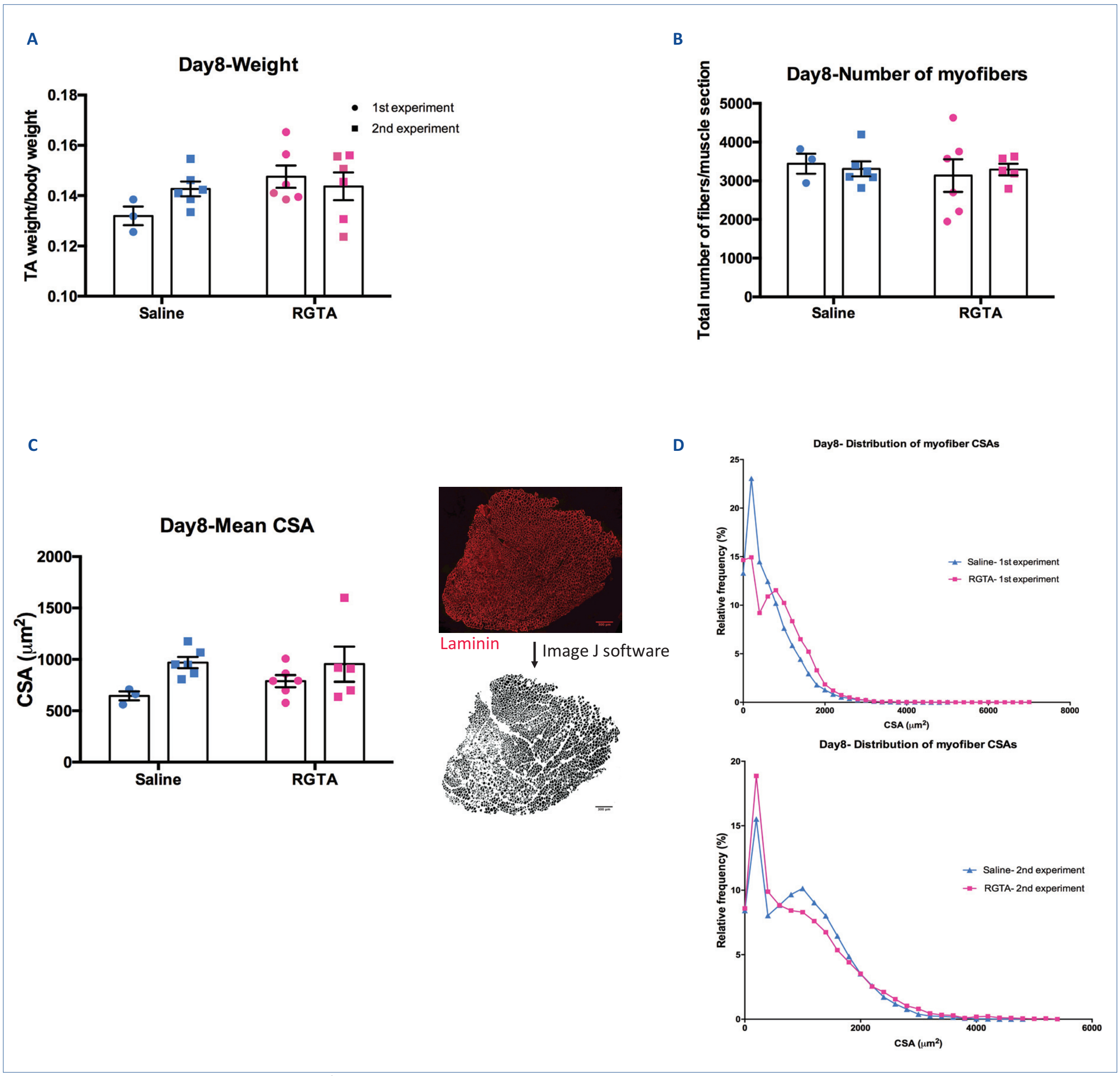

Figure 74. Effects of RGTA® on size and number of myofibers. TA muscles injected with saline solution (n=3 mice per experiment, 1 or 2 muscles per animal) or RGTA® (n=3 mice per experiment, 1 or 2 muscles per animal) were analyzed at 8 DPI. A) Ratio of TA mass per body mass, B) Number of nuclei per fiber, C) mean of myofiber CSA and D) its distribution were performed. Parametric two-way ANOVA was performed.

However the mean number of **nuclei per fiber** was increased in RGTA®-treated muscle (p=0.04), with a more pronounced effect in the first experiment (Figure 75A). The nuclei distribution was slightly shifted towards more nuclei per fiber (Figure 75B) with RGTA® administration in both experiments.

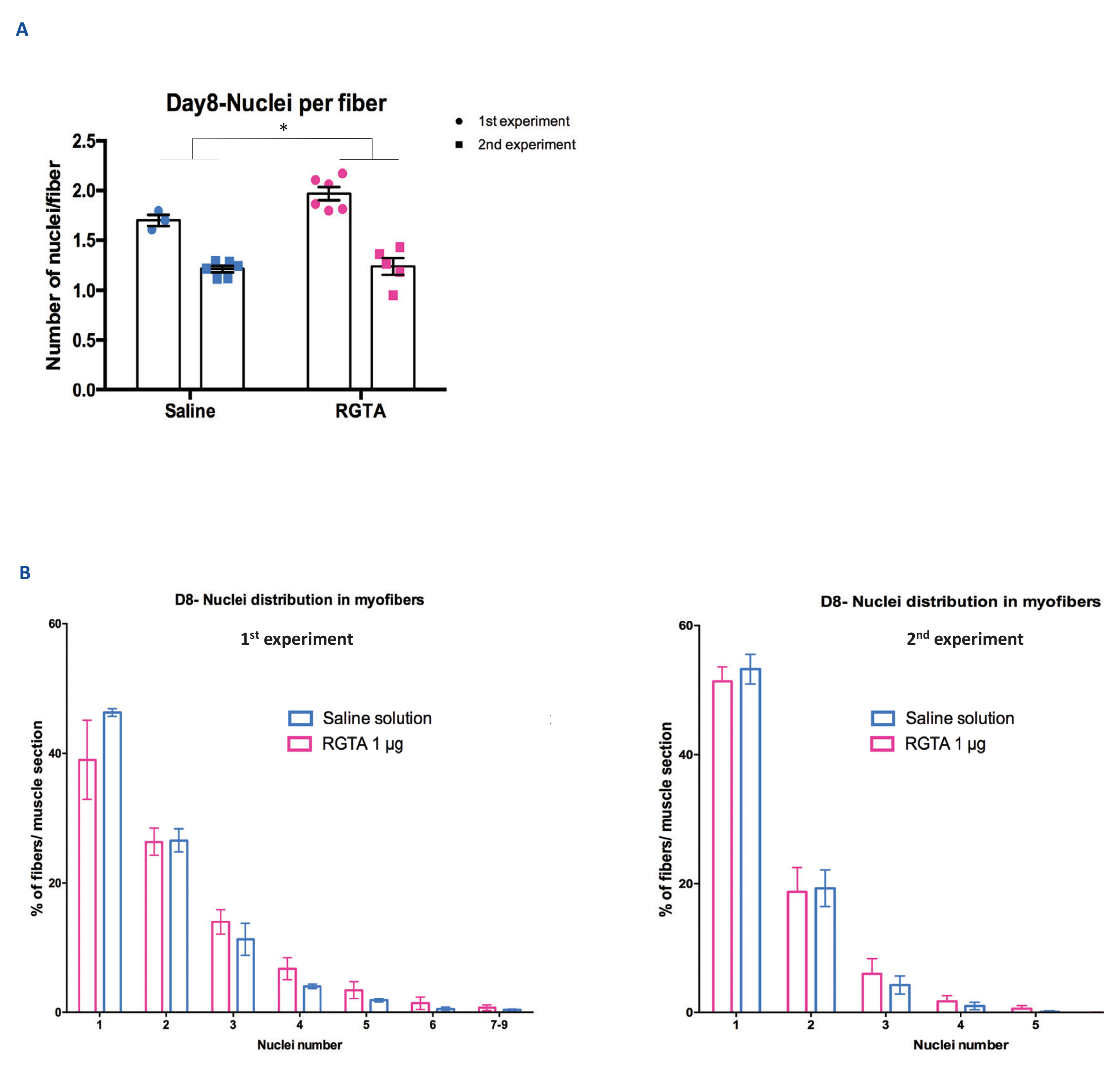

Figure 75. Effects of RGTA® on nuclei content in myofibers. TA muscles injected with saline solution (n=3 mice per experiment, 1 or 2 muscles per animal) or RGTA® (n=3 mice per experiment, 1 or 2 muscles per animal) were examined at 8 DPI. A) Number of nuclei per fiber and B) nuclei distribution per fiber were analyzed. Parametric two-way ANOVA was performed.

- A more efficient capillarization in RGTA® treated-muscle

We analyzed CD31 as a marker of endothelial cells. The capillaries per fiber ratio (C/F) per field was also quantified using a laminin staining. The two-way ANOVA have highlighted a significant interaction (p=0.043) between the two independent variables (C/F and experiment number), which did not allow to conclude on a global effect of RGTA® on angiogenesis. Therefore, for this parameter, a post-hoc test (Mann-Whitney test) was performed for each experiment. We highlighted in the first experiment a higher C/F after RGTA® administration, in favor of a more efficient muscle capillarization (Figure 76) with a mean of C/F at 2.1 in RGTA® condition versus 1.38 in control muscles (p=0.024).

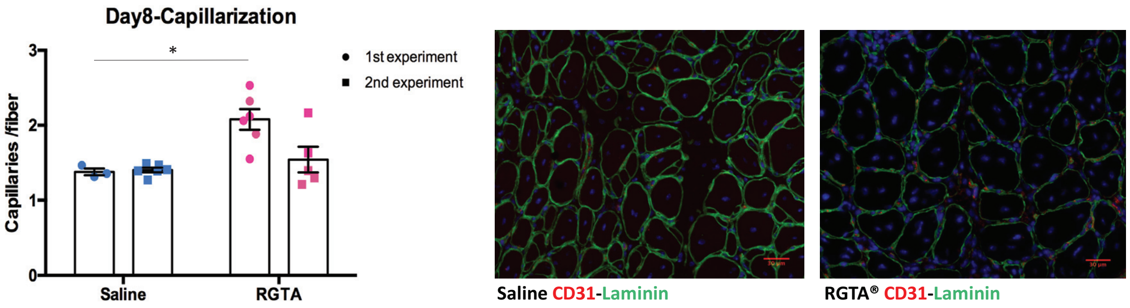

Figure 76. Effects of RGTA® on muscle capillarization. TA muscles were injected with saline solution (n=3 mice per experiment, 1 or 2 muscles per animal) or RGTA® (n=3 mice per experiment, 1 or 2 muscles per animal) were analyzed at 8 DPI. Capillaries per fiber ratio were measured and scale bar represent 30µm. Parametric two-way ANOVA and post-hoc test (Mann-Whitney test) were performed.

○ A greater quality of regeneration with decreased lipid droplets

Lipid droplets are a marker of an impaired muscle regeneration. They can be stained by Sudan Black and the black pixels were quantified on the entire muscle section. RGTA® treatment was associated with a reduction in lipid droplet content in favor of a better muscle regeneration (p=0.0497, Figure 77). In the first experiment, RGTA®-treated muscles displayed a mean area covered by lipid droplets of 0.08 % versus 0.09% in saline treated muscles. In the second experiment, younger mice had a higher area of lipid droplets at 0.12 % in muscles after RGTA® treatment and 0.29 % in muscle after saline injection.

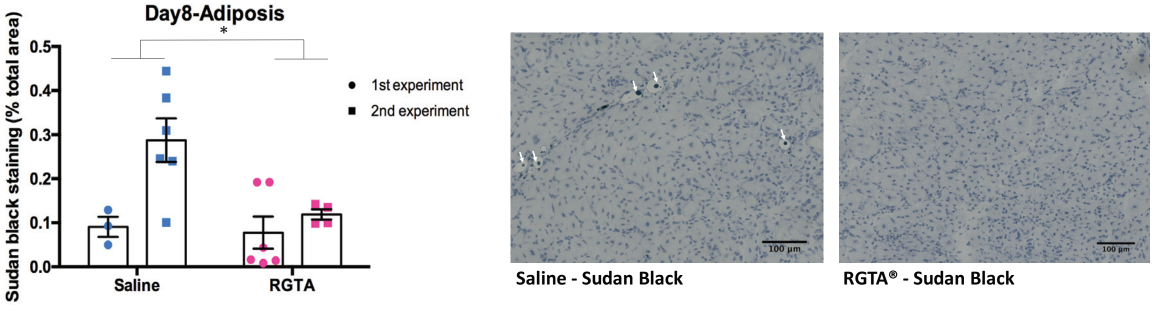

Figure 77. Effects of RGTA® on muscle adiposis. TA muscles were injected with saline solution (n=3 mice per experiment, 1 or 2 muscles per animal) or RGTA® (n=3 mice per experiment, 1 or 2 muscles per animal) were analyzed at 8 DPI. Quantification of lipid droplets was performed by Sudan black staining as a percentage of the total area. Scale bars represent 100µm. Parametric two-way ANOVA was performed.

Slight decrease of PDGFRα positive cells with no change in collagen I content

The quantitation of the amount of collagen I, the main structural collagen of skeletal muscle showed no difference attributable to the RGTA® treatment (p=0.272; Figure 78A). However, muscles from younger animals contained less collagen I with a mean total area of 17.22% in control condition of the second experiment versus 26.13% in control condition of the first experiment (p=0.0002). Fibroblastic PDGFRα positive cells sent prolonged cytoplasmic extension between myofibers and tended to be less present in muscles treated with RGTA®, especially in young animals with mean of total area at 1.67% versus 3.91% in control muscles (p=0.0792; Figure 78B).

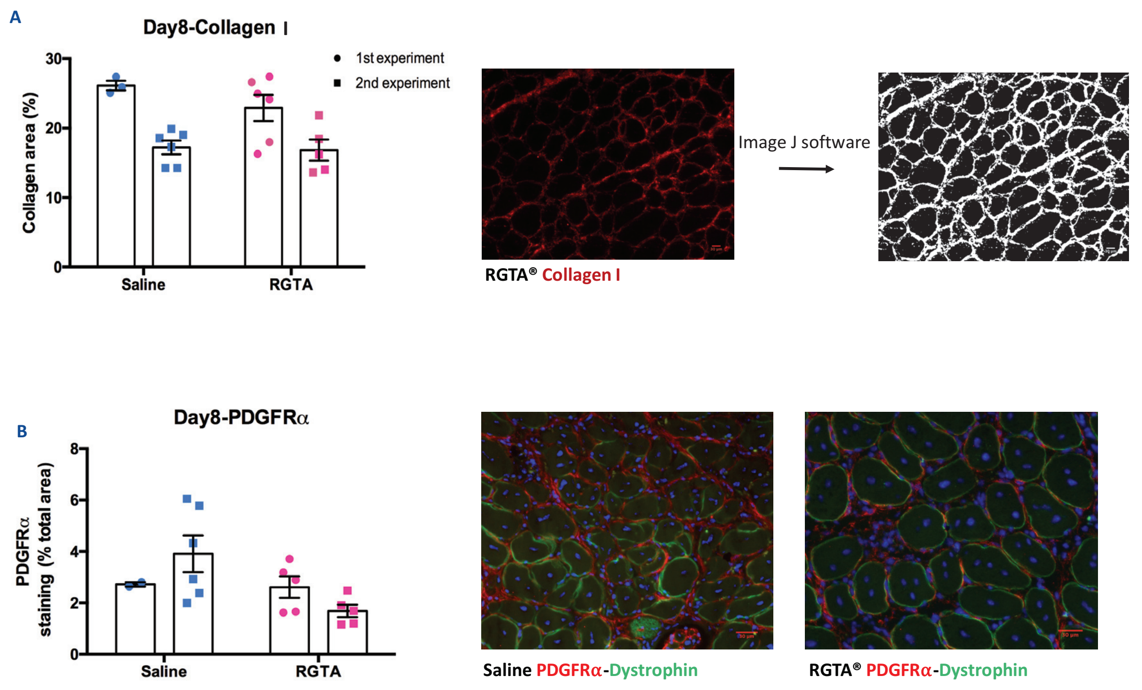

Figure 78. Effects of RGTA® on Collagen I and fibroblastic cells. TA muscles injected with saline solution (n=3 mice per experiment, 1 or 2 muscles per animal) or RGTA® (n=3 mice per experiment, 1 or 2 muscles per animal) were analyzed at 8 DPI. A) Collagen I was quantified as a percentage of the total area. B) Quantification of fibroblastic cells was performed by PDGFRα staining as a percentage of the total area. Scale bars represent 30μm. Parametric two-way ANOVA was performed.

No change in the number of F4-80 positive cells and variable effect on necrosis

We analyzed the number of necrotic cells by taking advantage of their affinity for untargeted IgGs. No effect of RGTA® on necrosis clearance (Figure 79) could be observed, partly due to the discrepancy in control groups necrosis between the two experiments. Highly necrotic regions were found in the first experiment (5.3% of total fibers) while almost no necrosis was found in young animals of the second experiment (mean at 0.14% of total fibers).

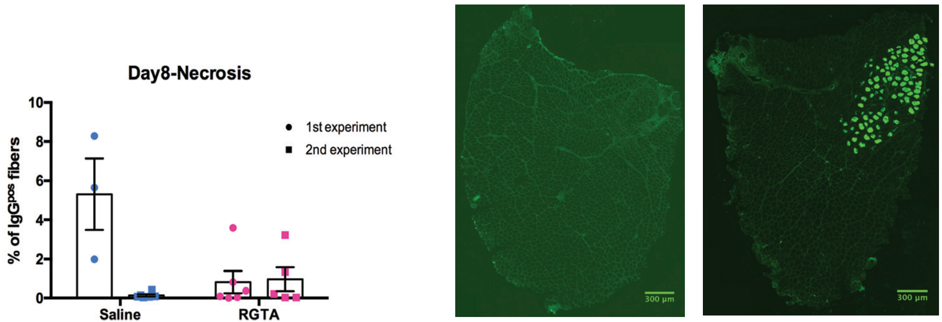

Saline - anti mouse IgG
2nd experiment

RGTA® - anti mouse IgG
2nd experiment

Figure 79. Effects of RGTA® on necrosis. TA muscles injected with saline solution (n=3 per experiment, 1 or 2 muscles per animal) or RGTA® (n=3 per experiment, 1 or 2 muscles per animal) were analyzed at 8 DPI. Necrotic myofibers were quantified as a percentage of total myofibers. Parametric two-way ANOVA was performed.

Macrophages were labeled with F4-80 antibodies. No effect of RGTA® on macrophage number could be detected (p=0.4; Figure 80) in the first experiment with a mean at 724 cells per mm^2 in control muscles versus 637 cells per mm^2 in muscles after RGTA® administration.

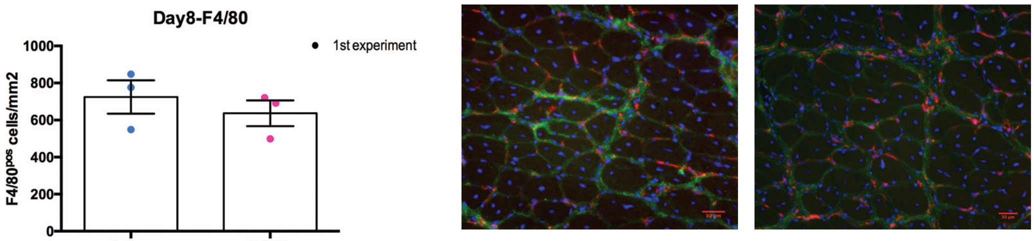

Saline F4-80-Collagen I

RGTA® F4-80-Collagen I

Figure 80. Effects of RGTA® on macrophage cells (experiment 1). TA muscles injected with saline solution (n=3 mice, 1 muscle per animal) or RGTA® (n=3 mice, 1 muscle per animal) were analyzed at 8 DPI. Number of macrophages was quantified by F4/80positive cells per mm^2. Scale bars represent 30µm. Mann-Whitney test was performed.

- No variation in satellite cell number and their proliferation

Satellite cells were identified by Pax7 immunostaining. After an injury, activated satellite cells express Ki67 while proliferating. The majority will differentiate and fuse to form new myofibers, while the rest will return to quiescence (characterized as Pax7positive Ki67negative cells). RGTA® administration did not affect the number of satellite cells with a mean of 0.27 Pax7 positive cells per fiber for RGTA® group and at 0.23 cells per fiber for the control group (Figure 81A). Similarly, the proportion of proliferative satellite cells remained unaffected with a mean at 22.98% in muscles after RGTA® treatment versus 26.77% in control condition (Figure 81B).

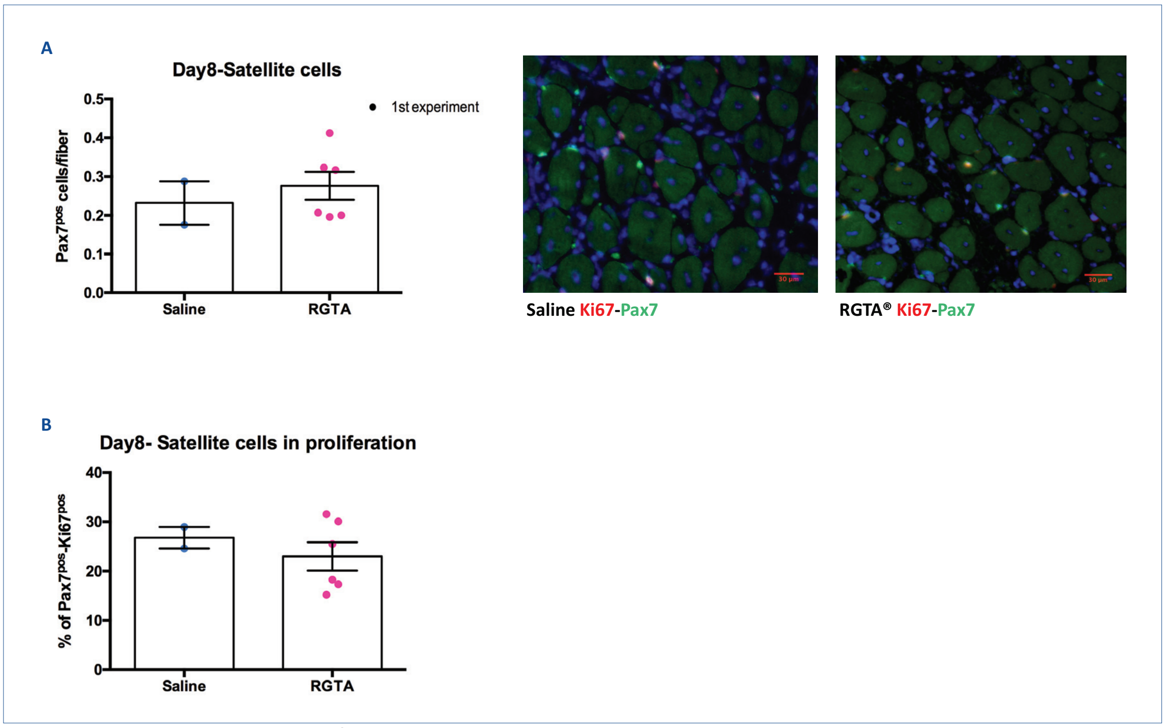

Figure 81. Effects of RGTA® on satellite cells (experiment 1). TA muscles injected with saline solution (n=2 mice, 1 muscle correctly injected per animal) or RGTA® (n=3 mice, 1 or 2 muscles per animal) were analyzed at 8 DPI. A) Number of satellite cells was quantified as pax7 positive cells per fiber. B) Proliferative satellite cells ($Ki67^{+}Pax7^{+}$) were analyzed as a percentage of total satellite cells. Scale bar represent 30µm. Mann-Whitney test was performed.

To sum up explorations at 8 DPI, relative muscle weight tended to increase after RGTA® administration, with a higher number of nuclei per fiber, more pronounced in the experiment 1 (older animals) but without modification of the number of myofibers or the mean CSA of myofibers.

The capillaries per fiber ratio was increased in RGTA® group (only in experiment 1) in favor of a more efficient muscle capillarization, associated with a reduction of lipid droplets indicating a higher quality of muscle regeneration.

The number of Fibroblastic PDGFRα positive cells tended to be lower than in control group, especially in experiment 2 (younger animals) where Collagen I content was decreased (as compared with experiment 1) but without modification by RGTA® treatment.

Macrophage and satellite cell numbers were not affected by RGTA® administration.

- R-II-3) RGTA® administration has a long-term effect on angiogenesis

We performed a histological analysis at a later time-point of regeneration, at 28 DPI (Figure 82) focusing on parameters improved at D8.

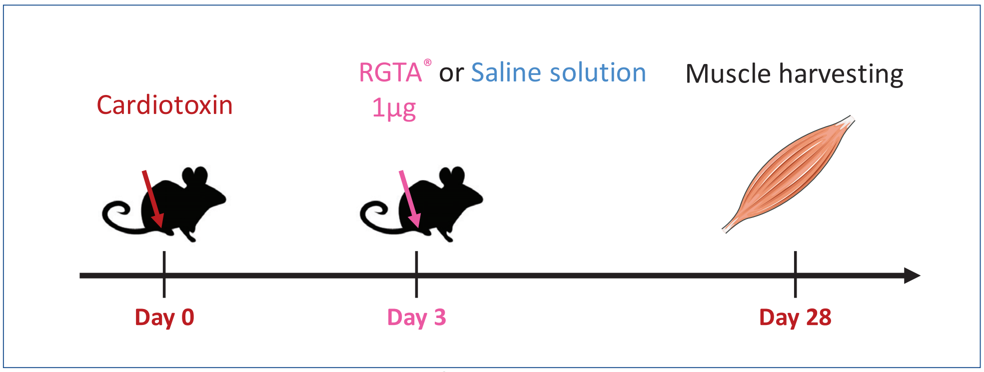

Figure 82. Protocol used to evaluate RGTA® in tardive phase of muscle regeneration. At day 0, CTX was injected in both TA muscles. Then, RGTA® (n=5) or saline solution (n=5) was injected in TA 3 DPI. Muscles were analyzed at 28 DPI.

The macroscopic observation of HE staining confirmed that muscles were correctly injected by cardiotoxin because central nuclei were observed in most muscle fibers (Figure 83A). Relative TA weights were not significantly different despite a trend towards lighter muscles in the RGTA® group (p=0.075; figure 83B) with a mean at 0.217 % of body weight versus 0.2319 % in RGTA® and control groups respectively.

In addition, the number of myofibers remained unchanged after RGTA® treatment (p=0.97; Figure 83C) with a mean 525 fibers per mm^2 in RGTA® and 523 per mm^2 in saline injected muscles. Myofiber size was unaffected (p=0.912; Figure 83D) with a mean CSA of 1375 µm^2 in RGTA® versus 1355 µm^2 in control group.

The C/F ratio remained higher in RGTA® treated muscles, compatible with long-term effect on angiogenesis (p=0.043; Figure 83E) with a mean C/F of 1.84 after RGTA® administration versus 1.51 in control group.

Conversely, no effect on lipid droplets content was observed at this late time point (p=0.63; figure 83F) with a mean total area occupied by lipid droplets at 0.084% in RGTA® versus 0.133% in control muscles.

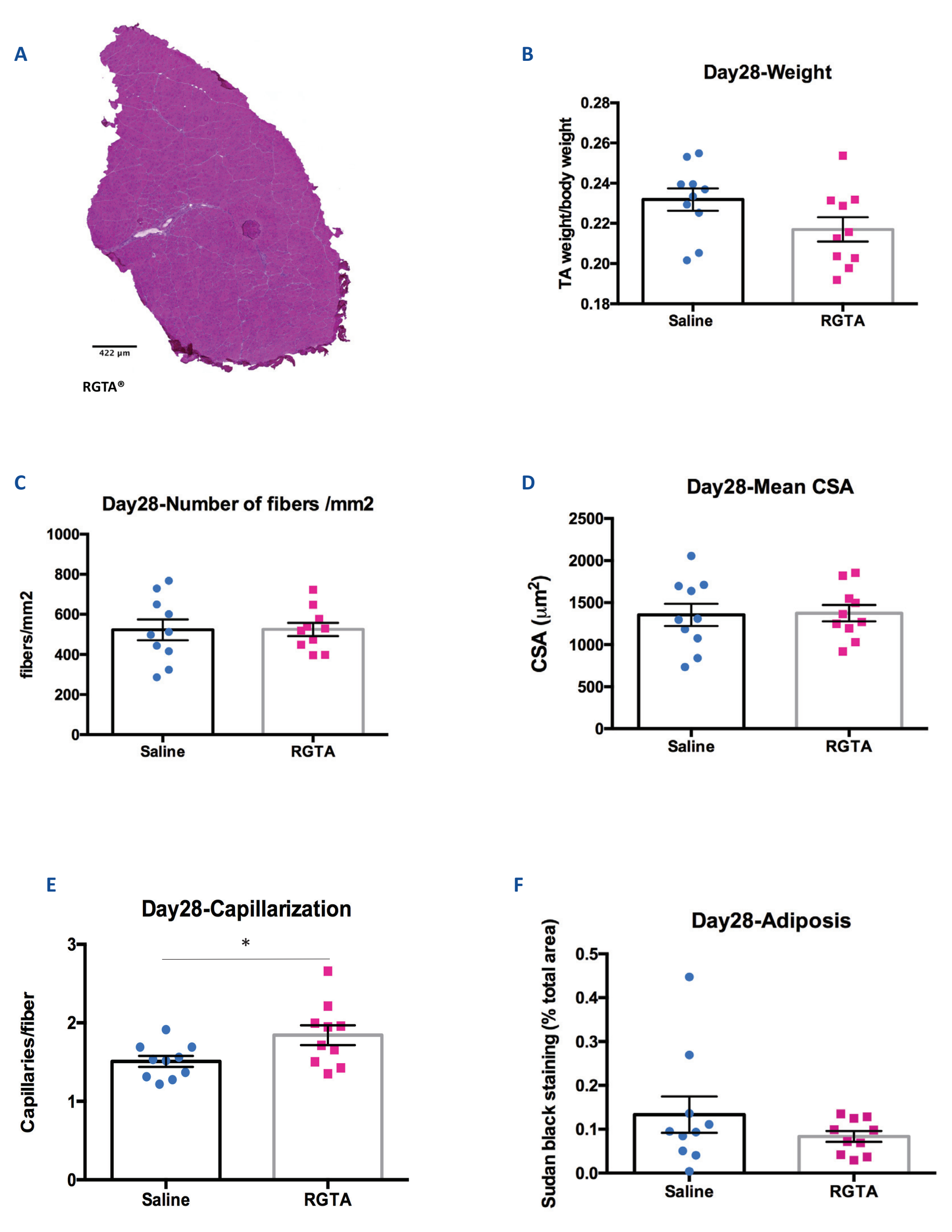

Figure 83. Effects of RGTA® on tardive phase of skeletal muscle regeneration. TA muscles injected with saline solution (n=5 mice, 2 muscles per animal) or RGTA® (n=5 mice, 1 or 2 muscles per animal) were analyzed at 28 DPI. A) Hematoxylin–eosin staining of TA muscle B) ratio of TA mass per body mass, C) Number of myofibers per mm^2 D) mean of myofibers CSA E) Capillaries per fiber ratio and F) Quantification of lipid droplets by Sudan black staining as a percentage of the total area were analyzed. Mann-Whitney test was performed.

Analyses at 28 DPI have highlighted a slight decrease in relative muscle weight after RGTA® administration, without modification of the number of myofibers or the myofiber CSA.

The capillaries per fiber ratio remained higher in RGTA® group, in favor of a long-term beneficial action on muscle capillarization without, prolonged effect on lipid droplets inside the muscle.

- R-II-4) *In vitro* explorations on the cellular effects of RGTA®

We performed *in vitro* analyses to dissect the effect of RGTA® on cells involved in muscle regeneration and particularly those where we have observed an enhancement *in vivo*.

o Myoblast proliferation is decreased by a specific dose of RGTA®

Primary mouse myoblasts (n=5 mice) were seeded at 3000 cell.cm^{-2} and RGTA® was added in the proliferation medium at 10 µg.mL^{-1} (figure 84A). Proliferation was then quantified by Ki67 immunolabelling performed at 24h of culture. Myoblast proliferation decreased significantly when cultured with GAG mimetic during 24h (p=0.031; figure 84B) with a mean of Ki67 positive cells representing 65.2% of total cells with RGTA® versus 80.2% in control conditions.

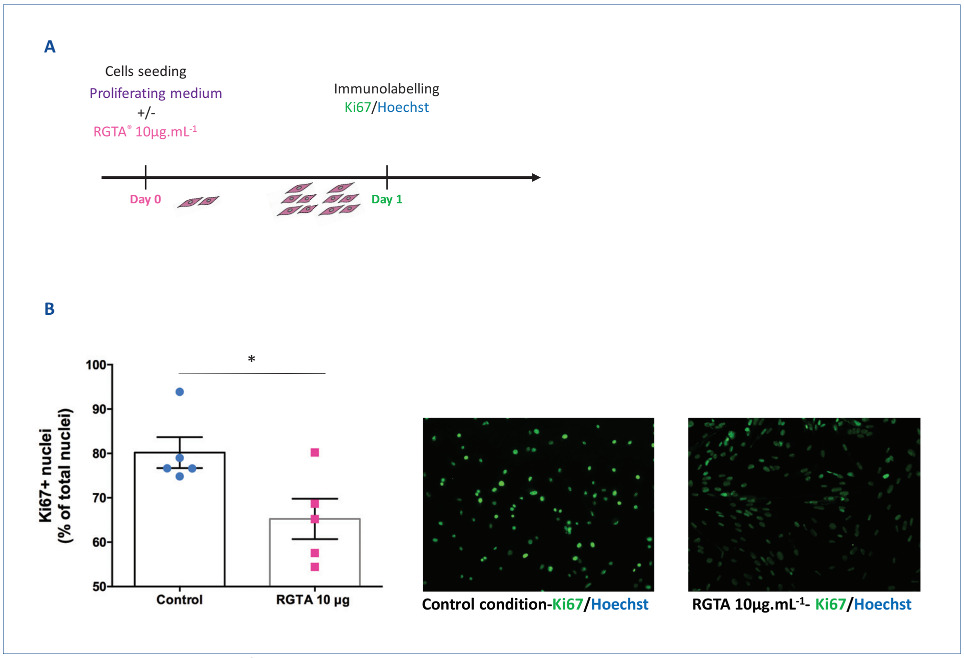

Figure 84. Effects of RGTA® on myoblast proliferation. A) Protocol used for the analysis of myoblasts proliferation by Ki67 labelling performed after 24 h of culture in proliferating medium containing or not RGTA® (n= 5 different myoblast cultures). B) Proliferation was measured as a percentage of Ki67 positive cells. Wilcoxon test was performed.

Myogenic progenitor fusion is enhanced by RGTA®

Mouse myogenic progenitors (n=3 donor mice) were used to study their differentiation/fusion in culture. Myoblasts were first seeded in proliferation medium, requisite for an efficient cell adhesion. After 6h, this medium was removed and replaced by differentiation medium with or without RGTA® component at 1, 10 and 50 $\mu g.mL^{-1}$ (Figure 85A). For all three primary cultures, we observed an acceleration of myotube formation. They contained more nuclei (Figure 85B), suggesting an increase in cell-merging as quantified by the fusion index. The effect was more heterogeneous for the 1 $\mu g.mL^{-1}$ dose (data not shown). For the 10 $\mu g.mL^{-1}$dose, mean fusion index was slightly increased, 41.53 versus 29.1 in control condition ($p=0.125$, figure 85C). Conversely, for a higher dose (i.e. 50 $\mu g.mL^{-1}$), the fusion index decreased (-8.5%) as compared with control condition.

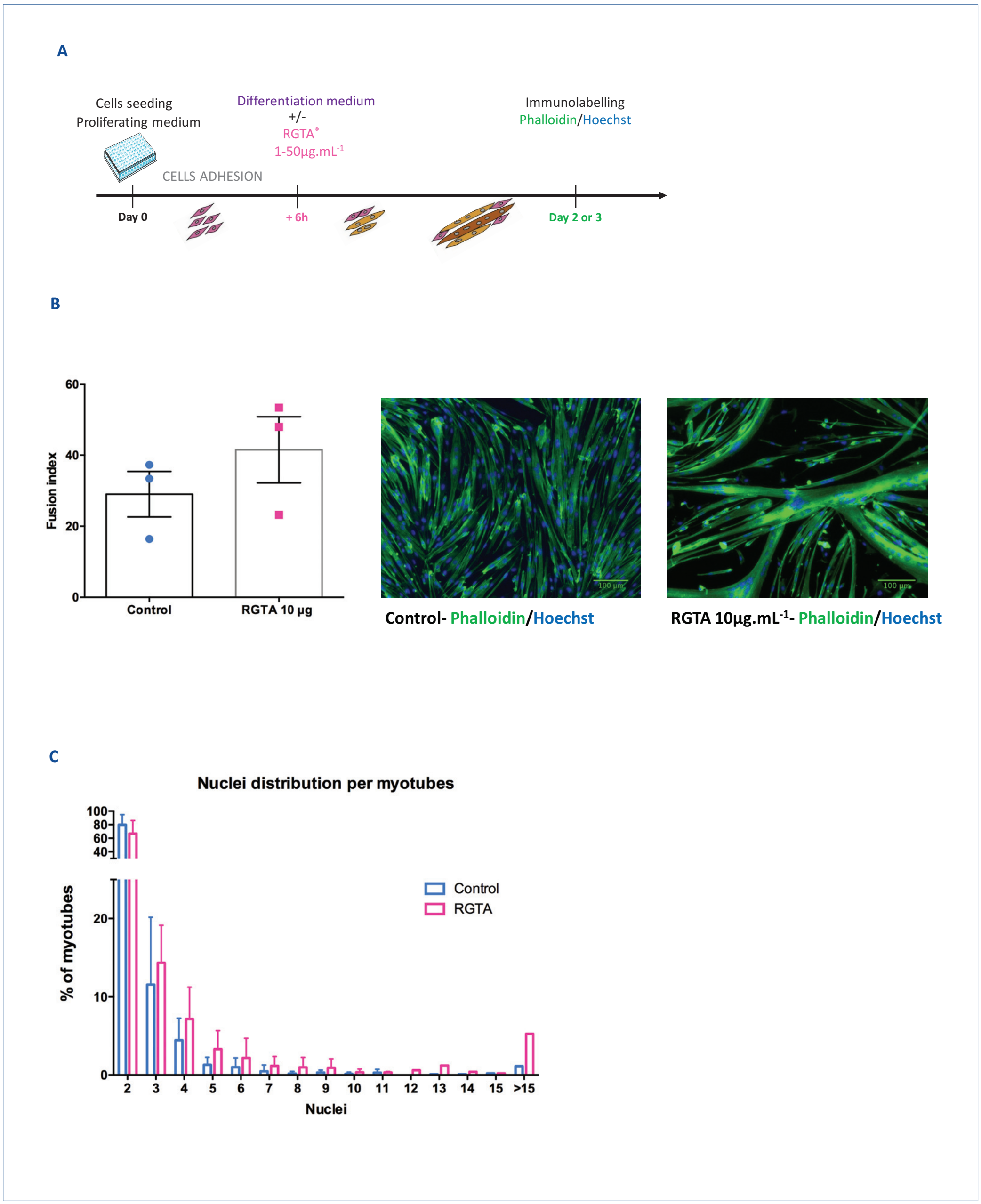

Figure 85. Effects of RGTA® on myoblast differentiation/fusion. A) Protocol used for myoblast differentiation/fusion by Phalloidin and Hoechst labelling performed after 2 or 3 days of culture in differentiation medium containing or not RGTA® (n= 3 different myoblast cultures). B) The fusion index was calculated as the number of nuclei within myotubes divided by the total number of nuclei. C) Nuclei distribution per myotube as a percentage of total cell population. Wilcoxon test was performed.

To sum up *in vitro* explorations, the presence of RGTA® in cell culture stimulated fusion of myogenic progenitors, in accordance with *in vivo* analysis. We observed a bell-shaped curve effect with a tendency to enhancement for the 10 µg.mL^{-1} dose, whereas the 50 µg.mL^{-1} dose decreased the fusion index.

This specific RGTA® dose of 10 µg.mL^{-1} has also an opposite effect on early phase of proliferation, with a significant decreased expression of Ki67 in myoblasts.

DISCUSSION

Our investigations focused on a clinical grade heparan sulfate mimetic having already yielded beneficial effects on several murine models of muscle injury (crush and ischemic lesions) where muscle injury and RGTA® injection are performed simultaneously[255,442–444,447]. Here, we studied the effect of this therapeutic with an in-situ administration at 3 DPI in a cardiotoxin injury model, a more realistic time-point for clinical use while primary care is rarely initiated immediately after a muscle injury. Our results support an accelerated myogenesis with RGTA® administration with a long-lasting effect on angiogenesis.

- Adequate RGTA® dose

RGTA® has a dose-dependent effect on tissue repair with a bell-shaped curve[422] and previous pharmacokinetic studies found a durable accumulation of the compound mainly at injured sites[446], suggesting that a single injection could be optimal. We therefore undertook a dose effect study relying on a single administration.

The dose range of RGTA® explored was chosen based on previous studies in rat hindlimb muscle regeneration (*extensor digitorum longus* and *soleus* muscles), where RGTA® was injected between 100 to 1 µg (corresponding to 500 to 5 ng per mg of muscle)[255,442,447]. In our study using a smaller rodent model, we downscaled this range to explore 0.01 up to 1µg (27 to 2.7 ng per mg per muscle) on early (8 DPI) histological parameters.

For subsequent experiments, we chose the dose of 1 µg per muscle, after observing an improvement of several parameters such as nuclei number per fiber and macroscopic aspect on HE staining (specially necrosis amount).

Administration of the tested molecule at the time of lesion induction[255,442–444,447] is not translatable to the clinical practice, therefore we have chosen an in-situ administration at 3 DPI. Timing administration is also a useful tool in dissecting the effects of broadly acting and long-lasting molecules on the complex repair process following muscle injury. Indeed, timing further allowed to eliminate a potentially purely anti-inflammatory and pro-survival effect of the molecule in this well characterized injury model.

- RGTA® in toxic model of muscle regeneration

Heparan sulfate are known to interact with CTX molecules by increasing their cell penetration[493,494]. However, we performed the RGTA® injection after the necrosis and inflammatory phases generated by CTX, avoiding interference with injury timing and intensity. Our data show an initial (at 8 DPI), slight increase in treated muscle weight, caught up by untreated muscles by 28 DPI. There was no change in the total number of myofibers or their size (no modification of CSA). However, nuclei number per myofiber is enhanced suggesting a positive effect of RGTA® on myogenic progenitors on their terminal differentiation and/or fusion.

We have analyzed other actors involved in muscle regeneration. The number of PDGFRα positive cells that are fibroblastic cells, tended to be reduced compared to control group, especially in younger animals, but without modification of Collagen I content in RGTA® group. Lipid droplets, a marker of an impaired regeneration, were decreased in RGTA®-treated muscles, in favor of an improvement in repair. Conversely, no clear change in necrosis clearance was found, despite a discrepancy between the 2 experiments.

Finally, administration of GAG mimetics also led to higher capillaries per fiber ratio, supporting a more efficient muscle capillarization, and this effect persisted at 28 DPI.

Taken together, these results are supportive of an accelerated myogenic process following RGTA® administration, yielding persistent histological benefit with a necessity to confirm their functional impact by assessment of muscle strength.

We performed our experiments on animals of various ages in experiments 1 and 2, possibly introducing some variability. To validate the results, an extra-cohort of mice is on-going (8-week old).

- RGTA® in other models of muscle regeneration

Several studies have consistently shown beneficial effects of GAGs, and particularly HS mimetics on skeletal muscle regeneration. To our knowledge, only one study used a clinical grade RGTA® in a preclinical model of muscle injury[255]. In an ischemic model of injury immediately followed by RGTA® administration, Chevalier et al, observed an improved angiogenesis and an increased number of myonuclei. Our study allows to confirm that a delayed treatment of RGTA® maintains these benefits. In contrast with previous results[255,442,447], we have not observed an increase in the size and number of myofibers. Fiber necrosis was lower in muscles treated by RGTA® but we observed a high heterogeneity between the two groups making difficult to conclude. In addition, we have not explored RGTA® action on muscle cell survival during the inflammatory phase, that could be responsible for the reduction of necrosis observed in previous studies. Although we have not explored innervation, we have performed an exhaustive analysis of the different actors involved in myogenesis. By comparing our results with the literature, the more robust effects of RGTA® were an improvement of angiogenesis and fusion of myogenic progenitors. We have also confirmed these observations on myogenic progenitors in *in vitro* experiments.

- *In vitro* analysis of RGTA® effects on myogenic cells

We have performed *in vitro* analysis in primary cultures of murine myoblasts where we observed an increase in the fusion index after RGTA® administration with a bell-shaped curve. The proliferation was inhibited by the optimal dose for differentiation/fusion. However, other studies have underscored an increase in differentiation and of proliferation[495] (maximal for dose as 1µg.mL^{-1}) with a bell-shaped dose response, by RGTA® or other type of GAG mimetics[496,497]. Interestingly, in vitro explorations have shown that RGTA® could protect VEGF from degradation[428]. Angiogenesis has also been explored: RGTA® triggers an enhancement of vessels in chicken embryo chorioallantoic membrane assay[428]. RGTA® also potentiated VEGF to induce proliferation and migration of human umbilical vein endothelial cells. Therefore using an in vitro model exploring the coupling myogenesis/angiogenesis[182] in presence of RGTA® will be informative.

- Mechanisms of action

RGTA® are clinical-grade molecules, close to heparin but devoid of anticoagulant activity[424]. These HS mimetics are composed of functional groups without toxic activity[417] and are obtained by a process respecting GMPs. RGTA® could have several intricate effects on tissue repair.

These compounds, as natural HS, hold a strong binding capacity for signaling factors providing stability and protection against enzymatic degradation[423]. Growth factors known to interact with HS include molecule such as FGF, VEGF, CXCL-12 or TGFβ. Because we have observed an increase in differentiation/fusion of myogenic progenitors using a dose inhibiting their proliferation, we can hypothesize that RGTA® act by protecting growth factors necessary for differentiation while inactivating factors involved in myogenic proliferation and/or known to decrease differentiation such as TGFβ. RGTA® likely interacts with VEGF, as improvement of angiogenesis is a recurrent effect in diverse models of tissue repair[430,432] with a higher amount of VEGF found in tissue samples after treatment[255]. This effect was confirmed by an in vivo Matrigel plug assay, leading to an increase of VEGF-induced angiogenesis[428].

In addition, other polysaccharide GAG mimetics such as malic acid[498] or fucoidan[415], improve muscle regeneration and share the capacity of linking HBGFs, emphasizing the importance of their interactions with growth factors.

RGTA® also act as an enzymatic inhibitor with a decrease in calpain activity during muscle regeneration, which was confirmed in myogenic progenitor culture[445,448]. Finally, RGTA® could facilitate natural ECM reorganization but we have only explored collagen I content at the early phase of regeneration so far, and this important aspect would require further studies.

Because RGTA® are HS mimetics, their benefit could confirm the role of HS in muscle regeneration, probably by interaction with growth factors. In addition, several RGTA® components can be used differing by their size, charges and conformation necessitating establishing which is the most optimal for a specific application, together with optimal timing and dosage.

Perspectives

an optimized biomaterial for VML injury

Numerous teams have investigated the promising use of decellularized scaffolds for treating VML injuries. However, these current data have highlighted that ECM biomaterials alone do not allow full muscle regeneration and especially they are not sufficient to efficiently attract progenitors that would rebuild the tissue. As a result, a fibrotic tissue often develops, remodeling the scaffold while a limited number of muscle fibers are found in periphery. Therefore, it is now obvious that important optimization is needed in ECM-based scaffold strategies. Teams have developed cumulated approaches with cells owning myogenic potential incorporated inside scaffolds[499]. But because skeletal muscle owns high regenerative capacities, we focused on an optimized biomaterial that could induce endogenous cell migration avoiding an additional complex cell-based therapy.

Some key facts should be underlined in ECM-biomaterial approaches. First, muscle ECM scaffolds have been investigated in preclinical studies in optimal conditions since muscle injury and implantation were always concomitant. Therefore, the activation of muscle progenitors or endothelial cells and the recruitment of circulating monocytes at the injury site are optimal. However, in a clinical perspective, such conditions are not conceivable since implantation can be performed only months after the initial injury, occurring in a fibrotic environment. Second the clinical interventions were performed with non-muscle ECM from animal models, therefore the 3D structure was rarely conserved or characterized.

Currently, biological activity and mechanical properties of decellularized biomaterials are still under exploration, necessitating a better characterization of its composition and microarchitecture to ameliorate their applications in tissue repair. However, some crucial points have emerged that we have tried to maintain using our decellularization protocol. Indeed, we focused on an efficient removal of major immunogenic cell components and the conservation of the three-dimensional structure, which could be a key point for efficient de novo muscle fiber creation. But even if the 3D structure is essential to improve myogenic progenitor migration, it seems insufficient to obtain a complete muscle regeneration in VML injury models[403]. So, we propose that major improvements in muscle ECM scaffolds are necessary and could be performed by enriching the ECM-based biomaterials with key molecules.

Hybrid biomaterials are an attractive strategy since they combine synthetic and natural biomaterials or yield an enrichment of trophic molecules such as GAG and/or growth factors. Despite our investigations, we have not found effective protocol maintaining both endogenous GAGs and microarchitecture of the scaffolds. Yet, our results together with previous reports show that providing GAG mimetic during muscle regeneration improves myogenesis and angiogenesis. Therefore, enriching decellularized scaffolds with GAG mimetics could be a very interesting option to improve their trophic effects on muscle repair. Heparin, the oldest anticoagulant clinically used, is a naturally highly sulfated GAG[500], chemically close to HS and their mimetics such as RGTA®. It has been widely used in combination with various biomaterials in human, providing useful clinical and pharmacological data. Heparin-based biomaterials are found in devices such as hemodialysis catheters or coronary stents to avoid thrombus formation[501]. Therefore heparin was added in scaffold surface, sometimes conjugated with chemokines such as CXCL-12, leading to an *in situ* endothelialization by progenitor mobilization[502]. Even decellularized tissues can be thrombogenic leading to graft failure[503], therefore some aortic valve were coated with heparin to improve their hemocompatibility and self-endothelialization[504]. Since heparin is a HS with several negative charges it can be coupled by electrostatic interaction or covalent liaison such as Michael addition[505]. Growth factors activity is known to be dependent on their spatial distribution. Therefore ECM scaffolds can be a platform for their delivery and could be conjugated with HS leading to a more prolonged release[475]. For the same reason than heparin, GAG mimetics such as fucoidan[506] or RGTA®[507] were physically adsorbed on some prostheses in combination with growth factors. The advantage to replace heparin is to decrease a potential hemorrhagic effect and heparin-induced thrombocytopenia. CXCL-12 is a chemokine particularly studied in angiogenesis[508] and inflammation[509], also driving the migration of other cells including myoblasts[510]. In decellularized aortic valve implantation, heparin coating enriched with CXCL-12 led to and efficient endothelial cell colonization of the scaffold. Therefore, to improve the recruitment of the cells necessary for an efficient muscle regeneration, we propose that it could be useful to couple the ECM-scaffold with chemoattractant such as CXCL-12 and RGTA®, which already improve myogenesis and angiogenesis.

Finally, VML lesion induces a fibrotic environment in remaining skeletal muscle that can progressively lead to ECM accumulation and stiffening, creating an autonomous feedback loop. Therefore, the implantation of ECM scaffold in such an environment leads to non-optimal response as illustrated in the clinical cohort. Because ECM modifications of remaining tissue can persist even after debridement, it could be an obstacle to a future biomaterial implantation. Currently, no preclinical implantation of muscle-ECM was performed in a scar muscle tissue, i.e. weeks after the initial VML. In addition, how and by which mechanisms the fibrotic environment could impair the biomaterial efficiency is unknown. This is an important point that needs to be investigated because transplantation in human cannot be performed before all injuries (bone, skin) are healed and stabilized. Therefore, further optimization of the biomaterials is necessary, as well as additional treatments, probably targeting the fibrotic elements[511].

References

1. Bolsterlee, B. *et al.* Three-dimensional architecture of the whole human soleus muscle in vivo. *PeerJ* **6**, e4610 (2018).

2. Ralston, E. *et al.* Blood vessels and desmin control the positioning of nuclei in skeletal muscle fibers. *J. Cell. Physiol.* **209**, 874–882 (2006).

3. Zammit, P. S. Function of the myogenic regulatory factors Myf5, MyoD, Myogenin and MRF4 in skeletal muscle, satellite cells and regenerative myogenesis. *Semin. Cell Dev. Biol.* **72**, 19–32 (2017).

4. Frantz, C., Stewart, K. M. & Weaver, V. M. The extracellular matrix at a glance. *J Cell Sci* **123**, 4195–4200 (2010).

5. Hynes, R. O. The extracellular matrix: not just pretty fibrils. *Science* **326**, 1216–1219 (2009).

6. Hynes, R. O. & Naba, A. Overview of the matrisome--an inventory of extracellular matrix constituents and functions. *Cold Spring Harb. Perspect. Biol.* **4**, a004903 (2012).

7. Huang, G. *et al.* Functional and Biomimetic Materials for Engineering of the Three-Dimensional Cell Microenvironment. *Chem. Rev.* **117**, 12764–12850 (2017).

8. Engler, A. J., Sen, S., Sweeney, H. L. & Discher, D. E. Matrix elasticity directs stem cell lineage specification. *Cell* **126**, 677–689 (2006).

9. Gilbert, P. M. *et al.* Substrate elasticity regulates skeletal muscle stem cell self-renewal in culture. *Science* **329**, 1078–1081 (2010).

10. Walters, N. J. & Gentleman, E. Evolving insights in cell-matrix interactions: elucidating how non-soluble properties of the extracellular niche direct stem cell fate. *Acta Biomater.* **11**, 3–16 (2015).

11. Kirkpatrick, C. A. & Selleck, S. B. Heparan sulfate proteoglycans at a glance. *J. Cell Sci.* **120**, 1829–1832 (2007).

12. Larsen, M., Artym, V. V., Green, J. A. & Yamada, K. M. The matrix reorganized: extracellular matrix remodeling and integrin signaling. *Curr. Opin. Cell Biol.* **18**, 463–471 (2006).

13. Streuli, C. Extracellular matrix remodelling and cellular differentiation. *Curr. Opin. Cell Biol.* **11**, 634–640 (1999).

14. Whitelock, J. M., Melrose, J. & Iozzo, R. V. Diverse cell signaling events modulated by perlecan. *Biochemistry* **47**, 11174–11183 (2008).

15. Ricard-Blum, S. & Salza, R. Matricryptins and matrikines: biologically active fragments of the extracellular matrix. *Exp. Dermatol.* **23**, 457–463 (2014).

16. Daley, W. P., Peters, S. B. & Larsen, M. Extracellular matrix dynamics in development and regenerative medicine. *J. Cell Sci.* **121**, 255–264 (2008).

17. Rozario, T. & DeSimone, D. W. The extracellular matrix in development and morphogenesis: a dynamic view. *Dev. Biol.* **341**, 126–140 (2010).

18. Mann, C. J. *et al.* Aberrant repair and fibrosis development in skeletal muscle. *Skelet. Muscle* **1**, 21 (2011).

19. Gattazzo, F., Urciuolo, A. & Bonaldo, P. Extracellular matrix: a dynamic microenvironment for stem cell niche. *Biochim. Biophys. Acta* **1840**, 2506–2519 (2014).

20. Bolean, M. *et al.* Biophysical aspects of biomineralization. *Biophys. Rev.* **9**, 747–760 (2017).

21. Massoudi, D., Malecaze, F. & Galiacy, S. D. Collagens and proteoglycans of the

cornea: importance in transparency and visual disorders. *Cell Tissue Res.* **363**, 337–349 (2016).

22. Purslow, P. P. The structure and functional significance of variations in the connective tissue within muscle. *Comp. Biochem. Physiol. A. Mol. Integr. Physiol.* **133**, 947–966 (2002).

23. Walls, E. W. *The Structure and Function of Muscle V1: Structure*. **Vol.6**, pp.**21–61**, (Academic Press, New York and London, 1960).

24. Gillies, A. R. & Lieber, R. L. Structure and function of the skeletal muscle extracellular matrix. *Muscle Nerve* **44**, 318–331 (2011).

25. Swatland, H. J. Morphology and Development of Endomysial Connective Tissue in Porcine and Bovine Muscle1. *J. Anim. Sci.* **41**, 78–86 (1975).

26. Rowe, R. W. Collagen fibrils of the perimysium and endomysium of sheep semitendinosus muscle. *Meat Sci.* **2**, 275–280 (1978).

27. Rowe, R. W. Morphology of perimysial and endomysial connective tissue in skeletal muscle. *Tissue Cell* **13**, 681–690 (1981).

28. Rowe, R. W. Electron Microscopy of bovine muscle, I-The native state of post rigor sarcolemma and endomysium. *Meat Sci.* **26**, 271–279 (1989).

29. Tidball, J. G. Force transmission across muscle cell membranes. *J. Biomech.* **24 Suppl 1**, 43–52 (1991).

30. Järvinen, T. A. H., Józsa, L., Kannus, P., Järvinen, T. L. N. & Järvinen, M. Organization and distribution of intramuscular connective tissue in normal and immobilized skeletal muscles. An immunohistochemical, polarization and scanning electron microscopic study. *J. Muscle Res. Cell Motil.* **23**, 245–254 (2002).

31. Purslow, P. P. & Trotter, J. A. The morphology and mechanical properties of endomysium in series-fibred muscles: variations with muscle length. *J. Muscle Res. Cell Motil.* **15**, 299–308 (1994).

32. Passerieux, E. *et al.* Structural organization of the perimysium in bovine skeletal muscle: Junctional plates and associated intracellular subdomains. *J. Struct. Biol.* **154**, 206–216 (2006).

33. Gillies, A. R. *et al.* High resolution three-dimensional reconstruction of fibrotic skeletal muscle extracellular matrix. *J. Physiol.* **595**, 1159–1171 (2017).

34. Knudsen, A. B. *et al.* The human myotendinous junction: an ultrastructural and 3D analysis study. *Scand. J. Med. Sci. Sports* **25**, e116-123 (2015).

35. Ricard-Blum, S., Baffet, G. & Théret, N. Molecular and tissue alterations of collagens in fibrosis. *Matrix Biol. J. Int. Soc. Matrix Biol.* **68–69**, 122–149 (2018).

36. Rouède, D. *et al.* Determination of extracellular matrix collagen fibril architectures and pathological remodeling by polarization dependent second harmonic microscopy. *Sci. Rep.* **7**, 12197 (2017).

37. Mohammadkhah, M., Simms, C. K. & Murphy, P. Visualisation of Collagen in fixed skeletal muscle tissue using fluorescently tagged Collagen binding protein CNA35. *J. Mech. Behav. Biomed. Mater.* **66**, 37–44 (2017).

38. Mohammadkhah, M., Murphy, P. & Simms, C. K. Collagen fibril organization in chicken and porcine skeletal muscle perimysium under applied tension and compression. *J. Mech. Behav. Biomed. Mater.* **77**, 734–744 (2018).

39. Huxley, A. F. Cross-bridge action: present views, prospects, and unknowns. *J. Biomech.* **33**, 1189–1195 (2000).

40. MacIntosh, B. R. Recent developments in understanding the length dependence of contractile response of skeletal muscle. *Eur. J. Appl. Physiol.* **117**, 1059–1071 (2017).

41. Purslow, P. P. Strain-induced reorientation of an intramuscular connective tissue network: implications for passive muscle elasticity. *J. Biomech.* **22**, 21–31 (1989).

42. Brown, S. H. M., Carr, J. A., Ward, S. R. & Lieber, R. L. Passive mechanical properties of rat abdominal wall muscles suggest an important role of the extracellular connective tissue matrix. *J. Orthop. Res. Off. Publ. Orthop. Res. Soc.* **30**, 1321–1326 (2012).

43. Huijing, P. A. Muscle as a collagen fiber reinforced composite: a review of force transmission in muscle and whole limb. *J. Biomech.* **32**, 329–345 (1999).

44. Lieber, R. L., Roberts, T. J., Blemker, S. S., Lee, S. S. M. & Herzog, W. Skeletal muscle mechanics, energetics and plasticity. *J. Neuroengineering Rehabil.* **14**, 108 (2017).

45. Battista, N. A., Strickland, W. C. & Miller, L. A. IB2d: a Python and MATLAB implementation of the immersed boundary method. *Bioinspir. Biomim.* **12**, 036003 (2017).

46. Jaka, O., Casas-Fraile, L., López de Munain, A. & Sáenz, A. Costamere proteins and their involvement in myopathic processes. *Expert Rev. Mol. Med.* **17**, e12 (2015).

47. Grounds, M. D., Sorokin, L. & White, J. Strength at the extracellular matrix-muscle interface. *Scand. J. Med. Sci. Sports* **15**, 381–391 (2005).

48. Carmignac, V. & Durbeej, M. Cell-matrix interactions in muscle disease. *J. Pathol.* **226**, 200–218 (2012).

49. Azizi, E., Deslauriers, A. R., Holt, N. C. & Eaton, C. E. Resistance to radial expansion limits muscle strain and work. *Biomech. Model. Mechanobiol.* **16**, 1633–1643 (2017).

50. Purslow, P. P. The structure and functional significance of variations in the connective tissue within muscle. *Comp. Biochem. Physiol. A. Mol. Integr. Physiol.* **133**, 947–966 (2002).

51. Thorsteinsdóttir, S., Deries, M., Cachaço, A. S. & Bajanca, F. The extracellular matrix dimension of skeletal muscle development. *Dev. Biol.* **354**, 191–207 (2011).

52. Listrat, A., Picard, B. & Geay, Y. Age-related changes and location of type I, III, IV, V and VI collagens during development of four foetal skeletal muscles of double-muscled and normal bovine animals. *Tissue Cell* **31**, 17–27 (1999).

53. Thomas, K., Engler, A. J. & Meyer, G. A. Extracellular matrix regulation in the muscle satellite cell niche. *Connect. Tissue Res.* **56**, 1–8 (2015).

54. Shoulders, M. D. & Raines, R. T. Collagen structure and stability. *Annu. Rev. Biochem.* **78**, 929–958 (2009).

55. Ricard-Blum, S. The collagen family. *Cold Spring Harb. Perspect. Biol.* **3**, a004978 (2011).

56. Light, N., Champion, A. E., Voyle, C. & Bailey, A. J. The rôle of epimysial, perimysial and endomysial collagen in determining texture in six bovine muscles. *Meat Sci.* **13**, 137–149 (1985).

57. Kurose, T., Asai, Y., Mori, E., Daitoku, D. & Kawamata, S. Distribution and change of collagen types I and III and elastin in developing leg muscle in rat. *Hiroshima J. Med. Sci.* **55**, 85–91 (2006).

58. Bönnemann, C. G. The collagen VI-related myopathies: muscle meets its matrix. *Nat. Rev. Neurol.* **7**, 379–390 (2011).

59. Iozzo, R. V. & Schaefer, L. Proteoglycan form and function: A comprehensive nomenclature of proteoglycans. *Matrix Biol. J. Int. Soc. Matrix Biol.* **42**, 11–55 (2015).

60. Karamanos, N. K. *et al.* Proteoglycan Chemical Diversity Drives Multifunctional Cell Regulation and Therapeutics. *Chem. Rev.* (2018). doi:10.1021/acs.chemrev.8b00354

61. Poulain, F. E. & Yost, H. J. Heparan sulfate proteoglycans: a sugar code for vertebrate development? *Dev. Camb. Engl.* **142**, 3456–3467 (2015).

62. Tavianatou, A. G. *et al.* Hyaluronan: molecular size-dependent signaling and

biological functions in inflammation and cancer. *FEBS J.* (2019). doi:10.1111/febs.14777

63. Silva, C., Novoa-Carballal, R., Reis, R. L. & Pashkuleva, I. Following the enzymatic digestion of chondroitin sulfate by a simple GPC analysis. *Anal. Chim. Acta* **885**, 207–213 (2015).

64. Meneghetti, M. C. Z. *et al.* Heparan sulfate and heparin interactions with proteins. *J. R. Soc. Interface* **12**, 0589 (2015).

65. Ghadiali, R. S., Guimond, S. E., Turnbull, J. E. & Pisconti, A. Dynamic changes in heparan sulfate during muscle differentiation and ageing regulate myoblast cell fate and FGF2 signalling. *Matrix Biol. J. Int. Soc. Matrix Biol.* **59**, 54–68 (2017).

66. van Wijk, X. M. R. & van Kuppevelt, T. H. Heparan sulfate in angiogenesis: a target for therapy. *Angiogenesis* **17**, 443–462 (2014).

67. Sugaya, N., Habuchi, H., Nagai, N., Ashikari-Hada, S. & Kimata, K. 6-O-sulfation of heparan sulfate differentially regulates various fibroblast growth factor-dependent signalings in culture. *J. Biol. Chem.* **283**, 10366–10376 (2008).

68. Brzoska, E. *et al.* Sdf-1 (CXCL12) improves skeletal muscle regeneration via the mobilisation of Cxcr4 and CD34 expressing cells. *Biol. Cell* **104**, 722–737 (2012).

69. Soares, M. A. *et al.* Heparan Sulfate Proteoglycans May Promote or Inhibit Cancer Progression by Interacting with Integrins and Affecting Cell Migration. *BioMed Res. Int.* **2015**, 453801 (2015).

70. Brandan, E. & Gutierrez, J. Role of skeletal muscle proteoglycans during myogenesis. *Matrix Biol. J. Int. Soc. Matrix Biol.* **32**, 289–297 (2013).

71. Durbeej, M. Laminins. *Cell Tissue Res.* **339**, 259–268 (2010).

72. Holmberg, J. & Durbeej, M. Laminin-211 in skeletal muscle function. *Cell Adhes. Migr.* **7**, 111–121 (2013).

73. Carmignac, V. & Durbeej, M. Cell-matrix interactions in muscle disease. *J. Pathol.* **226**, 200–218 (2012).

74. Aumailley, M. *et al.* A simplified laminin nomenclature. *Matrix Biol. J. Int. Soc. Matrix Biol.* **24**, 326–332 (2005).

75. Aumailley, M. The laminin family. *Cell Adhes. Migr.* **7**, 48–55 (2013).

76. Sabatelli, P. *et al.* Collagen VI deficiency affects the organization of fibronectin in the extracellular matrix of cultured fibroblasts. *Matrix Biol. J. Int. Soc. Matrix Biol.* **20**, 475–486 (2001).

77. Bradshaw, M. J. & Smith, M. L. Multiscale relationships between fibronectin structure and functional properties. *Acta Biomater.* **10**, 1524–1531 (2014).

78. Li, B., Moshfegh, C., Lin, Z., Albuschies, J. & Vogel, V. Mesenchymal stem cells exploit extracellular matrix as mechanotransducer. *Sci. Rep.* **3**, 2425 (2013).

79. Gee, E. P. S., Yüksel, D., Stultz, C. M. & Ingber, D. E. SLLISWD sequence in the 10FNIII domain initiates fibronectin fibrillogenesis. *J. Biol. Chem.* **288**, 21329–21340 (2013).

80. Naba, A. *et al.* The matrisome: in silico definition and in vivo characterization by proteomics of normal and tumor extracellular matrices. *Mol. Cell. Proteomics MCP* **11**, M111.014647 (2012).

81. Barrett, A. S. *et al.* Hydroxylamine Chemical Digestion for Insoluble Extracellular Matrix Characterization. *J. Proteome Res.* **16**, 4177–4184 (2017).

82. Krasny, L. *et al.* Comparative proteomic assessment of matrisome enrichment methodologies. *Biochem. J.* **473**, 3979–3995 (2016).

83. Li, Q. *et al.* Proteomic analysis of naturally-sourced biological scaffolds. *Biomaterials* **75**, 37–46 (2016).

84. Tainaka, K. *et al.* Whole-body imaging with single-cell resolution by tissue decolorization. *Cell* **159**, 911–924 (2014).

85. Verma, M., Murkonda, B. S., Asakura, Y. & Asakura, A. Skeletal Muscle Tissue Clearing for LacZ and Fluorescent Reporters, and Immunofluorescence Staining. *Methods Mol. Biol. Clifton NJ* **1460**, 129–140 (2016).

86. Kutchuk, L. *et al.* Muscle composition is regulated by a Lox-TGFβ feedback loop. *Dev. Camb. Engl.* **142**, 983–993 (2015).

87. Listrat, A. *et al.* Age-related changes and location of types I, III, XII and XIV collagen during development of skeletal muscles from genetically different animals. *Histochem. J.* **32**, 349–356 (2000).

88. Wessner, B., Liebensteiner, M., Nachbauer, W. & Csapo, R. Age-specific response of skeletal muscle extracellular matrix to acute resistance exercise: A pilot study. *Eur. J. Sport Sci.* 1–11 (2018). doi:10.1080/17461391.2018.1526974

89. DeQuach, J. A. *et al.* Simple and high yielding method for preparing tissue specific extracellular matrix coatings for cell culture. *PloS One* **5**, e13039 (2010).

90. Bönnemann, C. G. *et al.* A mutation in the alpha 3 chain of type IX collagen causes autosomal dominant multiple epiphyseal dysplasia with mild myopathy. *Proc. Natl. Acad. Sci. U. S. A.* **97**, 1212–1217 (2000).

91. Iyama, K. *et al.* Differential expression of two exons of the alpha1(XI) collagen gene (Col11a1) in the mouse embryo. *Matrix Biol. J. Int. Soc. Matrix Biol.* **20**, 53–61 (2001).

92. Lui, V. C., Kong, R. Y., Nicholls, J., Cheung, A. N. & Cheah, K. S. The mRNAs for the three chains of human collagen type XI are widely distributed but not necessarily co-expressed: implications for homotrimeric, heterotrimeric and heterotypic collagen molecules. *Biochem. J.* **311 (Pt 2)**, 511–516 (1995).

93. Imamura, Y., Scott, I. C. & Greenspan, D. S. The Pro-α3(V) Collagen Chain complete primary structure, expression domains in adult and developing tissues, and comparison to the structures and expression domains of the other types v and xi procollagen chains. *J. Biol. Chem.* **275**, 8749–8759 (2000).

94. Chiquet, M., Birk, D. E., Bönnemann, C. G. & Koch, M. Collagen XII: Protecting bone and muscle integrity by organizing collagen fibrils. *Int. J. Biochem. Cell Biol.* **53**, 51–54 (2014).

95. Kvist, A. P. *et al.* Lack of cytosolic and transmembrane domains of type XIII collagen results in progressive myopathy. *Am. J. Pathol.* **159**, 1581–1592 (2001).

96. Myers, J. C. *et al.* Biochemical and immunohistochemical characterization of human type XIX defines a novel class of basement membrane zone collagens. *Am. J. Pathol.* **151**, 1729–1740 (1997).

97. Koch, M. *et al.* Expression of type XXIII collagen mRNA and protein. *J. Biol. Chem.* **281**, 21546–21557 (2006).

98. Lukjanenko, L. *et al.* Loss of fibronectin from the aged stem cell niche affects the regenerative capacity of skeletal muscle in mice. *Nat. Med.* **22**, 897–905 (2016).

99. Whitelock, J. M., Melrose, J. & Iozzo, R. V. Diverse cell signaling events modulated by perlecan. *Biochemistry* **47**, 11174–11183 (2008).

100. Cifuentes-Diaz, C. *et al.* Regulated expression of the proteoglycan SPOCK in the neuromuscular system. *Mech. Dev.* **94**, 277–282 (2000).

101. Zanotti, S. *et al.* Decorin and biglycan expression is differentially altered in several muscular dystrophies. *Brain J. Neurol.* **128**, 2546–2555 (2005).

102. Henry, S. P. *et al.* Expression Pattern and Gene Characterization of asporin a newly

discovered member of the leucine-rich repeat protein family. *J. Biol. Chem.* **276**, 12212–12221 (2001).

103. Chan, C. Y. X. *et al.* Identification of differentially regulated secretome components during skeletal myogenesis. *Mol. Cell. Proteomics MCP* **10**, M110.004804 (2011).

104. Freire, P. P. *et al.* Osteoglycin inhibition by microRNA miR-155 impairs myogenesis. *PloS One* **12**, e0188464 (2017).

105. Tanaka, K. *et al.* Role of Osteoglycin in the Linkage between Muscle and Bone. *J. Biol. Chem.* **287**, 11616–11628 (2012).

106. Hunt, L. C. *et al.* Hyaluronan synthesis and myogenesis: a requirement for hyaluronan synthesis during myogenic differentiation independent of pericellular matrix formation. *J. Biol. Chem.* **288**, 13006–13021 (2013).

107. Han, R. *et al.* Basal lamina strengthens cell membrane integrity via the laminin G domain-binding motif of α-dystroglycan. *Proc. Natl. Acad. Sci.* **106**, 12573–12579 (2009).

108. Rogers, R. S. & Nishimune, H. The role of laminins in the organization and function of neuromuscular junctions. *Matrix Biol. J. Int. Soc. Matrix Biol.* **57–58**, 86–105 (2017).

109. Bentzinger, C. F. *et al.* Fibronectin regulates Wnt7a signaling and satellite cell expansion. *Cell Stem Cell* **12**, 75–87 (2013).

110. Roman, W., Martins, J. P. & Gomes, E. R. Local Arrangement of Fibronectin by Myofibroblasts Governs Peripheral Nuclear Positioning in Muscle Cells. *Dev. Cell* (2018). doi:10.1016/j.devcel.2018.05.031

111. Fox, M. A., Ho, M. S. P., Smyth, N. & Sanes, J. R. A synaptic nidogen: developmental regulation and role of nidogen-2 at the neuromuscular junction. *Neural Develop.* **3**, 24 (2008).

112. Korpos, É., Deák, F. & Kiss, I. Matrilin-2, an extracellular adaptor protein, is needed for the regeneration of muscle, nerve and other tissues. *Neural Regen. Res.* **10**, 866–869 (2015).

113. Piecha, D. *et al.* Matrilin-2 interacts with itself and with other extracellular matrix proteins. *Biochem. J.* **367**, 715–721 (2002).

114. Järvinen, T. A. H. *et al.* Mechanical loading regulates the expression of tenascin-C in the myotendinous junction and tendon but does not induce de novo synthesis in the skeletal muscle. *J. Cell Sci.* **116**, 857–866 (2003).

115. Dubost, A., Micol, D., Lethias, C. & Listrat, A. New insight of some extracellular matrix molecules in beef muscles. Relationships with sensory qualities. *Anim. Int. J. Anim. Biosci.* **10**, 821–828 (2016).

116. Frolova, E. G. *et al.* Control of organization and function of muscle and tendon by thrombospondin-4. *Matrix Biol. J. Int. Soc. Matrix Biol.* **37**, 35–48 (2014).

117. Vanhoutte, D. *et al.* Thrombospondin expression in myofibers stabilizes muscle membranes. *eLife* **5**, (2016).

118. Ozdemir, C. *et al.* Periostin is temporally expressed as an extracellular matrix component in skeletal muscle regeneration and differentiation. *Gene* **553**, 130–139 (2014).

119. Muriel, J. M. Fibulin-1C and Fibulin-1D splice variants have distinct functions and assemble in a hemicentin-dependent manner. *Development* **132**, 4223–4234 (2005).

120. Kannus, P. *et al.* Location and distribution of non-collagenous matrix proteins in musculoskeletal tissues of rat. *Histochem. J.* **30**, 799–810 (1998).

121. Burchett, M. E., Ling, I.-F. & Estus, S. FBN1 isoform expression varies in a tissue and development-specific fashion. *Biochem. Biophys. Res. Commun.* **411**, 323–328 (2011).

122. Saharinen, J., Hyytiäinen, M., Taipale, J. & Keski-Oja, J. Latent transforming growth

factor-beta binding proteins (LTBPs)--structural extracellular matrix proteins for targeting TGF-beta action. *Cytokine Growth Factor Rev.* **10**, 99–117 (1999).
123. Okamoto, O. & Fujiwara, S. Dermatopontin, a novel player in the biology of the extracellular matrix. *Connect. Tissue Res.* **47**, 177–189 (2006).
124. Forbes, E. G., Cronshaw, A. D., MacBeath, J. R. E. & Hulmes, D. J. S. Tyrosine-rich acidic matrix protein (TRAMP) is a tyrosine-sulphated and widely distributed protein of the extracellular matrix. *FEBS Lett.* **351**, 433–436 (1994).
125. Vannahme, C., Gösling, S., Paulsson, M., Maurer, P. & Hartmann, U. Characterization of SMOC-2, a modular extracellular calcium-binding protein. *Biochem. J.* **373**, 805–814 (2003).
126. Uaesoontrachoon, K. *et al.* Osteopontin and skeletal muscle myoblasts: Association with muscle regeneration and regulation of myoblast function in vitro. *Int. J. Biochem. Cell Biol.* **40**, 2303–2314 (2008).
127. Xiao, F. *et al.* Increased osteopontin in muscle and serum from patients with idiopathic inflammatory myopathies. *Clin. Exp. Rheumatol.* **33**, 399–404 (2015).
128. Demonbreun, A. R. *et al.* An actin-dependent annexin complex mediates plasma membrane repair in muscle. *J. Cell Biol.* **213**, 705–718 (2016).
129. Mis, K. *et al.* In Vitro Innervation as an Experimental Model to Study the Expression and Functions of Acetylcholinesterase and Agrin in Human Skeletal Muscle. *Mol. Basel Switz.* **22**, (2017).
130. Mofarrahi, M. *et al.* Angiopoietin-1 enhances skeletal muscle regeneration in mice. *Am. J. Physiol. Regul. Integr. Comp. Physiol.* **308**, R576-589 (2015).
131. Mofarrahi, M. & Hussain, S. N. A. Expression and functional roles of angiopoietin-2 in skeletal muscles. *PloS One* **6**, e22882 (2011).
132. Lee, S.-J. *et al.* Regulation of muscle mass by follistatin and activins. *Mol. Endocrinol. Baltim. Md* **24**, 1998–2008 (2010).
133. Hiroki, E. *et al.* A comparative study of myostatin, follistatin and decorin expression in muscle of different origin. *Anat. Sci. Int.* **86**, 151–159 (2011).
134. Feige, P., Brun, C. E., Ritso, M. & Rudnicki, M. A. Orienting Muscle Stem Cells for Regeneration in Homeostasis, Aging, and Disease. *Cell Stem Cell* **23**, 653–664 (2018).
135. Tierney, M. T., Stec, M. J., Rulands, S., Simons, B. D. & Sacco, A. Muscle Stem Cells Exhibit Distinct Clonal Dynamics in Response to Tissue Repair and Homeostatic Aging. *Cell Stem Cell* **22**, 119-127.e3 (2018).
136. Lepper, C., Partridge, T. A. & Fan, C.-M. An absolute requirement for Pax7-positive satellite cells in acute injury-induced skeletal muscle regeneration. *Dev. Camb. Engl.* **138**, 3639–3646 (2011).
137. von Maltzahn, J., Jones, A. E., Parks, R. J. & Rudnicki, M. A. Pax7 is critical for the normal function of satellite cells in adult skeletal muscle. *Proc. Natl. Acad. Sci. U. S. A.* **110**, 16474–16479 (2013).
138. Tedesco, F. S., Moyle, L. A. & Perdiguero, E. Muscle Interstitial Cells: A Brief Field Guide to Non-satellite Cell Populations in Skeletal Muscle. *Methods Mol. Biol. Clifton NJ* **1556**, 129–147 (2017).
139. Christov, C. *et al.* Muscle satellite cells and endothelial cells: close neighbors and privileged partners. *Mol. Biol. Cell* **18**, 1397–1409 (2007).
140. Seale, P. *et al.* Pax7 is required for the specification of myogenic satellite cells. *Cell* **102**, 777–786 (2000).
141. Relaix, F. *et al.* Pax3 and Pax7 have distinct and overlapping functions in adult muscle

progenitor cells. *J. Cell Biol.* **172**, 91–102 (2006).

142. Tidball, J. G. Regulation of muscle growth and regeneration by the immune system. *Nat. Rev. Immunol.* **17**, 165–178 (2017).

143. Gayraud-Morel, B. *et al.* Myf5 haploinsufficiency reveals distinct cell fate potentials for adult skeletal muscle stem cells. *J. Cell Sci.* **125**, 1738–1749 (2012).

144. Crist, C. G., Montarras, D. & Buckingham, M. Muscle satellite cells are primed for myogenesis but maintain quiescence with sequestration of Myf5 mRNA targeted by microRNA-31 in mRNP granules. *Cell Stem Cell* **11**, 118–126 (2012).

145. Cornelison, D. D. & Wold, B. J. Single-cell analysis of regulatory gene expression in quiescent and activated mouse skeletal muscle satellite cells. *Dev. Biol.* **191**, 270–283 (1997).

146. Zammit, P. S. *et al.* Muscle satellite cells adopt divergent fates: a mechanism for self-renewal? *J. Cell Biol.* **166**, 347–357 (2004).

147. Syverud, B. C., VanDusen, K. W. & Larkin, L. M. Growth Factors for Skeletal Muscle Tissue Engineering. *Cells Tissues Organs* **202**, 169–179 (2016).

148. Villena, J. & Brandan, E. Dermatan sulfate exerts an enhanced growth factor response on skeletal muscle satellite cell proliferation and migration. *J. Cell. Physiol.* **198**, 169–178 (2004).

149. Rodgers, J. T., Schroeder, M. D., Ma, C. & Rando, T. A. HGFA Is an Injury-Regulated Systemic Factor that Induces the Transition of Stem Cells into GAlert. *Cell Rep.* **19**, 479–486 (2017).

150. Husmann, I., Soulet, L., Gautron, J., Martelly, I. & Barritault, D. Growth factors in skeletal muscle regeneration. *Cytokine Growth Factor Rev.* **7**, 249–258 (1996).

151. Groux-Muscatelli, B., Bassaglia, Y., Barritault, D., Caruelle, J. P. & Gautron, J. Proliferating satellite cells express acidic fibroblast growth factor during in vitro myogenesis. *Dev. Biol.* **142**, 380–385 (1990).

152. Pawlikowski, B., Vogler, T. O., Gadek, K. & Olwin, B. B. Regulation of skeletal muscle stem cells by fibroblast growth factors. *Dev. Dyn. Off. Publ. Am. Assoc. Anat.* **246**, 359–367 (2017).

153. Conboy, I. M. & Rando, T. A. The regulation of Notch signaling controls satellite cell activation and cell fate determination in postnatal myogenesis. *Dev. Cell* **3**, 397–409 (2002).

154. Brack, A. S., Conboy, I. M., Conboy, M. J., Shen, J. & Rando, T. A. A temporal switch from notch to Wnt signaling in muscle stem cells is necessary for normal adult myogenesis. *Cell Stem Cell* **2**, 50–59 (2008).

155. Thakar, D. *et al.* Binding of the chemokine CXCL12α to its natural extracellular matrix ligand heparan sulfate enables myoblast adhesion and facilitates cell motility. *Biomaterials* **123**, 24–38 (2017).

156. González, M. N. *et al.* HGF potentiates extracellular matrix-driven migration of human myoblasts: involvement of matrix metalloproteinases and MAPK/ERK pathway. *Skelet. Muscle* **7**, 20 (2017).

157. Jiao, S. *et al.* Differential regulation of IGF-I and IGF-II gene expression in skeletal muscle cells. *Mol. Cell. Biochem.* **373**, 107–113 (2013).

158. Walker, N., Kahamba, T., Woudberg, N., Goetsch, K. & Niesler, C. Dose-dependent modulation of myogenesis by HGF: implications for c-Met expression and downstream signalling pathways. *Growth Factors Chur Switz.* **33**, 229–241 (2015).

159. Cavanaugh, E. & DiMario, J. X. Sp3 controls fibroblast growth factor receptor 4 gene activity during myogenic differentiation. *Gene* **617**, 24–31 (2017).

160. Florini, J. R. & Ewton, D. Z. Actions of transforming growth factor-β on muscle cells.

J. Cell. Physiol. **135**, 301–308 (1988).

161. Girardi, F. & Le Grand, F. Wnt Signaling in Skeletal Muscle Development and Regeneration. *Prog. Mol. Biol. Transl. Sci.* **153**, 157–179 (2018).

162. Sampath, S. C., Sampath, S. C. & Millay, D. P. Myoblast fusion confusion: the resolution begins. *Skelet. Muscle* **8**, 3 (2018).

163. Millay, D. P. *et al.* Myomaker: A membrane activator of myoblast fusion and muscle formation. *Nature* **499**, 301–305 (2013).

164. Leikina, E. *et al.* Myomaker and Myomerger Work Independently to Control Distinct Steps of Membrane Remodeling during Myoblast Fusion. *Dev. Cell* **0**, (2018).

165. Millay, D. P. *et al.* Structure-function analysis of myomaker domains required for myoblast fusion. *Proc. Natl. Acad. Sci. U. S. A.* **113**, 2116–2121 (2016).

166. Quinn, M. E. *et al.* Myomerger induces fusion of non-fusogenic cells and is required for skeletal muscle development. *Nat. Commun.* **8**, 15665 (2017).

167. van den Eijnde, S. M. *et al.* Transient expression of phosphatidylserine at cell-cell contact areas is required for myotube formation. *J. Cell Sci.* **114**, 3631–3642 (2001).

168. Leikina, E. *et al.* Extracellular annexins and dynamin are important for sequential steps in myoblast fusion. *J. Cell Biol.* **200**, 109–123 (2013).

169. Wosczyna, M. N. & Rando, T. A. A Muscle Stem Cell Support Group: Coordinated Cellular Responses in Muscle Regeneration. *Dev. Cell* **46**, 135–143 (2018).

170. Saclier, M., Cuvellier, S., Magnan, M., Mounier, R. & Chazaud, B. Monocyte/macrophage interactions with myogenic precursor cells during skeletal muscle regeneration. *FEBS J.* **280**, 4118–4130 (2013).

171. Broussard, S. R. *et al.* IL-1beta impairs insulin-like growth factor i-induced differentiation and downstream activation signals of the insulin-like growth factor i receptor in myoblasts. *J. Immunol. Baltim. Md 1950* **172**, 7713–7720 (2004).

172. Lu, H., Huang, D., Ransohoff, R. M. & Zhou, L. Acute skeletal muscle injury: CCL2 expression by both monocytes and injured muscle is required for repair. *FASEB J. Off. Publ. Fed. Am. Soc. Exp. Biol.* **25**, 3344–3355 (2011).

173. Segawa, M. *et al.* Suppression of macrophage functions impairs skeletal muscle regeneration with severe fibrosis. *Exp. Cell Res.* **314**, 3232–3244 (2008).

174. Saclier, M. *et al.* Differentially activated macrophages orchestrate myogenic precursor cell fate during human skeletal muscle regeneration. *Stem Cells Dayt. Ohio* **31**, 384–396 (2013).

175. Tonkin, J. *et al.* Monocyte/Macrophage-derived IGF-1 Orchestrates Murine Skeletal Muscle Regeneration and Modulates Autocrine Polarization. *Mol. Ther.* **23**, 1189–1200 (2015).

176. Mounier, R. *et al.* AMPKα1 regulates macrophage skewing at the time of resolution of inflammation during skeletal muscle regeneration. *Cell Metab.* **18**, 251–264 (2013).

177. Varga, T. *et al.* Highly Dynamic Transcriptional Signature of Distinct Macrophage Subsets during Sterile Inflammation, Resolution, and Tissue Repair. *J. Immunol. Baltim. Md 1950* **196**, 4771–4782 (2016).

178. Varga, T. *et al.* Macrophage PPARγ, a Lipid Activated Transcription Factor Controls the Growth Factor GDF3 and Skeletal Muscle Regeneration. *Immunity* **45**, 1038–1051 (2016).

179. Heredia, J. E. *et al.* Type 2 Innate Signals Stimulate Fibro/Adipogenic Progenitors to Facilitate Muscle Regeneration. *Cell* **153**, 376–388 (2013).

180. Panduro, M., Benoist, C. & Mathis, D. Treg cells limit IFN-γ production to control macrophage accrual and phenotype during skeletal muscle regeneration. *Proc. Natl. Acad.*

Sci. U. S. A. **115**, E2585–E2593 (2018).

181. Latroche, C. *et al.* Skeletal Muscle Microvasculature: A Highly Dynamic Lifeline. *Physiol. Bethesda Md* **30**, 417–427 (2015).

182. Latroche, C. *et al.* Coupling between Myogenesis and Angiogenesis during Skeletal Muscle Regeneration Is Stimulated by Restorative Macrophages. *Stem Cell Rep.* **9**, 2018–2033 (2017).

183. Abou-Khalil, R. *et al.* Autocrine and paracrine angiopoietin 1/Tie-2 signaling promotes muscle satellite cell self-renewal. *Cell Stem Cell* **5**, 298–309 (2009).

184. Li, J. *et al.* Synergistic effects of FGF-2 and PDGF-BB on angiogenesis and muscle regeneration in rabbit hindlimb ischemia model. *Microvasc. Res.* **80**, 10–17 (2010).

185. Gianni-Barrera, R. *et al.* PDGF-BB regulates splitting angiogenesis in skeletal muscle by limiting VEGF-induced endothelial proliferation. *Angiogenesis* (2018). doi:10.1007/s10456-018-9634-5

186. Delavar, H. *et al.* Skeletal myofiber VEGF is essential for the exercise training response in adult mice. *Am. J. Physiol. Regul. Integr. Comp. Physiol.* **306**, R586-595 (2014).

187. Joe, A. W. B. *et al.* Muscle injury activates resident fibro/adipogenic progenitors that facilitate myogenesis. *Nat. Cell Biol.* **12**, 153–163 (2010).

188. Lemos, D. R. *et al.* Nilotinib reduces muscle fibrosis in chronic muscle injury by promoting TNF-mediated apoptosis of fibro/adipogenic progenitors. *Nat. Med.* **21**, 786–794 (2015).

189. Stumm, J. *et al.* Odd skipped-related 1 (Osr1) identifies muscle-interstitial fibro-adipogenic progenitors (FAPs) activated by acute injury. *Stem Cell Res.* **32**, 8–16 (2018).

190. Mackey, A. L., Magnan, M., Chazaud, B. & Kjaer, M. Human skeletal muscle fibroblasts stimulate in vitro myogenesis and in vivo muscle regeneration. *J. Physiol.* **595**, 5115–5127 (2017).

191. Acharjee, S. *et al.* Sharp-1 regulates TGF-β signaling and skeletal muscle regeneration. *J. Cell Sci.* **127**, 599–608 (2014).

192. Fry, C. S., Kirby, T. J., Kosmac, K., McCarthy, J. J. & Peterson, C. A. Myogenic Progenitor Cells Control Extracellular Matrix Production by Fibroblasts during Skeletal Muscle Hypertrophy. *Cell Stem Cell* **20**, 56–69 (2017).

193. Jessen, K. R. & Mirsky, R. The repair Schwann cell and its function in regenerating nerves. *J. Physiol.* **594**, 3521–3531 (2016).

194. Apel, P. J. *et al.* Effect of locally delivered IGF-1 on nerve regeneration during aging: an experimental study in rats. *Muscle Nerve* **41**, 335–341 (2010).

195. McGeachie, A. B., Koishi, K., Imamura, T., McLennan, I. S. & Department of Anatomy and Structural Biology, University of Otago, Dunedin, New Zealand. Fibroblast growth factor-5 is expressed in Schwann cells and is not essential for motoneurone survival. *Neuroscience* **104**, 891–899 (2001).

196. Stratton, J. A. *et al.* Macrophages Regulate Schwann Cell Maturation after Nerve Injury. *Cell Rep.* **24**, 2561-2572.e6 (2018).

197. Scicchitano, B. M., Sica, G. & Musarò, A. Stem Cells and Tissue Niche: Two Faces of the Same Coin of Muscle Regeneration. *Eur. J. Transl. Myol.* **26**, 6125 (2016).

198. Gutiérrez, J. M. *et al.* Why is Skeletal Muscle Regeneration Impaired after Myonecrosis Induced by Viperid Snake Venoms? *Toxins* **10**, (2018).

199. Willett, N. J., Krishnan, L., Li, M. T. A., Guldberg, R. E. & Warren, G. L. Guidelines for Models of Skeletal Muscle Injury and Therapeutic Assessment. *Cells Tissues Organs* **202**, 214–226 (2016).

200. Goetsch, S. C., Hawke, T. J., Gallardo, T. D., Richardson, J. A. & Garry, D. J. Transcriptional profiling and regulation of the extracellular matrix during muscle regeneration. *Physiol. Genomics* **14**, 261–271 (2003).

201. Yin, H., Price, F. & Rudnicki, M. A. Satellite cells and the muscle stem cell niche. *Physiol. Rev.* **93**, 23–67 (2013).

202. Urciuolo, A. *et al.* Collagen VI regulates satellite cell self-renewal and muscle regeneration. *Nat. Commun.* **4**, 1964 (2013).

203. Baghdadi, M. B. *et al.* Reciprocal signalling by Notch–Collagen V–CALCR retains muscle stem cells in their niche. *Nature* (2018). doi:10.1038/s41586-018-0144-9

204. Ito, A. *et al.* Effects of type IV collagen on myogenic characteristics of IGF-I gene-engineered myoblasts. *J. Biosci. Bioeng.* **119**, 596–603 (2015).

205. Lehto, M., Sims, T. J. & Bailey, A. J. Skeletal muscle injury--molecular changes in the collagen during healing. *Res. Exp. Med. Z. Gesamte Exp. Med. Einschl. Exp. Chir.* **185**, 95–106 (1985).

206. Maley, M. A., Davies, M. J. & Grounds, M. D. Extracellular matrix, growth factors, genetics: their influence on cell proliferation and myotube formation in primary cultures of adult mouse skeletal muscle. *Exp. Cell Res.* **219**, 169–179 (1995).

207. Arnesen, S. *et al.* The Effects of Collagen Type I Topography on Myoblasts In Vitro. *Connect. Tissue Res.* **45**, 238–247 (2004).

208. Li, X., Wang, Z., Tong, H., Yan, Y. & Li, S. Effects of COL8A1 on the proliferation of muscle-derived satellite cells. *Cell Biol. Int.* (2018). doi:10.1002/cbin.10979

209. García, A. J., Vega, M. D. & Boettiger, D. Modulation of cell proliferation and differentiation through substrate-dependent changes in fibronectin conformation. *Mol. Biol. Cell* **10**, 785–798 (1999).

210. Yao, C. C., Ziober, B. L., Sutherland, A. E., Mendrick, D. L. & Kramer, R. H. Laminins promote the locomotion of skeletal myoblasts via the alpha 7 integrin receptor. *J. Cell Sci.* **109 (Pt 13)**, 3139–3150 (1996).

211. Patton, B. L. *et al.* Distribution of ten laminin chains in dystrophic and regenerating muscles. *Neuromuscul. Disord. NMD* **9**, 423–433 (1999).

212. Penton, C. M. *et al.* Laminin 521 maintains differentiation potential of mouse and human satellite cell-derived myoblasts during long-term culture expansion. *Skelet. Muscle* **6**, 44 (2016).

213. Ishii, K. *et al.* Recapitulation of Extracellular LAMININ Environment Maintains Stemness of Satellite Cells In Vitro. *Stem Cell Rep.* **0**, (2018).

214. Vaz, R., Martins, G. G., Thorsteinsdóttir, S. & Rodrigues, G. Fibronectin promotes migration, alignment and fusion in an in vitro myoblast cell model. *Cell Tissue Res.* **348**, 569–578 (2012).

215. Funanage, V. L., Smith, S. M. & Minnich, M. A. Entactin promotes adhesion and long-term maintenance of cultured regenerated skeletal myotubes. *J. Cell. Physiol.* **150**, 251–257 (1992).

216. Neu, R., Adams, S. & Munz, B. Differential expression of entactin-1/nidogen-1 and entactin-2/nidogen-2 in myogenic differentiation. *Differ. Res. Biol. Divers.* **74**, 573–582 (2006).

217. Grefte, S., Adjobo-Hermans, M. J. W., Versteeg, E. M. M., Koopman, W. J. H. & Daamen, W. F. Impaired primary mouse myotube formation on crosslinked type I collagen films is enhanced by laminin and entactin. *Acta Biomater.* **30**, 265–276 (2016).

218. Deák, F. *et al.* Extracellular deposition of matrilin-2 controls the timing of the

myogenic program during muscle regeneration. *J Cell Sci* **127**, 3240–3256 (2014).
219. Hurme, T. & Kalimo, H. Adhesion in skeletal muscle during regeneration. *Muscle Nerve* **15**, 482–489 (1992).
220. Irintchev, A., Salvini, T. F., Faissner, A. & Wernig, A. Differential expression of tenascin after denervation, damage or paralysis of mouse soleus muscle. *J. Neurocytol.* **22**, 955–965 (1993).
221. Calve, S., Odelberg, S. J. & Simon, H.-G. A transitional extracellular matrix instructs cell behavior during muscle regeneration. *Dev. Biol.* **344**, 259–271 (2010).
222. Watkins, S. C., Lynch, G. W., Kane, L. P. & Slayter, H. S. Thrombospondin expression in traumatized skeletal muscle. Correlation of appearance with post-trauma regeneration. *Cell Tissue Res.* **261**, 73–84 (1990).
223. Adams, J. C. & Lawler, J. Cell-type specific adhesive interactions of skeletal myoblasts with thrombospondin-1. *Mol. Biol. Cell* **5**, 423–437 (1994).
224. Lacour, F. *et al.* R-spondin1 Controls Muscle Cell Fusion through Dual Regulation of Antagonistic Wnt Signaling Pathways. *Cell Rep.* **18**, 2320–2330 (2017).
225. Hara, M. *et al.* Periostin Promotes Fibroblast Migration and Inhibits Muscle Repair After Skeletal Muscle Injury. *J. Bone Joint Surg. Am.* **100**, e108 (2018).
226. Molnar, P., Wang, W., Natarajan, A., Rumsey, J. W. & Hickman, J. J. Photolithographic patterning of C2C12 myotubes using vitronectin as growth substrate in serum-free medium. *Biotechnol. Prog.* **23**, 265–268 (2007).
227. Melouane, A., Carbonell, A., Yoshioka, M., Puymirat, J. & St-Amand, J. Implication of SPARC in the modulation of the extracellular matrix and mitochondrial function in muscle cells. *PloS One* **13**, e0192714 (2018).
228. Petersson, S. J. *et al.* SPARC is up-regulated during skeletal muscle regeneration and inhibits myoblast differentiation. *Histol. Histopathol.* **28**, 1451–1460 (2013).
229. Osses, N. & Brandan, E. ECM is required for skeletal muscle differentiation independently of muscle regulatory factor expression. *Am. J. Physiol. Cell Physiol.* **282**, C383-394 (2002).
230. Casar, J. C. *et al.* Heparan sulfate proteoglycans are increased during skeletal muscle regeneration: requirement of syndecan-3 for successful fiber formation. *J. Cell Sci.* **117**, 73–84 (2004).
231. Larraín, J., Alvarez, J., Hassell, J. R. & Brandan, E. Expression of perlecan, a proteoglycan that binds myogenic inhibitory basic fibroblast growth factor, is down regulated during skeletal muscle differentiation. *Exp. Cell Res.* **234**, 405–412 (1997).
232. Casar, J. C., McKechnie, B. A., Fallon, J. R., Young, M. F. & Brandan, E. Transient up-regulation of biglycan during skeletal muscle regeneration: delayed fiber growth along with decorin increase in biglycan-deficient mice. *Dev. Biol.* **268**, 358–371 (2004).
233. Amenta, A. R. *et al.* Biglycan is an extracellular MuSK binding protein important for synapse stability. *J. Neurosci. Off. J. Soc. Neurosci.* **32**, 2324–2334 (2012).
234. Stupka, N. *et al.* Versican processing by a disintegrin-like and metalloproteinase domain with thrombospondin-1 repeats proteinases-5 and -15 facilitates myoblast fusion. *J. Biol. Chem.* **288**, 1907–1917 (2013).
235. Cabello-Verrugio, C. *et al.* The internal region leucine-rich repeat 6 of decorin interacts with low density lipoprotein receptor-related protein-1, modulates transforming growth factor (TGF)-β-dependent signaling, and inhibits TGF-β-dependent fibrotic response in skeletal muscles. *J. Biol. Chem.* **287**, 6773–6787 (2012).
236. Goetsch, K. P. & Niesler, C. U. The extracellular matrix regulates the effect of decorin

and transforming growth factor beta-2 (TGF-β2) on myoblast migration. *Biochem. Biophys. Res. Commun.* **479**, 351–357 (2016).

237. Zeng, Q. J. *et al.* Decorin-induced proliferation of avian myoblasts involves the myostatin/Smad signaling pathway. *Poult. Sci.* **93**, 138–146 (2014).

238. Kishioka, Y. *et al.* Decorin enhances the proliferation and differentiation of myogenic cells through suppressing myostatin activity. *J. Cell. Physiol.* **215**, 856–867 (2008).

239. Lee, E. J., Nam, J. H. & Choi, I. Fibromodulin modulates myoblast differentiation by controlling calcium channel. *Biochem. Biophys. Res. Commun.* (2018). doi:10.1016/j.bbrc.2018.06.041

240. Lee, E. J. *et al.* Fibromodulin: a master regulator of myostatin controlling progression of satellite cells through a myogenic program. *FASEB J. Off. Publ. Fed. Am. Soc. Exp. Biol.* **30**, 2708–2719 (2016).

241. Madhavan, R. & Peng, H. B. HGF induction of postsynaptic specializations at the neuromuscular junction. *J. Neurobiol.* **66**, 134–147 (2006).

242. Brandan, E., Carey, D. J., Larraín, J., Melo, F. & Campos, A. Synthesis and processing of glypican during differentiation of skeletal muscle cells. *Eur. J. Cell Biol.* **71**, 170–176 (1996).

243. Gutiérrez, J. & Brandan, E. A novel mechanism of sequestering fibroblast growth factor 2 by glypican in lipid rafts, allowing skeletal muscle differentiation. *Mol. Cell. Biol.* **30**, 1634–1649 (2010).

244. Gutiérrez, J., Cabrera, D. & Brandan, E. Glypican-1 regulates myoblast response to HGF via Met in a lipid raft-dependent mechanism: effect on migration of skeletal muscle precursor cells. *Skelet. Muscle* **4**, 5 (2014).

245. Larraín, J., Carey, D. J. & Brandan, E. Syndecan-1 expression inhibits myoblast differentiation through a basic fibroblast growth factor-dependent mechanism. *J. Biol. Chem.* **273**, 32288–32296 (1998).

246. Velleman, S. G., Liu, X., Coy, C. S. & McFarland, D. C. Effects of syndecan-1 and glypican on muscle cell proliferation and differentiation: implications for possible functions during myogenesis. *Poult. Sci.* **83**, 1020–1027 (2004).

247. Pisconti, A., Cornelison, D. D. W., Olguín, H. C., Antwine, T. L. & Olwin, B. B. Syndecan-3 and Notch cooperate in regulating adult myogenesis. *J. Cell Biol.* **190**, 427–441 (2010).

248. Fuentealba, L., Carey, D. J. & Brandan, E. Antisense inhibition of syndecan-3 expression during skeletal muscle differentiation accelerates myogenesis through a basic fibroblast growth factor-dependent mechanism. *J. Biol. Chem.* **274**, 37876–37884 (1999).

249. Song, Y., McFarland, D. C. & Velleman, S. G. Fibroblast growth factor 2 and protein kinase C alpha are involved in syndecan-4 cytoplasmic domain modulation of turkey myogenic satellite cell proliferation. *Comp. Biochem. Physiol. A. Mol. Integr. Physiol.* **161**, 44–52 (2012).

250. Shin, J., McFarland, D. C. & Velleman, S. G. Migration of turkey muscle satellite cells is enhanced by the syndecan-4 cytoplasmic domain through the activation of RhoA. *Mol. Cell. Biochem.* **375**, 115–130 (2013).

251. Keller-Pinter, A. *et al.* Syndecan-4 influences mammalian myoblast proliferation by modulating myostatin signalling and G1/S transition. *FEBS Lett.* **592**, 3139–3151 (2018).

252. Song, Y., Nestor, K. E., McFarland, D. C. & Velleman, S. G. Effect of glypican-1 covalently attached chains on turkey myogenic satellite cell proliferation, differentiation, and fibroblast growth factor 2 responsiveness. *Poult. Sci.* **89**, 123–134 (2010).

253. Song, Y., McFarland, D. C. & Velleman, S. G. Critical amino acids in syndecan-4 cytoplasmic domain modulation of turkey satellite cell growth and development. *Comp. Biochem. Physiol. A. Mol. Integr. Physiol.* **161**, 271–278 (2012).

254. Droguett, R., Cabello-Verrugio, C., Riquelme, C. & Brandan, E. Extracellular proteoglycans modify TGF-beta bio-availability attenuating its signaling during skeletal muscle differentiation. *Matrix Biol. J. Int. Soc. Matrix Biol.* **25**, 332–341 (2006).

255. Chevalier, F. *et al.* A fine structural modification of glycosaminoglycans is correlated with the progression of muscle regeneration after ischaemia: towards a matrix-based therapy? *Eur. Cell. Mater.* **30**, 51–68 (2015).

256. Langsdorf, A., Do, A.-T., Kusche-Gullberg, M., Emerson, C. P. & Ai, X. Sulfs are regulators of growth factor signaling for satellite cell differentiation and muscle regeneration. *Dev. Biol.* **311**, 464–477 (2007).

257. Barbosa, I. *et al.* A synthetic glycosaminoglycan mimetic (RGTA) modifies natural glycosaminoglycan species during myogenesis. *J. Cell Sci.* **118**, 253–264 (2005).

258. Cornelison, D. D., Filla, M. S., Stanley, H. M., Rapraeger, A. C. & Olwin, B. B. Syndecan-3 and syndecan-4 specifically mark skeletal muscle satellite cells and are implicated in satellite cell maintenance and muscle regeneration. *Dev. Biol.* **239**, 79–94 (2001).

259. Cornelison, D. D. W. *et al.* Essential and separable roles for Syndecan-3 and Syndecan-4 in skeletal muscle development and regeneration. *Genes Dev.* **18**, 2231–2236 (2004).

260. Shin, J., McFarland, D. C. & Velleman, S. G. Heparan sulfate proteoglycans, syndecan-4 and glypican-1, differentially regulate myogenic regulatory transcription factors and paired box 7 expression during turkey satellite cell myogenesis: implications for muscle growth. *Poult. Sci.* **91**, 201–207 (2012).

261. Velleman, S. G. & Song, Y. Development and Growth of the Avian Pectoralis Major (Breast) Muscle: Function of Syndecan-4 and Glypican-1 in Adult Myoblast Proliferation and Differentiation. *Front. Physiol.* **8**, 577 (2017).

262. Hirata, A. *et al.* Expression profiling of cytokines and related genes in regenerating skeletal muscle after cardiotoxin injection: a role for osteopontin. *Am. J. Pathol.* **163**, 203–215 (2003).

263. Govindan, J. & Iovine, M. K. Dynamic remodeling of the extra cellular matrix during zebrafish fin regeneration. *Gene Expr. Patterns GEP* **19**, 21–29 (2015).

264. Liu, H., Niu, A., Chen, S.-E. & Li, Y.-P. Beta3-integrin mediates satellite cell differentiation in regenerating mouse muscle. *FASEB J. Off. Publ. Fed. Am. Soc. Exp. Biol.* **25**, 1914–1921 (2011).

265. McClure, M. J. *et al.* Role of integrin α7β1 signaling in myoblast differentiation on aligned polydioxanone scaffolds. *Acta Biomater.* **39**, 44–54 (2016).

266. Quach, N. L., Biressi, S., Reichardt, L. F., Keller, C. & Rando, T. A. Focal adhesion kinase signaling regulates the expression of caveolin 3 and beta1 integrin, genes essential for normal myoblast fusion. *Mol. Biol. Cell* **20**, 3422–3435 (2009).

267. Lan, M. A., Gersbach, C. A., Michael, K. E., Keselowsky, B. G. & García, A. J. Myoblast proliferation and differentiation on fibronectin-coated self assembled monolayers presenting different surface chemistries. *Biomaterials* **26**, 4523–4531 (2005).

268. Webster, M. T., Manor, U., Lippincott-Schwartz, J. & Fan, C.-M. Intravital Imaging Reveals Ghost Fibers as Architectural Units Guiding Myogenic Progenitors during Regeneration. *Cell Stem Cell* **18**, 243–252 (2016).

269. Hardy, D. *et al.* Comparative Study of Injury Models for Studying Muscle Regeneration in Mice. *PloS One* **11**, e0147198 (2016).

270. Alameddine, H. S., Hantay, D., Dehaupas, M. & Fardeau, M. Role of persisting basement membrane in the reorganization of myofibres originating from myogenic cell grafts in the rat. *Neuromuscul. Disord.* **1**, 143–152 (1991).

271. Vracko, R. & Benditt, E. P. basal lamina: the scaffold for orderly cell replacement: Observations on Regeneration of Injured Skeletal Muscle Fibers and Capillaries. *J. Cell Biol.* **55**, 406–419 (1972).

272. Parkin, J. D. *et al.* The collαgen III fibril has a 'flexi-rod' structure of flexible sequences interspersed with rigid bioactive domains including two with hemostatic roles. *PloS One* **12**, e0175582 (2017).

273. Gilbert, P. M. *et al.* Substrate elasticity regulates skeletal muscle stem cell self-renewal in culture. *Science* **329**, 1078–1081 (2010).

274. Tackling muscle fibrosis: From molecular mechanisms to next generation engineered models to predict drug delivery. *Adv. Drug Deliv. Rev.* **129**, 64–77 (2018).

275. Sciorati, C., Clementi, E., Manfredi, A. A. & Rovere-Querini, P. Fat deposition and accumulation in the damaged and inflamed skeletal muscle: cellular and molecular players. *Cell. Mol. Life Sci. CMLS* **72**, 2135–2156 (2015).

276. Györfi, A. H., Matei, A.-E. & Distler, J. H. W. Targeting TGF-β signaling for the treatment of fibrosis. *Matrix Biol.* **68–69**, 8–27 (2018).

277. An integrative modeling framework reveals plasticity of TGF-β signaling | BMC Systems Biology | Full Text. Available at: https://bmcsystbiol.biomedcentral.com/articles/10.1186/1752-0509-8-30. (Accessed: 8th August 2018)

278. Piersma, B., Bank, R. A. & Boersema, M. Signaling in Fibrosis: TGF-β, WNT, and YAP/TAZ Converge. *Front. Med.* **2**, (2015).

279. Bernasconi, R. & Nyström, A. Balance and circumstance: The renin angiotensin system in wound healing and fibrosis. *Cell. Signal.* **51**, 34–46 (2018).

280. Li, Z. B., Kollias, H. D. & Wagner, K. R. Myostatin directly regulates skeletal muscle fibrosis. *J. Biol. Chem.* **283**, 19371–19378 (2008).

281. Smith, L. R. & Barton, E. R. Regulation of fibrosis in muscular dystrophy. *Matrix Biol. J. Int. Soc. Matrix Biol.* (2018). doi:10.1016/j.matbio.2018.01.014

282. Hantaï, D., Labat-Robert, J., Grimaud, J. A. & Fardeau, M. Fibronectin, laminin, type I, III and IV collagens in Duchenne's muscular dystrophy, congenital muscular dystrophies and congenital myopathies: an immunocytochemical study. *Connect. Tissue Res.* **13**, 273–281 (1985).

283. Fadic, R. *et al.* Increase in decorin and biglycan in Duchenne Muscular Dystrophy: role of fibroblasts as cell source of these proteoglycans in the disease. *J. Cell. Mol. Med.* **10**, 758–769 (2006).

284. Morales, M. G. *et al.* CTGF/CCN-2 over-expression can directly induce features of skeletal muscle dystrophy. *J. Pathol.* **225**, 490–501 (2011).

285. Vetrone, S. A. *et al.* Osteopontin promotes fibrosis in dystrophic mouse muscle by modulating immune cell subsets and intramuscular TGF-β. *J. Clin. Invest.* **119**, 1583–1594 (2009).

286. Hakim, C. H., Grange, R. W. & Duan, D. The passive mechanical properties of the extensor digitorum longus muscle are compromised in 2- to 20-mo-old mdx mice. *J. Appl. Physiol. Bethesda Md 1985* **110**, 1656–1663 (2011).

287. Serrano, A. L. & Muñoz-Cánoves, P. Regulation and dysregulation of fibrosis in skeletal muscle. *Exp. Cell Res.* **316**, 3050–3058 (2010).
288. Sun, G. *et al.* Elevated plasma levels of tissue inhibitors of metalloproteinase-1 and their overexpression in muscle in human and mouse muscular dystrophy. *J. Neurol. Sci.* **297**, 19–28 (2010).
289. Nadarajah, V. D. *et al.* Serum matrix metalloproteinase-9 (MMP-9) as a biomarker for monitoring disease progression in Duchenne muscular dystrophy (DMD). *Neuromuscul. Disord. NMD* **21**, 569–578 (2011).
290. Arvanitidis, A., Henriksen, K., Karsdal, M. A. & Nedergaard, A. Neo-epitope Peptides as Biomarkers of Disease Progression for Muscular Dystrophies and Other Myopathies. *J. Neuromuscul. Dis.* **3**, 333–346 (2016).
291. Pakshir, P. & Hinz, B. The big five in fibrosis: Macrophages, myofibroblasts, matrix, mechanics, and miscommunication. *Matrix Biol. J. Int. Soc. Matrix Biol.* **68–69**, 81–93 (2018).
292. Cencetti, F. *et al.* TGFβ1 evokes myoblast apoptotic response via a novel signaling pathway involving S1P4 transactivation upstream of Rho-kinase-2 activation. *FASEB J. Off. Publ. Fed. Am. Soc. Exp. Biol.* **27**, 4532–4546 (2013).
293. Cencetti, F., Bernacchioni, C., Nincheri, P., Donati, C. & Bruni, P. Transforming growth factor-beta1 induces transdifferentiation of myoblasts into myofibroblasts via up-regulation of sphingosine kinase-1/S1P3 axis. *Mol. Biol. Cell* **21**, 1111–1124 (2010).
294. Lacraz, G. *et al.* Increased Stiffness in Aged Skeletal Muscle Impairs Muscle Progenitor Cell Proliferative Activity. *PloS One* **10**, e0136217 (2015).
295. Stearns-Reider, K. M. *et al.* Aging of the skeletal muscle extracellular matrix drives a stem cell fibrogenic conversion. *Aging Cell* **16**, 518–528 (2017).
296. Muñoz-Cánoves, P. & Serrano, A. L. Macrophages decide between regeneration and fibrosis in muscle. *Trends Endocrinol. Metab.* **26**, 449–450 (2015).
297. WHO | Guidelines for essential trauma care. *WHO* Available at: http://www.who.int/violence_injury_prevention/publications/services/guidelines_traumacare/en/. (Accessed: 9th August 2018)
298. WHO | Global status report on road safety 2015. *WHO* Available at: http://www.who.int/violence_injury_prevention/road_safety_status/2015/en/. (Accessed: 27th August 2018)
299. Vos, T. *et al.* Years lived with disability (YLDs) for 1160 sequelae of 289 diseases and injuries 1990-2010: a systematic analysis for the Global Burden of Disease Study 2010. *Lancet Lond. Engl.* **380**, 2163–2196 (2012).
300. GBD 2013 DALYs and HALE Collaborators *et al.* Global, regional, and national disability-adjusted life years (DALYs) for 306 diseases and injuries and healthy life expectancy (HALE) for 188 countries, 1990-2013: quantifying the epidemiological transition. *Lancet Lond. Engl.* **386**, 2145–2191 (2015).
301. WHO | World report on road traffic injury prevention. *WHO* Available at: http://www.who.int/violence_injury_prevention/publications/road_traffic/world_report/en/. (Accessed: 27th August 2018)
302. Rissanen, R., Berg, H.-Y. & Hasselberg, M. Quality of life following road traffic injury: A systematic literature review. *Accid. Anal. Prev.* **108**, 308–320 (2017).
303. Laver, L., Pengas, I. P. & Mei-Dan, O. Injuries in extreme sports. *J. Orthop. Surg.* **12**, (2017).
304. Bartholdson, S. & von Schreeb, J. Natural Disasters and Injuries: What Does a

Surgeon Need to Know? *Curr. Trauma Rep.* **4**, 103–108 (2018).

305. Saulnier, D. D., Brolin Ribacke, K. & von Schreeb, J. No Calm After the Storm: A Systematic Review of Human Health Following Flood and Storm Disasters. *Prehospital Disaster Med.* **32**, 568–579 (2017).

306. Bach, J. A. *et al.* The right team at the right time – Multidisciplinary approach to multi-trauma patient with orthopedic injuries. *Int. J. Crit. Illn. Inj. Sci.* **7**, 32–37 (2017).

307. Mathieu, L. *et al.* Surgical management of combat-related upper extremity injuries. *Chir. Main* **33**, 174–182 (2014).

308. Herter, F., Ninkovic, M. & Ninkovic, M. Rational flap selection and timing for coverage of complex upper extremity trauma. *J. Plast. Reconstr. Aesthetic Surg. JPRAS* **60**, 760–768 (2007).

309. Rigal, S., Mathieu, L. & de l'Escalopier, N. Temporary fixation of limbs and pelvis. *Orthop. Traumatol. Surg. Res. OTSR* **104**, S81–S88 (2018).

310. WHO | Collective violence. *WHO* Available at: http://www.who.int/violence_injury_prevention/violence/collective/en/. (Accessed: 9th August 2018)

311. Belmont, P. J., Schoenfeld, A. J. & Goodman, G. Epidemiology of combat wounds in Operation Iraqi Freedom and Operation Enduring Freedom: orthopaedic burden of disease. *J. Surg. Orthop. Adv.* **19**, 2–7 (2010).

312. Balazs, G. C., Blais, M. B., Bluman, E. M., Andersen, R. C. & Potter, B. K. Blurred front lines: triage and initial management of blast injuries. *Curr. Rev. Musculoskelet. Med.* **8**, 304–311 (2015).

313. Covey, D. C. & Born, C. T. Blast injuries: mechanics and wounding patterns. *J. Surg. Orthop. Adv.* **19**, 8–12 (2010).

314. Belmont, P. J. *et al.* The nature and incidence of musculoskeletal combat wounds in Iraq and Afghanistan (2005-2009). *J. Orthop. Trauma* **27**, e107-113 (2013).

315. Ramasamy, A. *et al.* Outcomes of IED foot and ankle blast injuries. *J. Bone Joint Surg. Am.* **95**, e25 (2013).

316. Belmont, P. J., Owens, B. D. & Schoenfeld, A. J. Musculoskeletal Injuries in Iraq and Afghanistan: Epidemiology and Outcomes Following a Decade of War. *J. Am. Acad. Orthop. Surg.* **24**, 341–348 (2016).

317. Belmont, P. J. *et al.* Incidence and epidemiology of combat injuries sustained during 'the surge' portion of operation Iraqi Freedom by a U.S. Army brigade combat team. *J. Trauma* **68**, 204–210 (2010).

318. Andersen, R. C. *et al.* Damage control orthopaedics: an in-theater perspective. *J. Surg. Orthop. Adv.* **19**, 13–17 (2010).

319. Ebrahimi, A., Nejadsarvari, N., Ebrahimi, A. & Rasouli, H. R. Early Reconstructions of Complex Lower Extremity Battlefield Soft Tissue Wounds. *World J. Plast. Surg.* **6**, 332–342 (2017).

320. Mathieu, L. *et al.* Temporary and definitive external fixation of war injuries: use of a French dedicated fixator. *Int. Orthop.* **38**, 1569–1576 (2014).

321. Mathieu, L. *et al.* Wartime upper extremity injuries: experience from the Kabul International Airport combat support hospital. *Chir. Main* **33**, 183–188 (2014).

322. Cross, J. D., Ficke, J. R., Hsu, J. R., Masini, B. D. & Wenke, J. C. Battlefield orthopaedic injuries cause the majority of long-term disabilities. *J. Am. Acad. Orthop. Surg.* **19 Suppl 1**, S1-7 (2011).

323. Owens, B. D., Kragh, J. F., Macaitis, J., Svoboda, S. J. & Wenke, J. C.

Characterization of extremity wounds in Operation Iraqi Freedom and Operation Enduring Freedom. *J. Orthop. Trauma* **21**, 254–257 (2007).

324. Barbier, O. *et al.* Surgical support during the terrorist attacks in Paris, November 13, 2015: Experience at Bégin Military Teaching Hospital. *J. Trauma Acute Care Surg.* **82**, 1122–1128 (2017).

325. Laughlin, M. D. *et al.* Occupational outcomes following combat-related gunshot injury: Cohort study. *Int. J. Surg. Lond. Engl.* **48**, 286–290 (2017).

326. Fleming, M., Waterman, S., Dunne, J., D'Alleyrand, J.-C. & Andersen, R. C. Dismounted complex blast injuries: patterns of injuries and resource utilization associated with the multiple extremity amputee. *J. Surg. Orthop. Adv.* **21**, 32–37 (2012).

327. Huh, J., Stinner, D. J., Burns, T. C., Hsu, J. R. & Late Amputation Study Team. Infectious complications and soft tissue injury contribute to late amputation after severe lower extremity trauma. *J. Trauma* **71**, S47-51 (2011).

328. Masini, B. D. *et al.* Resource utilization and disability outcome assessment of combat casualties from Operation Iraqi Freedom and Operation Enduring Freedom. *J. Orthop. Trauma* **23**, 261–266 (2009).

329. Mase, V. J. *et al.* Clinical application of an acellular biologic scaffold for surgical repair of a large, traumatic quadriceps femoris muscle defect. *Orthopedics* **33**, 511 (2010).

330. Grogan, B. F., Hsu, J. R. & Skeletal Trauma Research Consortium. Volumetric muscle loss. *J. Am. Acad. Orthop. Surg.* **19 Suppl 1**, S35-37 (2011).

331. Corona, B. T., Wenke, J. C. & Ward, C. L. Pathophysiology of Volumetric Muscle Loss Injury. *Cells Tissues Organs* **202**, 180–188 (2016).

332. Garg, K. *et al.* Volumetric muscle loss: persistent functional deficits beyond frank loss of tissue. *J. Orthop. Res. Off. Publ. Orthop. Res. Soc.* **33**, 40–46 (2015).

333. Mkandawire, N. C., Boot, D. A., Braithwaite, I. J. & Patterson, M. Musculoskeletal recovery 5 years after severe injury: long term problems are common. *Injury* **33**, 111–115 (2002).

334. Sluys, K. P., Shults, J. & Richmond, T. S. Health related quality of life and return to work after minor extremity injuries: A longitudinal study comparing upper versus lower extremity injuries. *Injury* **47**, 824–831 (2016).

335. Papadakaki, M. *et al.* Psychological distress and physical disability in patients sustaining severe injuries in road traffic crashes: Results from a one-year cohort study from three European countries. *Injury* **48**, 297–306 (2017).

336. MacKenzie, E. J. *et al.* Long-term persistence of disability following severe lower-limb trauma. Results of a seven-year follow-up. *J. Bone Joint Surg. Am.* **87**, 1801–1809 (2005).

337. Giannoudis, P. V. *et al.* Long-term quality of life in trauma patients following the full spectrum of tibial injury (fasciotomy, closed fracture, grade IIIB/IIIC open fracture and amputation). *Injury* **40**, 213–219 (2009).

338. Corona, B. T., Rivera, J. C., Owens, J. G., Wenke, J. C. & Rathbone, C. R. Volumetric muscle loss leads to permanent disability following extremity trauma. *J. Rehabil. Res. Dev.* **52**, 785–792 (2015).

339. Huh, W. W. & Skapek, S. X. Childhood rhabdomyosarcoma: new insight on biology and treatment. *Curr. Oncol. Rep.* **12**, 402–410 (2010).

340. Chao, A. H., Mayerson, J. L., Chandawarkar, R. & Scharschmidt, T. J. Surgical management of soft tissue sarcomas: extremity sarcomas. *J. Surg. Oncol.* **111**, 540–545 (2015).

341. Stranix, J. T. *et al.* Limb-sparing sarcoma reconstruction with functional composite thigh flaps. *Microsurgery* (2017). doi:10.1002/micr.30254

342. Corona, B. T. *et al.* Impact of volumetric muscle loss injury on persistent motoneuron axotomy. *Muscle Nerve* **57**, 799–807 (2018).

343. Corona, B. T. *et al.* The promotion of a functional fibrosis in skeletal muscle with volumetric muscle loss injury following the transplantation of muscle-ECM. *Biomaterials* **34**, 3324–3335 (2013).

344. Gao, Y., Waas, A. M., Faulkner, J. A., Kostrominova, T. Y. & Wineman, A. S. Micromechanical modeling of the epimysium of the skeletal muscles. *J. Biomech.* **41**, 1–10 (2008).

345. Paudyal, A., Slevin, M., Maas, H. & Degens, H. Time course of denervation-induced changes in gastrocnemius muscles of adult and old rats. *Exp. Gerontol.* **106**, 165–172 (2018).

346. Garg, K., Corona, B. T. & Walters, T. J. Losartan administration reduces fibrosis but hinders functional recovery after volumetric muscle loss injury. *J. Appl. Physiol. Bethesda Md 1985* **117**, 1120–1131 (2014).

347. Aguilar, C. A. *et al.* Multiscale analysis of a regenerative therapy for treatment of volumetric muscle loss injury. *Cell Death Discov.* **4**, 33 (2018).

348. Corona, B. T., Rivera, J. C. & Greising, S. M. Inflammatory and Physiological Consequences of Debridement of Fibrous Tissue after Volumetric Muscle Loss Injury. *Clin. Transl. Sci.* **11**, 208–217 (2018).

349. Hurtgen, B. J. *et al.* Severe muscle trauma triggers heightened and prolonged local musculoskeletal inflammation and impairs adjacent tibia fracture healing. *J. Musculoskelet. Neuronal Interact.* **16**, 122–134 (2016).

350. Beltran, M. J. *et al.* Fate of combat nerve injury. *J. Orthop. Trauma* **26**, e198-203 (2012).

351. Sicari, B. M. *et al.* An acellular biologic scaffold promotes skeletal muscle formation in mice and humans with volumetric muscle loss. *Sci. Transl. Med.* **6**, 234ra58 (2014).

352. Dziki, J. *et al.* An acellular biologic scaffold treatment for volumetric muscle loss: results of a 13-patient cohort study. *NPJ Regen. Med.* **1**, 16008 (2016).

353. Larouche, J., Greising, S. M., Corona, B. T. & Aguilar, C. A. Robust inflammatory and fibrotic signaling following volumetric muscle loss: a barrier to muscle regeneration. *Cell Death Dis.* **9**, 409 (2018).

354. Agostini, T., Lazzeri, D. & Spinelli, G. Anterolateral thigh flap: systematic literature review of specific donor-site complications and their management. *J. Cranio-Maxillo-fac. Surg. Off. Publ. Eur. Assoc. Cranio-Maxillo-fac. Surg.* **41**, 15–21 (2013).

355. Barbier, O., Ollat, D., Rigal, S. & Versier, G. Limb reconstructive surgery in austere settings: use of flaps in French forward surgical facilities. *Médecine Santé Trop.* 137–141 (20164-5-6). doi:10.1684/mst.2016.0573

356. Hurtgen, B. J. *et al.* Autologous minced muscle grafts improve endogenous fracture healing and muscle strength after musculoskeletal trauma. *Physiol. Rep.* **5**, (2017).

357. Greising, S. M., Dearth, C. L. & Corona, B. T. Regenerative and Rehabilitative Medicine: A Necessary Synergy for Functional Recovery from Volumetric Muscle Loss Injury. *Cells Tissues Organs* **202**, 237–249 (2016).

358. Greising, S. M. *et al.* Early rehabilitation for volumetric muscle loss injury augments endogenous regenerative aspects of muscle strength and oxidative capacity. *BMC Musculoskelet. Disord.* **19**, 173 (2018).

359. Rivera, J. C. & Corona, B. T. Muscle-related Disability Following Combat Injury

Increases With Time. *US Army Med. Dep. J.* 30–34 (2016).
360. Blair, J. A. *et al.* Return to duty after integrated orthotic and rehabilitation initiative. *J. Orthop. Trauma* **28**, e70-74 (2014).
361. Simon, C. G. *et al.* ASTM international workshop on standards and measurements for tissue engineering scaffolds. *J. Biomed. Mater. Res. B Appl. Biomater.* **103**, 949–959 (2015).
362. Nair, A. & Tang, L. Influence of scaffold design on host immune and stem cell responses. *Semin. Immunol.* **29**, 62–71 (2017).
363. Anderson, J. M., Rodriguez, A. & Chang, D. T. Foreign body reaction to biomaterials. *Semin. Immunol.* **20**, 86–100 (2008).
364. Lee, J. M. & Kim, Y. J. Foreign body granulomas after the use of dermal fillers: pathophysiology, clinical appearance, histologic features, and treatment. *Arch. Plast. Surg.* **42**, 232–239 (2015).
365. M. Sicari, B., Londono, R. & F. Badylak, S. Strategies for skeletal muscle tissue engineering: seed vs. soil. *J. Mater. Chem. B* **3**, 7881–7895 (2015).
366. Wolf, M. T., Dearth, C. L., Sonnenberg, S. B., Loboa, E. G. & Badylak, S. F. Naturally derived and synthetic scaffolds for skeletal muscle reconstruction. *Adv. Drug Deliv. Rev.* **84**, 208–221 (2015).
367. Udpa, N. *et al.* Effects of chitosan coatings on polypropylene mesh for implantation in a rat abdominal wall model. *Tissue Eng. Part A* **19**, 2713–2723 (2013).
368. Brandt, C. P., McHenry, C. R., Jacobs, D. G., Piotrowski, J. J. & Priebe, P. P. Polypropylene mesh closure after emergency laparotomy: morbidity and outcome. *Surgery* **118**, 736–740; discussion 740-741 (1995).
369. Ostrovidov, S. *et al.* Skeletal muscle tissue engineering: methods to form skeletal myotubes and their applications. *Tissue Eng. Part B Rev.* **20**, 403–436 (2014).
370. Ju, Y. M., Atala, A., Yoo, J. J. & Lee, S. J. In situ regeneration of skeletal muscle tissue through host cell recruitment. *Acta Biomater.* **10**, 4332–4339 (2014).
371. Ricotti, L. *et al.* Adhesion and proliferation of skeletal muscle cells on single layer poly(lactic acid) ultra-thin films. *Biomed. Microdevices* **12**, 809–819 (2010).
372. Sirivisoot, S. & Harrison, B. S. Skeletal myotube formation enhanced by electrospun polyurethane carbon nanotube scaffolds. *Int. J. Nanomedicine* **6**, 2483–2497 (2011).
373. Cha, S. H., Lee, H. J. & Koh, W.-G. Study of myoblast differentiation using multi-dimensional scaffolds consisting of nano and micropatterns. *Biomater. Res.* **21**, 1 (2017).
374. Torres-Rendon, J. G. *et al.* Bioactive gyroid scaffolds formed by sacrificial templating of nanocellulose and nanochitin hydrogels as instructive platforms for biomimetic tissue engineering. *Adv. Mater. Deerfield Beach Fla* **27**, 2989–2995 (2015).
375. Costantini, M. *et al.* Microfluidic-enhanced 3D bioprinting of aligned myoblast-laden hydrogels leads to functionally organized myofibers in vitro and in vivo. *Biomaterials* **131**, 98–110 (2017).
376. Mozetic, P., Giannitelli, S. M., Gori, M., Trombetta, M. & Rainer, A. Engineering muscle cell alignment through 3D bioprinting. *J. Biomed. Mater. Res. A* **105**, 2582–2588 (2017).
377. Lynn, A. K., Yannas, I. V. & Bonfield, W. Antigenicity and immunogenicity of collagen. *J. Biomed. Mater. Res. B Appl. Biomater.* **71**, 343–354 (2004).
378. Gilbert-Honick, J. *et al.* Engineering functional and histological regeneration of vascularized skeletal muscle. *Biomaterials* **164**, 70–79 (2018).
379. Pollot, B. E., Goldman, S. M., Wenke, J. C. & Corona, B. T. Decellularized extracellular matrix repair of volumetric muscle loss injury impairs adjacent bone healing in a

rat model of complex musculoskeletal trauma. *J. Trauma Acute Care Surg.* **81**, S184–S190 (2016).

380. Wang, W. *et al.* Compatibility of hyaluronic acid hydrogel and skeletal muscle myoblasts. *Biomed. Mater. Bristol Engl.* **4**, 025011 (2009).

381. Seif-Naraghi, S. B., Horn, D., Schup-Magoffin, P. J. & Christman, K. L. Injectable extracellular matrix derived hydrogel provides a platform for enhanced retention and delivery of a heparin-binding growth factor. *Acta Biomater.* **8**, 3695–3703 (2012).

382. Losi, P. *et al.* Tissue response to poly(ether)urethane-polydimethylsiloxane-fibrin composite scaffolds for controlled delivery of pro-angiogenic growth factors. *Biomaterials* **31**, 5336–5344 (2010).

383. Freeman, I. & Cohen, S. The influence of the sequential delivery of angiogenic factors from affinity-binding alginate scaffolds on vascularization. *Biomaterials* **30**, 2122–2131 (2009).

384. Gerli, M. F. M., Guyette, J. P., Evangelista-Leite, D., Ghoshhajra, B. B. & Ott, H. C. Perfusion decellularization of a human limb: A novel platform for composite tissue engineering and reconstructive surgery. *PloS One* **13**, e0191497 (2018).

385. Morris, A. H., Stamer, D. K. & Kyriakides, T. R. The host response to naturally-derived extracellular matrix biomaterials. *Semin. Immunol.* **29**, 72–91 (2017).

386. Agmon, G. & Christman, K. L. Controlling stem cell behavior with decellularized extracellular matrix scaffolds. *Curr. Opin. Solid State Mater. Sci.* **20**, 193–201 (2016).

387. Delgado, L. M., Bayon, Y., Pandit, A. & Zeugolis, D. I. To cross-link or not to cross-link? Cross-linking associated foreign body response of collagen-based devices. *Tissue Eng. Part B Rev.* **21**, 298–313 (2015).

388. Steffens, D., Braghirolli, D. I., Maurmann, N. & Pranke, P. Update on the main use of biomaterials and techniques associated with tissue engineering. *Drug Discov. Today* (2018). doi:10.1016/j.drudis.2018.03.013

389. Gilbert, T. W., Freund, J. M. & Badylak, S. F. Quantification of DNA in biologic scaffold materials. *J. Surg. Res.* **152**, 135–139 (2009).

390. Dettin, M. *et al.* Natural Scaffolds for Regenerative Medicine: Direct Determination of Detergents Entrapped in Decellularized Heart Valves. *BioMed Res. Int.* **2017**, 9274135 (2017).

391. Nie, X. *et al.* Comparison of Porcine Small Intestinal Submucosa versus Polypropylene in Open Inguinal Hernia Repair: A Systematic Review and Meta-Analysis. *PloS One* **10**, e0135073 (2015).

392. Fokin, A. A., Puente, I., Hus, N., Rodriguez, E. & Weisz, R. D. Extracellular Matrix Applications in the Treatment of Open Fractures With Complex Wounds and Large Soft Tissue Defects. *J. Orthop. Trauma* **32**, e76–e80 (2018).

393. Brown, B. N. *et al.* Surface characterization of extracellular matrix scaffolds. *Biomaterials* **31**, 428–437 (2010).

394. Fuoco, C., Petrilli, L. L., Cannata, S. & Gargioli, C. Matrix scaffolding for stem cell guidance toward skeletal muscle tissue engineering. *J. Orthop. Surg.* **11**, 86 (2016).

395. Barbier-Chassefière, V. *et al.* Matrix therapy in regenerative medicine, a new approach to chronic wound healing. *J. Biomed. Mater. Res. A* **90**, 641–647 (2009).

396. Barritault, D., Desgranges, P., Meddahi-Pellé, A., Denoix, J.-M. & Saffar, J.-L. RGTA®-based matrix therapy - A new branch of regenerative medicine in locomotion. *Jt. Bone Spine Rev. Rhum.* **84**, 283–292 (2017).

397. Aurora, A., Roe, J. L., Corona, B. T. & Walters, T. J. An acellular biologic scaffold

does not regenerate appreciable de novo muscle tissue in rat models of volumetric muscle loss injury. *Biomaterials* **67**, 393–407 (2015).
398. Corona, B. T., Ward, C. L., Baker, H. B., Walters, T. J. & Christ, G. J. Implantation of in vitro tissue engineered muscle repair constructs and bladder acellular matrices partially restore in vivo skeletal muscle function in a rat model of volumetric muscle loss injury. *Tissue Eng. Part A* **20**, 705–715 (2014).
399. Kasukonis, B. *et al.* Codelivery of Infusion Decellularized Skeletal Muscle with Minced Muscle Autografts Improved Recovery from Volumetric Muscle Loss Injury in a Rat Model. *Tissue Eng. Part A* **22**, 1151–1163 (2016).
400. McClure, M. J. *et al.* Decellularized Muscle Supports New Muscle Fibers and Improves Function Following Volumetric Injury. *Tissue Eng. Part A* **24**, 1228–1241 (2018).
401. Merritt, E. K. *et al.* Functional assessment of skeletal muscle regeneration utilizing homologous extracellular matrix as scaffolding. *Tissue Eng. Part A* **16**, 1395–1405 (2010).
402. Perniconi, B. *et al.* The pro-myogenic environment provided by whole organ scale acellular scaffolds from skeletal muscle. *Biomaterials* **32**, 7870–7882 (2011).
403. Urciuolo, A. *et al.* Decellularised skeletal muscles allow functional muscle regeneration by promoting host cell migration. *Sci. Rep.* **8**, 8398 (2018).
404. Turner, N. J. *et al.* Xenogeneic extracellular matrix as an inductive scaffold for regeneration of a functioning musculotendinous junction. *Tissue Eng. Part A* **16**, 3309–3317 (2010).
405. Turner, N. J., Badylak, J. S., Weber, D. J. & Badylak, S. F. Biologic scaffold remodeling in a dog model of complex musculoskeletal injury. *J. Surg. Res.* **176**, 490–502 (2012).
406. Greising, S. M. *et al.* Unwavering Pathobiology of Volumetric Muscle Loss Injury. *Sci. Rep.* **7**, 13179 (2017).
407. Corona, B. T., Rivera, J. C., Wenke, J. C. & Greising, S. M. Tacrolimus as an adjunct to autologous minced muscle grafts for the repair of a volumetric muscle loss injury. *J. Exp. Orthop.* **4**, 36 (2017).
408. Gentile, N. E. *et al.* Targeted rehabilitation after extracellular matrix scaffold transplantation for the treatment of volumetric muscle loss. *Am. J. Phys. Med. Rehabil.* **93**, S79-87 (2014).
409. Wang, L., Johnson, J. A., Chang, D. W. & Zhang, Q. Decellularized musculofascial extracellular matrix for tissue engineering. *Biomaterials* **34**, 2641–2654 (2013).
410. Wolf, M. T., Daly, K. A., Reing, J. E. & Badylak, S. F. Biologic scaffold composed of skeletal muscle extracellular matrix. *Biomaterials* **33**, 2916–2925 (2012).
411. Gillies, A. R., Smith, L. R., Lieber, R. L. & Varghese, S. Method for decellularizing skeletal muscle without detergents or proteolytic enzymes. *Tissue Eng. Part C Methods* **17**, 383–389 (2011).
412. Garg, K., Ward, C. L. & Corona, B. T. Asynchronous inflammation and myogenic cell migration limit muscle tissue regeneration mediated by a cellular scaffolds. *Inflamm. Cell Signal.* **1**, (2014).
413. Gandhi, N. S. & Mancera, R. L. The structure of glycosaminoglycans and their interactions with proteins. *Chem. Biol. Drug Des.* **72**, 455–482 (2008).
414. Busilacchi, A., Gigante, A., Mattioli-Belmonte, M., Manzotti, S. & Muzzarelli, R. A. A. Chitosan stabilizes platelet growth factors and modulates stem cell differentiation toward tissue regeneration. *Carbohydr. Polym.* **98**, 665–676 (2013).
415. Luyt, C.-E. *et al.* Low-molecular-weight fucoidan promotes therapeutic

revascularization in a rat model of critical hindlimb ischemia. *J. Pharmacol. Exp. Ther.* **305**, 24–30 (2003).
416. Wang, M. *et al.* Glycosaminoglycans (GAGs) and GAG mimetics regulate the behavior of stem cell differentiation. *Colloids Surf. B Biointerfaces* **150**, 175–182 (2017).
417. Papy-Garcia, D. *et al.* Nondegradative Sulfation of Polysaccharides. Synthesis and Structure Characterization of Biologically Active Heparan Sulfate Mimetics. *Macromolecules* **38**, 4647–4654 (2005).
418. Albanese, P. *et al.* Glycosaminoglycan mimetics-induced mobilization of hematopoietic progenitors and stem cells into mouse peripheral blood: structure/function insights. *Exp. Hematol.* **37**, 1072–1083 (2009).
419. Chevalier, F. *et al.* Glycosaminoglycan mimetic improves enrichment and cell functions of human endothelial progenitor cell colonies. *Stem Cell Res.* **12**, 703–715 (2014).
420. Frescaline, G. *et al.* Glycosaminoglycans mimetics potentiate the clonogenicity, proliferation, migration and differentiation properties of rat mesenchymal stem cells. *Stem Cell Res.* **8**, 180–192 (2012).
421. Faivre, L. *et al.* In vitro and in vivo evaluation of cord blood hematopoietic stem and progenitor cells amplified with glycosaminoglycan mimetic. *Stem Cell Res. Ther.* **7**, 3 (2016).
422. Barritault, D. *et al.* RGTA® or ReGeneraTing Agents mimic heparan sulfate in regenerative medicine: from concept to curing patients. *Glycoconj. J.* **34**, 325–338 (2017).
423. Rouet, V. *et al.* Heparin-like synthetic polymers, named RGTAs, mimic biological effects of heparin in vitro. *J. Biomed. Mater. Res. A* **78**, 792–797 (2006).
424. Charef, S., Tulliez, M., Esmilaire, L., Courty, J. & Papy-Garcia, D. Toxicological evaluation of RGTA OTR4120, a heparan sulfate mimetic. *Food Chem. Toxicol. Int. J. Publ. Br. Ind. Biol. Res. Assoc.* **48**, 1965–1968 (2010).
425. Lindahl, U., Couchman, J., Kimata, K. & Esko, J. D. Proteoglycans and Sulfated Glycosaminoglycans. in *Essentials of Glycobiology* (eds. Varki, A. et al.) (Cold Spring Harbor Laboratory Press, 2015).
426. Meddahi, A., Lemdjabar, H., Caruelle, J. P., Barritault, D. & Hornebeck, W. FGF protection and inhibition of human neutrophil elastase by carboxymethyl benzylamide sulfonate dextran derivatives. *Int. J. Biol. Macromol.* **18**, 141–145 (1996).
427. Ledoux, D. *et al.* Human plasmin enzymatic activity is inhibited by chemically modified dextrans. *J. Biol. Chem.* **275**, 29383–29390 (2000).
428. Rouet, V. *et al.* A synthetic glycosaminoglycan mimetic binds vascular endothelial growth factor and modulates angiogenesis. *J. Biol. Chem.* **280**, 32792–32800 (2005).
429. Meddahi, A., Caruelle, J. P., Gold, L., Rosso, Y. & Barritault, D. New concepts in tissue repair: skin as an example. *Diabetes Metab.* **22**, 274–278 (1996).
430. Garcia-Filipe, S. *et al.* RGTA OTR4120, a heparan sulfate mimetic, is a possible long-term active agent to heal burned skin. *J. Biomed. Mater. Res. A* **80**, 75–84 (2007).
431. Colombier, M. L. *et al.* A single low dose of RGTA, a new healing agent, hastens wound maturation and enhances bone deposition in rat craniotomy defects. *Cells Tissues Organs* **164**, 131–140 (1999).
432. Lafont, J. *et al.* Kinetic study of early regenerative effects of RGTA11, a heparan sulfate mimetic, in rat craniotomy defects. *Calcif. Tissue Int.* **75**, 517–525 (2004).
433. Frescaline, G. *et al.* Glycosaminoglycan mimetic associated to human mesenchymal stem cell-based scaffolds inhibit ectopic bone formation, but induce angiogenesis in vivo. *Tissue Eng. Part A* **19**, 1641–1653 (2013).
434. Jacquet-Guibon, S. *et al.* Randomized controlled trial demonstrates the benefit of

RGTA® based matrix therapy to treat tendinopathies in racing horses. *PloS One* **13**, e0191796 (2018).
435. Escartin, Q. *et al.* A new approach to treat tissue destruction in periodontitis with chemically modified dextran polymers. *FASEB J. Off. Publ. Fed. Am. Soc. Exp. Biol.* **17**, 644–651 (2003).
436. Lallam-Laroye, C. *et al.* ReGeneraTing agents matrix therapy regenerates a functional root attachment in hamsters with periodontitis. *Tissue Eng. Part A* **17**, 2359–2367 (2011).
437. Groah, S. L. *et al.* Regenerating matrix-based therapy for chronic wound healing: a prospective within-subject pilot study. *Int. Wound J.* **8**, 85–95 (2011).
438. Aifa, A., Gueudry, J., Portmann, A., Delcampe, A. & Muraine, M. Topical treatment with a new matrix therapy agent (RGTA) for the treatment of corneal neurotrophic ulcers. *Invest. Ophthalmol. Vis. Sci.* **53**, 8181–8185 (2012).
439. Sevik, M. O., Turhan, S. A. & Toker, E. Topical Treatment of Persistent Epithelial Defects with a Matrix Regenerating Agent. *J. Ocul. Pharmacol. Ther. Off. J. Assoc. Ocul. Pharmacol. Ther.* **34**, 621–627 (2018).
440. Fajnkuchen, F., Barritault, D. & Giocanti-Aurégan, A. Evaluation of a new matrix regenerating agent in patients with Sjögren syndrome and superficial ulcerative keratitis resistant to conventional therapy: A report of 3 cases. *Medicine (Baltimore)* **97**, e9935 (2018).
441. Blanquaert, F. *et al.* Heparan-like molecules induce the repair of skull defects. *Bone* **17**, 499–506 (1995).
442. Gautron, J., Kedzia, C., Husmann, I. & Barritault, D. [Acceleration of the regeneration of skeletal muscles in adult rats by dextran derivatives]. *C. R. Acad. Sci. III* **318**, 671–676 (1995).
443. Aamiri, A., Mobarek, A., Carpentier, G., Barritault, D. & Gautron, J. [Effects of substituted dextran on reinnervation of a skeletal muscle in adult rats during regeneration]. *C. R. Acad. Sci. III* **318**, 1037–1043 (1995).
444. Aamiri, A., Butler-Browne, G. S., Martelly, I., Barritault, D. & Gautron, J. Influence of a dextran derivative on myosin heavy chain expression during rat skeletal muscle regeneration. *Neurosci. Lett.* **201**, 243–246 (1995).
445. Zimowska, M. *et al.* Heparan sulfate mimetics modulate calpain activity during rat Soleus muscle regeneration. *J. Cell. Physiol.* **188**, 178–187 (2001).
446. Meddahi, A. *et al.* Pharmacological studies of RGTA(11), a heparan sulfate mimetic polymer, efficient on muscle regeneration. *J. Biomed. Mater. Res.* **62**, 525–531 (2002).
447. Desgranges, P., Barbaud, C., Caruelle, J. P., Barritault, D. & Gautron, J. A substituted dextran enhances muscle fiber survival and regeneration in ischemic and denervated rat EDL muscle. *FASEB J. Off. Publ. Fed. Am. Soc. Exp. Biol.* **13**, 761–766 (1999).
448. Zimowska, M. *et al.* Novel glycosaminoglycan mimetic (RGTA, RGD120) contributes to enhance skeletal muscle satellite cell fusion by increasing intracellular Ca2+ and calpain activity. *J. Cell. Physiol.* **205**, 237–245 (2005).
449. Papy-Garcia, D. *et al.* Glycosaminoglycan mimetics (RGTA) modulate adult skeletal muscle satellite cell proliferation in vitro. *J. Biomed. Mater. Res.* **62**, 46–55 (2002).
450. Siebert, T. *et al.* Three-Dimensional Muscle Architecture and Comprehensive Dynamic Properties of Rabbit Gastrocnemius, Plantaris and Soleus: Input for Simulation Studies. *PLOS ONE* **10**, e0130985 (2015).
451. Siebert, T., Tomalka, A., Stutzig, N., Leichsenring, K. & Böl, M. Changes in three-dimensional muscle structure of rabbit gastrocnemius, flexor digitorum longus, and tibialis anterior during growth. *J. Mech. Behav. Biomed. Mater.* **74**, 507–519 (2017).

452. Stern, M. M. *et al.* The influence of extracellular matrix derived from skeletal muscle tissue on the proliferation and differentiation of myogenic progenitor cells ex vivo. *Biomaterials* **30**, 2393–2399 (2009).

453. Crapo, P. M., Gilbert, T. W. & Badylak, S. F. An overview of tissue and whole organ decellularization processes. *Biomaterials* **32**, 3233–3243 (2011).

454. Agbulut, O., Li, Z., Mouly, V. & Butler-Browne, G. S. Analysis of skeletal and cardiac muscle from desmin knock-out and normal mice by high resolution separation of myosin heavy-chain isoforms. *Biol. Cell* **88**, 131–135 (1996).

455. Naba, A. *et al.* The extracellular matrix: Tools and insights for the 'omics' era. *Matrix Biol. J. Int. Soc. Matrix Biol.* **49**, 10–24 (2016).

456. Yang, Z. *et al.* Characteristic properties of muscular-derived extracellular matrix and its application in rat abdominal wall defects. *Regen. Med.* **13**, 503–517 (2018).

457. Aurora, A., Wrice, N., Walters, T. J., Christy, R. J. & Natesan, S. A PEGylated platelet free plasma hydrogel based composite scaffold enables stable vascularization and targeted cell delivery for volumetric muscle loss. *Acta Biomater.* **65**, 150–162 (2018).

458. Cornelison, R. C. *et al.* Development of an apoptosis-assisted decellularization method for maximal preservation of nerve tissue structure. *Acta Biomater.* **77**, 116–126 (2018).

459. Kasukonis, B. M., Kim, J. T., Washington, T. A. & Wolchok, J. C. Development of an infusion bioreactor for the accelerated preparation of decellularized skeletal muscle scaffolds. *Biotechnol. Prog.* **32**, 745–755 (2016).

460. Jank, B. J. *et al.* Engineered composite tissue as a bioartificial limb graft. *Biomaterials* **61**, 246–256 (2015).

461. Aamodt, J. M. & Grainger, D. W. Extracellular matrix-based biomaterial scaffolds and the host response. *Biomaterials* **86**, 68–82 (2016).

462. Edgington, S. M. & Stollar, B. D. Immunogenicity of Z-DNA depends on the size of polynucleotide presented in complexes with methylated BSA. *Mol. Immunol.* **29**, 609–617 (1992).

463. Zhang, J. *et al.* Perfusion-decellularized skeletal muscle as a three-dimensional scaffold with a vascular network template. *Biomaterials* **89**, 114–126 (2016).

464. Karayel, E. *et al.* The TLR-independent DNA recognition pathway in murine macrophages: Ligand features and molecular signature. *Eur. J. Immunol.* **39**, 1929–1936 (2009).

465. Bolland, F. *et al.* Development and characterisation of a full-thickness acellular porcine bladder matrix for tissue engineering. *Biomaterials* **28**, 1061–1070 (2007).

466. Rashtbar, M. *et al.* Characterization of decellularized ovine small intestine submucosal layer as extracellular matrix-based scaffold for tissue engineering. *J. Biomed. Mater. Res. B Appl. Biomater.* **106**, 933–944 (2018).

467. Galili, U. Induced anti-non gal antibodies in human xenograft recipients. *Transplantation* **93**, 11–16 (2012).

468. Ansaloni, L. *et al.* Immune response to small intestinal submucosa (surgisis) implant in humans: preliminary observations. *J. Investig. Surg. Off. J. Acad. Surg. Res.* **20**, 237–241 (2007).

469. Zheng, M. H. *et al.* Porcine small intestine submucosa (SIS) is not an acellular collagenous matrix and contains porcine DNA: possible implications in human implantation. *J. Biomed. Mater. Res. B Appl. Biomater.* **73**, 61–67 (2005).

470. McPherson, T. B., Liang, H., Record, R. D. & Badylak, S. F. Galalpha(1,3)Gal epitope in porcine small intestinal submucosa. *Tissue Eng.* **6**, 233–239 (2000).

471. Raeder, R. H., Badylak, S. F., Sheehan, C., Kallakury, B. & Metzger, D. W. Natural anti-galactose alpha1,3 galactose antibodies delay, but do not prevent the acceptance of extracellular matrix xenografts. *Transpl. Immunol.* **10**, 15–24 (2002).
472. Schenke-Layland, K. *et al.* Impact of decellularization of xenogeneic tissue on extracellular matrix integrity for tissue engineering of heart valves. *J. Struct. Biol.* **143**, 201–208 (2003).
473. Voytik-Harbin, S. L., Brightman, A. O., Kraine, M. R., Waisner, B. & Badylak, S. F. Identification of extractable growth factors from small intestinal submucosa. *J. Cell. Biochem.* **67**, 478–491 (1997).
474. Hodde, J. P., Record, R. D., Liang, H. A. & Badylak, S. F. Vascular endothelial growth factor in porcine-derived extracellular matrix. *Endothel. J. Endothel. Cell Res.* **8**, 11–24 (2001).
475. Yi, H. *et al.* Tissue-specific extracellular matrix promotes myogenic differentiation of human muscle progenitor cells on gelatin and heparin conjugated alginate hydrogels. *Acta Biomater.* **62**, 222–233 (2017).
476. Marçal, H., Ahmed, T., Badylak, S. F., Tottey, S. & Foster, L. J. R. A comprehensive protein expression profile of extracellular matrix biomaterial derived from porcine urinary bladder. *Regen. Med.* **7**, 159–166 (2012).
477. Sadtler, K. *et al.* Proteomic composition and immunomodulatory properties of urinary bladder matrix scaffolds in homeostasis and injury. *Semin. Immunol.* **29**, 14–23 (2017).
478. Veiseh, O. *et al.* Size- and shape-dependent foreign body immune response to materials implanted in rodents and non-human primates. *Nat. Mater.* **14**, 643–651 (2015).
479. Chang, Y., Lee, M.-H., Liang, H.-C., Hsu, C.-K. & Sung, H.-W. Acellular bovine pericardia with distinct porous structures fixed with genipin as an extracellular matrix. *Tissue Eng.* **10**, 881–892 (2004).
480. Bergmeister, H. *et al.* Effect of laser perforation on the remodeling of acellular matrix grafts. *J. Biomed. Mater. Res. B Appl. Biomater.* **74B**, 495–503 (2005).
481. Sheridan, W. S., Duffy, G. P. & Murphy, B. P. Mechanical characterization of a customized decellularized scaffold for vascular tissue engineering. *J. Mech. Behav. Biomed. Mater.* **8**, 58–70 (2012).
482. Lin, C.-H., Kao, Y.-C., Ma, H. & Tsay, R.-Y. An investigation on the correlation between the mechanical property change and the alterations in composition and microstructure of a porcine vascular tissue underwent trypsin-based decellularization treatment. *J. Mech. Behav. Biomed. Mater.* **86**, 199–207 (2018).
483. Dziki, J. L. *et al.* Solubilized extracellular matrix bioscaffolds derived from diverse source tissues differentially influence macrophage phenotype. *J. Biomed. Mater. Res. A* **105**, (2017).
484. Chen, P. *et al.* Collagen VI regulates peripheral nerve regeneration by modulating macrophage recruitment and polarization. *Acta Neuropathol. (Berl.)* **129**, 97–113 (2015).
485. Sicari, B. M. *et al.* The promotion of a constructive macrophage phenotype by solubilized extracellular matrix. *Biomaterials* **35**, 8605–8612 (2014).
486. Li, F. *et al.* Low-molecular-weight peptides derived from extracellular matrix as chemoattractants for primary endothelial cells. *Endothel. J. Endothel. Cell Res.* **11**, 199–206 (2004).
487. Köckerling, F. *et al.* What is the evidence for the use of biologic or biosynthetic meshes in abdominal wall reconstruction? *Hernia J. Hernias Abdom. Wall Surg.* **22**, 249–269 (2018).

488. Sadtler, K. *et al.* Developing a pro-regenerative biomaterial scaffold microenvironment requires T helper 2 cells. *Science* **352**, 366–370 (2016).
489. Keane, T. J., Londono, R., Turner, N. J. & Badylak, S. F. Consequences of ineffective decellularization of biologic scaffolds on the host response. *Biomaterials* **33**, 1771–1781 (2012).
490. Selders, G. S., Fetz, A. E., Radic, M. Z. & Bowlin, G. L. An overview of the role of neutrophils in innate immunity, inflammation and host-biomaterial integration. *Regen. Biomater.* **4**, 55–68 (2017).
491. Perniconi, B. *et al.* Muscle acellular scaffold as a biomaterial: effects on C2C12 cell differentiation and interaction with the murine host environment. *Front. Physiol.* **5**, 354 (2014).
492. Desgeorges, T. *et al.* Open-CSAM, a new tool for semi-automated analysis of myofiber cross-sectional area in regenerating adult skeletal muscle. *Skelet. Muscle* **9**, 2 (2019).
493. Sue, S.-C. *et al.* Heparin binding stabilizes the membrane-bound form of cobra cardiotoxin. *J. Biol. Chem.* **277**, 2666–2673 (2002).
494. Tjong, S.-C., Chen, T.-S., Huang, W.-N. & Wu, W.-G. Structures of heparin-derived tetrasaccharide bound to cobra cardiotoxins: heparin binding at a single protein site with diverse side chain interactions. *Biochemistry* **46**, 9941–9952 (2007).
495. Stockholm, D. *et al.* Studies on calpain expression during differentiation of rat satellite cells in primary cultures in the presence of heparin or a mimic compound. *Exp. Cell Res.* **252**, 392–400 (1999).
496. Sangaj, N. *et al.* Heparin mimicking polymer promotes myogenic differentiation of muscle progenitor cells. *Biomacromolecules* **11**, 3294–3300 (2010).
497. Jeanbat-Mimaud, V. *et al.* Bioactive functionalized polymer of malic acid for bone repair and muscle regeneration. *J. Biomater. Sci. Polym. Ed.* **11**, 979–991 (2000).
498. Bioactive functionalized polymer of malic acid for bone repair and muscle regeneration: Journal of Biomaterials Science, Polymer Edition: Vol 11, No 9. Available at: https://www-tandfonline-com.gate2.inist.fr/doi/abs/10.1163/156856200744147. (Accessed: 5th May 2018)
499. Pantelic, M. N. & Larkin, L. M. Stem Cells for Skeletal Muscle Tissue Engineering. *Tissue Eng. Part B Rev.* (2018). doi:10.1089/ten.TEB.2017.0451
500. Oduah, E. I., Linhardt, R. J. & Sharfstein, S. T. Heparin: Past, Present, and Future. *Pharm. Basel Switz.* **9**, (2016).
501. Biran, R. & Pond, D. Heparin coatings for improving blood compatibility of medical devices. *Adv. Drug Deliv. Rev.* **112**, 12–23 (2017).
502. Cui, Y. *et al.* In Situ Endothelialization Promoted by SEMA4D and CXCL12 for Titanium-Based Biomaterials. *Semin. Thromb. Hemost.* **44**, 70–80 (2018).
503. Kasimir, M.-T. *et al.* Decellularization does not eliminate thrombogenicity and inflammatory stimulation in tissue-engineered porcine heart valves. *J. Heart Valve Dis.* **15**, 278–286; discussion 286 (2006).
504. Zhou, J. *et al.* Development of decellularized aortic valvular conduit coated by heparin-SDF-1α multilayer. *Ann. Thorac. Surg.* **99**, 612–618 (2015).
505. Rnjak-Kovacina, J., Tang, F., Whitelock, J. M. & Lord, M. S. Glycosaminoglycan and Proteoglycan-Based Biomaterials: Current Trends and Future Perspectives. *Adv. Healthc. Mater.* **7**, e1701042 (2018).
506. Marinval, N. *et al.* Fucoidan/VEGF-based surface modification of decellularized

pulmonary heart valve improves the antithrombotic and re-endothelialization potential of bioprostheses. *Biomaterials* **172**, 14–29 (2018).

507. Desgranges, P., Caruelle, J. P., Carpentier, G., Barritault, D. & Tardieu, M. Beneficial use of fibroblast growth factor 2 and RGTA, a new family of heparan mimics, for endothelialization of PET prostheses. *J. Biomed. Mater. Res.* **58**, 1–9 (2001).

508. Yin, Y. *et al.* SDF-1alpha involved in mobilization and recruitment of endothelial progenitor cells after arterial injury in mice. *Cardiovasc. Pathol. Off. J. Soc. Cardiovasc. Pathol.* **19**, 218–227 (2010).

509. Yu, L., Yu, L., Pham, Q. & Wang, T. T. Y. Transcriptional and translational-uncoupling in regulation of the CXCL12 and its receptors CXCR4, 7 in THP-1 monocytes and macrophages. *Immun. Inflamm. Dis.* **6**, 106–116 (2018).

510. Kowalski, K. *et al.* Stem cells migration during skeletal muscle regeneration - the role of Sdf-1/Cxcr4 and Sdf-1/Cxcr7 axis. *Cell Adhes. Migr.* **11**, 384–398 (2017).

511. Walraven, M. & Hinz, B. Therapeutic approaches to control tissue repair and fibrosis: Extracellular matrix as a game changer. *Matrix Biol. J. Int. Soc. Matrix Biol.* (2018). doi:10.1016/j.matbio.2018.02.020

Scientific Publications and Communications

Publications

Trignol A*, Bouvière J*, Hoang DH, Delcarmine P, Goriot ME, Ben Larbi S, Barritault D, Banzet S, Chazaud B. Heparan sulfate mimetic ReGeneraTing Agents (RGTA®) accelerate post-injury skeletal muscle regeneration (submitted in Tissue Engineering Journal)

Desgeorges T, Liot S, Lyon S, Bouvière J, Kemmel A, **Trignol A**, Rousseau D, Chapuis B, Gondin J, Mounier R, Chazaud B and Juban G. Open-CSAM, a new tool for semi-automated analysis of myofiber cross-sectional area in regenerating adult skeletal muscle. *Skelet. Muscle*

Oral communications

Journée des doctorants de l'IRBA (january 2019)
Utilisation de matrice extracellulaire comme biomatériau pour optimiser la régénération musculaire
Trignol A, Bouvière J, Goriot ME, Chiappini F, Sineriz F, Delcarmine P, Mounier R, Barritault D, Banzet S, Chazaud B.

Journée des doctorants de l'IRBA (january 2018)
Analyses in vitro et in vivo des interactions entre la matrice extracellulaire et les cellules impliquées dans la régénération musculaire
Trignol A, Goriot ME, Mounier R, Banzet S, Chazaud B.

Internal seminar at Institut NeuroMyoGène in Lyon (may 2017)
In-vitro and in-vivo analysis of the interaction between extracellular matrix and cells involved in skeletal muscle regeneration
Trignol A, Goriot ME, Mounier R, Banzet S, Chazaud B.

Journée des doctorants de l'IRBA (january 2017)
Analyses in vitro et in vivo des interactions entre la matrice extracellulaire et les cellules impliquées dans la régénération musculaire
Trignol A, Goriot ME, Mounier R, Banzet S, Chazaud B.

21^{e} EDISS day in Lyon (october 2016)
Analyse in vitro et in vivo des interactions entre la matrice extracellulaire et les cellules impliquées dans la régénération musculaire
Trignol A, Goriot ME, Mounier R, Banzet S, Chazaud B.

Poster communications

First price in 8^{e} Biennale de l'IRBA in Paris (january 2018)
Etude de l'effet de mimétiques de glycosaminoglycanes au cours de la réparation musculaire
Trignol A, Bouviere J, Goriot ME, Chiappini F, Sineriz F, Delcarmine P, Mounier R, Barritault D, Banzet S, Chazaud B.

Colloque Jeunes chercheurs AFM Téléthon in Paris (june 2017)
Fundamental analysis of the interaction between extracellular matrix and cells involved in skeletal muscle regeneration to optimize muscle biomaterial
Trignol A, Goriot ME, Barritault D, Chiappini F, Sineriz F, Mounier R, Banzet S, Chazaud B.

Gordon Research Conference and Seminar Tissue repair and Regeneration in New London (june 2017)
Fundamental analysis of the interaction between extracellular matrix and cells involved in skeletal muscle regeneration to optimize muscle biomaterial
Trignol A, Goriot ME, Barritault D, Chiappini F, Sineriz F, Mounier R, Banzet S, Chazaud B.

Journée des internes et des assistants du Val de Grâce in Paris (september 2015)
Biomatériaux décellularisés et lésions musculaires avec perte de substance : analyse des interactions entre la matrice extracellulaire et les cellules impliquées dans la régénération musculaire
Trignol A, Goriot ME, Mounier R, Banzet S, Chazaud B.

Journée des internes et des assistants du Val de Grâce in Paris (october 2016)
Etude de l'effet de mimétiques de glycosaminoglycanes au cours de la réparation musculaire
Trignol A, Barritault D, Rice K, Sineriz F, Mounier R, Banzet S, Chazaud B.

ANNEX 1

Desgeorges *et al. Skeletal Muscle* _####################_
https://doi.org/10.1186/s13395-018-0186-6

Skeletal Muscle

METHODOLOGY **Open Access**

Open-CSAM, a new tool for semi-automated analysis of myofiber cross-sectional area in regenerating adult skeletal muscle

Thibaut Desgeorges[1], Sophie Liot[1], Solene Lyon[2], Jessica Bouvière[1], Alix Kemmel[1], Aurélie Trignol[1], David Rousseau[2], Bruno Chapuis[3], Julien Gondin[1], Rémi Mounier[1], Bénédicte Chazaud[1*] and Gaëtan Juban[1*]

Abstract

Adult skeletal muscle is capable of complete regeneration after an acute injury. The main parameter studied to assess muscle regeneration efficacy is the cross-sectional area (CSA) of the myofibers as myofiber size correlates with muscle force. CSA analysis can be time-consuming and may trigger variability in the results when performed manually. This is why programs were developed to completely automate the analysis of the CSA, such as SMASH, MyoVision, or MuscleJ softwares. Although these softwares are efficient to measure CSA on normal or hypertrophic/atrophic muscle, they fail to efficiently measure CSA on regenerating muscles. We developed Open-CSAM, an ImageJ macro, to perform a high throughput semi-automated analysis of CSA on skeletal muscle from various experimental conditions. The macro allows the experimenter to adjust the analysis and correct the mistakes done by the automation, which is not possible with fully automated programs. We showed that Open-CSAM was more accurate to measure CSA in regenerating and dystrophic muscles as compared with SMASH, MyoVision, and MuscleJ softwares and that the inter-experimenter variability was negligible. We also showed that, to obtain a representative CSA measurement, it was necessary to analyze the whole muscle section and not randomly selected pictures, a process that was easily and accurately be performed using Open-CSAM. To conclude, we show here an easy and experimenter-controlled tool to measure CSA in muscles from any experimental condition, including regenerating muscle.

Background

Skeletal muscle is capable of complete regeneration after an acute injury [1]. Skeletal muscle integrity is usually assessed by histological analyses, consisting of staining and/or immunofluorescent labeling of various cellular or molecular structural components of the tissue. Among these analyses, myofiber cross-sectional area (CSA) is widely used because it reflects the regenerative capacity of the muscle, i.e., the formation of new myofibers from the activation, proliferation, differentiation, and fusion of muscle stem cells [1]. CSA measurement is usually performed after immunofluorescent staining of laminin, a component of the basal lamina surrounding each myofiber, or of dystrophin that is located at the inside face of the sarcolemma.

Analysis methods range from manual quantification to programs showing various levels of automation. Manual quantification is potentially the most accurate method as the experimenter keeps total control over the myofibers being analyzed. However, the manual procedure is highly time-consuming and may present variability between experimenters. This is why automated programs were developed to limit the experimenter input and save time [2–7]. For example, SMASH [7] is a semi-automated open source MATLAB script allowing the assessment of several parameters, including CSA. MyoVision, a Windows program [2], was developed to fully automate the quantification process. This program combines several

---

* Correspondence: benedicte.chazaud@inserm.fr; gaetan.juban@univ-lyon1.fr
[1] Institut NeuroMyoGène, Univ Lyon, Université Claude Bernard Lyon 1, CNRS UMR 5310, INSERM U1217, 8 Avenue Rockfeller, F-69008 Lyon, France
Full list of author information is available at the end of the article

algorithms that were previously used separately in other programs, thus reducing the errors in the fiber identification and leading to a more accurate CSA measurement compared to SMASH on uninjured muscle [2]. Recently, MuscleJ, a fully automated plug-in in ImageJ described the fully automated quantification of various skeletal muscle parameters, including CSA [8].

Most of the automated softwares were tested on normal muscle or under conditions triggering atrophy/hypertrophy. In this context, the shape of the myofibers keeps polygonal and angular, myofibers keeping their contact with each other. On the contrary, regenerating muscle is characterized by the presence of round-shaped regenerating myofibers of highly variable size that, for the smallest ones, do not regularly contact surrounding fibers. Thus, variable myofiber shape, size, and extrafiber space characterize the regenerating muscle, rendering the automated quantification more difficult.

Here, we present a semi-automated CSA quantification method for skeletal muscle images applicable on any type of muscle and under any condition, including early and late regenerating muscle and dystrophic muscle. This method, named Open-CSAM (for Open [free]-Cross Sectional Area Measurement), is based on an ImageJ macro designed to automatically quantify CSA on immunofluorescent picture of the whole skeletal muscle section. It also includes some level of flexibility for the experimenter, allowing manual correction of the mistakes made by the automation. Moreover, it allows the analysis of the size of the myofibers on the whole muscle section, which we show here to be necessary to obtain an accurate measurement.

Methods

Animals and tissue preparation

C57BL/6 and mdx mice were used according to the French legislation. All experiments were performed on mice between 8- and 12-week-old, except for old mice, which were 2-year-old. In injury experiments, *Tibialis Anterior* (TA) muscles were injected with 50 μl of cardiotoxin (Latoxan) at 12 μM as previously described [9]. Fibrotic dystrophic mice (Fib-mdx) were generated as previously described [10] and mice were analyzed 1 week after the last injuries. TA muscles were mounted on pieces of cork and fixed with tragacanth gum. Then, they were frozen in isopentane cooled by liquid nitrogen and further stored at − 80 °C. TA muscles were sectioned thanks to a cryomicrotome (CM3050s, Leica), and the thickness of cryosection was 8 to 10 μm. The slides were then stored at − 80 °C until immunostaining. TA muscles showing more than 15% of uninjured area (i.e., without centrally located nuclei), indicating that CTX did not spread into the entire muscle, were excluded from the study.

Immunofluorescence

Slides were dried for 10 min at room temperature. Muscle cryosections were encircled with a hydrophobic pen (Dako) and were incubated with PBS containing Triton 0.5% for 10 min and then washed three times with PBS. They were incubated with BSA 2% for 1 h at room temperature and then incubated overnight with a rabbit anti-laminin antibody (1:200, L9393, Sigma-Aldrich) at 4 °C in a moist chamber. Slides were washed three times with PBS and incubated with FITC-conjugated donkey anti-rabbit secondary antibody (1:200; 711–095-152, Jackson Laboratories) at 37 °C for 45 min. Sections were soaked for 10 s in Hoechst solution H 33342 (1:1000, B2261, Sigma-Aldrich) and were washed once with PBS before mounting with antifading Fluoromount G medium (FP-483331, Interchim). Slides were stored at 4 °C protected from light until picture acquisition.

Image acquisition and quantification

As much as possible, the various conditions to be compared (e.g., WT vs. KO, normal vs. dystrophic muscle) should be recorded in similar conditions (microscope, magnification, exposure time, binning). For Open-CSAM validation and comparison with other softwares, at least 10 images were acquired manually at × 20 of magnification on an Axio Imager.Z1 microscope (Zeiss) connected to a CoolSNAP MYO CCD camera (photometrics) using MetaMorph Software (molecular devices). For whole cryosection analysis, slides were automatically scanned at × 10 of magnification using an Axio Observer.Z1 (Zeiss) connected to a CoolSNAP HQ2 CCD Camera (photometrics). The image of the whole cryosection was automatically reconstituted in MetaMorph Software. Open-CSAM was able to analyze images up to 110 Mo in 8 bit or 220 Mo in 16 bit. In case the final picture was too big to be analyzed at once because of limitation of ImageJ capacities, the picture was split into several parts (two to four) for the automated analysis. Between 2000 and 4000 fibers were analyzed in a few seconds. Open-CSAM workflow is presented in Fig. 1. The detailed macro code and explanations of the various functions are given in Additional file 1: Figure S1. If necessary, at the end of the automated measurement, manual correction is performed using ImageJ. The selection tools in the ROI Manager were used to remove “false” myofibers created by the automation, and the “Freehand selections” tool was used for hand-drawing “lacking” myofibers missed by the automation. These tools were used for full manual quantification. A tutorial is provided in Additional file 2: Figure S2.

MyoVision and MuscleJ analyses were performed as described [2, 8]. SMASH analysis was implemented with

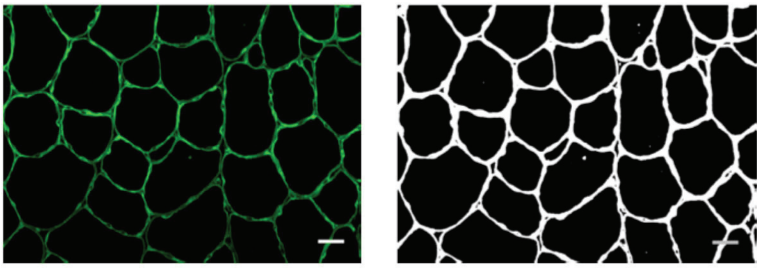

1. Open original image - Laminin staining

2. Threshold "Huang" - Binarization

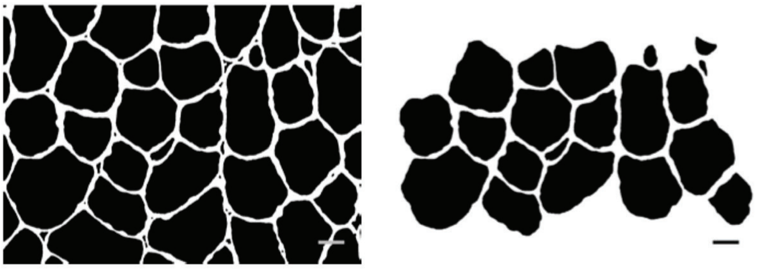

3. Open fonction + Fill holes

4. Selection of entire myofibers

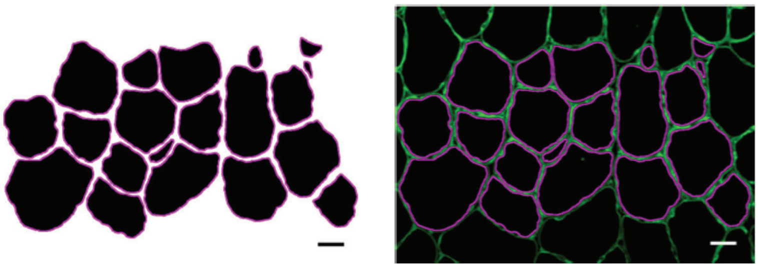

5. CSA Measure of entire myofibers

6. Overlay for visual checking

Fig. 1 Open-CSAM workflow. Step *1:* When the macro starts, a window automatically opens to select the image to be analyzed (here muscle cryosections immunostained for laminin). Step *2:* Open-CSAM applies the ImageJ threshold "Huang" on the image. Huang threshold was chosen by empiric assays. Threshold application allows image binarization. Step *3*: open function allows to adjust the myofiber contours. Myofibers are filled by the function "fill holes." Step *4:* Only the entire myofibers are selected to be analyzed. Other selected parameters as circularity and the size are used to avoid the inclusion of too many false myofibers. Step *5:* The area of the selected myofibers is measured. Step *6:* At the end of the measurement, all the region of interests (ROI, here the myofibers) are automatically superimposed for visual checking. It is then possible to manually delete or add new myofibers. Bars = 25 μm

a segmentation filter set to 11 [7]. This was empirically determined by testing values between 5 and 12 and visually inspecting the results. For MuscleAnalyzer analysis, the TIFF pipeline was tested following recommendations provided in the tutorial video [11]. Several threshold values were tested from 1 to 0.955 with no difference on the results. In all analyses, the applied size filter was the same as the one used for Open-CSAM (Table 1).

Statistical analyses

All images were acquired from at least two independent TA muscles per experimental condition and at least five randomly selected images per muscle were analyzed.

Table 1 Recommended size and circularity thresholds

Muscle type	Size threshold	Circularity threshold
D0 (young and old)	200 μm^{2*}	0.4
D8	50 μm^2 then adjust*	0.4
D14	100 μm^2 then adjust*	0.4
D28 (young and old)	150 μm^2 then adjust*	0.4
Fib-mdx	50 μm^2	0.4

*If too many small myofibers are missed, progressively decrease the size threshold by testing on 2–3 representative pictures

The Student t test, two-way ANOVA, or Spearman correlation test were used for statistical analyses. $P < 0.05$ was considered significant.

Results

Open-CSAM is more accurate than previously described softwares

In order to test the accuracy of Open-CSAM, its performance was compared with a fully manual quantification, a semi-automated software (SMASH), as well as two fully automated softwares: MyoVision and MuscleJ (Fig. 2). We analyzed TA muscle from various conditions, including uninjured muscle, regenerating muscle at several time points after acute injury (D8 and D14) in young and old mice, and a model of fibrotic dystrophy (Fib-mdx). Quantification was performed on cryosections immunofluorescently labeled with anti-laminin antibody, which labels the myofiber basal lamina. Immunolabeling against dystrophin or sarcolemal proteins was not used as this precludes the analysis in dystrophies where these proteins are lacking or altered. As previously described [2], MyoVision produced significantly higher mean CSA values as compared with manual quantification (Fig. 2a, between 4.3 and 47.7% increase depending on the experimental condition). Mean CSA values obtained with MuscleJ were similar to the manual quantification for uninjured young as well as 14 and 28 days post-injury muscles. However, it gave higher mean CSA values in 8 days post-injury regenerating muscles, old muscles (uninjured and 28 days post-injury), and dystrophic muscles (Fig. 2a, between 3.2 and 19.4% increase). Mean CSA values obtained with SMASH were very close to the manual quantification in uninjured old and young 8- and 28-days post-injury muscles. However, SMASH produced higher mean CSA values in uninjured muscles (young and old) (+ 3 and + 1%, respectively), and lower mean CSA values in 14 days post-injury muscles (− 4%) (Fig. 2a). On the other hand, Open-CSAM without manual correction gave mean CSA values close to those obtained manually, with a slight underestimation (between 2 and 7.3% decrease as compared with manual quantification), except in Fib-mdx muscles where it was slightly overestimated (+ 4.4%) (Fig. 2a). This was explained by the fact that Open-CSAM measured the area inside the basal lamina staining, which corresponds to the true area of the myofiber. With manual quantification, the experimenter tends to draw the limits of the myofibers more on the laminin staining, thus including a small part of the basal lamina, therefore slightly overestimating the myofiber area (Fig. 2a). In the case of Fib-mdx muscle, the overestimation by Open-CSAM was explained by an oversight of small myofibers (see below). During the revision process of this manuscript, MuscleAnalyzer, a customized pipeline within the CellProfiler program allowing fully automated CSA measurement, was released [11]. We tested this pipeline on the same samples as above (Additional file 3: Figure S3). As it strongly overestimated mean CSA as compared with manual quantification (between 38.4% and 254.8% increase depending on the condition), this software was not considered for further analysis.

Despite an increased CSA value obtained using MyoVision, the correlation between MyoVision and manual quantification for each picture was strong in uninjured muscles (young and old mice), as well as 14 and 28 days post-injury regenerating muscles (Fig. 2b and Additional file 4: Figure S4A, $R^2 > 0.95$), suggesting that in these conditions, CSA overestimation by MyoVision was similar on all the pictures and did not introduce a specific bias. On the contrary, the correlation was much lower on muscles at 8 days post-injury, 28 days post-injury in old mice and in fibrotic muscles (Fig. 2b and Additional file 4: Figure S4A, $R^2 < 0.89$), which represent conditions exhibiting smaller myofibers and/or defects in regeneration. Similarly, overall correlation between MuscleJ and manual quantification was very strong in uninjured muscles (young and old mice, Fig. 2b and Additional file 4: Figure S4A, $R^2 > 0.97$). Although this correlation was lower on young 8 days and old 28 days post-injury as well as on fibrotic muscles, it was better than MyoVision. Finally, correlation was lower with MuscleJ than with MyoVision for the 14 and 28 days post-injury conditions. Correlation between SMASH and manual quantification was strong in uninjured young muscles (Fig. 2b, $R^2 = 0.97$). However, correlation was less good when compared with MyoVision and MuscleJ in 28 days post-injury muscles (young and old mice, Additional file 4: Figure S4A, $R^2 = 0.8352$ for young and 0.9278 for old). For all other conditions, SMASH accuracy compared with manual quantification was intermediate between that of MyoVision and of MuscleJ (Additional file 4: Figure S4A, $0.8489 < R^2 < 0.9364$). These data indicate that the differences observed between manual quantification and MyoVision, MuscleJ, or SMASH are condition-dependent, thus introducing a bias. We then used Open-CSAM, first without applying any manual correction. The correlation between Open-CSAM and manual quantification was better or equivalent to that of MyoVision, MuscleJ, or SMASH in all the analyzed experimental conditions (Fig. 2b and Additional file 4: Figure S4A, $R^2 > 0.9454$). This suggests that Open-CSAM performance was more consistent through the various experimental conditions.

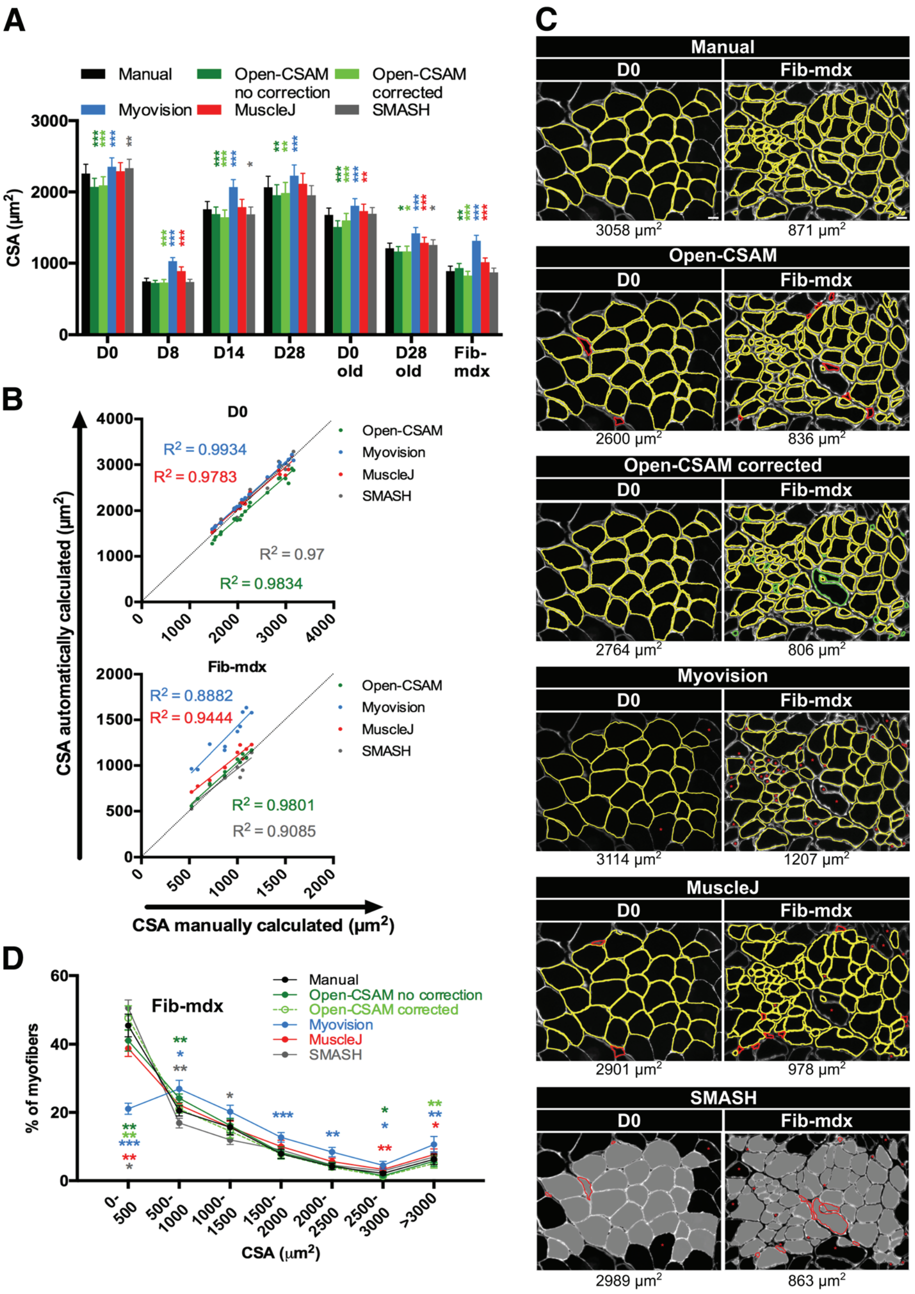

Fig. 2 Open-CSAM comparison with MyoVision, MuscleJ, and SMASH softwares. The same pictures were analyzed either by manual measurement or using Open-CSAM (with or without manual correction), MyoVision, MuscleJ, or SMASH softwares. **a** Mean cross-section area (CSA) obtained on various *Tibialis Anterior* (TA) muscles. Muscles were isolated from 8- to 12-week-old mice uninjured (D0) or 8 days (D8), 14 days (D14), and 28 days (D28) post-cardiotoxin (CTX) injury, from 2-year-old mice uninjured (D0 old) or 28 days post-CTX injury (D28 old) and from dystrophic fibrotic mice (Fib-mdx). Results are mean ± SEM of 10 images from 2 muscles (Fib-mdx), 20 images from 2 muscles (D0 and D0 old), 30 images from 3 muscles (D28 and D28 old), 40 images from 4 muscles (D8), and 45 images from 4 muscles (D14). **b** Correlation between manual measurement (*X* axis) and Open-CSAM (without manual correction), MyoVision, MuscleJ, or SMASH (*Y* axis) measurements performed on the same images used in **a**. Each dot represents a picture. The dotted line represents the identity line. **c** Representative images measured manually, by Open-CSAM (before and after correction), MyoVision, MuscleJ, or SMASH softwares. Red fibers were false myofibers identified by the softwares, and green fibers were myofibers not considered by the Open-CSAM software and manually drawn. Lacking myofibers using MyoVision, MuscleJ, or SMASH softwares are shown by red asterisks. **d** Distribution of the CSA obtained with the six methods using the Fib-mdx samples used in **a**. Results are mean ± SEM of 10 images from 2 muscles (Fib-mdx). White bar = 25 µm. $^{*}p < 0.05$, $^{**}p < 0.01$, and $^{***}p < 0.001$ as compared with manual quantification

Manual correction is necessary for best accuracy

Figure 2c shows two examples of quantification performed on a single image from an uninjured muscle (left panel) and a dystrophic fibrotic muscle (right panel). In the uninjured muscle picture, Open-CSAM and MuscleJ identified two false myofibers (red lines), which were manually removed with Open-CSAM (Open-CSAM corrected). On the other hand, MyoVision missed two myofibers (red asterisks) while SMASH both identified three false myofibers and missed two myofibers. However, as the myofiber size was quite homogeneous in this picture, this did not really impact the calculated CSA value. In the fibrotic muscle picture (Fig. 2c, right panel), Open-CSAM identified 7 false myofibers (red lines) and missed 16 myofibers that were manually corrected afterwards (green lines). MyoVision missed 33 myofibers (red asterisks) and identified 1 false fiber, which could be excluded by size filter in MyoVision software (red line), inducing a 29% artificial increase in CSA, as compared with manual quantification. Similarly, MuscleJ identified 7 false myofibers (red lines) and missed 14 fibers (red asterisks), leading to a 12.3% increase as compared with manual quantification. Finally, SMASH missed 14 myofibers and misidentified 9 fibers, leading to an 8.2% decrease of mean CSA compared to manual quantification. The distribution of the myofiber CSA in Fib-mdx muscles (same samples as in Fig. 2a) clearly showed that MyoVision and MuscleJ, and to a lower extent, Open-CSAM, preferentially missed the small myofibers ($< 500\ \mu m^2$) (Fig. 2d), thus artificially overestimating the mean CSA. On the contrary, SMASH overestimated the proportion of small myofibers. Taken together, these results show that Open-CSAM accuracy is more consistent as compared with other softwares through various experimental conditions. However, despite its performance, manual correction is necessary for best accuracy. Open-CSAM was designed to enable easy manual correction, allowing the user to directly draw missing fibers and delete the false ones at the same time in ImageJ (Additional file 2: Figure S2). As shown in Additional file 4: Figure S4B, manual correction applied to Open-CSAM improved the measurement accuracy in all conditions ($R^2 > 0.97$) except in old mice 28 days post-injury ($R^2 = 0.9665$ before and 0.962 after correction). In Fib-mdx muscle, this was associated with a convergence of the overall myofiber size distribution towards the distribution obtained with manual quantification (Fig. 2d), notably with a better consideration of small myofibers ($< 500\ \mu m^2$).

Whole section analysis is necessary for best accuracy

CSA analysis is usually performed on a subset of images randomly taken throughout the muscle section. Depending on the experimenter, the number of images and thus the number of analyzed myofibers can be variable. Moreover, within the same muscle, myofiber size can be quite heterogeneous and a bias can be introduced depending on the choice of the pictures. Figure 3a shows an example of an entire reconstituted muscle picture. We measured CSA on individual images, calculated the mean CSA on several subsets of images, and compared the results with the CSA obtained on the whole section. When the measurement was made only using a subset of pictures, the myofiber CSA differed from 5 to 28% to that measured on the whole muscle (Fig. 3b). We particularly observed that CSA was overestimated when the left half of the muscle was measured, that corresponded in this example to the peripheral part of the muscle where regeneration is ended. Inversely, measuring the right part of the muscle, here corresponding to smaller regenerating myofibers localized at the center of the muscle, underestimated CSA value. Thus, because TA regeneration after a toxic injury is a centripetal process that ends first at the periphery of the muscle, the whole muscle section should be analyzed when measuring CSA of regenerating muscle in order to obtain an unbiased picture of the process. Moreover, as in diseased muscle, foci of fiber damage or remodeling can occur anywhere, analyzing the whole section also insures an accurate measurement in this context.

Use of Open-CSAM is robust among users

In a whole muscle section, the number of manual corrections can be variable depending on the quality of the muscle section and of the immunostaining. Considering a high quality of both, we found that the amount of false plus lacking fibers, which needed to be manually removed or re-drawn, ranged from 5% in non-damaged muscles to 10 to 25% in damaged muscles (Fig. 4a). As the manual corrections after Open-CSAM analysis can represent up to 25% of the myofibers, thus potentially introducing variability among users, we tested the robustness of this method. To do so, three independent experimenters analyzed the same image taken from an adult TA muscle 28 days post-CTX injury, where the majority of the muscle has fully regenerated and some central areas are still regenerating (Fig. 4b, c). This muscle was chosen because of the high number of required manual corrections. Using a $100\ \mu m^2$ size filter and a 0.4 circularity threshold (see Additional file 1: Figure S1 and Table 1), Open-CSAM identified 3757 fibers (Fig. 4c, left images), resulting in a CSA of $1566.8\ \mu m^2$ (Fig. 4b, left). As shown in Fig. 4c, two areas showed a large number of fibers missed by Open-CSAM. The first area (blue box) was composed of fibers showing a high variability in size where Open-CSAM missed mainly very small fibers. The second area (red box) was composed of medium- to large-sized fibers but with a lower laminin staining intensity. In this area, Open-CSAM failed to identify most of the fibers. Depending on the user, 50 to 145 false fibers were deleted and 860 to 1019 fibers

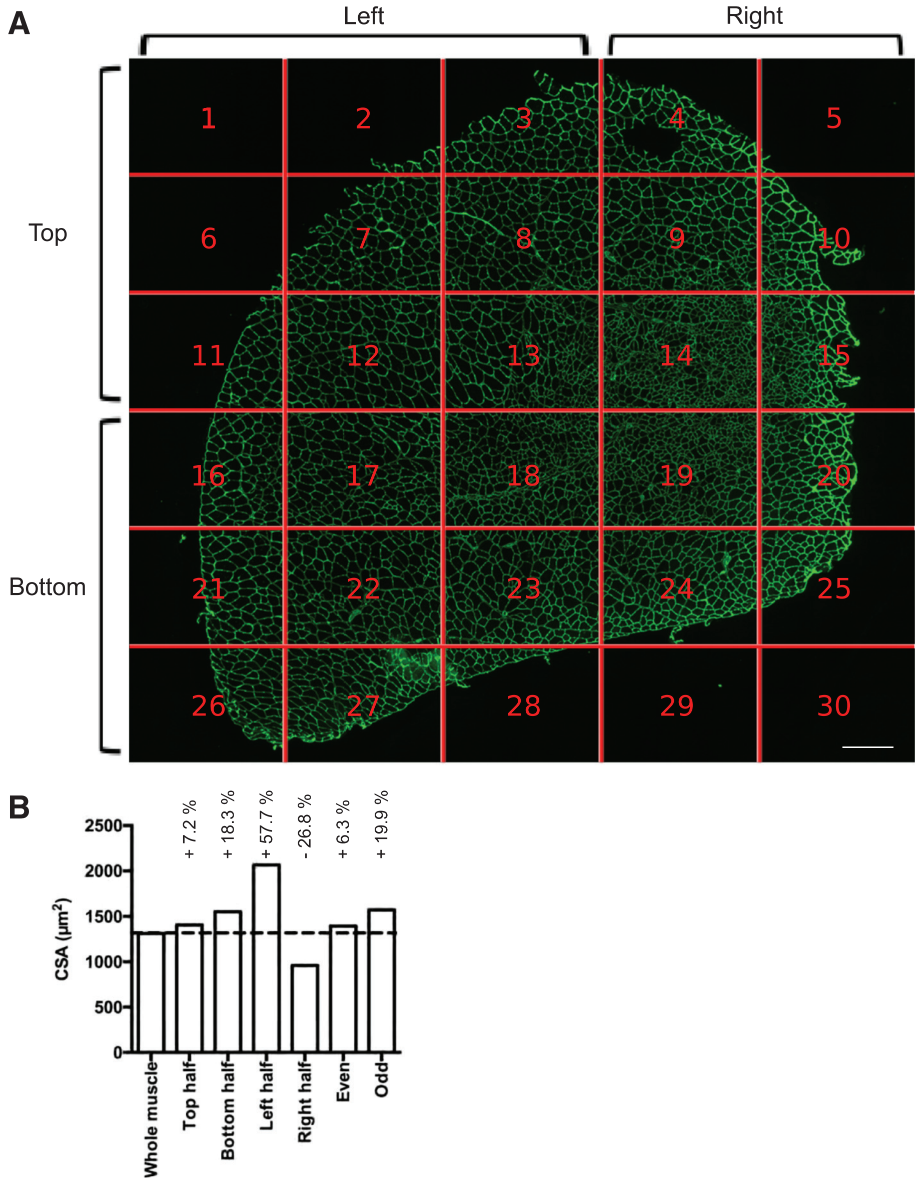

Fig. 3 Whole muscle analysis by Open-CSAM. **a** Whole reconstitution of a laminin-stained cryosection of a TA muscle 28 days post-CTX injury (30 pictures were automatically recorded and assembled by MetaMorph software). The position of each individual image is highlighted by the red lines. White bar = 250 µm. **b** Mean cross-section area obtained after various subsettings of pictures in **a**

were manually added (Fig. 4b, right). Despite this variability in the number of manual corrections performed by each user, the corrected CSA reached 1454, 1437, and 1456 µm^2, meaning that variability between users was below 1%. Altogether, these results show that despite the manual corrections required by Open-CSAM, there is no bias introduced by the experimenter.

Open-CSAM is an accurate tool for whole muscle CSA analysis in regenerating muscle

As we showed that CSA quantification with Open-CSAM was highly accurate on individual images in various experimental conditions and that whole muscle analysis was necessary, we tested its performance on several whole muscle images and compared it to fully automated quantification by MyoVision and MuscleJ, as well as to SMASH. We analyzed whole muscle images from young uninjured, 8 days post-injury and 28 days post-injury mice (Fig. 5 and Additional file 5: Figure S5). As we showed for × 20 individual pictures in uninjured muscle (Fig. 2), MyoVision, MuscleJ, and SMASH modestly overestimated the CSA as compared with corrected Open-CSAM (Fig. 5a, + 11.7%, + 16.5%, and + 13.9%, respectively) (Fig. 5a). On the same muscle, manual correction had negligible impact on

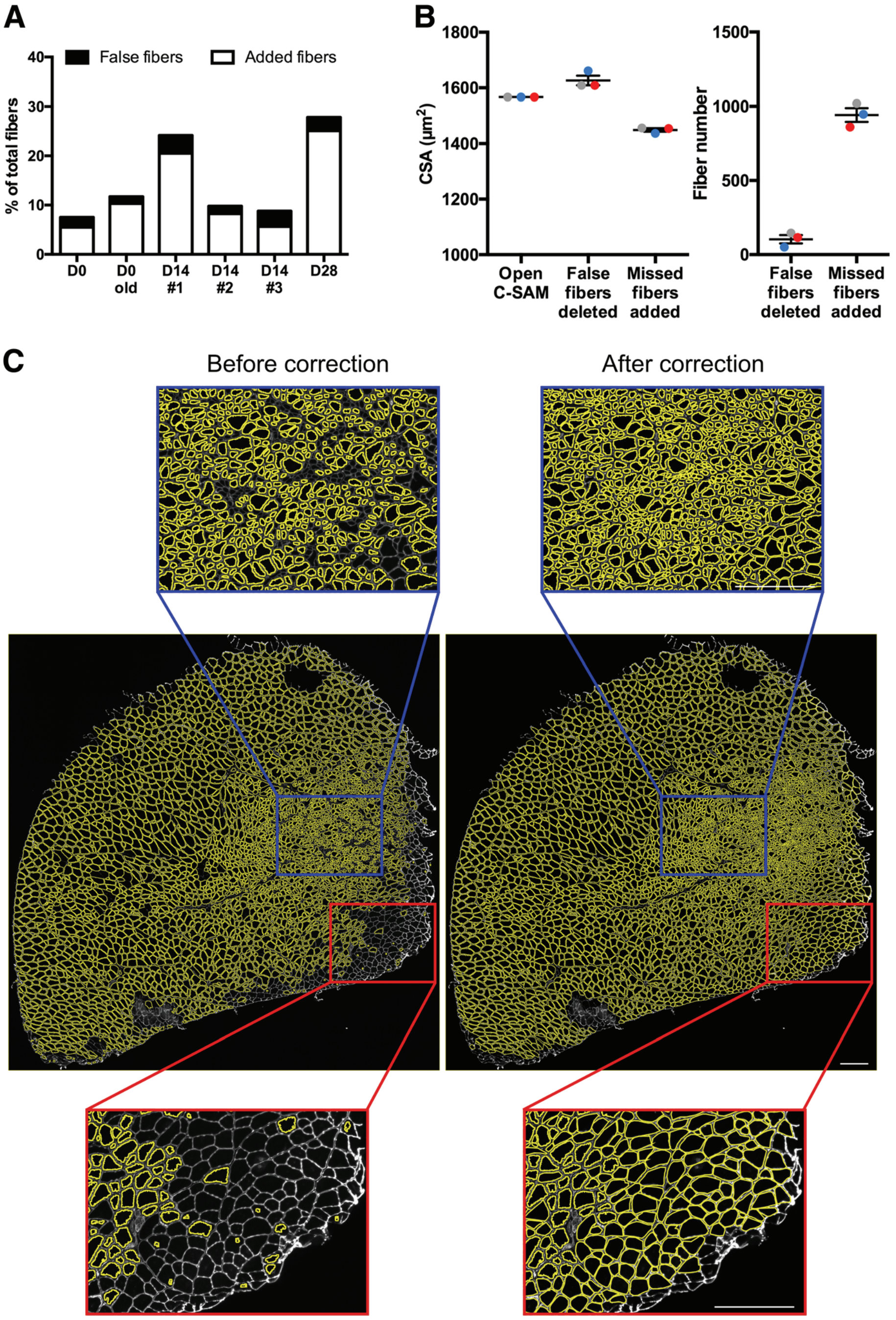

Fig. 4 Manual corrections after Open-CSAM analysis. **a** Percentage of false myofibers detected (black histograms) and missed myofibers (white histograms) by Open-CSAM that needed manual correction for TA muscles from young and old uninjured mice as well as from 3 muscles analyzed 14 days post-CTX injury. **b**, **c** Open-CSAM analysis of a TA muscle 28 days post-CTX injury. **b** CSA (left graph) and number of fibers manually corrected (right graph) after analysis by Open-CSAM by three different users (each color represents a single user). **c** Whole image of the TA muscle analyzed in **b** showing myofibers (yellow) detected by Open-CSAM before (left panel) and after (right panel) manual correction. Blue and red boxes represent zoom-in examples of two specific areas that needed extensive manual correction. White bar = 250 µm

CSA obtained by Open-CSAM, highlighting its high performance on uninjured whole muscle section (Fig. 5a, − 1.1% before correction). Corroborating this observation, CSA distribution was identical for Open-CSAM before and after correction (Fig. 5d). On the contrary, MyoVision, MuscleJ, and SMASH overlooked small fibers (< 1000 µm^2) and overestimated bigger fibers (> 3000 µm^2). In the D8

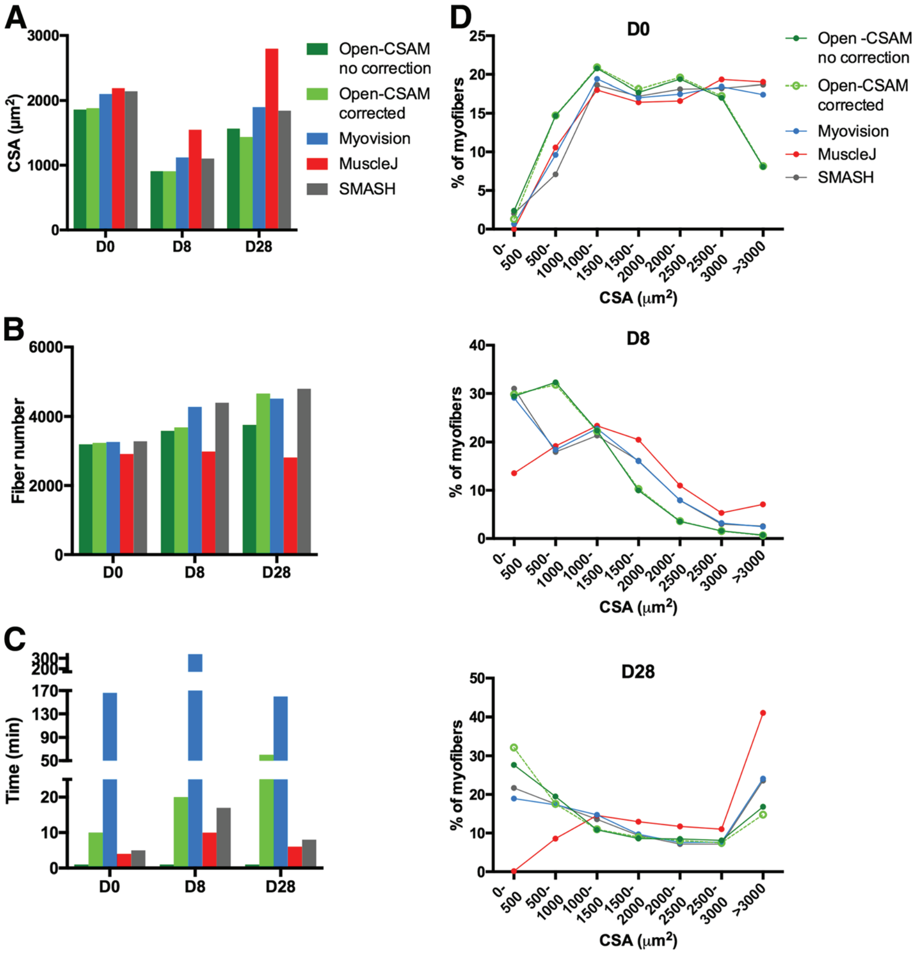

Fig. 5 Comparison of Open-CSAM, MyoVision, MuscleJ, and SMASH CSA quantification on whole muscle sections. CSA was measured using Open-CSAM (with or without manual correction), MyoVision, MuscleJ, or SMASH on whole TA muscle images obtained from uninjured (D0) or 8 days (D8) and 28 days (D28) post-CTX injury. **a** Mean CSA measured by the different softwares. **b** Number of fibers identified by the softwares. **c** Total analysis time required by the softwares. **d** Distribution of CSA obtained by the five methods on D0 (top graph), D8 (middle graph), and D28 (bottom graph) whole muscles

condition, where small fibers represent an important part of the whole muscle section area and the D28 condition, where small myofibers are still concentrated in specific areas (see Fig. 4), MyoVision (+ 24 and + 32.1%, respectively), MuscleJ (+ 71.2 and + 92.3%, respectively), and SMASH (+ 22 and 26.8%, respectively) accounted for a much higher CSA than Open-CSAM. This is mainly due to the non-detection of the small myofibers (Fig. 5d) and, in the case of MuscleJ, to the merging of several myofibers into one (Additional file 5: Figure S5B, Fig. 5b). Again, correction in Open-CSAM induced a negligible change in CSA measurement on day 8 post-injury muscle (Fig. 5a, + 0.3% before correction). Finally, manual correction of Open-CSAM in day 28 post-injury muscle corrected a slight underestimation of small fibers (Fig. 5d), leading to an artificial increase in CSA (Fig. 5a, + 7.8% before correction).

The main defect of Open-CSAM is the time of experimenter that is required for the complete implementation of CSA measurement. Although running Open-CSAM macro in ImageJ took less than 1 min (even for the whole muscle pictures), which was faster compared to other softwares (4 to 10 min for MuscleJ, 5 to 17 min for SMASH, and 166 to 340 min for MyoVision), the post-automation manual corrections lasted between 10 and 60 min in the examples provided (Fig. 5c, Additional file 5: Figure S5). However, those corrections are required for achieving a full analysis of the whole muscle in order to provide an accurate CSA value. Taken together, these results show that Open-CSAM is a highly accurate tool to measure myofiber CSA on whole muscle section images from different experimental conditions, including regenerating muscle.

Discussion

Histology is the gold standard technique to assess some characteristics of skeletal muscle. Measurement of myofiber CSA is classically used as a parameter of normal and pathological skeletal muscle regeneration after labeling with anti-laminin or anti-dystrophin antibodies. However, there are various strategies to analyze images and CSA measurement that can give highly heterogeneous results. On the one hand, manual quantification, consisting in manually drawing the myofiber contour to measure the area, is extremely time-consuming and potentially variable between experimenters as it is meticulousness-dependent. According to our experience, it takes about 1 h to draw 1000 fibers. On the other hand, automated programs that were developed to reduce the impact of the experimenter, and to save time, give satisfactory results in uninjured muscle [2–8] but fail to be accurate in regenerating muscle.

Among the recent described softwares are SMASH, MyoVision, and MuscleJ. SMASH is a MATLAB application which is also available as a free Windows program (SMASH Stand Alone). MyoVision is a program operating in Windows environment whereas MuscleJ is a macro working in ImageJ program (Table 2). They were developed to automate, with various levels of flexibility, the quantification of several muscle parameters including fiber number, CSA, myonuclei number and fiber type distribution. As previously described [2], MyoVision showed a significant CSA overestimation as compared with manual quantification. This could be explained by the stronger overlapping of MyoVision outlines with the laminin staining (Fig. 2c), thus integrating a part of the basal lamina into the myofiber area. Despite this overestimation of the mean CSA as compared with manual quantification, MyoVision performed accurately on isolated images from uninjured muscles. However, regenerating, old and dystrophic muscles are characterized by high myofiber size heterogeneity. In this context, MyoVision measurement was still good at day 14 and 28 after injury, i.e. at time points when regenerating myofibers are already formed. On the contrary, correlation with manual estimation was much lower in muscles at 8 days post-injury in young mice, at 28 days post-injury in old mice and in muscles of dystrophic fibrotic mice. These three conditions are characterized by a lower mean CSA and the presence of high numbers of very small myofibers, which are not considered by MyoVision, thus overestimating the mean CSA. MuscleJ software was efficient in measuring mean CSA in individual × 20 pictures from uninjured young as well as 14 and 28 days post-injury muscles. However, it measured higher mean CSA values in 8 days post-injury regenerating muscles, old muscles (uninjured and 28 days post-injury) and dystrophic muscles, even though the values were closer to manual quantification than that calculated by MyoVision. Here again, this was due to an oversight of small myofibers. Finally, SMASH showed high accuracy in uninjured young muscles. For the other conditions, even though mean CSA was relatively close to manual quantification, the accuracy was very variable between images, leading to overestimation of small myofibers in Fib-mdx (Fig. 2d) and oversight of these same small fibers in regenerating muscles (Fig. 5d), making it not reliable to analyze and compare various conditions.

In order to provide a tool usable in various biological conditions, we developed Open-CSAM, an ImageJ macro allowing the automatic measurement of CSA with the possibility for the experimenter to apply manual corrections afterwards. CSA values obtained with Open-CSAM were very close to the values obtained manually in all tested conditions. Generally, Open-CSAM omitted only few myofibers in muscles containing small fibers

Table 2 Comparison of software characteristics

Program	Software base	OS	Minimal configuration tested		Manual correction
			PC	MAC	
Open-CSAM	ImageJ plugin	Mac OS/ Windows	Windows 10-Intel core i3 CPU 550 3.2 GHz-4 Go RAM	Mac OS 10.12/Intel core i3–3.2 GHz/12 Go RAM	Yes—during the analysis ➔ Draw/delete ImageJ tools
MyoVision	Windows application	Windows	Windows 10-Intel core i3 CPU 550 3.2 GHz-4 Go RAM (single image analysis)/Windows 7-Intel core i5 vpro 3.1 GHz/16 Go RAM (whole muscle analysis)	Not applicable	No
MuscleJ	ImageJ plugin	Mac OS/ Windows	Windows 10-Intel core i3 CPU 550 3.2 GHz-4 Go RAM	Mac OS 10.13/Intel core i5–2.7 GHz/16 Go RAM	Yes—after the analysis ➔ Open picture ➔ Import ROI file on the picture ➔ Draw/delete ImageJ tools
SMASH Stand Alone	Windows application	Windows	Windows 10-Intel core i3 CPU 550 3.2 GHz-4 Go RAM	Not applicable	Yes—during the analysis ➔ Step 1 draw—validate ➔ Step 2 delete—validate (cumbersome: small screen, no back and forth allowed between steps 1 and 2)

(regenerating muscle, old muscle, dystrophic muscles). Then, lacking myofibers are easily manually drawn and incorporated into the analysis using ImageJ, which is not possible using the fully automated softwares. The main drawback of Open-CSAM is that it identifies some false myofibers in the interstitial space between myofibers, notably when this space is large in early regenerating and fibrotic muscles. This issue can be overcome by increasing the size and the circularity thresholds but this also increases the risk of omitting real myofibers. Because it is faster to delete false myofibers than manually drawing lacking myofibers, we recommend to keep thresholds as low as possible to reduce the number of lacking myofibers. We therefore provided starting thresholds for the different conditions we have tested, that have to be adjusted depending on the specific experiment (Table 1). According to our experience, the false fibers identified by Open-CSAM represented less than 5% of the total fibers in all the muscles we have analyzed so far.

CSA measurement is usually performed on a subset of images randomly taken throughout the muscle section. However, myofiber size is quite heterogeneous within the same muscle, and we showed that considering only a part of the muscle section led to the introduction of bias depending on the image selection, potentially hiding a relevant phenotype or artificially creating a non-relevant one. Of note, image acquisition and reconstitution of the whole muscle section is automatically performed, saving time, as compared with manually recording random pictures. Then, Open-CSAM is capable of measuring the myofiber CSA on the whole section in a few seconds. Depending on the size of the image, it may be necessary to split it in two or four parts. This may be also useful when the laminin labeling intensity is not homogenous on the entire section since Open-CSAM may omit faint labeled areas.

When measuring CSA on whole muscle section pictures, using uninjured or 8-day and 28-day regenerating muscles, we found that Open-CSAM (including the manual post-automation corrections) was the most accurate way to measure myofiber CSA. MuscleJ program was efficient at implementing CSA from uninjured muscle (still with overestimated values) but failed to accurately measure myofiber CSA of regenerating muscle, due to failure to detect small fibers and to merging of several myofibers into one. Even though MuscleJ was built as a ready-to-use toolbox to avoid experimenter intervention, post-automation corrections are possible. Indeed, the user may generate a file containing the ROIs analyzed that can be imported back into ImageJ to perform manual corrections in a similar way as Open-CSAM. However, given its poor performance on whole regenerating muscle section as compared with Open-CSAM, the amount of manual corrections and thus the time spent would be not competitive towards Open-CSAM measurement. SMASH and MyoVision gave similar results, as they moderately overestimated mean CSA in uninjured muscle, an overestimation that was amplified in 8-day and 28-day regenerating muscles which contain a higher proportion of small rounded-shape myofibers. MyoVision was very slow in implementing the analysis of the whole muscle images (between 166 and 340 min), making it not competitive towards manual measurement. Moreover, it does not allow manual correction. SMASH was faster (between 5 and 17 min), and it was designed to allow the user to perform manual corrections during the analysis. However, the correction process has several drawbacks. First, the application cannot be displayed into full screen, which makes inconvenient to easily detect the myofiber delimitations. Second, after the segmentation, the correction process is composed of 2 sequential steps. The first step allows to manually split merged fibers or draw the missed ones. After validation of the drawing, the second step allows manual deletion of the false fibers identified by the program. Unfortunately, at this point, it is not possible anymore to come back to correct merged or missed fibers that would have appeared after the second step. Given this lack of flexibility, performing manual correction in Open-CSAM is much easier and faster.

According to our experience with Open-CSAM, the amount of manual corrections required after the automatic measurement depends on the status of the muscle, the quality of the cryosection, and the quality of the immunolabeling. We recommend performing a new cryosection and/or labeling rather than trying to analyze poor quality images. Typically, if we consider a high-quality image, the analysis of an uninjured TA lasts less than 15 min to process 2000 to 3000 myofibers. In the worst condition we experienced, processing of a regenerating TA can last from 15 min to 1 h for the experimenter to obtain an accurate measurement of myofiber CSA (as compared with 1 h per 1000 fibers in the case of a full manual quantification, thus 2–3 h per muscle). Moreover, we showed that despite the relatively high level of manual correction required for some muscles, the difference in corrected CSA obtained by independent experimenters was negligible (less than 1%), highlighting the robustness of this method.

Conclusion

The use of Open-CSAM program on whole muscle sections is a powerful strategy to measure myofiber CSA of muscles from various experimental conditions in an easy, highly accurate, and reproducible way, providing values very close to the absolute values. This user-friendly (tutorial in Additional file 2: Figure S2) method is semi-automated and therefore requires the commitment of the experimenter (who is still the best expert to define what a myofiber is), allowing the most accurate CSA measurement of regenerating muscle so far.

Additional files

Additional file 1: Figure S1. Macro to be run for the implementation of Open-CSAM program (left) and related explanations of the functions (right column). (PDF 31 kb)

Additional file 2: Figure S2. Tutorial for the use of Open-CSAM. (PDF 785 kb)

Additional file 3: Figure S3. The same pictures as in Fig. 2 were analyzed either by manual measurement or using MuscleAnalyzer. The mean CSA obtained with the two methods is shown. ***$p < 0.001$ as compared with manual quantification by two-way ANOVA analysis. (PDF 80 kb)

Additional file 4: Figure S4. Mean CSA was measured manually and with Open-CSAM, MyoVision, MuscleJ, or SMASH softwares on the same samples as described in Fig. 2a. Muscles were isolated from 8- to 12-week-old mice 8 days (D8), 14 days (D14), and 28 days (D28) post-CTX injury, from uninjured (D0 old) or 28 days post-CTX injury (D28 old) 2-year-old mice. **A** The correlation between manual measurement (*X* axis) and Open-CSAM (without manual correction), MyoVision, MuscleJ, or SMASH (*Y* axis) measurements is presented. **B** Correlation between manual measurement (*X* axis) and Open-CSAM (*Y* axis) before and after manual correction. Each dot represents a picture. The dotted line represents the identity line. (PDF 833 kb)

Additional file 5: Figure S5. CSA was measured using Open-CSAM, MyoVision, MuscleJ, or SMASH softwares on whole TA muscle images obtained from uninjured (D0) or 8 days (D8) and 28 days (D28) post-CTX injury. **A** Pictures showing the myofibers (yellow shapes except for SMASH which is in gray) detected by Open-CSAM, MyoVision, SMASH, and MuscleJ. The white dotted lines show where the images were split for Open-CSAM and MyoVision analysis. **B** Red boxes represent zoom-in examples of specific areas obtained by MuscleJ. Red asterisks show examples of group of myofibers that are merged. White bar = 250 µm. (PDF 12792 kb)

Abbreviations

CSA: Cross-sectional area; CTX: Cardiotoxin; Fib-mdx: Fibrotic dystrophic mice; ROI: Region of interest; TA: Tibialis anterior

Funding

Chazaud Lab is funded by CNRS, INSERM, and UCBL.

Availability of data and materials

N/A.

Authors' contributions

RM and BC helped in the conceptualization. TD, SLy, BC, DR, JG, RM, BC, and GJ contributed to the methodology. TD, JG, RM, BC, and GJ helped in the validation and formal analysis. TD, SLi, SLy JB, AK, AT, and GJ carried out the investigation. TD and GJ wrote the original draft and helped in the visualization. TD, SL, AT, DR, JG, RM, BC, and GJ helped in writing the review and editing. BC and GJ supervised the study. All authors read and approved the final manuscript.

Ethics approval and consent to participate

N/A

Consent for publication

N/A

Competing interests

The authors declare that they have no competing interests.

Publisher's Note

Author details

[1]Institut NeuroMyoGène, Univ Lyon, Université Claude Bernard Lyon 1, CNRS UMR 5310, INSERM U1217, 8 Avenue Rockfeller, F-69008 Lyon, France. [2]CREATIS, Univ Lyon, Université Claude Bernard Lyon 1, CNRS UMR 5220, INSERM U1206, INSA Lyon, 69100 Villeurbanne, France. [3]CIQLE, Lyon Bio Image, Univ Lyon, Université Claude Bernard Lyon 1, Structure Fédérative de Recherche santé Lyon-Est CNRS UMS3453/INSERM US7, 69008 Lyon, France.

Received: 17 September 2018 Accepted: 4 December 2018
[redacted]

References

1. Yin H, Price F, Rudnicki MA. Satellite cells and the muscle stem cell niche. Physiol Rev. 2013;93:23–67.
2. Wen Y, Murach KA, Vechetti IJ Jr, Fry CS, Vickery C, Peterson CA, et al. MyoVision: software for automated high-content analysis of skeletal muscle immunohistochemistry. J Appl Physiol. 2018;124:40–51.
3. Miazaki M, Viana MP, Yang Z, Comin CH, Wang Y, Costa L d F, et al. Automated high-content morphological analysis of muscle fiber histology. Comput Biol Med. 2015;63:28–35 Elsevier.
4. Liu F, Fry CS, Mula J, Jackson JR, Lee JD, Peterson CA, et al. Automated fiber-type-specific cross-sectional area assessment and myonuclei counting in skeletal muscle. J Appl Physiol. 2013;115:1714–24.
5. Kostrominova TY, Reiner DS, Haas RH, Ingermanson R, McDonough PM. Automated methods for the analysis of skeletal muscle fiber size and metabolic type. Int Rev Cell Mol Biol. 2013;306:275–332.
6. Kim Y-J, Brox T, Feiden W, Weickert J. Fully automated segmentation and morphometrical analysis of muscle fiber images. Cytometry. 2007;71A:8–15.
7. Smith LR, Barton ER. SMASH–semi-automatic muscle analysis using segmentation of histology: a MATLAB application. Skelet Muscle. 2014;4:21–16.
8. Mayeuf-Louchart A, Hardy D, Thorel Q, Roux P, Gueniot L, Briand D, et al. Muscle J: a high-content analysis method to study skeletal muscle with a new Fiji tool. Skelet Muscle. 2018;8:25.
9. Théret M, Gsaier L, Schaffer B, Juban G, Ben Larbi S, Weiss Gayet M, et al. AMPKα1-LDH pathway regulates muscle stem cell self-renewal by controlling metabolic homeostasis. EMBO J. 2017;36:1946–62.
10. Desguerre I, Arnold L, Vignaud A, Cuvellier S, Yacoub-Youssef H, Gherardi RK, et al. A new model of experimental fibrosis in hindlimb skeletal muscle of adult mdx mouse mimicking muscular dystrophy. Muscle Nerve. 2012;45:803–14.
11. Lau YS, Xu L, Gao Y, Han R. Automated muscle histopathology analysis using CellProfiler. Skelet Muscle. 2018;8:32.